



**Politecnico  
di Torino**

CAPONNETTO HUEBER

**Politecnico di Torino**

Facoltà di Ingegneria

Corso di Laurea Magistrale in Ingegneria Aerospaziale

October 2022

Master's Thesis

**Verification and Validation in CFD for  
Benchmarking Hydrodynamics Simulations  
using RANS Turbulence Models**

Academic supervisors

Prof. D. D'Ambrosio

Prof. G. Mattiazzo

Corporate supervisors

Eng. M. Brito

Candidate

Ignazio Alessio Giudice

s278057

Academic year 2021/2022



## Disclaimer

This thesis shows a study performed by the author using instruments and guidelines provided by Caponnetto Hueber and Siemens together with materials present in literature. Nevertheless the results and the comments presented should not be linked with Caponnetto Hueber but only with the person of the Author himself.

## ABSTRACT

Since the 1990s Computational Fluid Dynamics (CFD) has had an upsurge of interest due to the availability of more powerful high-performance computing hardware, as well as more efficient and robust algorithms. Indeed, in the last decade, it has gained more and more credibility becoming a powerful tool for scientists and engineers in the design process. It gives the possibility to design and test a model without the necessity to build a real one, hence saving considerable costs.

Nevertheless, not all problems are solved with CFD, as the users of this tool must have a certain degree of experience to model reality. To tackle this issue, and increase confidence in the know-how, a process called Verification and Validation (V&V) has been developed by the CFD community.

The goal of this study is to use CFD settings and guidelines provided by Caponnetto Hueber, a consultancy CFD company in the marine industry, and Siemens to benchmark hydrodynamics simulations. To accomplish this, four experimental test cases provided by research institutes are thus benchmarked: propeller, ship, planing hull, and sailing yacht.

The CFD studies are carried out trying to replicate as close as possible the conditions of the towing tank test. After having carried out the simulations, the results are post-processed, analyzed, and subjected to the V&V process based on the work carried out by Luis *Eça* and Martin *Hoekstra* in 2014 *A procedure for the estimation of the numerical uncertainty of CFD calculations based on grid refinement studies* [1]. For each condition analyzed, the numerical uncertainty is calculated, and together with the experimental one, the validation uncertainty is calculated as well. In the end, the validation uncertainty is compared with the comparison error, i.e. the difference between the experimental and the numerical result, and the validation process is completed.

The results obtained shows the capability of the CFD settings in predicting the flow field and the performance characteristics of the marine craft and propulsive device analyzed. Further studies may be addressed towards the optimization of the tools thanks to the result and conclusion achieved in the present study.





## Nomenclature

|                 |   |
|-----------------|---|
| $10K_Q$         | Propeller's coefficient of torque multiplied per 10     |
| $\eta_0$        | Propeller's efficiency                                  |
| $\lambda$       | Scale ratio   |
| $\nu [m^2/s]$   | kinematic viscosity                                     |
| $\phi_0$        | Interpolated solution/ "estimate" of the exact solution |
| $\phi_i$        | Numerical solution                                      |
| $\rho [kg/m^3]$ | Density   |
| BS              | Base Size   |
| $C_F$           | Coefficient of friction                                 |
| $C_F$           | Degree of Freedoms                                      |
| $C_p$           | Coefficient of pressure                                 |
| D               | Diameter  |
| E               | Comparison error  |
| E[%]            | Comparison error in percentage                          |
| Fr              | Froude number   |
| $h_i$           | grid spacing  |
| J               | Advancing Ratio   |
| $K_Q$           | Propeller's coefficient of torque                       |
| $K_T$           | Propeller's coefficient of thrust                       |
| $L_{OA}$        | Length Overall  |
| $L_{PP}$        | Length between Perpendicular                            |
| $L_{WL}$        | Length Of Waterline                                     |
| MRF             | Moving reference Frame                                  |
| $n[1/s]$        | Number of revolutions                                   |
| p               | Observed order of convergence                           |
| Re              | Reynolds number   |
| $U_{CFD}$       | Numerical uncertainty                                   |
| $U_{EFD}$       | Experimental uncertainty                                |
| $U_I$           | Iterative uncertainty                                   |

|           |   |
|-----------|---|
| $U_{Val}$ | Validation uncertainty                  |
| $Wb$      | Weber number                            |
| $AP$      | Aft Perpendicular                       |
| $BFBI$    | Dynamic Fluid Body Interaction          |
| $BL$      | Boundary Layer                          |
| $CAD$     | Computer Aided Design                   |
| $CB$      | Center of Buoyancy                      |
| $Cb$      | Block Coefficient                       |
| $CFD$     | Computational Fluid Dynamics            |
| $CFL$     | Courant Friedrichs Lewy                 |
| $CGorCoG$ | Center of Gravity                       |
| $CH$      | Caponnetto Hueber                       |
| $CSys$    | Coordinate System                       |
| $EFD$     | Experimental Fluid Dynamics             |
| $FP$      | Forward Perpendicular                   |
| $FS$      | Free Surface                            |
| $HRIC$    | High Resolution Interface Capturing     |
| $ITTC$    | International Towing Tank Conference    |
| $KCS$     | Kriso Container Ship                    |
| $LCB$     | Longitudinal Center of Buoyancy         |
| $LCG$     | Longitudinal Center of Gravity          |
| $MARIN$   | Maritime Research Institute Netherlands |
| $PPTC$    | Potsdam Propeller Test Case             |
| $Q$       | Torque                                  |
| $RANS$    | Reynolds Averaged Navier Stokes         |
| $RPS$     | Revolution Per Second                   |
| $SDR$     | Specific Dissipation Rate               |
| $T$       | Thrust                                  |
| $TDR$     | Turbulence Dissipation Rate             |
| $TKE$     | Turbulence Kinetic Energy               |



*TS* Time Step

*V&V* Verification and Validation

*VCB* Vertical Center of Buoyancy

*VCG* Vertical Center of Gravity

*VOF* Volume Of Fluid



## Contents

|   |           |
|---|-----------|
| <b>1. Introduction</b>                                  | <b>13</b> |
| <b>2. Hull classification</b>                           | <b>14</b> |
| <b>3. Boat nomenclature</b>                             | <b>14</b> |
| <b>4. Dimensionless coefficients</b>                    | <b>16</b> |
| 4.1. Reynolds number . . . . .                          | 16        |
| 4.2. Froude number . . . . .                            | 16        |
| 4.3. Weber number . . . . .                             | 17        |
| 4.4. Hydrodynamic similarity . . . . .                  | 17        |
| <b>5. Decomposition of resistance</b>                   | <b>19</b> |
| 5.1. Viscous Resistance ( $R_V$ ) . . . . .             | 19        |
| 5.1.1. Friction Resistance . . . . .                    | 21        |
| 5.1.2. Viscous Pressure Resistance . . . . .            | 22        |
| 5.2. Wave resistance . . . . .                          | 23        |
| 5.2.1. Wave Speed . . . . .                             | 24        |
| 5.3. Air Resistance ( $R_{AA}$ ) . . . . .              | 25        |
| 5.4. Other type of Resistance . . . . .                 | 25        |
| <b>6. Planing</b>                                       | <b>28</b> |
| 6.1. Force on a planing hull . . . . .                  | 29        |
| <b>7. Marine propeller</b>                              | <b>31</b> |
| <b>8. Governing Equations</b>                           | <b>34</b> |
| 8.1. Continuity equation . . . . .                      | 34        |
| 8.1.1. Eulerian point of view . . . . .                 | 34        |
| 8.2. Momentum balance equation . . . . .                | 35        |
| 8.2.1. Eulerian point of view . . . . .                 | 35        |
| <b>9. Numerical modelling</b>                           | <b>36</b> |
| 9.1. Navier-Stokes solution . . . . .                   | 36        |
| 9.2. Computational Fluid Dynamics . . . . .             | 36        |
| 9.3. Pre processor . . . . .                            | 36        |
| 9.3.1. Domain Discretization: mesh generation . . . . . | 36        |
| 9.3.2. Boundaries . . . . .                             | 37        |
| 9.4. Solver . . . . .                                   | 37        |
| 9.4.1. Modelling Turbulence . . . . .                   | 38        |
| 9.4.2. RANS . . . . .                                   | 38        |
| 9.4.3. $K-\epsilon$ . . . . .                           | 39        |
| 9.4.4. $k-\omega$ . . . . .                             | 40        |
| 9.4.5. VOF . . . . .                                    | 41        |
| 9.4.6. HRIC . . . . .                                   | 42        |
| 9.4.7. DFBI . . . . .                                   | 43        |
| 9.4.8. Boundary layer modelling . . . . .               | 44        |
| 9.5. Post processor . . . . .                           | 46        |



---

|   |            |
|---|------------|
| <b>10.Verification And Validation</b>                               | <b>47</b>  |
| 10.1.Error VS Uncertainty . . . . .                                 | 47         |
| 10.2.Error Classification . . . . .                                 | 48         |
| 10.2.1. Modelling errors . . . . .                                  | 48         |
| 10.2.2. Programming errors . . . . .                                | 48         |
| 10.2.3. Numerical Errors . . . . .                                  | 48         |
| 10.3.Verification . . . . .   | 49         |
| 10.3.1. Code verification . . . . .                                 | 49         |
| 10.3.2. Solution verification . . . . .                             | 50         |
| 10.4.Validation . . . . .   | 56         |
| 10.5.MARIN Institute: Numerical Uncertainty Analysis tool . . . . . | 57         |
| <br>  |            |
| <b>11.Potsdam Propeller Test Case</b>                               | <b>59</b>  |
| 11.1.Open Water Characteristics . . . . .                           | 60         |
| 11.2.Experimental Test . . . . .                                    | 60         |
| 11.3.Benchmarking Conditions . . . . .                              | 62         |
| 11.4.CFD . . . . .  | 63         |
| 11.4.1. Geometry . . . . .  | 63         |
| 11.4.2. Mesh . . . . .  | 66         |
| 11.4.3. Physical Setup . . . . .                                    | 69         |
| 11.5.Results . . . . .  | 71         |
| 11.6.Solution Verification . . . . .                                | 76         |
| 11.6.1. Iterative error . . . . .                                   | 76         |
| 11.6.2. Grid refinement study . . . . .                             | 78         |
| 11.6.3. Uncertainty calculation . . . . .                           | 80         |
| 11.6.4. Validation . . . . .  | 82         |
| <br>  |            |
| <b>12.Kriso Container Ship (KCS)</b>                                | <b>84</b>  |
| 12.1.Experimental Test . . . . .                                    | 86         |
| 12.2.Benchmarking Conditions . . . . .                              | 86         |
| 12.3.CFD . . . . .  | 87         |
| 12.3.1. Geometry . . . . .  | 87         |
| 12.3.2. Mesh . . . . .  | 92         |
| 12.3.3. Physical Setup . . . . .                                    | 96         |
| 12.3.4. Results . . . . .   | 100        |
| 12.4.Solution verification . . . . .                                | 106        |
| 12.4.1. Iterative error . . . . .                                   | 106        |
| 12.4.2. Grid Convergence study . . . . .                            | 107        |
| 12.4.3. Uncertainty calculation . . . . .                           | 109        |
| 12.5.Validation . . . . .   | 109        |
| <br>  |            |
| <b>13.Planing hull</b>  | <b>113</b> |
| 13.1.Experimental Tests . . . . .                                   | 114        |
| 13.2.Benchmarking Conditions . . . . .                              | 115        |
| 13.3.CFD . . . . .  | 117        |
| 13.3.1. Geometry . . . . .  | 117        |
| 13.3.2. Mesh . . . . .  | 121        |
| 13.4.Physics set-up . . . . .                                       | 124        |
| 13.5.Results . . . . .  | 127        |

---



|   |            |
|---|------------|
| 13.6. Solution Verification . . . . .                             | 131        |
| 13.6.1. Iterative error . . . . .                                 | 131        |
| 13.6.2. Grid convergence study . . . . .                          | 133        |
| 13.7. Numerical uncertainty calculation . . . . .                 | 134        |
| 13.8. Validation . . . . .  | 134        |
| <b>14. Sailing yacht</b>  | <b>138</b> |
| 14.1. Experimental Tests . . . . .                                | 139        |
| 14.2. Benchmarking conditions . . . . .                           | 141        |
| 14.3. CFD . . . . .   | 142        |
| 14.3.1. Initial tests . . . . .                                   | 142        |
| 14.3.2. Geometry . . . . .  | 143        |
| 14.3.3. Mesh . . . . .  | 147        |
| 14.3.4. Physical Setup . . . . .                                  | 149        |
| 14.3.5. Results . . . . .   | 151        |
| 14.4. Solution verification . . . . .                             | 155        |
| 14.4.1. Iterative error . . . . .                                 | 155        |
| 14.4.2. Grid Convergence study . . . . .                          | 155        |
| 14.4.3. Uncertainty calculation . . . . .                         | 155        |
| 14.5. Validation . . . . .  | 159        |
| <b>15. Conclusion</b>   | <b>160</b> |
| <b>A. PPTC Pre Tests</b>  | <b>165</b> |
| <b>B. VOF WAVE Forcing and Damping</b>                            | <b>166</b> |
| <b>C. Numerical Ventilation</b>                                   | <b>167</b> |
| C.1. Possible strategies to fix the ventilation problem . . . . . | 167        |
| <b>D. DFBI: Equilibrium</b>                                       | <b>170</b> |
| <b>E. Wide &amp; Light M-1108</b>                                 | <b>171</b> |
| E.1. Towing tank test . . . . .                                   | 171        |
| <b>F. TEST B1-9841</b>  | <b>174</b> |

## List of Figures

|     |   |    |
|-----|---|----|
| 2.  | Hull nomenclature . . . . .   | 14 |
| 3.  | Components of hull resistance for a ship [5] . . . . .                                | 19 |
| 4.  | Components of hull resistance for different vessels [4] . . . . .                     | 20 |
| 5.  | Ideal flow around a submerged body [5] . . . . .                                      | 20 |
| 6.  | Flow around a submerged body [6] . . . . .  | 21 |
| 7.  | Laminar and turbulent boundary layer profile normal to the hull surface [6] . . . . . | 22 |
| 8.  | ITTC57 correlation Line [6] . . . . .   | 23 |
| 9.  | Pressure distribution with and without separation [6] . . . . .                       | 24 |
| 10. | Wave pattern generated by a moving object in the water [5] . . . . .                  | 24 |
| 11. | Wave pattern generated by a ship [5] . . . . .  | 25 |
| 12. | Ship Wave Patterns sum [4] . . . . .  | 25 |
| 13. | Wave Patterns vs. Speed [5] . . . . .   | 26 |
| 14. | Humps and hollows on the wave resistance curve [6] . . . . .                          | 26 |
| 15. | Pressure and velocity distribution beneath a planing flat plate (principle) . . . . . | 28 |
| 16. | Force on a flat planing surface . . . . .   | 29 |
| 17. | Force on a planing hull . . . . .   | 30 |
| 18. | Cylindrical blade section definition [7] . . . . .                                    | 31 |
| 19. | Propeller Pitch [5] . . . . .   | 31 |
| 20. | Cut through a propeller blade [6] . . . . .   | 32 |
| 21. | Propeller Characteristics [6] . . . . .   | 33 |
| 22. | Control volume [8] . . . . .  | 34 |
| 23. | Structured vs. unstructured [9] . . . . .   | 37 |
| 24. | Cell Volume of fluid fraction [14] . . . . .  | 41 |
| 25. | Rigid body with its DOF [13] . . . . .  | 43 |
| 26. | Boundary layer over a flat plate . . . . .  | 45 |
| 27. | Law of the wall: applicability of wall treatments [13] . . . . .                      | 46 |
| 28. | VV process [17] . . . . .   | 47 |
| 29. | Verification process [17] . . . . .   | 49 |
| 30. | Validation process [17] . . . . .   | 56 |
| 31. | VP1304 [28] . . . . .   | 60 |
| 32. | Dynamometer H39 with VP1304 [28] . . . . .  | 61 |
| 33. | Test arrangement in the towing tank [28] . . . . .                                    | 61 |
| 34. | CFD Propeller geometry . . . . .  | 63 |
| 35. | Coordinate system . . . . .   | 63 |
| 36. | Computational Domain . . . . .  | 64 |
| 37. | Rotating region . . . . .   | 64 |
| 38. | Volume refinements . . . . .  | 65 |
| 39. | Propeller mesh . . . . .  | 66 |
| 40. | Propeller prism layer . . . . .   | 67 |
| 41. | Coarsest VS Finest mesh . . . . .   | 68 |
| 42. | Moving Reference Frame [13] . . . . .   | 70 |
| 43. | Computational Domain with boundaries Stationary + Rotating region . . . . .           | 71 |
| 44. | Open water characteristics vs $J$ at different grids . . . . .                        | 72 |
| 45. | Pressure Coefficient . . . . .  | 74 |
| 46. | Friction Coefficient . . . . .  | 75 |
| 47. | Normalized residuals Vs iterations . . . . .  | 76 |



|   |     |
|---|-----|
| 49. Residuals Vs iterations . . . . .   | 77  |
| 50. Kt Grid Refinement study at different $J$ . . . . .                             | 78  |
| 51. $10K_Q$ Grid refinement study at different $J$ . . . . .                        | 79  |
| 52. $\eta_0$ Grid refinement study at different $J$ . . . . .                       | 79  |
| 53. Coefficients Interpolated vs grid refinement with uncertainty bar . . . . .     | 81  |
| 54. KCS hull [35] . . . . .   | 84  |
| 55. KCS provided geometry . . . . .   | 87  |
| 56. KCS provided geometry: particular of the sharp edges . . . . .                  | 87  |
| 57. KCS new geometry: particular of the edges . . . . .                             | 88  |
| 58. KCS CFD geometry . . . . .  | 89  |
| 59. KCS old coordinate system . . . . .   | 89  |
| 60. KCS coordinate system . . . . .   | 89  |
| 61. Computational domain: side and top view . . . . .                               | 90  |
| 62. Kelvin refinements . . . . .  | 92  |
| 63. Free surface refinement . . . . .   | 92  |
| 64. Other refinements . . . . .   | 93  |
| 65. KCS hull mesh . . . . .   | 93  |
| 66. KCS hull mesh details . . . . .   | 94  |
| 67. Domain mesh and prism layer . . . . .   | 95  |
| 68. Time step variation . . . . .   | 97  |
| 69. Computational Boundaries . . . . .  | 98  |
| 70. $C_T$ , trim and sinkage . . . . .  | 100 |
| 71. $Y^+$ on the hull . . . . .   | 102 |
| 72. Vof . . . . .   | 103 |
| 73. Dynamic Pressure Field . . . . .  | 104 |
| 74. Wave pattern at different froudes . . . . .                                     | 104 |
| 75. Wave pattern Froude 0.26 . . . . .  | 105 |
| 76. residuals . . . . .   | 106 |
| 77. Drag convergence . . . . .  | 107 |
| 78. Trim and sinkage convergence . . . . .  | 108 |
| 80. Open water characteristics vs grid refinement with error bar at $V_1$ . . . . . | 110 |
| 81. Open water characteristics vs grid refinement with error bar at $V_2$ . . . . . | 110 |
| 82. Open water characteristics vs grid refinement with error bar at $V_3$ . . . . . | 111 |
| 83. AZ95rph cruising [41] . . . . .   | 113 |
| 84. Naked hull geometry . . . . .   | 115 |
| 85. TEST B1 – 9841 . . . . .  | 115 |
| 86. Initial geometry . . . . .  | 117 |
| 87. Final geometry . . . . .  | 117 |
| 88. Coordinate systems . . . . .  | 118 |
| 89. Computational domain . . . . .  | 119 |
| 90. Volumetric refinements . . . . .  | 120 |
| 91. Hull Mesh with refinement area . . . . .  | 121 |
| 92. Hull Mesh with refinement particulars . . . . .                                 | 122 |
| 93. Hull Mesh prism layer . . . . .   | 123 |
| 94. Domain mesh: kelvin, free surface refinements and overset mesh . . . . .        | 123 |
| 95. Propeller force . . . . .   | 125 |
| 96. Boundary conditions . . . . .   | 126 |
| 97. $C_T$ , trim and sinkage . . . . .  | 127 |

|  |     |
|--|-----|
| 98. $Y^+$ on the hull . . . . .  | 128 |
| 99. Dynamic pressure coefficient . . . . .   | 129 |
| 100. VOF at different grids . . . . .  | 130 |
| 101. Wave pattern experimental (17.5 Kn) vs CFD ( $V_1 = 18 Kn$ ) . . . . .          | 130 |
| 102. Residuals . . . . .   | 131 |
| 103. Drag convergence . . . . .  | 132 |
| 104. Trim and sinkage convergence . . . . .  | 132 |
| 105. Convergence study . . . . .   | 133 |
| 106. Open water characteristics vs grid refinement with error bar at $V_1$ . . . . . | 135 |
| 107. Open water characteristics vs grid refinement with error bar at $V_2$ . . . . . | 135 |
| 108. Open water characteristics vs grid refinement with error bar at $V_3$ . . . . . | 136 |
| 109. M-1108 geometry . . . . .   | 139 |
| 110. Model Test Set Up . . . . .   | 140 |
| 111. Unstable simulations . . . . .  | 142 |
| 112. Geometry problem . . . . .  | 143 |
| 113. New geometry appended . . . . .   | 143 |
| 114. Coordinate systems . . . . .  | 144 |
| 115. New domain dimensions . . . . .   | 145 |
| 116. Volumetric Refinements . . . . .  | 146 |
| 117. Hull mesh . . . . .   | 147 |
| 118. Hull mesh details . . . . .   | 148 |
| 119. Domain and prism layer mesh . . . . .   | 148 |
| 120. Computational boundaries . . . . .  | 150 |
| 121. Drag, Trim and Sinkage . . . . .  | 151 |
| 122. $Y^+$ on the Hull . . . . .   | 152 |
| 123. Dynamic pressure Coefficient . . . . .  | 153 |
| 124. Bottom view . . . . .   | 153 |
| 125. Wave pattern . . . . .  | 154 |
| 126. Residuals . . . . .   | 155 |
| 127. Variables convergence . . . . .   | 155 |
| 128. Variables vs $n^\circ$ of cells . . . . .                                       | 156 |
| 129. Open water characteristics vs grid refinement with error bar at $V_1$ . . . . . | 157 |
| 130. Open water characteristics vs grid refinement with error bar at $V_2$ . . . . . | 157 |
| 131. Open water characteristics vs grid refinement with error bar at $V_3$ . . . . . | 158 |
| 132. Pre Tests . . . . .   | 165 |
| 133. Hull with ventilation . . . . .   | 167 |
| 134. Hull with ventilation: last layer . . . . .                                     | 168 |
| 135. Air entering in the cell . . . . .  | 168 |
| 136. M-1108 waterlines . . . . .   | 171 |
| 137. Towing test M-1108 upright, forward . . . . .                                   | 172 |
| 138. Towing test M-1108 upright, backward . . . . .                                  | 173 |
| 139. Towing test 9841 . . . . .  | 174 |

## List of Tables

|     |   |     |
|-----|---|-----|
| 1.  | VP1304 Datasheet . . . . .  | 59  |
| 2.  | Dynamometer Characteristics . . . . .   | 60  |
| 3.  | Operations Conditions . . . . .   | 62  |
| 4.  | Measured open water characteristics for 15 RPS (by polynomials) . . . . .                         | 62  |
| 5.  | $n^\circ$ of cells per base size . . . . .  | 66  |
| 6.  | Settings . . . . .  | 70  |
| 7.  | $K_T$ , $10K_Q$ and $\eta_0$ vs $J$ at different grids with comparison error . . . . .            | 73  |
| 8.  | Propeller's Characteristics UniGe 1.5 M cells for single blade . . . . .                          | 73  |
| 9.  | Kt interpolated solution, CFD solution, Uncertainty and order of accuracy. . . . .                | 80  |
| 10. | $10K_q$ interpolated solution, CFD solution, Uncertainty and order of accuracy. . . . .           | 80  |
| 11. | $\eta_0$ interpolated solution, CFD solution, Uncertainty and order of accuracy. . . . .          | 80  |
| 12. | Comparison error and validation uncertainty . . . . .   | 82  |
| 13. | Validation Results (Validated, NV- Not Validated) . . . . .                                       | 83  |
| 14. | Validation Results for $K - \omega$ SST turbulence model (Validated, NV- Not Validated) . . . . . | 83  |
| 15. | KCS Ship features . . . . .   | 85  |
| 16. | Experimental Test conditions . . . . .  | 86  |
| 17. | Benchmarking conditions . . . . .   | 86  |
| 18. | Hydrostatics data from the original model scale and the one used in the CFD simulation . . . . .  | 88  |
| 19. | $n^\circ$ of cells per base size . . . . .  | 92  |
| 20. | First cell height value . . . . .   | 94  |
| 21. | Initial conditions . . . . .  | 98  |
| 22. | Model Setup . . . . .   | 99  |
| 23. | EFD and CFD with comparison error in percentage of the experimental value . . . . .               | 101 |
| 24. | Average Results without irregular values from Tokyo 2015 Workshop . . . . .                       | 101 |
| 25. | Numerical uncertainty . . . . .   | 109 |
| 26. | Comparison error and validation uncertainty . . . . .   | 109 |
| 27. | Validation . . . . .  | 111 |
| 28. | Az95rph characteristics . . . . .   | 113 |
| 29. | Operations Conditions . . . . .   | 114 |
| 30. | Benchmarking conditions . . . . .   | 116 |
| 31. | TEST B1 – 9841 Hydrostatic Data . . . . .   | 116 |
| 32. | $n^\circ$ of cells per base size . . . . .  | 121 |
| 33. | First cell height value . . . . .   | 122 |
| 34. | Model Setup . . . . .   | 124 |
| 35. | Initial conditions . . . . .  | 125 |
| 36. | EFD and CFD results with comparison error . . . . .   | 128 |
| 37. | Iterative uncertainty as a percentage of the experimental value . . . . .                         | 131 |
| 38. | Numerical Uncertainty . . . . .   | 134 |
| 39. | Comparison error and validation uncertainty . . . . .   | 137 |
| 40. | Validation . . . . .  | 137 |
| 41. | W&L M-1108 Characteristics . . . . .  | 140 |
| 42. | Benchmarking conditions . . . . .   | 141 |
| 43. | Hydrostatics old and new hull . . . . .   | 144 |
| 44. | $n^\circ$ of cells per base size . . . . .  | 147 |
| 45. | Computational Model Setup . . . . .   | 150 |



|   |     |
|---|-----|
| 46. EFD and CFD with comparison error . . . . .           | 151 |
| 47. Numerical uncertainty . . . . .                       | 156 |
| 48. Comparison error and validation uncertainty . . . . . | 159 |
| 49. Validation . . . . .                                  | 159 |
| 50. Experimental Uncertainty Analysis . . . . .           | 172 |

## 1. Introduction

During the last three or four decades, computer simulations of physical processes have been used in scientific research and in the analysis and design of engineered systems.

For engineered systems, terminology such as “virtual prototyping” and “virtual testing” is now being used in engineering development to describe numerical simulation for the design, evaluation, and “testing” of new hardware and even entire systems.

Users and developers of computational simulations today face a critical issue: How should confidence in modeling and simulation be critically assessed? Verification and validation (V&V) of computational simulations are the primary methods for building and quantifying this confidence, *Oberkampf and Trucano* [2]

The goal of this study is to use CFD settings and guidelines provided by Caponnetto Hueber, a consultancy CFD company in the marine industry, and Siemens to benchmark hydrodynamics simulations. To accomplish this, four experimental test cases provided by research institutes are thus benchmarked: propeller, ship, planing hull, and sailing yacht. The work is completed by submitting the results to V&V process based on the work carried out by *Luis Eça and Martin Hoekstra* in 2014 *A procedure for the estimation of the numerical uncertainty of CFD calculations based on grid refinement studies*.

The first phase of this thesis was to understand the procedure of Verification and Validation to which the test cases were going to be subjected. The one developed by *Luis Eça and Martin Hoekstra* [1] for the marine environment has been adopted. This is implemented in a tool released by the Maritime Research Institute Netherlands.

This phase was followed by the collection of the experimental data and the CAD geometries to use in CFD simulation. While performing this task, some difficulties have been encountered due to the lack of some data, damaged geometries and difficulties in the towing tank reports interpretation.

Subsequently one after the other the four test cases have been simulated.

Each test case is characterized by a first phase where the computational domain is created and the geometry placed trying to replicate the tank test conditions. Then, among the experimental conditions provided, the ones to be benchmarked have been chosen and the simulations performed. In order to carry out the VV process, for each condition a grid refinement study has been performed.

The results have been then analyzed and compared with the experimental one. When available a comparison between results and settings used in this thesis and results and settings used by other companies/workshop participants have been made.

Once the results were ready the verification process began. The MARINE tool was used to calculate the numerical uncertainty over the grids used, for each condition analysed. The tool output also the exponent of the interpolation polynomial to be used as quality indicator.

Verification was followed by Validation phase. The numerical uncertainty has been then added with the experimental one giving the validation uncertainty. The latter was compared with the comparison error, the difference between the experimental and the numerical result, thus completing the validation process.

It must be underlined that for the propeller test case an additional analysis with a different turbulence model has been carried out, while for the sailing yacht a new set of settings has been implemented.

## 2. Hull classification

Before going into the test cases analyzed, a distinction between the main two typologies of vessel's hull, displacement and planing, must be done.

**Displacement Hull** Displacement hulls lie in the water and displace it when moving. This generates a lot of resistance, so boats with displacement hulls tend to be slower. Water resistance increases as the speed increases, creating a kind of built-in speed limit called hull speed or displacement speed.

Displacement hulls tend (but it is not generally true) to have a deep draft. That means that more of the vessel's hull is in the water, which makes it easier to handle in waves and rough conditions.

**Planing hull** Planing hulls are usually found on smaller, lighter boats that are built for speed. Planing hulls displace water when moving slowly, but as they go faster, the shape of the hull and the speed work together to generate lift, bringing the boat right out of the water so that it skims over the surface.

Boats with planing hulls can move much faster than those that displace water, but they make for a bumpier ride and are more easily affected by waves.

## 3. Boat nomenclature

For clarification a few of the terms specific to the ship building community are here explained since they are used both throughout this thesis as well as in many of the references. They are defined in the *Dictionary of Ship Hydrodynamics* by ITTC [3] and they could be applied to sailing and planing yachts as well. Special terms characterizing the latter will be also reported.

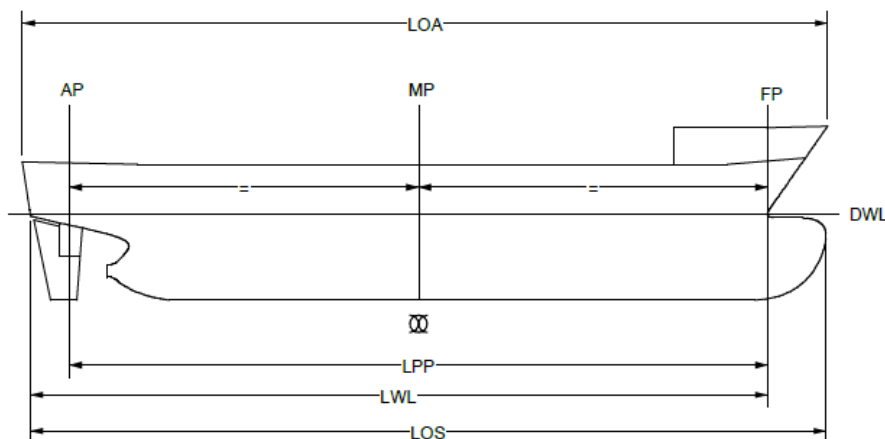


Figure 2: Hull nomenclature

- $L_{OA}$  is the Length overall: is the maximum length of the hull from the most forward point on the stem to the extreme after end;

- $L_{PP}$ : length between perpendicular. Is the length between the forward (FP) and Aft perpendicular (AP): the forward perpendicular (FP) is the forward end of the designed waterline, while the aft perpendicular (AP) is the centre of the rudder stock
- $L_{WL}$  is the length on waterline: The length of the designed waterline;
- *Draft*, the maximum draft of the ship when floating on the designed waterline.
- *Depth* The vertical distance from the deepest point of the keel to the sheer line.
- *Displacement* is the mass ( $m$ ) or volume of water ( $V$ ) displaced by the ship;
- *Midship section*. For ships, this section is located midway between the fore and aft perpendiculars. For yachts it is more common to put it midway between the fore and aft ends of the waterline. It is indicated with a particular symbol showed in Figure 84;
- *Block coefficient* ( $C_b$ ) The ratio of displacement volume  $\nabla$  to the volume of a rectangular block having length  $L_{WL}$ , beam equal to the waterline beam  $B_{WL}$  and draft,  $T$ .

$$C_b = \frac{\nabla}{L_{WL} \cdot B_{WL} \cdot T}$$

- *Centre of buoyancy* (CB): The geometric centroid,  $B$  of the submerged volume of a body or ship through which the total buoyancy may be assumed to act. Its position, measured as the distance from midship or from the fore ( $\overline{FB}$ ) or after perpendicular ( $\overline{AB}$ ) is called the Longitudinal centre of buoyancy (LCB), and from the base line or keel ( $KB$ ) the Vertical centre of buoyancy (VCB).
- *Centre of gravity* (CG): The centre through which all the weights constituting the ship and its contents may be assumed to act. The distance measured from midships, from the fore perpendicular ( $\overline{FG}$ ) or from the after perpendicular ( $\overline{AG}$ ), and from the base-line or keel ( $\overline{KG}$ ) are called Longitudinal (LCG) and Vertical (VCG) centre of gravity respectively.
- *Sheer line*: The projection on to the plane of symmetry of the intersection of deck with the side, or the intersection of a deck with the plane of symmetry of a ship. The amount of rise of a sheer line above its lowest point is called the **Sheer**, forward or aft.
- *Trim*
  - in ship geometry is the difference between the draught forward  $TF$  and the draught aft  $TA$  for a ship with a designed level keel:  $Trim = TF - TA$ . In non dimensional form the trim is expressed as a fraction of the ship length, i.e.  $(TF - TA)/L$  and is called the trim ratio. It is referred to as trim by the bow or head if the forward draught is the greater, level trim if both are the same and trim by the stern if the draught aft is the greater. If the ship has a designed initial trim (raked keel or drag) the trim is generally measured with respect to this initial longitudinal inclination.
  - ( $\theta$ ), in seakeeping/manoeuvring, is the angle measured about a horizontal axis, between the position of the longitudinal axis of a ship at rest and the horizontal plane.

## 4. Dimensionless coefficients

Likewise aerospace engineering, naval engineering, as well, use dimensionless coefficients to describe the performance of a system, to compare different systems to each other and to describe the design and the performance of a ship's hull.

Dimensionless coefficients allow engineers to compare the performance of several hull types or propellers by carrying out tests on model's scale instead of full scale.

### 4.1. Reynolds number

The Reynolds number is physically a measure of the ratio of inertia forces to viscous forces in a flow and is one of the most known parameters in fluid dynamics; it permits to determine the behaviour of the flow in different fluid flow situations.

It is defined as:

$$Re = \frac{UL\rho}{\mu} = \frac{UL}{\nu}$$

where

- $U$  [m/s] is the speed of the flow;
- $L$  [m] is the characteristics length of the body;
- $\rho$  [kg/m<sup>3</sup>] is the density of the fluid;
- $\mu$  [Pa · s] is the dynamics viscosity of the fluid;
- $\nu$  [m<sup>2</sup>/s] is the kinematic viscosity of the fluid.

Knowing the Reynolds number of a phenomenon let us understand if we are in the *laminar* or *turbulent* regime and, consequently, apply the correct formulas and draw the right conclusions regarding the behaviour of the fluid flow.

### 4.2. Froude number

The *Froude number* is the ratio between inertia forces and gravitational forces. In naval architecture, the Froude number have an estimation of what the wave pattern around a floating body could look like; is a significant Figure that is used in the determination of the resistance of the partially submerged object that is moving through the water.

The  $Fn$  could be expressed as:

$$Fr = \frac{U}{\sqrt{gL_{PP}}} \quad (1)$$

where:

- $U$  is the boat speed;
- $g$  is the gravity acceleration;
- $L_{pp}$  is the *Length between perpendiculars*.



It plays a similar role for the wave resistance as the Reynolds number does for viscous resistance. The Froude number quantify how many waves there are along the hull; for instance, at  $Fr = 0.40$  there is one wave, at 0.28 there are two, etc.

We can show that for an incompressible liquid in a channel, bounded at the bottom, the height of the the free surface depends on the Froude number.

### 4.3. Weber number

It expresses the ratio between the fluid's inertia and the surface tension. It is defined as:

$$Wn = \frac{\rho U^2 L}{\gamma}$$

where

- $\rho$  [ $kg/m^3$ ] is the density of the fluid;
- $U$  [ $m/s$ ] is the speed of the body;
- $L$  [ $m$ ] is the characteristic length of the body;
- $\gamma$  [ $N/m$ ] is the surface tension.

When scaling avessel, it must be the same to achieve the correct effect of the surface tension. This means that spray and wave-breaking which contain water drops and air bubbles with small radii, are correctly scaled.

### 4.4. Hydrodynamic similarity

Generally, as already pointed out, the experimental tests are conducted on model scale ship and thus there is the need to transfer to full scale the data acquired on model scale; similarities can be geometric, kinematic, dynamic, total, or incomplete.

- **Geometric similarity:** the coordinates of homologous points are correlated with one scale factor.
- **Kinematic similarity:** Speeds of homologous points are correlated in absolute value with one scale factor; they hold their directionn.
- **Dynamic similarity** forces acting the fluid hold their direction related on geometric scale; the absolute value is correlated with one scale factor. Dynamic similarity implies geometric and cinematic similarities.
- **Complete similarity:** it is present when dynamic similarity is achieved on all forces acting on the fluid.
- **Incomplete similarity:** It is present when some parameters of the dynamic similarity could not be held.

In Tank Tests it is **impossible satisfy at the same time all requirements**.

Considering the effects of incorrect scaling, it turns out that a wrong Weber number has the smallest effect on the flow around the hull and the resistance. The remaining two parameters are both very important for the resistance and for the flow around the hull.[4]

According to Froude hypothesis, the total resistance to the advancement of a ship is given

by the sum of a term dependent exclusively from the viscous effects and therefore from the Reynolds number and a term dependent by gravitational forces alone and therefore by the Froude number in which the dominant part of the resistance is given by that of wave generation. Froude proposed to carry out the scale tests by realizing the geometric and kinematic similarity according to the Froude number and then to carry out the conservation of the functional relationship of the wave resistance. By carrying out the scale tests while keeping the Froude number, the major driving force for the waves, namely the gravity, is correctly scaled and the full scale ship wave resistance can be calculated from the measurement of the wave resistance on the model.

## 5. Decomposition of resistance

As mentioned before, when a ship moves through calm water, there are many factors that combine to form the total resistance force acting on the hull, *US Naval Academy* [5]. The principle factors affecting ship resistance are the friction and viscous effects of water acting on the hull, the energy required to create and maintain the ship's characteristic bow and stern waves, and the resistance that air provides to ship motion. In mathematical terms, total resistance can be written as:

$$R_T = R_V + R_W + R_{AA} \quad (2)$$

where

- $R_T$  = total hull resistance
- $R_V$  = viscous resistance
- $R_W$  = Wave making resistance
- $R_{AA}$  = air resistance caused by ship moving through calm air

Figure 3 shows how the magnitude of each component of resistance varies with ship speed. At low speeds viscous resistance dominates, and at high speeds the total resistance curve turns upward dramatically as wave making resistance begins to dominate.

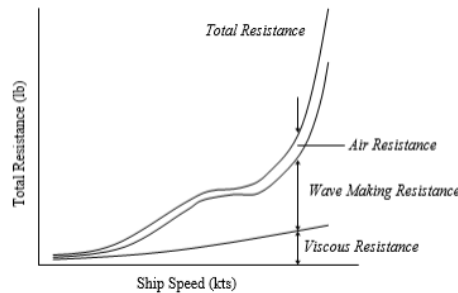


Figure 3: Components of hull resistance for a ship [5]

Figure 4 shows how the different components of the hull resistance are allocated into the different vessels.

### 5.1. Viscous Resistance ( $R_V$ )

Figure 5 shows a body submerged in an ideal (inviscid) fluid. As the fluid flows around the body, there is a pressure distribution normal to the body. In the forward section of the hull there is a component of pressure resisting motion, and in the aft section of the body there is a component of pressure assisting motion. In an ideal fluid these pressure forces are equal and the body experiences **no resistance**.

Unfortunately, water is not an ideal fluid, and therefore the body will experience resistance. Figure 6 shows a hull submerged in a real fluid with viscosity. Fluid particles stick to the body (**no slip condition**), resulting in the formation of a *boundary layer*, where the flow

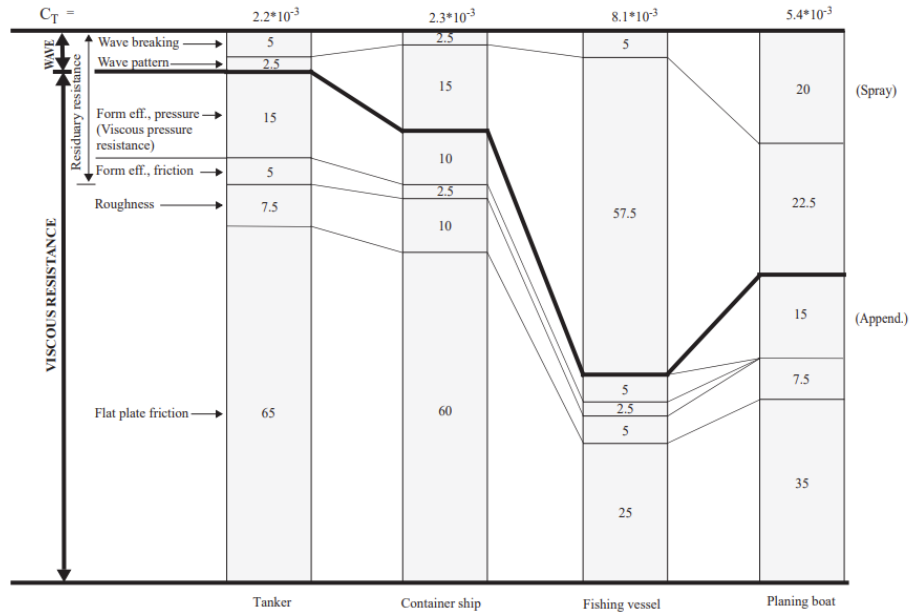


Figure 4: Components of hull resistance for different vessels [4]

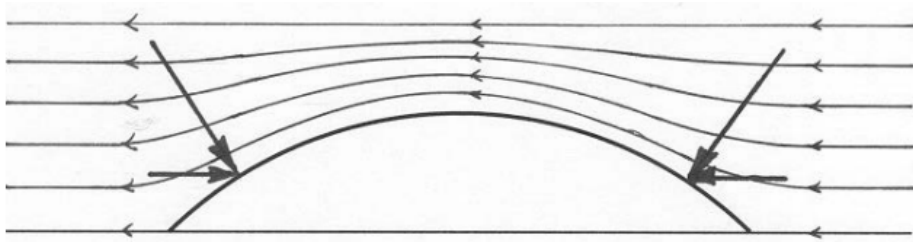


Figure 5: Ideal flow around a submerged body [5]

rapidly changes speed, from zero speed at the side of the body, to the free-stream speed. Near the bow the flow within the boundary layer is smooth. The velocity in one layer is slightly larger than in the layer just inside. This is the laminar part of the boundary layer. After a certain distance from the bow disturbances start to occur, and shortly thereafter the flow structure breaks down into a seemingly chaotic state: turbulence. The boundary layer is now characterized by eddies of different sizes and frequencies. The fluctuating velocities caused by the eddies are, however, considerably smaller than the mean velocity at all points in the boundary layer, so the flow is always moving backwards.

Inside the turbulent boundary layer we can distinguish two regions: the **inner** and the **outer layer**. In the first one we don't have an explicit dependence by the body geometry. This region could in turn be divided into three sublayers: the **viscous**, the **buffer** and the **logarithmic** layer. They will be deepened in the following sections.

The viscous sublayer plays quite an important role, particularly in connection with surface roughness. In the viscous sublayer the flow is mainly laminar, but it is sometimes disturbed by turbulent bursts, located at isolated spots, moving downstream with the flow.

The area where the flow changes from laminar to turbulent is called the transition region and is normally very short.

Close to the stern another flow phenomenon, called separation, may occur. When this ap-

pens, as the name suggests, the flow it's not attached to the hull anymore. While it is impossible in practice to avoid transition to turbulence in the boundary layer on the hull, separation should definitely be avoided, since it increases the resistance considerably. three forms of resistance happen as a result of viscosity:

- **Friction Resistance**
- **Viscous Pressure Resistance**
- **Increase in friction due to the surface roughness**

Friction arises from the shear stresses in the fluid and acts tangential to the body. Viscous pressure resistance acts normal to the body.

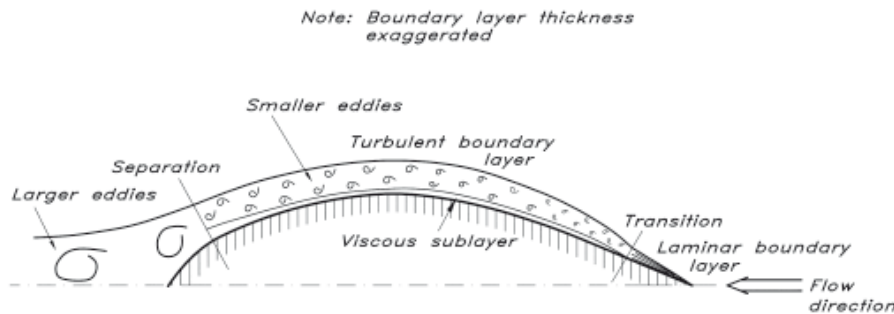


Figure 6: Flow around a submerged body [6]

### 5.1.1. Friction Resistance

As a ship moves through the water, the friction of the water acting over the entire wetted surface of the hull causes a net force opposing the ship's motion. This frictional resistance is a function of the hull's wetted surface area, surface roughness, water viscosity and speed squared. Viscosity is a temperature dependent property of a fluid that describes its resistance to flow. The frictional force is also proportional to the rate at which the speed varies along the boundary layer, normal to the surface. Considering this, we can say that reducing the wetted surface and/or reducing the temperature will decrease the frictional resistance; as the friction resistance is proportional to the velocity gradient, looking at figure 7 we can notice that it is higher in the turbulent boundary layer; the laminar one is preferred.

In 1957 the ITTC (International Towing Tank Conference) introduced a formula, the *Correlation line*, figure 8 that permits to calculate the skin friction coefficient of an hull based on the Reynolds number. The latter is influenced by the boat speed, the water kinematic viscosity and the  $L_{WL}$  of the boat.

with

$$Re_n = \frac{V \cdot L}{\nu}$$

where

- $V$  is the velocity of the yacht;

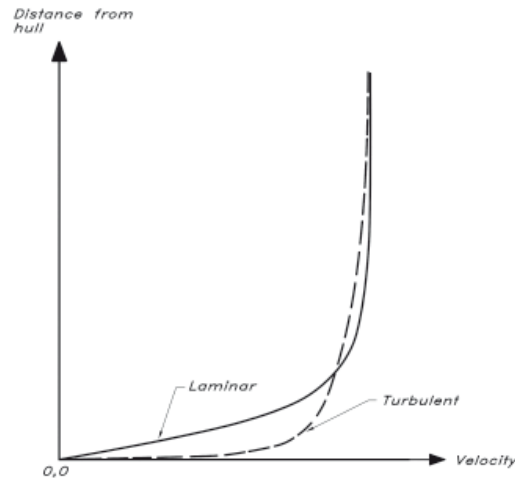


Figure 7: Laminar and turbulent boundary layer profile normal to the hull surface [6]

- $L = 0.7 \cdot L_{WL}$ ;
- $\nu$  is the kinematic viscosity;

Note that, when the friction of the hull is computed, only 70% of the waterline length is used for defining the Reynolds number. This is because water particles do not generally follow the entire length of the bottom. For instance, those hitting the hull near maximum beam will follow the hull only a short distance before leaving it for the wake behind the hull.

### 5.1.2. Viscous Pressure Resistance

In the forward portion of the hull pressure forces act normal to the surface with a component directed in the flow direction; however, in the aft portion of the hull the boundary layer modifies the pressure distribution reducing the component of pressure acting in the opposite direction. This reduction in pressure aft of the vessel results in a net resistance force. This increase in resistance due to pressure is called “viscous pressure drag” or “form drag”, and is sometimes also referred to as the normal component of viscous resistance. If the flow separates a large reduction in pressure will occur, and the pressure resistance considerably increases. In figure 9.

The shape of a ship’s hull influence the magnitude of viscous pressure drag. Ships that are short in length with wide beams (a low length to beam ratio) will have greater form drag than those with a larger length to beam ratio. Also, ships that are fuller near the bow (e.g. bulk oil tanker) will have greater form drag than ships with fine bows (e.g. destroyer). While the frictional resistance is set mainly by the wetted surface, the viscous pressure resistance depends on the shape of the hull. This is also the case for the wave resistance, and both appear due to pressure imbalances, so it is very common to lump both together into one component: the **Residuary resistance**.

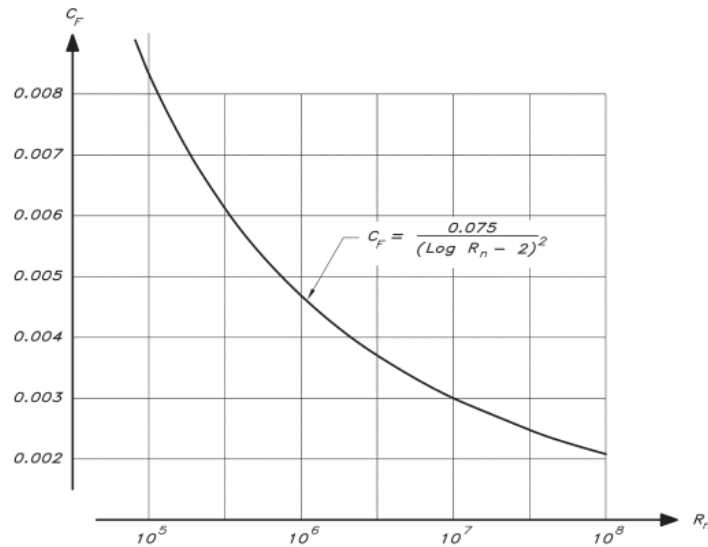


Figure 8: ITTC57 correlation Line [6]

## 5.2. Wave resistance

Another important component of hull resistance is the resistance due to wave making. While a ship moves, it displaces a certain quantity of water, generating perturbations among the latter. The creation of waves requires energy. As ship speed increases, the height of the waves produced by the ship increases and therefore the energy required to produce these waves also increases. This lost energy is referred to as **Wave making Resistance** and often becomes a limiting factor in the speed of a ship. An object moving through the water creates both divergent waves, which spread outward from the ship, and transverse waves, illustrated in figure 10; this is called **Kelvin wave system**. It can be shown that the angle between the object's trajectory and the wave fronts, the Kelvin angle, is around  $19.47^\circ$  regardless of the speed of the object.

Unlike the simple wave pattern developed by a moving pressure point (Figure 10), a real ship creates many wave systems, most prominently the bow and stern wave systems, shown in figure 11. These wave systems can interact with each other, either partially canceling the waves made by a ship (and reducing the wavemaking resistance) or by adding and increasing the wavemaking resistance. The effects waves have on each other waves as they collide and overlap is called **constructive** (adding) or **destructive** (reducing) interference.

In Figure 12 it is showed how the different wave patterns generated along different position of a wedged hull combine to form the resulting wave profile.

This latter contains five contributions:

1. A near field disturbance of the surface;
2. The bow wave system, beginning with a crest;
3. the fore shoulder wave, starting with a trough;
4. The Aft shoulder wave, starting with a trough;
5. The stern wave system, starting with a crest.

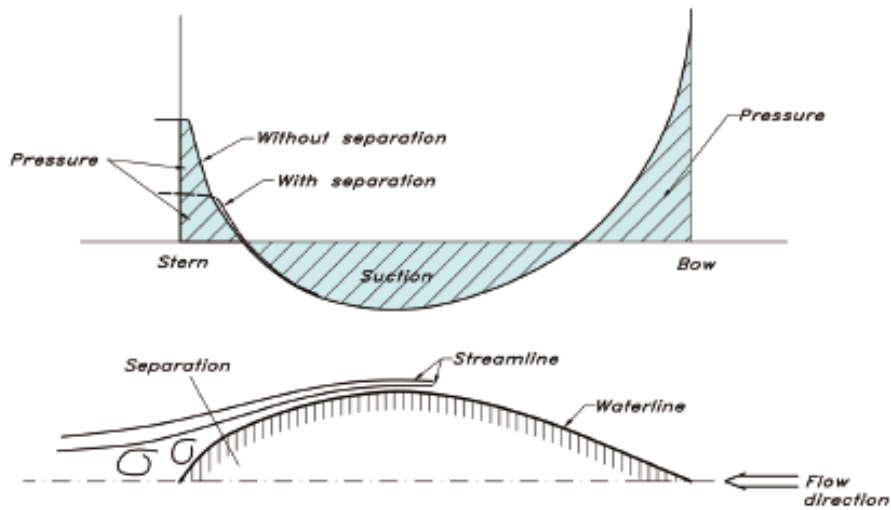


Figure 9: Pressure distribution with and without separation [6]

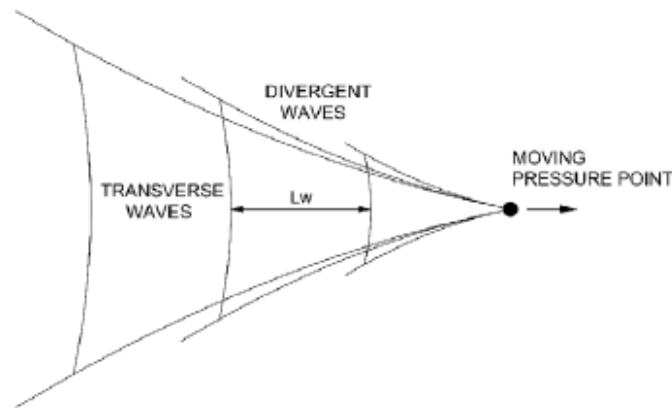


Figure 10: Wave pattern generated by a moving object in the water [5]

### 5.2.1. Wave Speed

There is a very simple relation between wavelength and travelling speed for surface waves:

$$\text{Wave speed} = \sqrt{\frac{g \cdot \lambda}{2\pi}} = 1.25 \sqrt{\lambda} \quad \text{m/s} \quad (3)$$

Figure 13 shows the appearance of the wave patterns along the side of the ship at various speeds. At low speeds, there are more wave crests on the side of the hull. At high speeds, the wavelength increases. The speed dependence of the waves gives rise to an important phenomenon: **interference**. The figure shows that at certain speeds, there is a crest at the stern, and at others, there is a trough. These crests and troughs can either partially cancel the stern wave system, or partially add to it, resulting in some speeds with higher resistance due to interference.

This fact causes the plot of total resistance coefficient versus speed (Figure 14) to have *humps and hollows*. It is best to operate the ship in a hollow for fuel economy. The figure shows a large increase in resistance at a Froude of 0.4. This is the froude value at which the wavelength is equal to the length of the ship. It is known as “hull speed,” which is the last



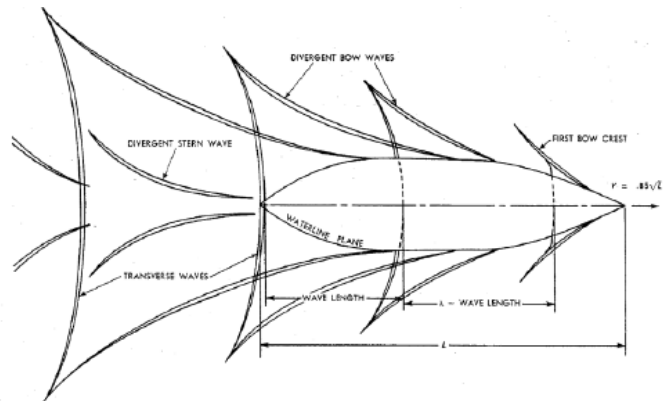


Figure 11: Wave pattern generated by a ship [5]

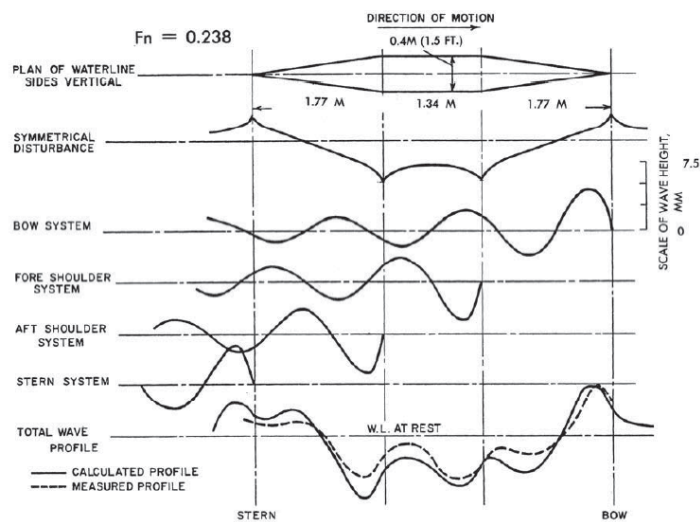


Figure 12: Ship Wave Patterns sum [4]

efficient speed for a displacement ship. In practice, for sailing yacht in example, it occurs at a higher Froude number, a higher speed. This is because the overhangs at the bow and stern cause the distance between the bow and stern waves to be larger than the nominal waterline length. The last hump thus occurs normally at a Froude number of about 0.5.

### 5.3. Air Resistance ( $R_{AA}$ )

Air resistance is the resistance caused by the flow of air over the ship with no wind present. This component of resistance is affected by the shape of the ship above the waterline, the area of the ship exposed to the air, and the ship's speed through the water. The larger is the the area above the waterline, the larger is the air resistance.

### 5.4. Other type of Resistance

According to *US Naval Accademy* [5] There are several other types of resistance that will influence the total resistance experienced by the ship, the sailing boat or the planing hull and not included in Total Hull Resistance such as:

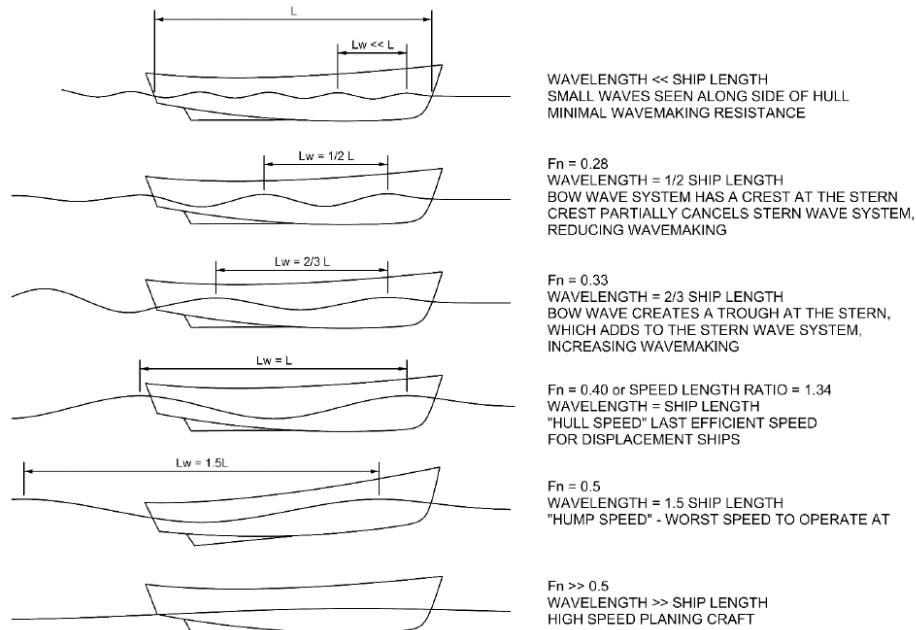


Figure 13: Wave Patterns vs. Speed [5]

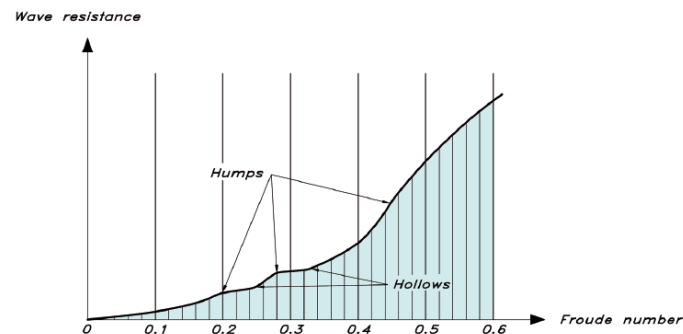


Figure 14: Humps and hollows on the wave resistance curve [6]

- **Appendage resistance:** Appendage resistance is the drag caused by all the underwater appendages such as:
  - for a ship the propeller, propeller shaft, struts, rudder, bilge keels, pit sword, and sea chests;
  - for sailing yachts the presence of rudder, keel, bulb and foils influences significantly the resistance of the hull, especially for the induced drag due to the generation of a side force, for rudder and keel, or lift in the case of foils.
  - for planning hulls the propeller, propeller shaft, stabilizer fins, other structures.
- **Steering Resistance:** Steering resistance is added resistance caused by the motion of the rudder. Every time the rudder is moved to change course, the movement of the rudder creates additional drag;
- **Added resistance due to waves:** Added resistance due to waves refers to ocean waves



caused by wind and storms, and is not to be confused with wave making resistance. Ocean waves cause the ship to expend energy by increasing the wetted surface area of the hull (added viscous resistance), and to expend additional energy by rolling, pitching, and heaving;

- **Increased resistance in shallow water.**

## 6. Planing

When the a vessel approaches  $Froude \approx 1$  the Hydrodynamic forces starts to overcome the buoyancy forces and the planing phenomenon starts to occur.

According to Archimedes, the buoyancy of a body wholly or partly submerged in a fluid is equal to the weight of the displaced volume of fluid. At zero speed this force balances exactly the weight of a floating body. However, as soon as the body starts moving, the hull puts water particles into motion by exerting a force on each particle. The same force, but in the opposite direction, is exerted on the hull. This force per unit area may be called the *hydrodynamic pressure*; it is responsible for both the viscous pressure resistance and the wave resistance. These two resistance components are caused by the longitudinal component of the pressure force over the hull surface. In the vertical direction the hydrodynamic pressure causes the hull to sink (or rise) and trim. At high speed this vertical pressure force may be considerably larger than the buoyancy, lifting the hull more or less completely out of the water. A hull predominantly supported by the hydrodynamic pressure is considered to be **planing**.

Figure 15 can explain the principles of planing; it shows the flow beneath a flat plate skimming along the water surface.

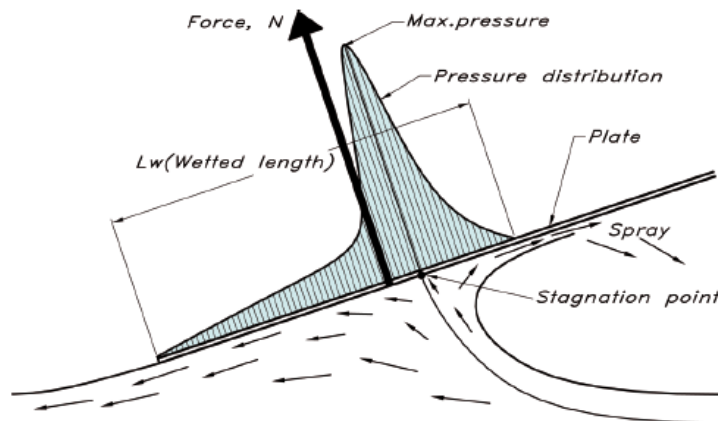


Figure 15: Pressure and velocity distribution beneath a planing flat plate (principle)

Velocity vectors are displayed to show the direction of the flow relative to the plate. It is seen that at one point the flow hits the plate at right angles. This is the *stagnation point*, where the flow is divided into two parts, one going backwards and one forwards. At the stagnation point the pressure (hydrodynamic) is very high, since all the kinematic energy has been converted into pressure. There is no flow relative to the plate at this position. On both sides of the stagnation point the pressure is reduced and eventually it drops to zero. This happens at the trailing edge and at the forward location where the velocity has become parallel to the plate. Further forward the thin water sheet breaks down into spray, which drops down onto the water surface. The high pressure creates a force at right angles to the plate, i.e. a force tilted backwards from the vertical at the same angle as the pitch angle of the plate. The vertical component is the *lift*, which has to balance the weight of the boat, while the horizontal component is the total pressure resistance, essentially the *wave*

*resistance*. The reality is somewhat more complicated than the idealized picture above. First, there is always some hydrostatic pressure present. Obviously this component is also at right angles to the plate.

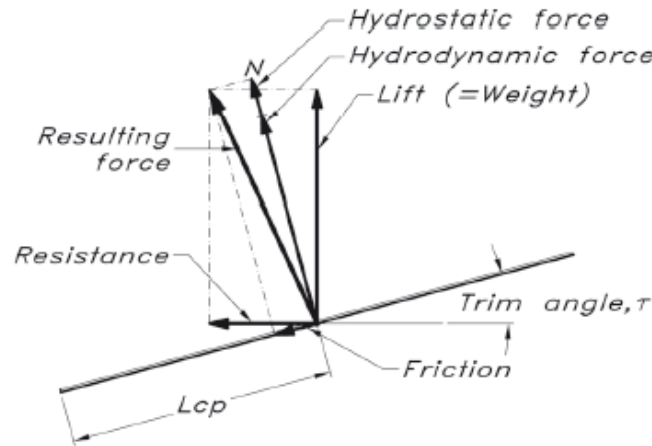


Figure 16: Force on a flat planing surface

As appears from Figure 16, this means an increase in both lift and drag. There is thus a resistance component caused by the hydrostatic pressure. For a displacement hull the hydrostatic pressure forces acting backwards on the forebody are more or less balanced by those on the afterbody acting forwards. The latter forces are almost entirely missing on a planing hull where the transom is dry.

A second complicating factor is friction, which is parallel to the plate. Although there is some component in the forward direction in front of the stagnation point, the resulting frictional force essentially points backwards and increases resistance. There is also a small reduction in the lift force. It is interesting to note that if it were not for the friction the resistance of the plate would be uniquely defined by its weight (which is equal to the total lift) and the trim angle. If the weight of the plate is changed the lift has to change correspondingly. A weight increase may thus be compensated by an increase in trim or wetted surface. In the latter case the plate is sunk a little deeper into the water and the friction is increased. To increase the trim angle the centre of gravity has to be moved backwards.

A flat plate skimming along a water surface may be useful for explaining the basic principles of planing, and it may be of interest for surfboards and water skis, but powerboat hulls almost inevitably have V-shaped sections, i.e. a so-called deadrise. The reason for this is the seakeeping qualities of the hull. A completely flat bottom would be impossible in a seaway, since the vertical accelerations would be too large. However, the deadrise reduces the lift, so a larger wetted surface or trim angle is required, which both increase resistance.

### 6.1. Force on a planing hull

Figure 17 shows a planing hull with the most important forces acting on the hull displayed.  $N$  corresponds to the pressure force in figure 16 (hydrostatic and hydrodynamic contributions) and  $R_f$  is the friction. There is also the propeller thrust  $T$  and the resistance of the

propeller drive, denoted  $R_a$ , where the index 'a' stands for appendage. For a hull with a propeller on a shaft the resistance from all appendages like the shaft, shaft brackets and rudder must be considered, *Larsson et al., Principles of yacht design* [6].

Figure 17 shows a planing hull with the most important forces acting on the hull displayed.

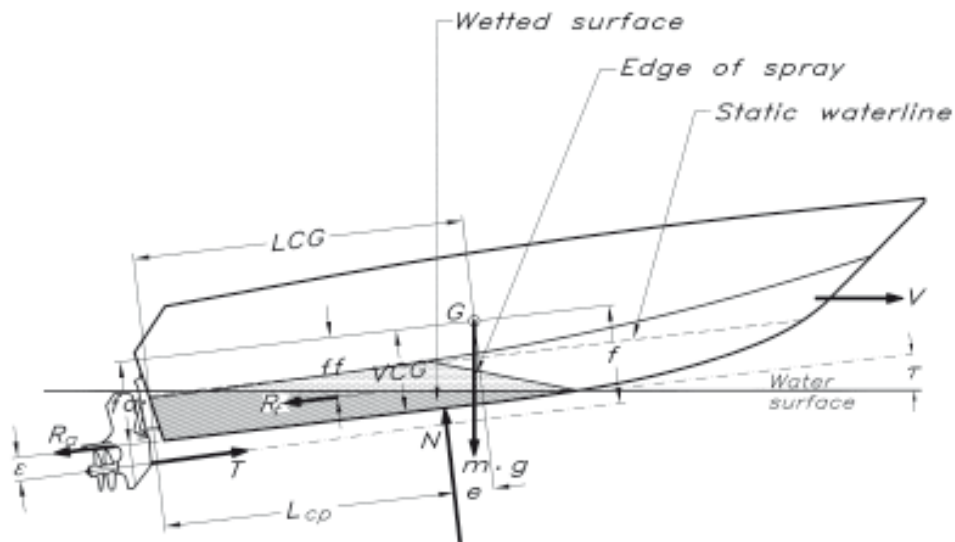


Figure 17: Force on a planing hull

- $N$  is the pressure force;
- $R_f$  is the friction;
- $T$  is the propeller thrust;
- $R_a$  is the resistance of the propeller drive;

## 7. Marine propeller

Propeller blades act as wings when the propeller rotates and advances through the water.

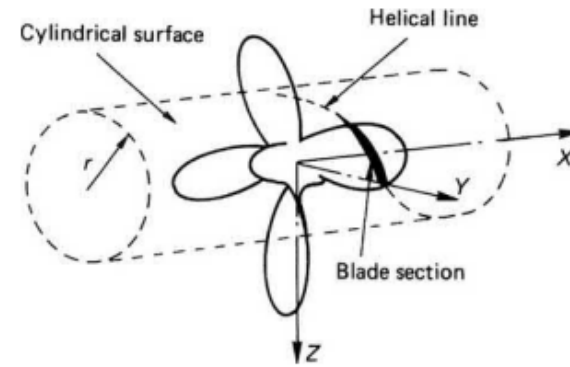


Figure 18: Cylindrical blade section definition [7]

A section of a blade at a certain radius is shown in Figure 20. It can be seen that the resulting velocity, to which the blade is exposed, is composed of the axial component (due to the forward motion) and the tangential component (due to the rotation). The former is normally not exactly equal to the vessel speed, but somewhat lower, since the propeller operates in the wake behind the hull. This effect can be quite significant for bluff ships.

The tangential component is proportional to the local radius and the rate of revolutions. It thus increases linearly with the radius, which means that the angle of the approaching flow gets smaller and smaller towards the tip. Therefore, the blades have to be twisted to become more and more at right angles to the propeller shaft further out. In fact, the propeller is normally designed so that the sections at all radii would advance the same distance for one turn of the propeller, had they been free from the others and cutting through a solid body. This distance is called the **pitch**, and is, together with the diameter, the most significant property of the propeller.

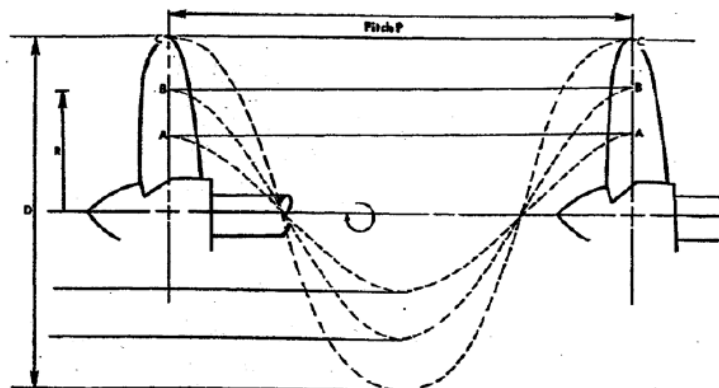


Figure 19: Propeller Pitch [5]

The pitch should be large enough to create a suitable angle of attack between the section and the approaching flow (Figure 20). A resulting force, more or less at right angles to the flow, is then developed. Had there been no resistance the angle would have been exactly

90°, but, since we have both induced and viscous resistance, the resulting force points more backwards. The force has one component in the axial direction, the useful thrust, and one in the tangential direction, giving rise to an unwanted torque.

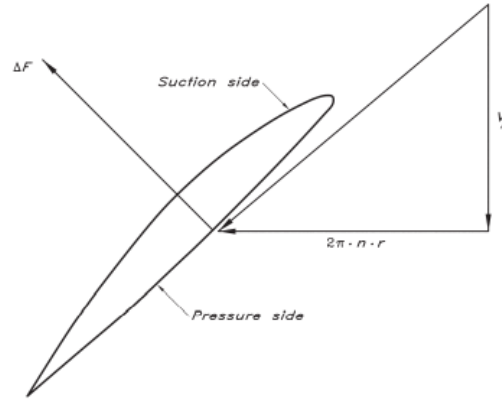


Figure 20: Cut through a propeller blade [6]

However, a typical velocity in the present case is the diameter ( $D$ ) multiplied by the rate of revolutions ( $n$ ), and a typical area is the diameter squared. If these replace the normal velocity and area, a thrust and torque coefficients may be defined:

$$K_T = \frac{T}{\rho \cdot (D \cdot n)^2 (D^2)} = \frac{T}{\rho \cdot D^4 \cdot n^2}$$

$$K_Q = \frac{Q}{\rho \cdot (D \cdot n)^2 (D^2) D} = \frac{Q}{\rho \cdot D^5 \cdot n^2}$$

with  $T$  and  $Q$  respectively equal to *Thrust* and *Torque*.

The advance ratio

$$J = \frac{U_A}{D \cdot n}$$

where  $U_A$  is the advancing velocity

is a measure of the angle of the approaching flow. By dividing the effective power (thrust times axial velocity) by the delivered power (torque times angular frequency), the efficiency of the propeller can be found:

$$\eta_0 = \frac{J}{2\pi} \cdot \frac{K_T}{K_Q}$$

The thrust and torque coefficients and the efficiency are called the propeller characteristics, and they are normally given as functions of the advance ratio, Figure 21.

To obtain the diagram in Figure 21, the propeller is run in free water, often on a long shaft in front of a very slender hull containing the measuring equipment. Systematic variations in advance ratio are made either by varying the speed for a given rate of revolutions or vice versa. At zero speed a large thrust and torque are developed, but the efficiency is zero, since the propeller does not move forwards. At high speeds both the thrust and the torque go to zero, since the angle of attack of the blades approaches to the one that generates zero lift. At still higher speeds the propeller start working as a turbine and negative thrusts and torques



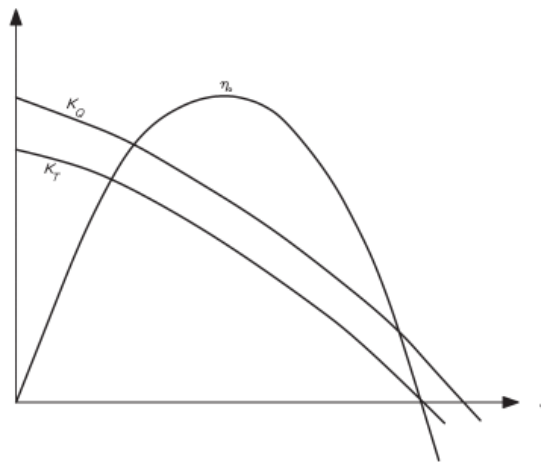


Figure 21: Propeller Characteristics [6]

are developed. When the thrust is zero the efficiency is also zero. At some intermediate speed the efficiency reaches its maximum, and it is important to design the propeller for this condition.

## 8. Governing Equations

The Governing equations of fluid dynamics are the equations that regulate the variation of the fluiddynamic variables of a certain fluid. They are the mathematical statements of three fundamental physical principles upon which all of fluid dynamics is based:

- mass is conserved;
- $F = ma$  (Newton's 2nd law);
- energy is conserved

Their fundamental form is the Boltzmann equation which describes the statistical behaviour of a thermodynamic system not in a state of equilibrium. Through a series expansion of this latter it is possible to obtain:

- Euler equation (order 0);
- Navier-Stokes equations (order 1)
- Burnett Equations (order 2)

The *Navier Stokes equations* in particular, express the 3 principles mentioned above applied to a fluid through a control volume. They are subject to boundary condition of the considered case and are valid provided that the fluid can be considered as a **continuum**.

The control volume could be considered **fixed**, crossed by the fluid, or **moving** with the fluid, composed always by the same particles; the way this latter is chosen, defines two different point of view: respectively **Eulerian** and **Lagrangian**. The control volume can even be **finite** or **infinitesimal**.

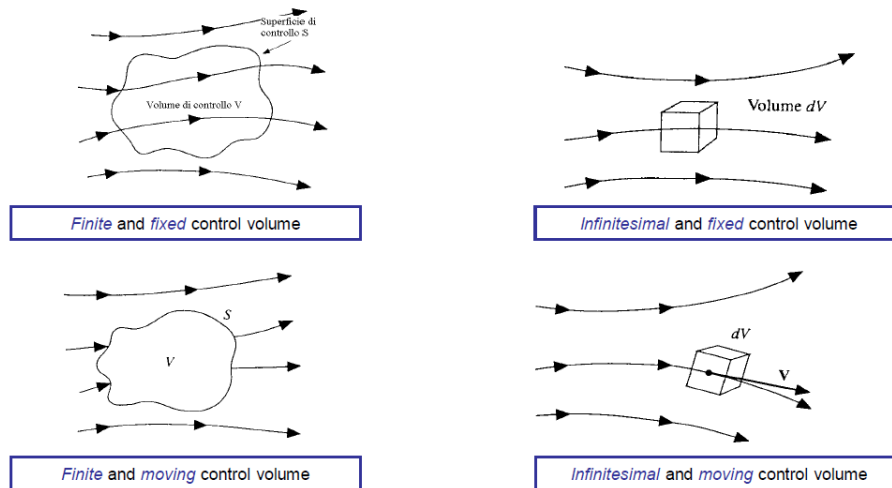


Figure 22: Control volume [8]

### 8.1. Continuity equation

#### 8.1.1. Eulerian point of view

Defining an infinitesimal control volume  $dV = dx dy dz$  with an external surface  $dS$ , we can say that:

Net flux of mass coming out from the control volume through control surface is equal to the time rate of reduction of the mass contained inside the control volume that mathematically speaking result in:

$$\nabla \cdot (\rho \vec{v}) dV = -\frac{\partial \rho}{\partial t} dV \quad \rightarrow \quad \frac{\partial \rho}{\partial t} + \nabla \cdot (\rho \vec{v}) = 0 \quad \text{Continuity equation (Eul)} \quad (4)$$

Applying the same formulation to a finite control volume result in the integral form of the continuity equation:

$$\int_S \rho \vec{v} \cdot \vec{n} dS = -\frac{\partial}{\partial t} \int_V \rho dV \quad \rightarrow \quad \frac{\partial}{\partial t} \int_V \rho dV + \int_S \rho \vec{v} \cdot \vec{n} dS = 0 \quad (5)$$

## 8.2. Momentum balance equation

### 8.2.1. Eulerian point of view

In the same way as it was done for the continuity equation, we can rewrite the momentum equations in the conservative form. Considering the definition of the Lagrangian derivative

$$\rho \frac{Du}{Dt} = \rho \left( \frac{\partial u}{\partial t} + \vec{v} \cdot \nabla u \right) = \rho \frac{\partial u}{\partial t} + \rho \vec{v} \cdot \nabla u$$

and keeping in mind the mass balance equation 4, we obtain the *momentum balance equations in differential and conservative form*:

$$\frac{\partial(\rho u)}{\partial t} + \nabla \cdot (\rho u \vec{v}) + \frac{\partial p}{\partial x} = \nabla \cdot \tau_x + \rho f_x \quad \text{where} \quad \tau_x = \tau_{xx} \vec{i} + \tau_{xy} \vec{j} + \tau_{xz} \vec{k} \quad (6)$$

$$\frac{\partial(\rho v)}{\partial t} + \nabla \cdot (\rho v \vec{v}) + \frac{\partial p}{\partial y} = \nabla \cdot \tau_y + \rho f_y \quad \text{where} \quad \tau_y = \tau_{yx} \vec{i} + \tau_{yy} \vec{j} + \tau_{yz} \vec{k} \quad (7)$$

$$\frac{\partial(\rho w)}{\partial t} + \nabla \cdot (\rho w \vec{v}) + \frac{\partial p}{\partial z} = \nabla \cdot \tau_z + \rho f_z \quad \text{where} \quad \tau_z = \tau_{zx} \vec{i} + \tau_{zy} \vec{j} + \tau_{zz} \vec{k} \quad (8)$$

in *integral form* we get:

$$\frac{\partial}{\partial t} \int_V \rho u dV + \int_S \rho u \vec{v} \cdot \vec{n} dS + \int_S p n_x dS = \int_S \tau_x \cdot \vec{n} dS + \int_V \rho f_x dV \quad (9)$$

$$\frac{\partial}{\partial t} \int_V \rho v dV + \int_S \rho v \vec{v} \cdot \vec{n} dS + \int_S p n_y dS = \int_S \tau_y \cdot \vec{n} dS + \int_V \rho f_y dV \quad (10)$$

$$\frac{\partial}{\partial t} \int_V \rho w dV + \int_S \rho w \vec{v} \cdot \vec{n} dS + \int_S p n_z dS = \int_S \tau_z \cdot \vec{n} dS + \int_V \rho f_z dV \quad (11)$$

## 9. Numerical modelling

### 9.1. Navier-Stokes solution

The *Continuity* and *Momentum* equations are also called **Navier Stoke equations** (N-S) and as aforementioned they describe the motion of a viscous fluid. Except for few simplified problems, there are no analytical solution to the N-S equations, thus they must be solved in a iterative and discretized way. This is what is carried out by the Computational Fluid Dynamics.

### 9.2. Computational Fluid Dynamics

A Computational Fluid Dynamic (CFD) simulation aims to replicate computationally the motion and the behaviour of a fluid under certain conditions. Over time this science has gained more and more credibility becoming a powerful weapon in the hands of scientist and engineers in the design process. It contributed in reducing the number of expensive experiments that use to take place during the design process.

A CFD analysis splits basically in three parts:

- Pre processor;
- Solver
- Post processor

### 9.3. Pre processor

This phase is characterized, at first, by the creation of the geometry which involves both the object with which the flow will exchange forces and the computational domain that is a representation of the physical one. The computational domain must respect certain dimensions in order not to influence the physical behaviour of the flow.

#### 9.3.1. Domain Discretization: mesh generation

Ones the computational domain is defined, it must be discretized; there are different techniques that can be chosen, The one adopted in this study and implemented in Star CCM+ is the Finite Volume Method (FVM). It consists in dividing the domain into control volumes, called **cells**, and integrate the differential equation over this volume and apply the divergence theorem.

The result is a set of linear algebraic equation, one for each control volume, that are solved iteratively (segregated) or simultaneously (coupled). In the present work the *segregated* one, is used. With the segregated method, the momentum equations are initially solved for all cells and then the energy equation is subsequently solved.

**Type of mesh** The FVM, for its characteristics, gives the possibility to adopt in this study a grid type called *Unstructure grid* in contrast with the one called *Structured grid*. The structured grids are characterized by the grid nodes addressed by indices  $i,j,k$  and by grid lines passing all through domain. These grids involve a lower cells number but are difficult to generate in complex geometries.

The Unstructured grids instead, do not provide for a indexing to locate the cells nodes, the latter are arranged in an arbitrary fashion. Although the increase in the computational cost,

these grid type let the user generate grids over complex geometries. Figure 23 shows an example of structured and unstructured grid.

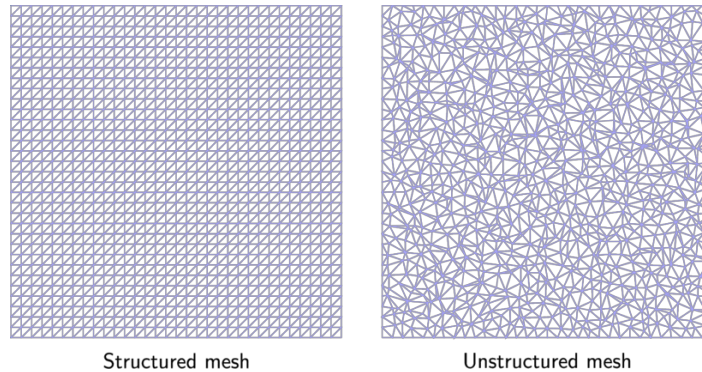


Figure 23: Structured vs. unstructured [9]

### 9.3.2. Boundaries

The next stage is the definition of the boundary conditions, a required component of the mathematical model when solving the N-S equations. They direct motion of flow; boundaries and internal surfaces are represented by face zone.

They are the physical representation of the mathematical *Dirichlet* and *Neumann* conditions. In the first case, the value of the variable is prescribed at the boundary, in the second one its gradient normal to the boundary.

There are different types of boundaries, the most common for the vessel hydrodynamics are:

- *Velocity Inlet*: it defines velocity vector and scalar properties of flow at the inlet boundaries;
- *Pressure outlet*: it defines the static/gauge pressure at the outlet boundary. This is interpreted as the static pressure of the environment into which the flow exhausts. Usually, the static pressure is assumed to be constant over the outlet;
- *Symmetry*: it is used to reduce computational effort. Flow field and geometry must be symmetric: zero normal velocity and zero normal gradients of all values at symmetry plane.
- *Wall*: it is used to bound fluid and solid regions; in this type of boundary no-slip condition is enforced.

A. Bakker [10].

### 9.4. Solver

Once the mesh has been generated and the boundary conditions are set, it is time to choose the equation to be solved and the numerical model to solve the latter. The choice of the right equation and the right models for a certain problem can strongly influence the computational cost and time, and the accuracy of the simulation.

#### 9.4.1. Modelling Turbulence

The majority of flows with an engineering interest are characterized by turbulence. The word turbulence comes together with the word *random*, meaning that it cannot be predicted in detail but only statistically. It contains a wide range of different scales. There are many way to numerically model turbulence:

- **DNS**, Direct Numerical Simultions
- **LES**, Large Eddy Simulations
- **RANS**, Reynolds Averaged Navier Stokes

In DNS the Unsteady, three Dimensional Navier-Stokes equations are numerically resolved; all the motion scales must be resolved. DNS does not involve approximations, other than those due to discretization. The latter are characterized by an high computational cost.

The LES are characterized by the decomposition of the flow quantities into a large scale contribution and a small scale contribution by a spatial filter. The large scale contribution are explicitly calculated, whereas the effects of the small scale contributions on the large scale flow may be described by a model.

The methods just described requires a massive computational cost that is often suitable for research center but not for CFD companies which have to make a compromise between computational precision and cost. For this reason RANS equations are adopted in the present study and deepened in the following section.

#### 9.4.2. RANS

Reynolds in 1895 proposed to decompose the instantaneous turbulent flow variables in a mean and a fluctuating value:

$$u_i = U_i + u'_i \quad (12)$$

$$p = P + p' \quad (13)$$

where the term at the left hand side is the instantaneous variable, the first term at the RHS is the mean value and the second is the fluctuating value around the mean one.

Substituting  $u_i$  and  $p$  in the continuity and momentum equations we get the mean flow equations:

$$\frac{\partial U_i}{\partial x_i} = 0 \quad (14)$$

$$\frac{\partial U_i}{\partial x t} + U_j \frac{\partial U_i}{\partial x_j} = -\frac{1}{\rho} \frac{\partial P}{\partial x_i} + \nu \frac{\partial^2 U_i}{\partial x_j \partial x_j} - \frac{\partial \overline{u'_i u'_j}}{\partial x_j} \quad (15)$$

where  $-\overline{\rho u'_i u'_j}$  is the Reynolds stress tensor and represents the mean flux of momentum due to turbulent fluctuations and its divergence appears as volumetric forcing of the mean flow. The Reynolds stresses are unknowns and are determine by a turbulence model, either via:

- the turbulent viscosity hypotesis;
- the modelled Reynolds-stress transport equations.

**Turbulent Viscosity Hypothesis (TVH)** Generally, the TVH is the method preferred for modelling the Reynolds stress tensor. In 1877 Boussinesq, proposed to connect the Reynold stresses with the mean rates of deformation, obtaining:

$$-\rho \overline{u'_i u'_j} + \frac{2}{3} \rho k \delta_{ij} \equiv -\rho \cdot a_{ij} = \rho \nu_T \left( \frac{\partial U_i}{\partial x_j} + \frac{\partial U_j}{\partial x_i} \right) \equiv 2\rho \nu_T \bar{S}_{ij} \quad (16)$$

where

- $k = \overline{u'_i u'_i} / 2$  is the mean turbulent kinetic energy (TKE) per unit mass;
- $\bar{S}_{ij}$  is the mean rate of strain tensor;
- $a_{ij}$  is the anisotropy tensor;
- $\nu_T(\vec{x}, t)$  is the turbulent viscosity or eddy viscosity;
- $\delta_{ij}$  is the Kronecker delta;

Assuming the TVH, Reynolds equations have the same form as the N-S. With the equation we have now we can't completely define the flow field variables, so a turbulence model is needed in order to define an expression for  $\nu_T$ .

There are different type of Models that can be adopted and that expresses the relation with the fluid and the turbulent viscosity. They depends on how far we want to go in the mathematical complexity and how much we are willing to spend in terms of computational cost. The most used models are the two equations models. In this thesis the  $k - \epsilon$ ,  $k - \omega$  where used together with a modification of the  $k - \omega$  one.

#### 9.4.3. $k - \epsilon$

This is the most widely used complete turbulence model.

In this model  $\nu_T$  is defined as

$$\nu_T = C_\mu \frac{k^2}{\epsilon} \quad (17)$$

where

- $C_\mu$  is one of the five constant values present in this model;
- $k$  is the TKE;
- $\epsilon$  is the turbulent dissipation rate (TDR).

This model is a two equations model because we need to define  $k$  and  $\omega$ , and these are:

$$\frac{\partial k}{\partial t} + U_i \frac{\partial k}{\partial x_i} = \Pi - \epsilon - \frac{\partial I_i}{\partial x_i} \quad (18)$$

$$\frac{\partial \epsilon}{\partial t} + U_i \frac{\partial \epsilon}{\partial x_i} = C_{\epsilon 1} \frac{\epsilon}{k} \Pi - C_{\epsilon 2} \frac{\epsilon^2}{k} + \frac{\partial}{\partial x_i} \left( \frac{\nu_T}{\sigma_\epsilon} \frac{\partial \epsilon}{\partial x_i} \right) \quad (19)$$

where

- $\Pi = -\overline{u'_i u'_j} \frac{\partial U_i}{\partial x_j}$

- $I_i = -\frac{\nu_T}{\sigma_k} \frac{\partial k}{\partial x_i}$

This model is best viewed as being entirely empirical, standard values of the five constants presents in the equations are obtained by empirical fitting of predictions and experiments:  $C_\mu = 0.09$ ,  $C_{\epsilon 1} = 1.44$ ,  $C_{\epsilon 2} = 1.92$ ,  $\sigma_k = 1.0$ ,  $\sigma_\epsilon = 1.3$ .

This is usually acceptable for simple flows, it can be quite inaccurate for complex flows, presence of separation, boundary layer with adverse pressure gradient, recirculating zones, secondary flows, strong swirls, strong streamline curvature, low reynolds numbers.

*D. Tordella [11]*

#### 9.4.4. $k-\omega$

The  $k - \omega$  turbulence model is, as for the previous one, a two equations turbulence model. This time, instead of  $\epsilon$ , the Specific Dissipation Rate  $\omega$  is present. *CFD online [12]*

The model holds the same structure seen before, which consists in two equations and six constants:

$$\frac{\partial k}{\partial t} + U_j \frac{\partial k}{\partial x_j} = \tau_{ij} \frac{\partial U_i}{\partial x_j} - \beta^* k \omega + \frac{\partial}{\partial x_j} \left[ (\nu + \sigma^* \nu_T) \frac{\partial k}{\partial x_j} \right] \quad (20)$$

$$\frac{\partial \omega}{\partial t} + U_j \frac{\partial \omega}{\partial x_j} = \alpha \frac{\omega}{k} \tau_{ij} \frac{\partial U_i}{\partial x_j} - \beta \omega^2 + \frac{\partial}{\partial x_j} \left[ (\nu + \sigma \nu_T) \frac{\partial \omega}{\partial x_j} \right] \quad (21)$$

with  $\alpha = \frac{5}{9}$ ,  $\beta = \frac{3}{40}$ ,  $\beta^* = 9/100$ ,  $\sigma = \frac{1}{2}$ ,  $\sigma^* = \frac{1}{2}$ ,  $\epsilon = \beta^* \omega k$ .

One reported advantage of the  $k - \omega$  model over the  $k - \epsilon$  model is its improved performance for boundary layers under adverse pressure gradients. Perhaps the most significant advantage, however, is that it may be applied throughout the boundary layer, including the viscous-dominated region, without further modification. Furthermore, the standard  $k - \omega$  model can be used in this mode without requiring the computation of wall distance.

The biggest disadvantage of the  $k - \omega$  model, in its original form, is that boundary layer computations are sensitive to the values of  $\omega$  in the free-stream. This translates into extreme sensitivity to inlet boundary conditions for internal flows, a problem that does not exist for the  $k - \epsilon$  models. *StarCCM+ User Guide [13]*



#### 9.4.5. VOF

The Volume Of Fluid (VOF) Multiphase model is suited to simulating flows of several immiscible fluids on numerical grids capable of resolving the interface between the phases of the mixture.

The VOF Multiphase model is used to solve problems involving immiscible fluid mixtures, free surfaces, and phase contact time. In such cases, there is no need for extra modeling of inter-phase interaction, and the model assumption that all phases share velocity, pressure, and temperature fields becomes a discretization error.

The Volume of Fluid (VOF) multiphase model implementation in Simcenter STAR-CCM+ belongs to the family of interface-capturing methods that predict the distribution and the movement of the interface of immiscible phases. This modeling approach assumes that the mesh resolution is sufficient to resolve the position and the shape of the interface between the phases.

The distribution of phases and the position of the interface are described by the fields of phase volume fraction  $\alpha_i$ . The volume fraction of phase  $i$  is defined as:

$$\beta_i = \frac{V_i}{V} \quad (22)$$

where  $V_i$  is the volume of phase  $i$  in the cell and  $V$  is the volume of the cell. The volume fractions of all phases in a cell must sum up to one:

$$\sum_{i=1}^N \beta_i = 1 \quad (23)$$

where  $N$  is the total number of faces.

Depending on the value of the volume fraction, the presence of different phases or fluids in a cell can be distinguished:

- $\beta_i = 0$ : the cell is completely void of phase  $i$ :
- $\beta_i = 1$ : the cell is completely filled with phase  $i$ :
- $0 < \beta_i < 1$  values between the two limits indicate the presence of an interface between phases;

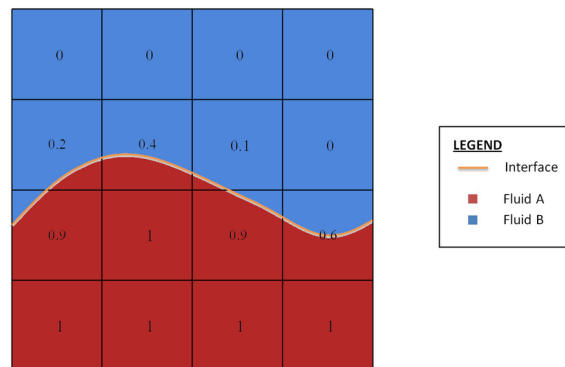


Figure 24: Cell Volume of fluid fraction [14]

Figure 24 shows an example of how the volume fraction is applied to cells.

The material properties that are calculated in the cells containing the interface depend on the material properties of the constituent fluids. The fluids that are present in the same interface-containing cell are treated as a mixture:

$$\rho = \sum_i \rho_i \beta_i \quad (24)$$

$$\mu = \sum_i \mu_i \beta_i \quad (25)$$

$$C_p = \sum_i \frac{(C_p)_i \rho_i}{\rho} \beta_i \quad (26)$$

where  $\rho_i$  is the density,  $\mu_i$  is the dynamic viscosity, and  $(C_p)_i$  is the specific heat of phase  $i$ .

**Volume fraction transport equation** The distribution of phase  $i$  is driven by the phase mass conservation equation:

$$\frac{\partial}{\partial t} \int_V \beta_i dV + \int_A \beta_i \vec{v} \cdot \vec{n} dS = \int_V \left( F_{\beta_i} - \frac{\beta_i}{\rho_i} \frac{D\rho_i}{Dt} \right) dV - \int_V \frac{1}{\rho_i} \nabla \cdot (\beta_i \rho_i \vec{v}_{d,i}) dV \quad (27)$$

where

- $\vec{v}$  is the mixture (mass-averaged) velocity;
- $v_{d,i}$  is the diffusion velocity;
- $F_{\beta_i}$  is a user-defined source term of phase  $i$ ;
- $D\rho_i/Dt$  is the material or Lagrangian derivative of the phase densities  $\rho_i$ .

#### 9.4.6. HRIC

An important quality of a system of immiscible phases (for example, air and water) is that the fluids always remain separated by a sharp interface. In order to do so, in *STAR CCM+* the VOF multiphase model come with The *High-Resolution Interface Capturing* (HRIC) scheme, which is designed to mimic the convective transport of immiscible fluid components, resulting in a scheme that is suited for tracking sharp interfaces, *Siemens StarCCM+ User Guide*[13].

A simple higher-order scheme (for example, central differencing scheme (CDS) or second-order upwind scheme (SOU)) would fail in approximating large spatial variations of phase volume fractions, which are best represented by the Heaviside unit step function. The front sharpening aspect of the downwind scheme is just what is needed when the interface is perpendicular to the flow. However, when the interface is parallel to the flow direction, the downwind scheme tends to wrinkle it.

For this reason, the HRIC model adopts a forward (upwind) and backward (downwind) interpolation function in order to get the best of both worlds.

#### 9.4.7. DFBI

The **D.F.B.I.** (Dynamic Fluid Body Interaction) is a numerical model that was used in this work to define the motion of the ship and boats taken into account.

It let us model the motion of a rigid body in response to applied forces and moments and solves the governing equations of rigid body motion to find the new position of the rigid body.

**Rigid Body** A rigid body is an object in which the relative distance between internal points does not change. It is possible for a rigid body to translate along and rotate around the three axes ( $x, y, z$ ).

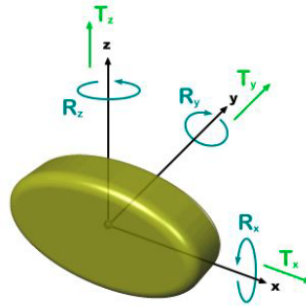


Figure 25: Rigid body with its DOF [13]

In our case the rigid body is the vessel that moves in the water.

The motion of the vessel can be modelled considering only the motion of the center of mass of this latter; for the translational motion we need to know the mass of the body, for the rotational one, the moments of inertia; for rotation and translation, we need to know both mass and moments of inertia.

#### Governing Equations of Motion

- **Translation** The equation for the translation of the center of mass is:

$$m \frac{d\vec{v}}{dt} = \vec{f} \quad (28)$$

where

- $m$  represents the mass of the body
- $\vec{f}$  is the resultant force acting on the body
- $\vec{v}$  is the velocity of the center of mass
- **Rotation** The equation of rotation of the body is formulated in the Body Local Coordinate System with the origin in the center of mass of the body:

$$\vec{M} \frac{d\vec{\omega}}{dt} + \vec{\omega} \times \vec{M} \vec{\omega} = \vec{n} \quad (29)$$

where

- $\vec{M}$  is the tensor of moments of inertia
- $\vec{\omega}$  is the angular velocity of the rigid body
- $\vec{n}$  is the resultant moment acting on the body

**Constraints** For the present work, but also in general, it can be useful to consider kinematic constraints for the simulation of body motion. These constraints allow certain degrees of freedom and restrict others.

The analytical expression of constraint equations for a rigid body can be written as:

$$\xi_k(\vec{d}, t) = 0; \quad (30)$$

where

- $t$  is the time
- $\vec{d}$  is the dependent coordinate vector:

$$\vec{d} = (r_x, r_y, r_z, \phi, \theta, \psi)$$

its components corresponds to the coordinate along and around the three axes.

For a constrained body, not all components of  $\vec{d}$  are independent. The minimum number of independent variables that are required to describe the motion of the rigid body is given by the number of degrees of freedom for the constrained body:

$$DoF = 6 - l \quad (31)$$

where  $l$  is the total number of constraints.

**2-DoF** In the present work a maximum of 2 Dof was taken into account:

- the translation along the  $z$ -axis, the **Sinkage**;
- the rotation around the  $y$ -axis, the **Trim**.

#### 9.4.8. Boundary layer modelling

An important phase of the CFD process is the right modelling of the *Boundary Layer* (BL). The BL is that region in the proximity of a wall in a viscous fluid where the majority of the viscous stress are concentrated and where vorticity is generated, thus a right modelling is mandatory.

In order to describe the Boundary layer structure, figure 26a shows the BL over a flat plate. It can be seen that it generates from the leading edge and it develops moving away from the latter along the  $x$  axis as the local Reynolds number increases.

Due to the the  $Re$  involved, the interest of this thesis is turned towards the turbulent BL. This, showed in figure 26b, presents a multi-layer structures and can be divided in two regions: the inner and outer layer. The latter in its turn can split in three layers going moving from the wall along the vertical axis:

- *Viscous sublayer*: is characterized by the predominance of the shear stress flux over the Reynolds stress;

- *Buffer layer*: in this region the majority of the turbulent structures are generated;
- *Logarithmic layer*: it is the outer region of the inner layer and it is characterized by a logarithmic law between the coordinates.

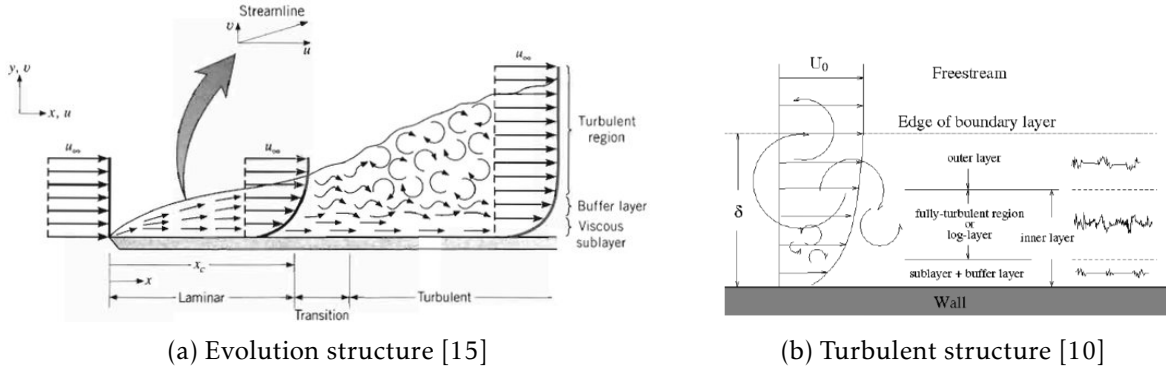


Figure 26: Boundary layer over a flat plate

To better describe these three regions the inner variable can be introduced:  $u^+$  and  $y^+$ . These are dimensionless variables that take into account what is happening at the wall. They are defined as:

$$y^+ = \frac{y}{l_\tau} \quad (32)$$

$$u^+ = \frac{u}{u_\tau} \quad (33)$$

where

- $l_\tau$  is the shear length and is defined as  $\frac{\nu}{u_\tau}$ ;
- $u_\tau$  is the shear velocity and it is defined as  $\sqrt{\frac{\tau_w}{\rho}}$  where  $\tau_w$  is the shear stress at the wall.

With the use of these variables:

- the viscous sublayer results characterized by a linear dependence between the two coordinates  $u^+ = y^+$  and it ranges between  $0 < y^+ < 5$ ;
- the logarithmic layer is thus characterized by a logarithmic law  $u^+ = \frac{1}{0.41} \log y^+ + 5$  and ranges between  $30 < y^+ < 750$ ;
- the buffer layer is not characterized by a specific law.

In order to model the mesh a specific Wall Treatment has to be chosen. A wall treatment in STAR-CCM+ is the set of assumptions for modeling near-wall turbulence quantities such as wall shear stress, turbulent production and turbulent dissipation. Traditionally, the two basic types of wall treatment are :

- High  $y^+$  wall treatment is the classic wall-function approach, where wall shear stress, turbulent production and turbulent dissipation are all derived from equilibrium turbulent boundary layer theory. It is assumed that the near-wall cell lies within the logarithmic region of the boundary layer, therefore the centroid of the cell attached to the wall should have  $y^+ > 30$ .

- The low  $y^+$  wall treatment assumes that the viscous sublayer is well resolved by the mesh, and thus wall laws are not needed. It should only be used if the entire mesh is fine enough for  $y^+$  to be approximately 1 or less.

In order to deal with coarse and fine meshes, in this thesis the **All  $y^+$**  treatment is used. The all  $y^+$  wall treatment is an additional hybrid wall treatment that attempts to combine the high  $y^+$  wall treatment for coarse meshes and the low  $y^+$  wall treatment for fine meshes. It is designed to give results similar to the low- $y^+$  treatment as  $y^+ < 1$  and to the high- $y^+$  treatment for  $y^+ > 30$ . It is also formulated to produce reasonable answers for meshes of intermediate resolution, when the wall-cell centroid falls within the buffer region of the boundary layer, i.e. when  $1 < y^+ < 30$ .

Figure 27 shows the *law of the wall*, i.e. the correlation between  $u^+$  and  $y^+$  at different  $y^+$  from the wall, and the applicability of the wall treatments.

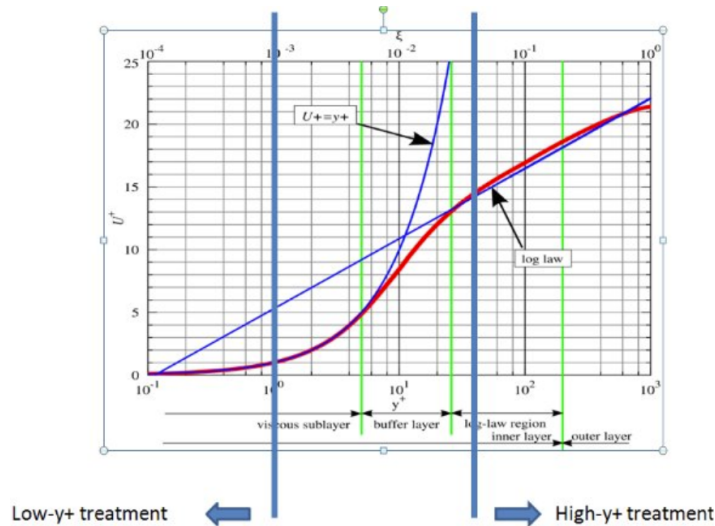


Figure 27: Law of the wall: applicability of wall treatments [13]

## 9.5. Post processor

Finally after all the computations have been carried out, the results can be processed and showed with plots and images in order to be easily interpreted and to draw conclusions.

## 10. Verification And Validation

Many practical problems of fluid dynamics are currently analysed by numerical solution of the mathematical models that simulate the physics of the flows, i.e. by Computational Fluid Dynamics (CFD). In the early years of the development of CFD, it was an achievement already to demonstrate the ability to address the problems using numerical solutions. However, in many current applications of CFD it is no longer enough to produce "a solution". The credibility of the simulations must be established with *Verification and Validation*, Eça *et al.* [16].

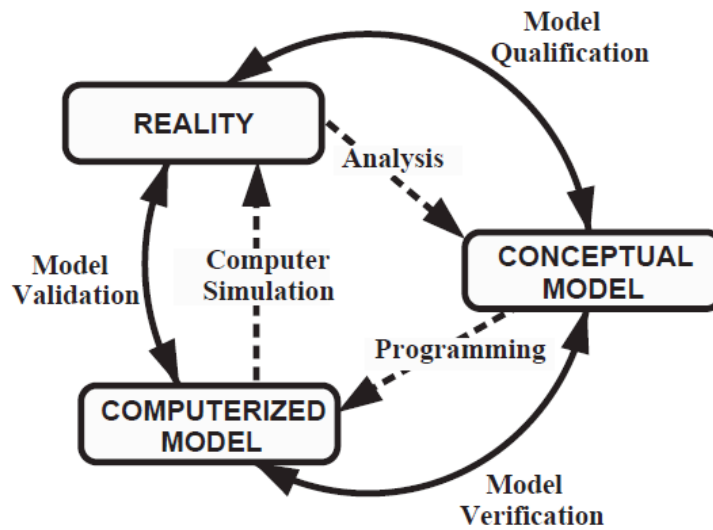


Figure 28: VV process [17]

### 10.1. Error VS Uncertainty

Before defining the various types of errors that could be encountered during Verification and validation, following Roache [18], it's good to distinguish between: **errors** and **uncertainty**.

- An **Error** is defined as the difference between a given solution and what is considered its "true/exact" value. It has a sign and it requires the knowledge of the "truth". The "truth" depends on which type of error we want to evaluate.

$$Error = \phi_{exact} - \phi_i;$$

where

- $\phi_{exact}$  is the exact solution;
- $\phi_i$  is the numerical solution;
- An **uncertainty** defines an interval that should contain the "true/exact" value with a certain degree of confidence. It is defined with a sign, i.e. it signifies an error band for the numerical result so that the true solution can be expected to be within that error band (usually with 95% confidence), L. Eça and M. Hoekstra [19]

## 10.2. Error Classification

### 10.2.1. Modelling errors

Physical modelling errors are a consequence of the representation of the physical world by a mathematical model. Their detection and quantification is the goal of *Validation*.

### 10.2.2. Programming errors

The discretisation of the selected set of partial differential equations and the procedure to solve the resulting equations numerically is incorporated into a computer code. Programming errors (bugs), often simple typos in the code, are likely to appear. Code Verification aims at detecting and removing such type of errors.

### 10.2.3. Numerical Errors

In CFD prediction we can distinguish between three types of numerical errors:

**Round off error** Consequence of the finite precision of the computers; its importance tends to increase with grid refinement.

**Iterative error** : related to the non linearity of the mathematical equations solved by CFD. Source of non linearity, i.e. for the solutions of RANS are:

- The convective terms;
- Deferred corrections in the discretisation schemes of the continuity and momentum equations;
- The turbulence closure.

**Truncation error and Discretisation error** Consequence of the approximations made to transform the partial differential equations of the continuum formulation into a system of algebraic equations: the first is a measure of the accuracy of the approximation and determine the rate at which error decreases as the grid is refined.

$$\epsilon_\tau = (h_i)^m \alpha_{m+1} + (h_i)^{m+1} \alpha_{m+2} + \dots + (h_i)^n \alpha_{n+1}$$

where

- $h_i$  is the grid spacing;
- $m$  is the exponent of the leading truncation term;
- $n$  is the exponent of the smallest term

If we take into account an Algebraic equation system,  $L(\Phi)$ , and an Algebraic equation system discretised,  $L_{h_i}(\Phi)$ , considering  $\Phi$  the exact solution of the system:

$$L(\Phi) = L_{h_i}(\Phi) + \tau_{h_i} = 0$$

the two systems differ for a quantity equal to the truncation error,  $\tau_{h_i}$ .



If we now consider the discretised solution,  $\Phi_{h_i}$ :

$$\Phi = \Phi_{h_i} + \epsilon_{h_i}$$

the exact solution of the discretized system differs from the exact solution of the differential equations by the discretization error  $\epsilon_{h_i}$ .

For sufficiently refined grids, the truncation error (and the discretization error as well) is proportional to the leading term of those terms neglected in the Taylor series

$$\epsilon_{h_i} \approx \alpha h_i^p + H$$

where  $\alpha$  and  $p$  are respectively the coefficient and the exponent of the leading term.  $H$  contains the terms neglected.

### 10.3. Verification

Verification is a purely mathematical exercise that intends to show that we are “solving the equations right”, that aims at quantifying the numerical error/uncertainty. It does not require any experimental data, but it may require exact solutions of the selected mathematical model, *L. Eça and M. Hoekstra* [19].

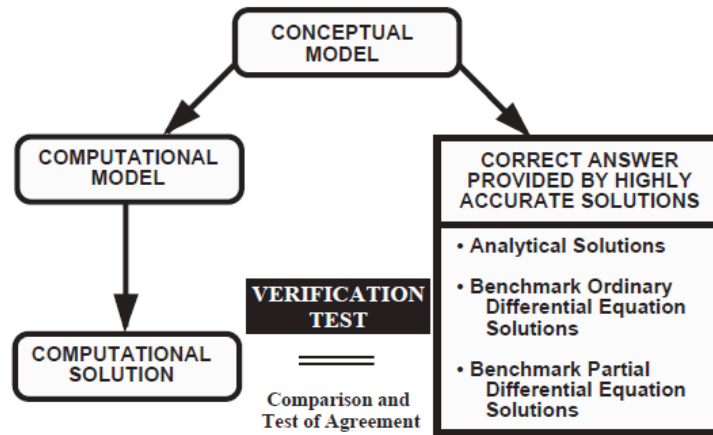


Figure 29: Verification process[17]

Verification splits in two parts:

- *Code verification*
- *Solution Verification*

#### 10.3.1. Code verification

Code Verification is a fundamental step in the development of any CFD code. Its goal is to ensure that a given flow solver is correctly coded (no bugs). A typical way to demonstrate code correctness is by showing that in a series of systematically refined grids the discretisation error goes to zero with an observed order of accuracy matching the theoretical order of the method. This requires analytical solutions to allow the direct evaluation of the discretisation error; but, **there are no analytical, realistic-flow solutions available for the RANS equations.**

**Code verification procedure** In this Thesis only the Solution Verification will be carried out since no analytical solution exists for URANS and the flow field in the test cases selected is too complicated to build a manufactured solution which goal is to “manufacture” an exact solution to a slightly modified equation. However a clear and complete understanding of the procedure for code verification is reported in *L.Eça and M.Hoekstra* [19] and *L.Eça and G.Vaz* [20].

### 10.3.2. Solution verification

The goal of Solution Verification is to estimate the uncertainty of a given numerical prediction  $U_{CFD}$ :

$$\phi_i - U_{CFD} \leq \phi_{exact} \leq \phi_i + U_{CFD} \quad (34)$$

where

- $\phi_i$  is the numerical solution;
- $\phi_{exact}$  is the exact solution;
- $U_{CFD}$  is the numerical uncertainty

In section 10.2.3, it was underlined that we can distinguish in three types of numerical errors. It is commonly reported in procedures to assume *Round off* and *Iterative error* negligible.

For the first one, the simulations are performed in single precision, but due to the difficulty in the estimation of the round-off error, it is **not quantified in the current study**. Nevertheless according to *GH.Yeoh* [21], it is noted that the *round off* error is usually not the dominant contributor to the source of solution errors when compared with the discretization error. For what concerning iterative error, in principle one should be able to reduce it to the level of the round off error. This may not be always practically feasible though, particularly in complex flows. As suggested in *L.Eça and M.Hoekstra* [22], the iterative error should be two or three order of magnitude smaller than the discretization error in order not to disturb the estimation of the numerical error. One way to do so is to monitor residuals norms; in section 11.4 a clear explanation is reported.

Many methods for solution verification exists in literature, in this thesis the one proposed by *L.Eça and M.Hoekstra* [1] is reported. It can be considered as an evolution of the Richardson Extrapolation; it is based on the estimation of the discretization error with truncated power series expansions.

The basic equation for estimating the discretization error  $\epsilon_{h_i}$  is:

$$\epsilon_{h_i} \simeq \delta_{RE} = \phi_i - \phi_0 = \alpha h_i^p \quad (35)$$

where

- $\phi_0$  is the "estimate" of the exact solution
- $\alpha$  is a constant to be determined
- $p$  is the observed order of grid convergence.

The estimation of  $\phi_0$  requires the determination of  $\phi_i$ ,  $\alpha$  and  $p$ .

The assumptions inherent in the application of equation 35 are:

- The grids must be in the “asymptotic range” to guarantee that the leading term of the power series expansion (high-order terms are neglected) is sufficient to estimate the error.
- The density of the grids is representable by a single parameter, the typical cell size of the grids,  $h_i$ . This requires the grids to be geometrically similar, i.e. the grid refinement ratio must be constant in the complete field and grid properties like the deviation from orthogonality, skewness, etc. must remain unaffected.

With equal grid refinement ratios between medium/fine and coarsest/medium grids, i.e.  $h_2/h_1 = h_3/h_2$ , a grid triplet suffices to estimate the apparent grid convergence behaviour based on the discriminating ratio:

$$R = \frac{\phi_1 - \phi_2}{\phi_2 - \phi_3}, \quad (36)$$

where the subscripts 1, 2 and 3 stands to fine, medium and coarse grid, respectively.

- Monotonic Convergence for  $0 < R < 1$
- Monotonic divergence for  $R > 1$
- Oscillatory convergence for  $R < 0$  and  $|R| < 1$
- Oscillatory divergence for  $R < 0$  and  $|R| > 1$

In fact, the discriminating ratio  $R$  is related to the observed order of grid convergence  $p$  and the grid refinement ratios  $h_2/h_1$  and  $h_3/h_2$  by

$$\log(R) = \left(\frac{h_1}{h_2}\right)^p \left( \frac{\left(\frac{h_2}{h_1}\right)^2 - 1}{\left(\frac{h_3}{h_2}\right)^2 - 1} \right) \quad (37)$$

which for  $h_2/h_1 = h_3/h_2$  reduces to

$$\log R = p \log \frac{h_1}{h_2} \quad (38)$$

Hence, in such conditions,  $p > 0$  is equivalent to  $0 < R < 1$  and  $p < 0$  to  $R > 1$  ( $\frac{h_1}{h_2} < 1$ )

Obviously, we can estimate  $\epsilon_\phi$  from Eq.35 only when  $p > 0$ , the expected outcome when the three grids are in the “asymptotic range” and the data have no scatter (and the code producing the data has been verified). In simple problems (simple geometry and simple equations) such requirements are easy to satisfy and Eq.35 suffices to make a reliable error estimation. However, for “practical problems”, i.e. complex geometries and complex equations (turbulent flow), it is really hard (if not impossible) to comply with all these assumptions. The consequence is that scatter appears in the data.

A main contributor to noisy data is the lack of geometrical similarity of the grids[14]. While structured grids essentially allow geometrical similarity to be obtained, this is hardly true for unstructured grids, that as we will see, it is our case. Other source of scatter in the data are flux limiters, commonly used in the discretization of convective terms, as well as damping functions and switches being part of many present-day turbulence models. Therefore, in complex flows it is an exception rather than a rule that the conditions required for the reliable use of Eq.35 are met.

In order to be able to deal with the shortcomings of "practical calculations", assuming that the CFD code is theoretically second order accurate, we can consider three more error estimator:

$$\epsilon_{h_i} \simeq \delta_1 \quad \quad \quad = \phi_i - \phi_o = \alpha h_i \quad (39)$$

$$\epsilon_{h_i} \simeq \delta_2 \quad \quad \quad = \phi_i - \phi_o = \alpha h_i^2 \quad (40)$$

$$\epsilon_{h_i} \simeq \delta_{12} \quad \quad \quad = \phi_i - \phi_o = \alpha h_i + \alpha_2 h_i^2 \quad (41)$$

These three alternatives are only used if the estimation with equation 35 is impossible or not reliable, i.e. the observed order of accuracy is either too small or too large ( $p < 0.5$  or  $p > 2$ ). The first two options are suitable for monotonically converging solutions only whereas the latter can be used as well with non-monotonic convergence.

The error estimators presented above require three grids or two grids to estimate an error. But error estimation based on three (or two) grids is not reliable for noisy data due to the extreme sensitivity of the determination of  $p$  to small perturbations in the data. Redundancy, and therefore the possibility of a quality check on the value of  $p$ , only occurs when the fourth grid is added! Therefore it is **highly recommendable** to use at least **four grids** when some scatter in the data is expected, i.e. for most engineering flow problems.

In such conditions ( $n_g \geq 4$ ), it is possible to do the error estimation in the least/squares sense, i.e. to determine  $\phi_0$  from the minimum of the functions:

$$S_{RE}(\phi_0, \alpha, p) = \sqrt{\sum_{i=1}^{n_g} (\phi_i - (\phi_0 + \alpha h_i^p))^2} \quad (42)$$

$$S_1(\phi_0, \alpha) = \sqrt{\sum_{i=1}^{n_g} (\phi_i - (\phi_0 + \alpha h_i))^2} \quad (43)$$

$$S_2(\phi_0, \alpha) = \sqrt{\sum_{i=1}^{n_g} (\phi_i - (\phi_0 + \alpha h_i^2))^2} \quad (44)$$

$$S_{12}(\phi_0, \alpha_1, \alpha_2)(\phi_0, \alpha) = \sqrt{\sum_{i=1}^{n_g} (\phi_i - (\phi_0 + \alpha_1 h_i + \alpha_2 h_i^2))^2} \quad (45)$$

If in a practical application a flow field is computed on four (or more) grids, one may wish to give more value to the finer than the coarser grid solutions. Therefore, alternative least-squares error estimators with weights are also adopted, leading to the minimization of the following functions:

$$S_{RE}^w(\phi_0, \alpha, p) = \sqrt{\sum_{i=1}^{n_g} w_i (\phi_i - (\phi_0 + \alpha h_i^p))^2} \quad (46)$$

$$S_1^w(\phi_0, \alpha) = \sqrt{\sum_{i=1}^{n_g} w_i (\phi_i - (\phi_0 + \alpha h_i))^2} \quad (47)$$

$$S_2^w(\phi_0, \alpha) = \sqrt{\sum_{i=1}^{n_g} w_i (\phi_i - (\phi_0 + \alpha h_i^2))^2} \quad (48)$$

$$S_{12}^w(\phi_0, \alpha_1, \alpha_2) = \sqrt{\sum_{i=1}^{n_g} w_i (\phi_i - (\phi_0 + \alpha_1 h_i + \alpha_2 h_i^2))^2} \quad (49)$$

The weights  $w_i$  are based on the typical cell size:

$$w_i = \frac{\frac{1}{h_i}}{\sum_{i=1}^{n_g} \frac{1}{h_i}}$$

guaranting that

$$\sum_{i=1}^{n_g} w_i = 1 \quad (50)$$

**Solution verification procedure: Discretization error estimation** Below a procedure for the estimation of the discretization error is proposed. The procedure relies on the availability of at least four data points, on the proper choice of a typical cell size and on the assumption that, as previously stated, the round-off and iterative errors are negligible relative to the discretization error.

1. The first step of the procedure is to determine the observed order of grid convergence  $p$  from the minimum of  $S_{RE}$  (eq. 42 e 46);
2.
  - If both solutions produce a  $p > 0$ , we choose the best fit as the one with the smallest standard deviation.
  - If one of the solutions yields a negative  $p$  it is discarded.
  - If both give negative  $p$ , the data behaviour is classified as anomalous.

Notice that oscillatory convergence is included as anomalous behaviour.

• **Monotonically convergent data,  $p > 0$**

If the observed order of convergence is positive we proceed as follows. From what has been identified as the best fit the observed order of grid convergence  $p$ , the constant  $\alpha$  and the estimate of the exact solution,  $\phi_0$ , are read. If the value of  $p$  is within an acceptable range (compared to the theoretical order of the method), the error is estimated

from  $\delta_{RE}$ , eq. 35. For a second-order method, the acceptable range is empirically defined here as  $0.5 \leq p \leq 2$ .

A value of  $p$  greater than the formal order of grid convergence (i.e.  $p > 2$ ) is likely to cause too small error estimates. In that case,  $\delta_{RE}$  is dropped and replaced by  $\delta_1$ , eq. 39 or  $\delta_2$ , eq. 40. By solving Eqs.43,47, 44 and 48, four fits are determined and the best fit (and the associated error estimator) is again decided from the smallest value of the standard deviation of the fit.

If on the other hand  $p$  becomes too small ( $p < 0.5$ ),  $\delta_{RE}$  produces a too conservative error estimate (when  $p \rightarrow 0$ ,  $\delta_{RE}$  tends to infinity). So for  $p < 0.5$  we also drop the value of  $\delta_{RE}$  in favor of the alternative error estimators with fixed exponents. In order to guarantee that we are not becoming under-conservative, we also include  $\delta_{12}$  41 in the error estimation. It means that six fits are performed in this case and the one with the smallest standard deviation is selected.

- **Anomalous data behaviour** Equation 35 is useless for any data set that does not have  $p > 0$ . However, Eqs.39, 40 and 41 may be used for any data behaviour, including non-monotonic convergence in the case of Eq.41. Therefore, for all anomalous (non-monotonically convergent) cases the error is estimated from  $\delta_1$  39,  $\delta_2$  40 or  $\delta_{12}$  41 with  $\phi_0$ ,  $\alpha$ ,  $\alpha_1$  and  $\alpha_2$  determined in the least-squares sense with and without weights. As before, these selected solution is the fit involving the smallest standard deviation. As we mentioned above, oscillatory convergence is also included in anomalous behaviour. In that case, it can be argued that we are making a very poor error estimation. However, if that is the case, this will be reflected in the value of  $\sigma$  and as we will describe below this will have consequences for the estimated uncertainty.

**Solution verification procedure: Uncertainty estimation** In the previous section, we described the procedure to estimate the discretization error  $\epsilon_\phi$ . The procedure gives also a measure of the quality of the error estimation, viz. the standard deviation of the fit  $\sigma$ , and in some cases the observed order of grid convergence  $p$ . All three quantities are used now to reach the final goal: an estimate of the uncertainty  $U_{CFD}$ , i.e. an interval that contains the exact solution with 95% coverage, eq. 34.

First judgement is made of the quality of the data fit. To that end we define a data range parameter as

$$\Delta_\phi = \frac{(\phi)_{max} - (\phi)_{min}}{n_g - 1} \quad (51)$$

The error estimation is considered **reliable** if the solution is monotonically convergent with  $0.5 \leq p \leq 2.1$ <sup>1</sup> and if  $\sigma < \Delta_\phi$ .

Following the Grid Convergence Index (GCI) procedure ([23],[18]), the safety factor is chosen as  $Fs = 1.25$  if the error estimate is deemed reliable, else  $Fs = 3$ .

The determination of  $U_{CFD}$ , usually for the finest grid (best) solution, but essentially for

<sup>1</sup> Although the error estimation does not allow  $p > 2$  it is reasonable to assume a tolerance for the change in the safety factor

any  $\phi_i$  of a data set, is not only dependent on  $F_s$ . Two different expressions are adopted for “good” and “bad” error estimations, respectively for  $\sigma \leq \Delta_\phi$  or  $\sigma \geq \Delta_\phi$ .

- For  $\sigma \leq \Delta_\phi$  :

$$U_{CFD}(\phi_i) = 1.25\epsilon_\phi(\phi_i) + \sigma + |\phi_i - \phi_{fit}| \quad (52)$$

- For  $\sigma \geq \Delta_\phi$  :

$$U_{CFD}(\phi_i) = 3 \frac{\sigma}{\Delta_\phi} (\epsilon_\phi(\phi_i) + \sigma + |\phi_i - \phi_{fit}|) \quad (53)$$

The estimated uncertainty has therefore three components:

- the absolute value of the estimated discretization error times a safety factor;
- the standard deviation of the fit;
- the difference between the real data point and the value obtained from the fit for the same grid density.

The latter two quantities are just a consequence of scatter in the data. Consequently, for a grid refinement study with monotonically convergent smooth data the method reduces to the well-known GCI ([23],[18]).

It could be argued that in the cases with  $\sigma > \Delta_\phi$  it is not allowed to base an uncertainty estimation on the present error estimators. However, the estimated uncertainty with Eq.53 will then be high, indicating clearly that the data quality is bad (due to e.g. grids without similarity, incomplete iterative convergence, programming mistakes in the code...), thus still conveying a useful message.

The procedure just described is summarized and schematized in the appendices A and B of [1], together with the determination of the standard deviation  $\sigma$ .

**Time step Uncertainty estimation** In this thesis three out of four cases present an unsteady solution; in these case a time step refinement should be carried out in order to determine the time step uncertainty. Nevertheless, the cases in question are characterized by a **quasi steady solution** in which the ship, the boat or the sailing yacht aim to a constant state/attitude. G. Chen et al. [24] when performing a VV study over the KCS stated that the time step refinement uncertainty was negligible compared to the discretisation one. A. De marco et al. [25], while performing a V&V study over a planing hull achieved the same conclusion. Under these consideration, in the following test cases no time step convergence study is carried out.

#### 10.4. Validation

The goal of Validation is to quantify the modelling uncertainty, i.e. to quantify how well the mathematical models represent the physical world, i.e. we want to show that we are "solving the right equation", according to *L.Eça and M.Hoekstra* [19].

At First it should be defined what are the quantities of interest; a given model may be adequate in determining some flow quantities, but fall short to simulate others. Once such decision has been made, a second challenge appears: what is the most appropriate Validation metric?

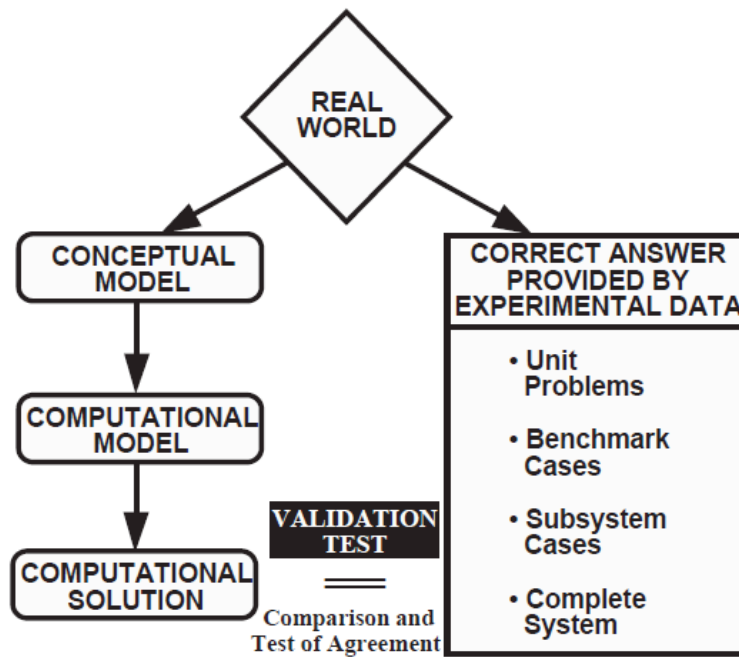


Figure 30: Validation process [17]

**ASME VV 20 Standard** The goal of the procedure is to estimate the interval that contains the modelling error,  $\delta_{model}$  model, with 95% confidence.

The validation uncertainty,  $U_{val}$  is composed of three contributions:

- $U_{CFD}$ : estimated numerical uncertainty;
- $U_{EFD}$ : estimated experimental uncertainty;
- $U_{input}$ : parametrical uncertainty.

$$U_{val} = \sqrt{U_{CFD}^2 + U_{EFD}^2 + U_{input}^2} \quad (54)$$

$U_{input}$  is supposed to include all uncertainty contributions due to lack of knowledge in the flow conditions. This latter term, being complex to be calculated, it is assumed to be 0 in accordance to AIAA - 3<sup>rd</sup> Lisbon workshop.



$$[E - U_{val}, E + U_{val}] \quad (55)$$

where

- $E$  is the validation comparison error,  $E = CFD - EFD$ ;
- $CFD$  is the simulation value;
- $EFD$  is the experimental data value.

$E$  can be also expressed in percentage of the experimental data:

$$E[\%] = \frac{CFD - EFD}{|EFD|} \quad (56)$$

The latter nomenclature is used in this thesis.

**Validation procedure** The procedure is the following one:

- If  $|E| \gg U_{val}$ , the CFD-model is apparently not good enough as a representation of the flow physics;
- if  $|E| \leq U_{val}$ , the validation exercise indicates that the CFD-model is apparently good enough to represent the physics but within the level of  $U_{val}$ . The smaller  $U_{val}$ , the stronger the conclusion is.

This evaluation is done per problem and per selected and quantity of interest. Consequently, we cannot speak of a “validated code”, *L.Eça and M.Hoekstra* [19] and *K. Dowding et al.*[26]

## 10.5. MARIN Institute: Numerical Uncertainty Analysis tool

The procedure explained in section 10.3.2 based on the work carried out by *L. Eça* and *M. Hoekstra* and others professors and researchers from *Instituto Superior Técnico (IST)* and *Maritime Research Institute Netherlands* has been implemented in a tool able to calculate the numerical uncertainty.

This tool was used in this thesis: giving as an input the solutions obtained from the CFD analysis,  $\phi_1$ , together with the corresponding numbers of cells, and specifying the solution on which calculate the uncertainty, it outputs:

- the estimated solution,  $\phi_0$ ;
- the order of convergence,  $p$ ;
- the numerical uncertainty,  $U_{CFD}$



## Benchmark Test Cases

## 11. Potsdam Propeller Test Case

The Potsdam Model Basin (SVA) is part of a more than 120-year tradition of ship and hydraulic engineering and scientific research and development in Berlin-Brandenburg. As a result of the 2nd World War and the division of Germany, the SVA was established. Since 1955, towing tests and diverse scientific work for the shipbuilding industry have been carried out at SVA.

The PPTC is a test case with the intention to offer research groups the possibility to test and validate their numerical tools the SVA investigates the controllable pitch propeller VP1304. The measurements shall contribute to a better numerical prediction of open water characteristics. Furthermore the propeller VP1304 shall become a standard test propeller within the SVA and is presented by the name PPTC, an acronym for “Potsdam Propeller Test Case”. Therefore extensive tests shall expand the measurement data of this propeller, *SVA Potsdam* [27]

*PPTC Open water tests* [28] presents the description of the propeller, the tests performed and the data collected during the latter.

**PPTC VP1304** The propeller was designed by the SVA in 1998. For the manufacture of the propeller coldrolled brass was used as raw material. The blades were manufactured on a CNC-based milling machine with HSC (high speed cutting) technology.

The propeller is a controllable pitch propeller. This affects the propeller blade design near the hub and results in a 0.3 mm gap between hub and propeller blade near the leading and trailing edge of the propeller.

| Scale Ratio                  | $\lambda$            | [-]  | 12           | 1      |
|------------------------------|----------------------|------|--------------|--------|
| Propeller Diameter           | $D$                  | [mm] | 250.0000     | 3000.0 |
| Pitch at $r/R = 0.7$         | $P_{0.7}$            | [mm] | 408.7500     | 4905.0 |
| Pitch at $r/R = 0.75$        | $P_{0.75}$           | [mm] | 407.3804     | 4888.6 |
| Mean pitch                   | $P_{Mean}$           | [mm] | 391.8812     | 4702.6 |
| Chord length at $r/R = 0.7$  | $C_{0.7}$            | [mm] | 104.1670     | 1250.0 |
| Chord length at $r/R = 0.75$ | $C_{0.75}$           | [mm] | 106.3476     | 1276.2 |
| Thickness at $r/R=0.75$      | $t_{0.7}$            | [mm] | 3.7916       | 45.5   |
| Pitch Ratio                  | $\frac{P_{0.7}}{D}$  | [mm] | 1.6350       |        |
| Mean pitch ratio             | $\frac{P_{mean}}{D}$ | [-]  | 1.5675       |        |
| Area ratio                   | $\frac{A_E}{A_0}$    | [-]  | 0.7790       |        |
| Skew                         | $\theta_{eff}$       | [-]  | 18.8000      |        |
| Hub diameter ratio           | $\frac{d_h}{D}$      | [-]  | 0.3000       |        |
| Number of blades             | $z$                  | [-]  | 5            |        |
| Direction of rotation        |                      |      | right-handed |        |

Table 1: VP1304 Datasheet



(a) Propeller



(b) Propeller, hub and shaft

Figure 31: VP1304 [28]

### 11.1. Open Water Characteristics

The propeller operations conditions are defined by the advance coefficient  $J$  and the open water characteristics are expressed in the coefficients  $K_T, K_Q$  and  $\eta_0$ , presented in section 7. In order to be represented in the same graph with the same scale of  $K_T$  and  $\eta_0$ ,  $10K_Q$  could be used instead of  $K_Q$ .

The Reynolds number is defined based on the propeller blade chord length at  $0.7R$  and the resulting onset velocity at that radius:

$$Re = \frac{c_{0.7R} \sqrt{U^2 + (n\pi 0.7D)^2}}{\nu}$$

where  $\nu$  is the fluid kinematic viscosity.

### 11.2. Experimental Test

The model propeller VP1304 was tested in the towing tank of the Potsdam Model Basin in homogeneous flow. Open water characteristics were measured at two different numbers of revolutions ( $n = 10$  and  $15 \text{ s}^{-1}$ ). Furthermore the resistance and idle torque of the propeller hub was investigated at the same velocities and numbers of revolutions with a dummy hub.

**Test Arrangement** For the open water tests the dynamometer H39 from Kempf Remmers has been arranged behind the propeller model, figure 32.

| Dynamometer H39 |                     |
|-----------------|---------------------|
| $n_{MAX}$       | $60 \text{ s}^{-1}$ |
| $T_{MAX}$       | $1 \text{ kN}$      |
| $Q_{MAX}$       | $50 \text{ Nm}$     |

Table 2: Dynamometer Characteristics

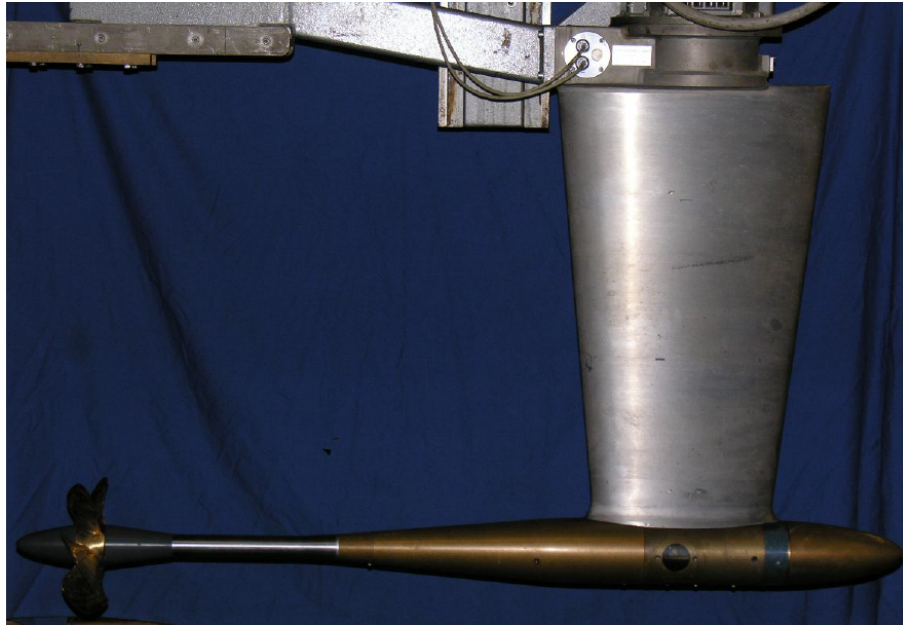


Figure 32: Dynamometer H39 with VP1304 [28]

The configuration is with the shaft in upstream direction. The drag, the torque and the number of revolutions as well as the inflow speed have been measured during the tests.

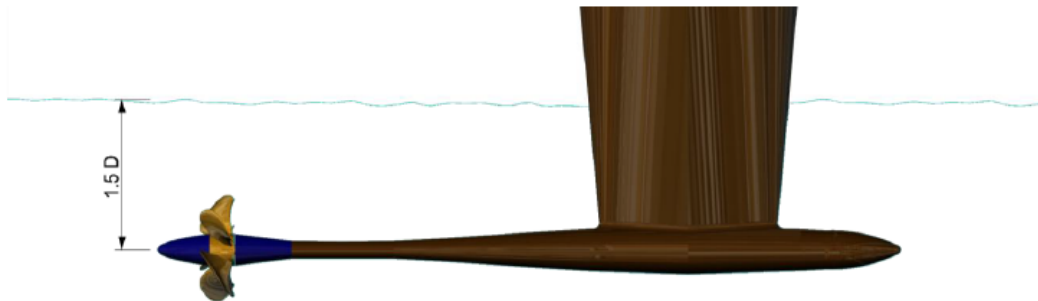


Figure 33: Test arrangement in the towing tank [28]

**Test procedures** Apart from the calibration of the measuring device, runs have been made in order to measure the idle torque and the resistance of the hub cap with the dummy hub, having the same shape and mass as the real propeller hub.

During each run the measured values of drag, torque, rotational speed and inflow speed have been recorded, together with time series, maximum and minimum values and standard deviations of the signals.

The open water tests were carried out at two different numbers of revolutions to evaluate the dependency on the Reynolds number.

### 11.3. Benchmarking Conditions

The Experimental conditions selected for the benchmarking were the followings:

|                       |        |          |                       |
|-----------------------|--------|----------|-----------------------|
| Water density         | $\rho$ | $kg/m^3$ | 998.67                |
| Kinematic viscosity   | $\nu$  | $m^2/s$  | $1.070 \cdot 10^{-6}$ |
| Number of revolutions | $n$    | $1/s$    | 15.00                 |

Table 3: Operations Conditions

| $J$ | $K_T$  | $10K_Q$ | $\eta_0$ | $Re$              |
|-----|--------|---------|----------|-------------------|
| 0.6 | 0.6288 | 1.3964  | 0.4300   | $1.81 \cdot 10^6$ |
| 0.8 | 0.5100 | 1.1780  | 0.5512   | $2.41 \cdot 10^6$ |
| 1.0 | 0.3994 | 0.9749  | 0.6520   | $3.01 \cdot 10^6$ |
| 1.2 | 0.2949 | 0.7760  | 0.7258   | $3.61 \cdot 10^6$ |
| 1.4 | 0.1878 | 0.5588  | 0.7487   | $4.21 \cdot 10^6$ |

Table 4: Measured open water characteristics for 15 RPS (by polynomials)

The benchmark was carried out in **model scale**.

## 11.4. CFD

### 11.4.1. Geometry

The propeller geometry used for the CFD analysis is presented below.

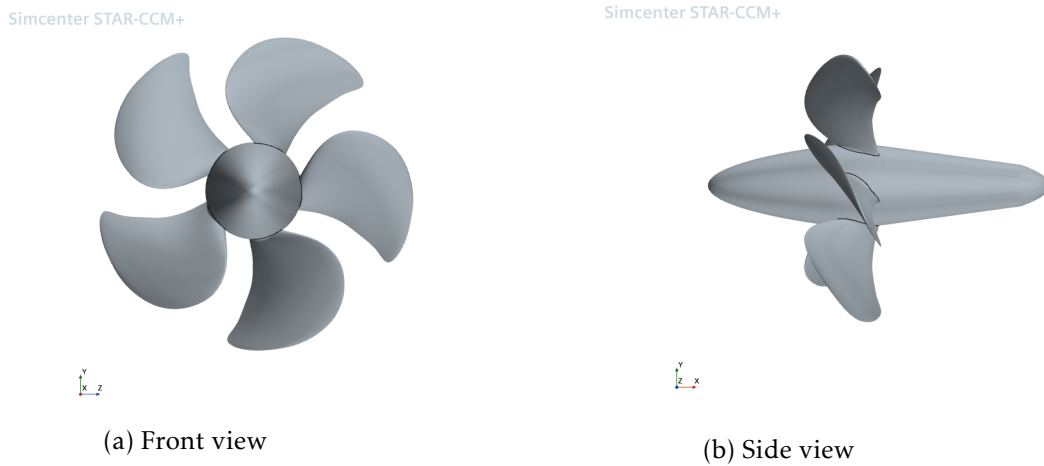


Figure 34: CFD Propeller geometry

As can be noticed, the configuration adopted for the CFD analysis, is composed by the blades and the hub without the shaft, following the guidelines of Caponnetto-Hueber.

**Coordinate system** Figure 35 shows the position of the coordinate system: it is placed in the center of the propeller disk, with the  $x$  axes aligned with the rotational axes and directed in the direction of the flow. The CAD coordinate system and the Laboratory coordinate system are coincident.

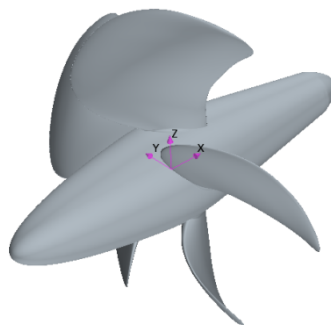


Figure 35: Coordinate system

**Computational Domain** Once the geometry was chosen, the computational domain was defined. This latter must respect some dimensional characteristics. Indeed, if it is too small, it can influence the properties of the flow around the propeller and consequently alter the simulation's results. On the other hand, if too big, it can result in an excessive number of cells leading to an increase in the computational cost. Taken in to account these constraints, following the guidelines of the company, it result in

the domain in Figure 36. As reference length the diameter,  $D$ , was used. The inlet is positioned at 5 times the  $D$  from the center of the propeller disk, while the *outlet* is placed 15 times  $D$  behind this latter. Finally, the lateral boundary, that owns a cylinder shape, measures 3.5 times  $D$ , therefore, 1.725 times  $D$  distant from the propeller disk's center.

Simcenter STAR-CCM+

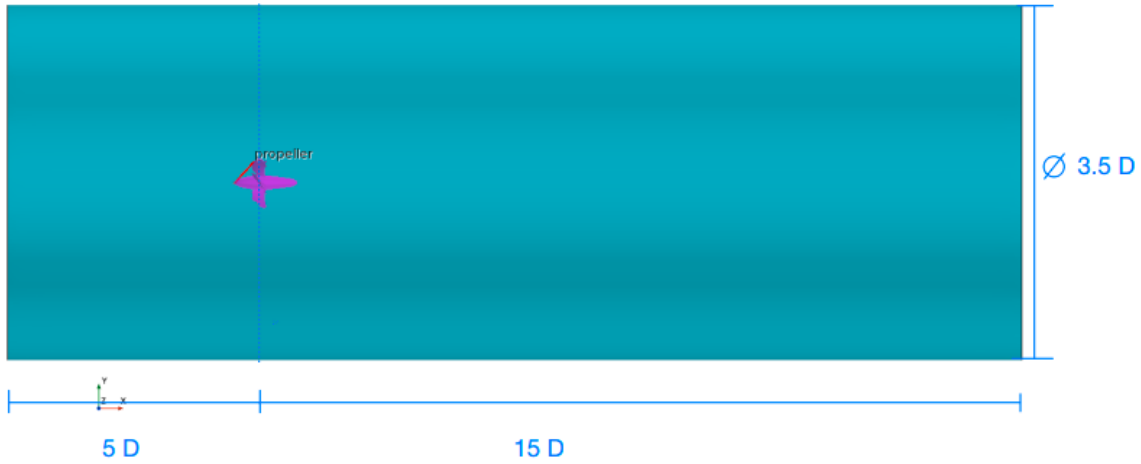


Figure 36: Computational Domain

As it will further detailed in the next section, a *Moving Reference Frame* was used during this simulation so a Rotating region cylinder surrounding the propeller was created with the dimensions based on the hub's length and its boundary layer; they are reported in figure 37.

Simcenter STAR-CCM+

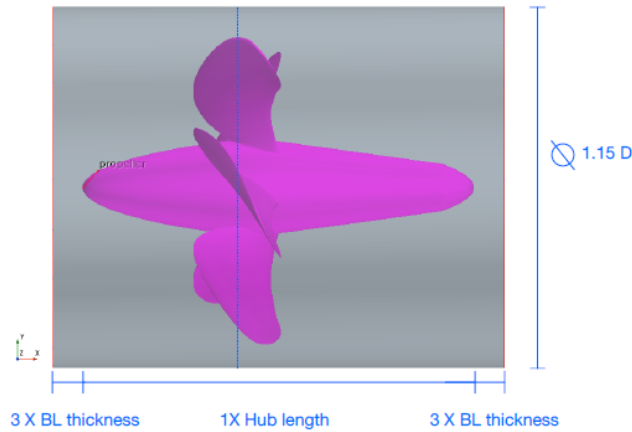


Figure 37: Rotating region

**Refinement Volumes** In order to best capture the rotational flow field around the propeller, 3 cylindrical volume refinements were created and showed in in figure 38. One of this presents a diameter slightly bigger than the propeller's one and it continues more afterwards than the previous two, this is suited to capture the wake generated by the propeller.



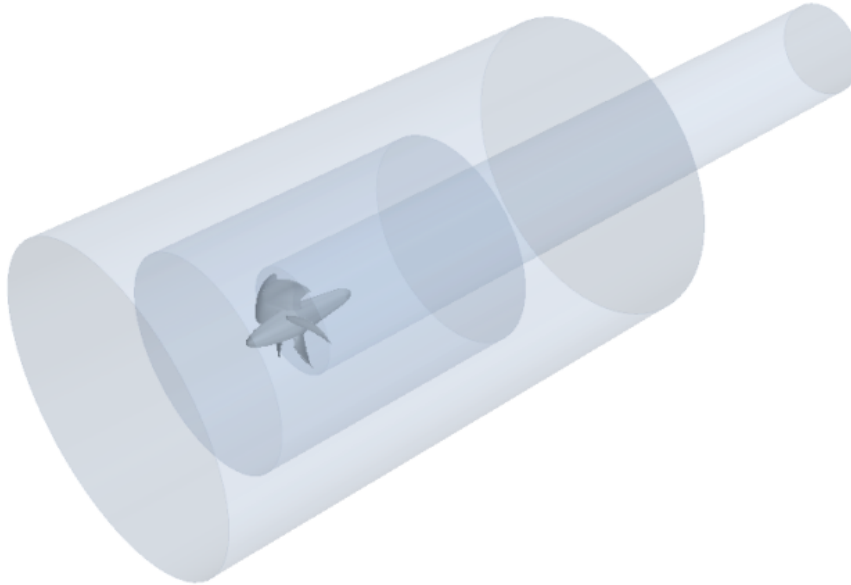


Figure 38: Volume refinements

### 11.4.2. Mesh

In order to perform a grid refinement study described in section 11.6.2, 4 different unstructured grids, ranging from 1.48  $M$  cells to 15.6  $M$  cells have been generated. The refinement value chosen is  $\sqrt{2}$ : this is one of the most common value found in literature and therefore it is suggested in *ITTC 7.5-03-01-01*[29]. Table 5 shows the grids with number of cells and their relative base size.

| Grid number | Base size [m] | $n^\circ$ Cells   |
|-------------|---------------|-------------------|
| #1          | 0.250         | $1.48 \cdot 10^6$ |
| #2          | 0.177         | $3.00 \cdot 10^6$ |
| #3          | 0.125         | $6.58 \cdot 10^6$ |
| #4          | 0.088         | $15.6 \cdot 10^6$ |

Table 5:  $n^\circ$  of cells per base size

**Mesher** A **Polyhedral mesher** was chosen in order to create the grid in which the flow field was solved. This choice was driven by different reasons: the presence of only one fluid phase together with the presence of a strong swirling flow and the use of a *Moving Reference Frame* suggested the use of this mesher; moreover, this mesher is preferred in order to create a conformal mesh at the interface between the rotating and the stationary region. The polyhedral meshing model utilizes an arbitrary polyhedral cell shape in order to build the core mesh. Volume cell sizes grow from the surface to the far field or core mesh (depending on application). In STAR-CCM+, a special dualization scheme is used to create the polyhedral mesh from an underlying tetrahedral mesh, which is automatically created as part of the process. STAR-CCM+ calculates the initial cell count from this underlying tetrahedral mesh. The polyhedral cells that are created typically have an average of 14 cell faces, *Star CCM+ User Guide* [13].

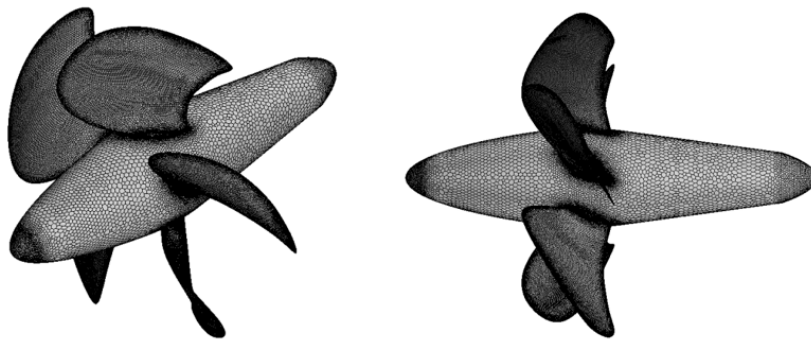


Figure 39: Propeller mesh

From figure 39 it can be noted that the cell size around the propeller is not constant, this is because different refinements were used: the idea was to increase the refinement, reducing the cell size, in that parts of the geometry characterized by an high curvature and therefore by an high pressure and velocity gradient. This has mainly been done at the leading and trailing edges of the blades, and at their intersection with the hub. The hub has also been refined front and aft, where the highest pressure peaks are located.

The *prism layer mesh model* was used to generate orthogonal prismatic cells next to wall

surfaces. This layer of cells is necessary to improve the accuracy of the flow solution and to best capture the speed profile inside the boundary layer, figure 40.

Following the CH guidelines a  $y^+ = 120$  was chosen as target. This value guarantee that the first cell height falls in the *logarithmic layer*. The value of  $y^+$  is calculated, by the macro script, using the skin friction coefficient given by the flat plate law. As it will be reminded many times in this thesis, it must be underlined that the  $y^+$  is a "target" value, so the real value obtained has to be checked during the post processing by mapping the  $y^+$  value on the propeller.

Propeller simulations at different advancing ratio are carried out at CH by meshing the propeller and then increasing  $J$  once that the convergence criteria are satisfied. Only one mesh is created so, in order to be able to capture the *boundary layer*, at each speed, the mesh is designed on the slowest speed were the BL is thicker. With this  $y^+$ , it resulted in a first cell high equal to  $8.27 \cdot 10^{-5} \text{ m}$ . The number of prism layer was set to 4 and it resulted in a *Prism layer total thickness* equal to  $2.17 \cdot 10^{-3} \text{ m}$ .

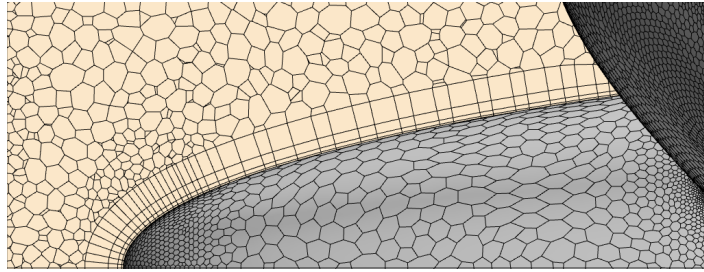
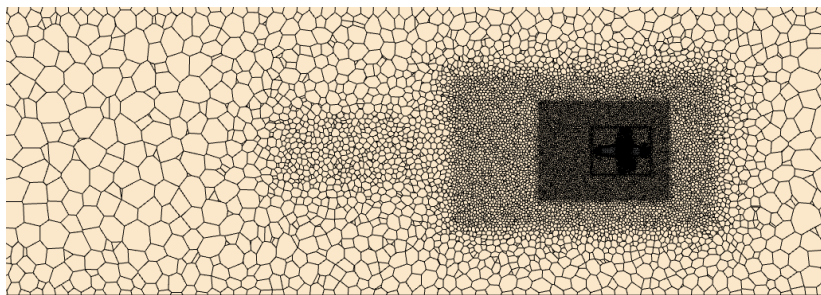
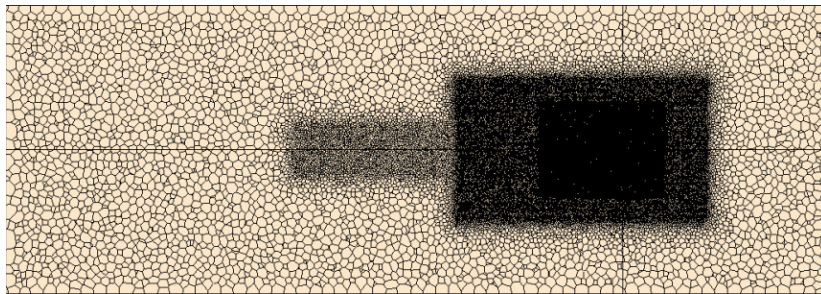


Figure 40: Propeller prism layer

In figure 41 the coarsest and refined mesh are presented. It is easily noted the huge decrease in the cell size and the corresponding increase in the cell number. In figures 41a and 41b in particular, could also be noted the 3 volumetric refinements previously mentioned in section 11.4.1.

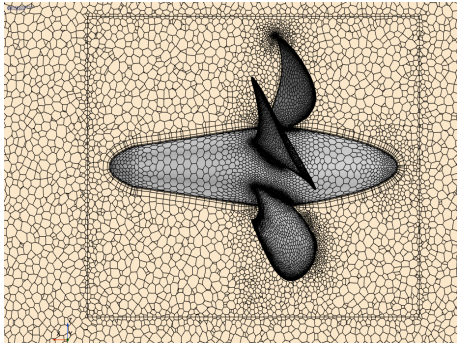


(a) Domain coarsest

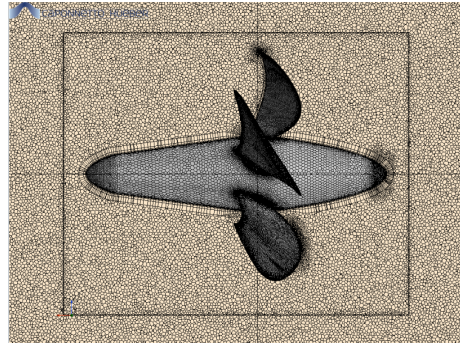


(b) Domain finest

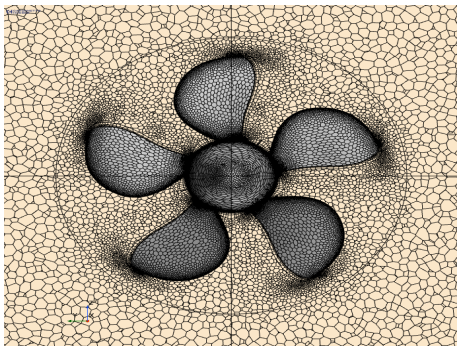




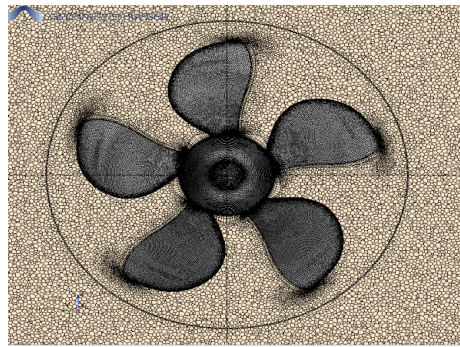
(c) Rotating region and propeller coarsest side view



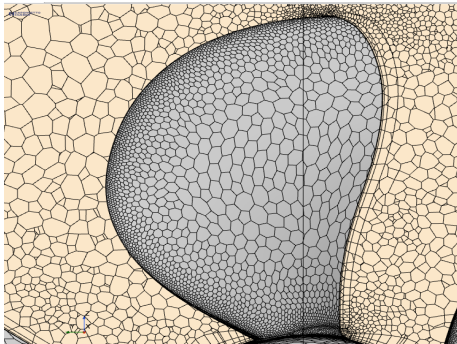
(d) Rotating region and propeller finest Side view



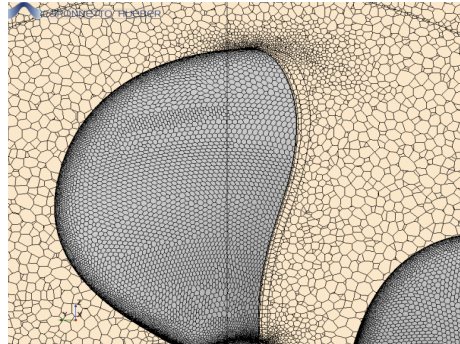
(e) Rotating region and propeller coarsest front view



(f) Rotating region and propeller finest front view



(g) Blade coarsest



(h) Blade finest

Figure 41: Coarsest VS Finest mesh

### 11.4.3. Physical Setup

In the following, the physical settings adopted for the simulation are described.

Being the propeller fully submerged and therefore being surrounded by only water, a mono-phase simulation is thus setup. The segregated flow solver was selected; the latter, solves the conservation equations of mass and momentum in a sequential manner. The non-linear governing equations are solved iteratively one after the other for the solution variables, *Star CCM+ User Guide* [13].

**Turbulence Model** The turbulence model set was the  $k - \epsilon$ . This one was set in its variant *Realizable  $k - \epsilon$  Two layer* that combines the Realizable K-Epsilon model with the two-layer approach.

The first one contains a new transport equation for the turbulent dissipation rate  $\epsilon$ . Also, a variable damping function  $f_\mu$  expressed as a function of mean flow and turbulence properties is applied to a critical coefficient of the model  $C_\mu$ . This procedure lets the model satisfy certain mathematical constraints on the normal stresses consistent with the physics of turbulence (realizability). This concept of a damped  $C_\mu$  is also consistent with experimental observations in boundary layers.

The second one is an alternative to the low-Reynolds number approach that allows the  $k - \epsilon$  model to be applied in the viscous-affected layer (including the viscous sub-layer and the buffer layer).

In this approach, the computation is divided into two layers. In the layer next to the wall, the turbulent dissipation rate  $\epsilon$  and the turbulent viscosity  $\mu_T$  are specified as functions of wall distance. The values of  $\epsilon$  specified in the near-wall layer are blended smoothly with the values computed from solving the transport equation far from the wall. The equation for the turbulent kinetic energy is solved across the entire flow domain. This explicit specification of  $\epsilon$  and  $\mu_t$  is arguably no less empirical than the damping function approach, and the results are often as good or better, *Star CCM+ User Guide* [13].

**Boundary layer treatment** Together with the modified  $k - \epsilon$  turbulence model, the *All  $y^+$  treatment* was selected. It is deepened in section 9.4.8. but shortly it gives the possibility to deal with coarse and fine meshes with  $y^+$  values  $< 1$  and  $> 30$ . It is also formulated to produce reasonable answers for meshes of intermediate resolution, when the wall-cell centroid falls within the buffer region of the boundary layer, i.e. when  $1 < y^+ < 30$ .

**Rotating region and Moving Reference Frame** The propeller operates in homogeneous inflow at constant rate of revolution. Thus, two regions are required for this simulation

1. a stationary region, to model the homogeneous inflow;
2. a rotating region, to model the propeller rotation motion.

Inside the rotating region a *Moving Reference Frame* is defined. In this region, the propeller is fixed and only the fluid surrounding it has a rotation rate.

One use of reference frames is to mimic the effect of a constant motion without actually moving the vertices of the mesh. This approach means that a **steady** solution only is required, without the need for a transient method. In steady simulations, or in transient simulations that do not require a time-accurate solution, moving reference frames provide a way of modeling rotations and translations as a steady-state problem, while leaving the

mesh stationary.

Applying an MRF to a region will generate constant rotational forces in the rotating domain to mimic rotating effects, *Star CCM+ User Guide* [13].

This method is generally applied to simplify the computation, saving computational time and cost.

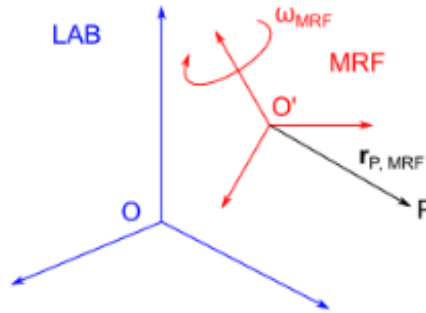


Figure 42: Moving Reference Frame [13]

**Boundary Conditions** Based on what stated previously, the domain boundary condition were set.

As can be seen from figure 43, the settings for the stationary region are the typical one: **Velocity inlet** for the most forward boundary, **Pressure outlet** for the backward boundary and **Symmetry** for the surrounding one. The presence of the *MRF* imposed to set as **Wall** the cylinder containing the latter both in the stationary and in the rotating region; this condition was completed with an **internal interface boundary**. Finally, the propeller was set as *Wall*.

**Stopping Criteria** The variables of *Thrust*  $T$  and *Torque*  $Q$  were monitored. For each advancing ratio a maximum of 800 iterations were performed. If in the last 100 iterations  $T$  and  $Q$  varied by less then the 0.01 percentage, the simulation moved to a new  $J$  or stopped.

In table 6 the physics settings are summarized.

| Parameter                | Solver setting   |
|--------------------------|--|
| Tool                     | Star CCM+ ver. 17.02.007   |
| Solver                   | 3D segregated, constant density  |
| Time                     | steady   |
| Turbulence model         | $k - \epsilon$   |
| Boundary layer treatment | two layer all $y^+$ treatment<br>realizable K-epsilon two-layer approaches |

Table 6: Settings

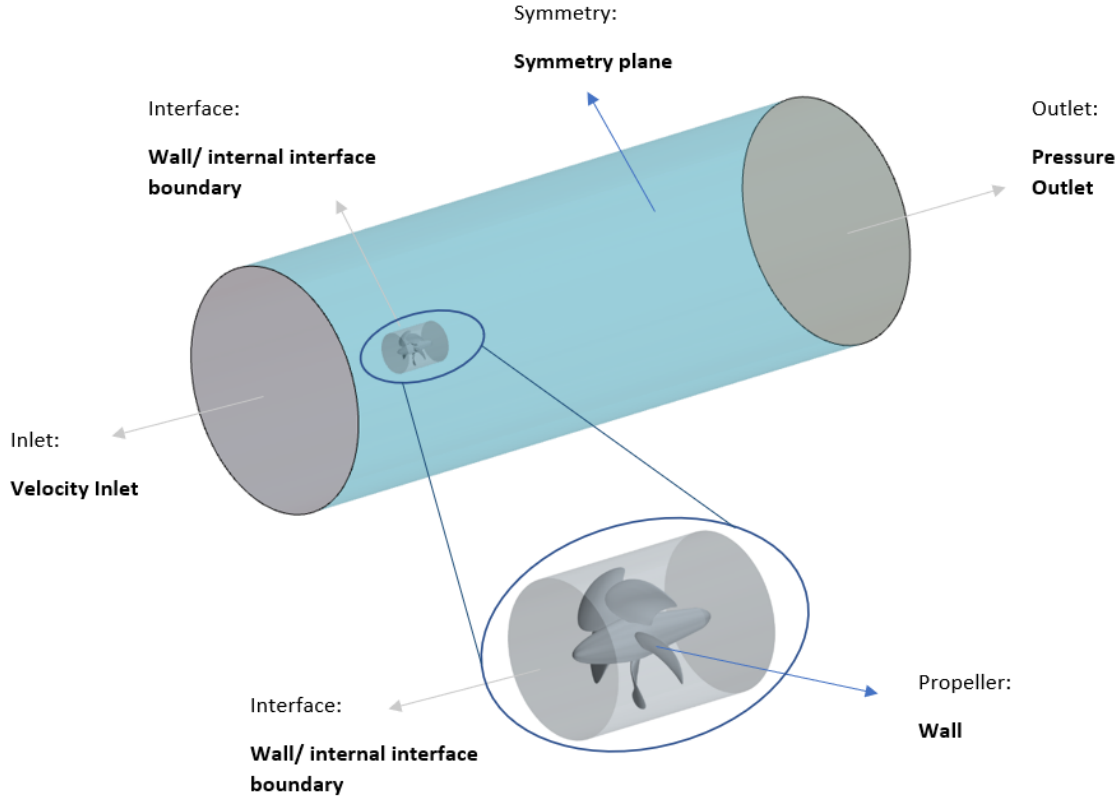


Figure 43: Computational Domain with boundaries  
Stationary + Rotating region

### 11.5. Results

In figure 44 the results for  $K_T$ ,  $10K_Q$  and  $\eta_0$  are reported and the numerical values are reported in table 7.

Looking at the graphs we can see that the settings are good in predicting the behaviour open water characteristics of the propeller, especially for  $K_T$  and  $10K_Q$ ; the first one is slightly underpredicted while increasing  $J$ , while  $K_Q$  tends to be overpredicted at low values of  $j$ . However, the CFD tends to underpredict the efficiency  $\eta_0$  more and more as the advancing ratio increases and also the numerical results tend to diverge from the experimental one as the speed increases.

If looking at the results in table 7 it could be noted that the difference from one grid to another at each  $j$  is generally proportional to  $10^{-2}$  meaning that also the coarsest grid is good enough in predicting the characteristics. This is confirmed by looking at the comparison error expressed in percentage of the experimental value. The difference in the error value between the coarsest and the finest is less than the 1%.

Therefore,  $10K_Q$  error is the smallest of the three and it never exceeds the 2.3%. The remaining two,  $K_T$  and  $\eta_0$  face an increase in the error while increasing  $J$  up to  $\sim 14\%$ .

Finally it could also be said that the behaviour of the error while refining at different  $J$  is different for the three characteristics:

- for  $K_T$  at low  $J$  it decreases while refining, but at higher  $J$  the behavior is the opposite,

it increases.

- for  $10K_Q$  at the lowest and highest  $J$  it increases while refining, but at the  $J$ 's in the middle it decreases while refining.
- for  $\eta_0$  is always reducing while refining.

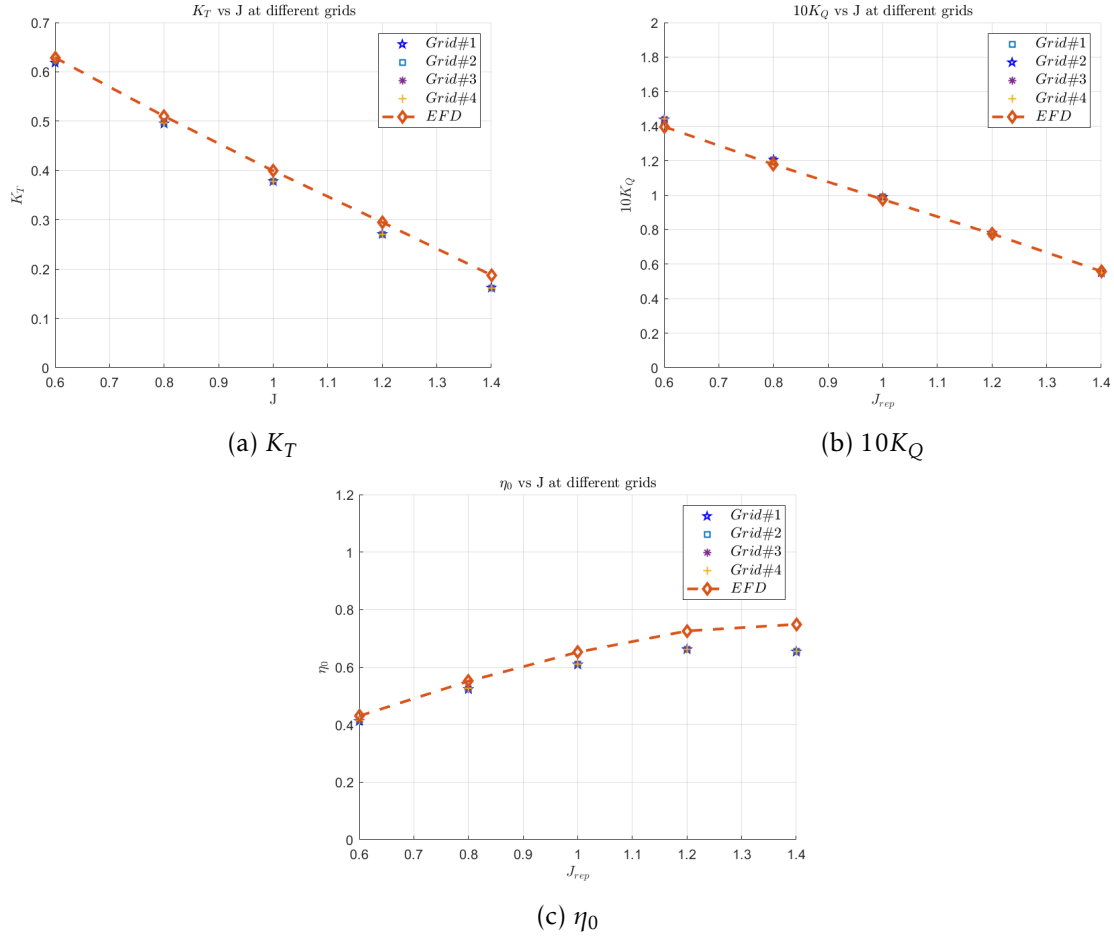


Figure 44: Open water characteristics vs  $J$  at different grids

**Comparison** In *PPTC Open Water characteristics Case 2.1*[30] the results from the other participants at the PPTC smp'11 Workshop in Hamburg are presented.

A particular attention was given to the study conducted by the University of Genoa (with the  $k - \epsilon$  turbulence model) considering that their software and settings were similar to the one used in this thesis.

Making a comparison between the errors obtained by Unige, reported in table 8, and the error obtained during this study and reported in table 7, can be noted that due to the similar settings used, the errors obtained for the open water characteristics at different  $J$ 's are almost the same, although the ones from Unige are slightly lower.



|           | Grid | Cells    | $K_T$  | $E_{K_T}[\%]$ | $10K_Q$ | $E_{10K_Q}[\%]$ | $\eta_0$ | $E_{\eta_0}[\%]$ |
|-----------|------|----------|--------|---------------|---------|-----------------|----------|------------------|
| $J = 0.6$ | EFD  |          | 0.6290 |               | 1.3964  |                 | 0.4300   |                  |
|           | #1   | 1479489  | 0.6185 | -1.6440       | 1.4332  | 2.6336          | 0.4121   | -4.1666          |
|           | #2   | 3003770  | 0.6221 | -1.0585       | 1.4377  | 2.9556          | 0.4132   | -3.8977          |
|           | #3   | 6582935  | 0.6257 | -0.4985       | 1.4428  | 3.3197          | 0.4141   | -3.6943          |
|           | #4   | 15600000 | 0.6265 | -0.3608       | 1.4404  | 3.1515          | 0.4154   | -3.4038          |
| $J = 0.8$ | EFD  |          | 0.5100 |               | 1.1780  |                 | 0.5512   |                  |
|           | #1   | 1479489  | 0.4951 | -2.9255       | 1.2045  | 2.2509          | 0.5233   | -5.0569          |
|           | #2   | 3003770  | 0.4960 | -2.7432       | 1.2045  | 2.2469          | 0.5243   | -4.8748          |
|           | #3   | 6582935  | 0.4967 | -2.6120       | 1.2047  | 2.2634          | 0.5250   | -4.7619          |
|           | #4   | 15600000 | 0.4964 | -2.6657       | 1.2023  | 2.0650          | 0.5257   | -4.6294          |
| $J = 1.0$ | EFD  |          | 0.3990 |               | 0.9749  |                 | 0.6520   |                  |
|           | #1   | 1479489  | 0.3782 | -5.2993       | 0.9887  | 1.4164          | 0.6089   | -6.6175          |
|           | #2   | 3003770  | 0.3784 | -5.2632       | 0.9883  | 1.3714          | 0.6094   | -6.5404          |
|           | #3   | 6582935  | 0.3782 | -5.2956       | 0.9875  | 1.2919          | 0.6096   | -6.4991          |
|           | #4   | 15600000 | 0.3782 | -5.3194       | 0.9868  | 1.2190          | 0.6099   | -6.4552          |
| $J = 1.2$ | EFD  |          | 0.2950 |               | 0.7760  |                 | 0.7258   |                  |
|           | #1   | 1479489  | 0.2709 | -8.1299       | 0.7818  | 0.7519          | 0.6618   | -8.8160          |
|           | #2   | 3003770  | 0.2709 | -8.1419       | 0.7811  | 0.6576          | 0.6623   | -8.7426          |
|           | #3   | 6582935  | 0.2707 | -8.2133       | 0.7804  | 0.5702          | 0.6624   | -8.7342          |
|           | #4   | 15600000 | 0.2704 | -8.3211       | 0.7796  | 0.4590          | 0.6624   | -8.7405          |
| $J = 1.4$ | EFD  |          | 0.1880 |               | 0.5588  |                 | 0.7487   |                  |
|           | #1   | 1479489  | 0.1621 | -13.6591      | 0.5530  | -1.0334         | 0.6533   | -12.7415         |
|           | #2   | 3003770  | 0.1620 | -13.7307      | 0.5517  | -1.2890         | 0.6544   | -12.6000         |
|           | #3   | 6582935  | 0.1617 | -13.9188      | 0.5502  | -1.5570         | 0.6547   | -12.5589         |
|           | #4   | 15600000 | 0.1614 | -14.0744      | 0.5489  | -1.8062         | 0.6551   | -12.5025         |

Error expressed in percentage of the experimental value

Table 7:  $K_T$ ,  $10K_Q$  and  $\eta_0$  vs  $J$  at different grids with comparison error

| Error/J  | 0.6   | 0.8   | 1.0   | 1.2   | 1.4    |
|----------|-------|-------|-------|-------|--------|
| $K_T$    |       |       |       |       |        |
| $E[\%]$  | 1.09  | -0.01 | -3.21 | -6.77 | -11.90 |
| $10K_Q$  |       |       |       |       |        |
| $E[\%]$  | 4.77  | 4.35  | 2.13  | 0.31  | -1.75  |
| $\eta_0$ |       |       |       |       |        |
| $E[\%]$  | -3.52 | -4.18 | -5.23 | -7.05 | -10.33 |

Error expressed in percentage of the experimental value

Table 8: Propeller's Characteristics UniGe  
1.5  $M$  cells for single blade

$C_p$  and  $C_F$  Figure 45 shows the pressure coefficient at all the advancing ratios. We can see a reduction in the suction peak while increasing the advancing ratio and tends to become uniform. In correspondence of the root of each blade, due to the high thickness it is possible to find a low value of  $C_p$  considering that we are looking at the suction side.

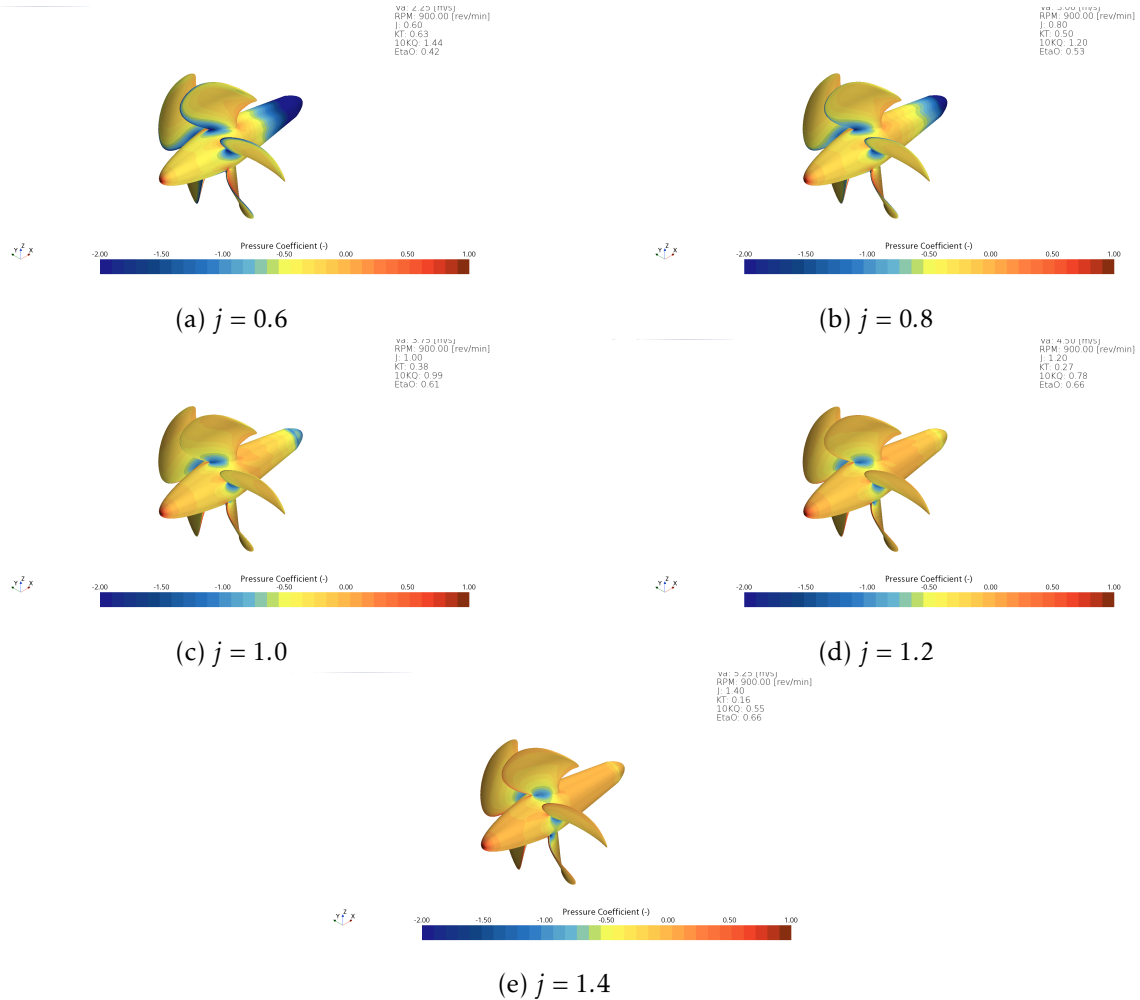


Figure 45: Pressure Coefficient

An opposite behaviour characterises the friction coefficient. The latter reduces its value while increasing the advancing ratio; this could be noted especially at the leading and trailing edge of the hub. This behaviour is because of the influence that the Reynolds exerts on friction coefficient.

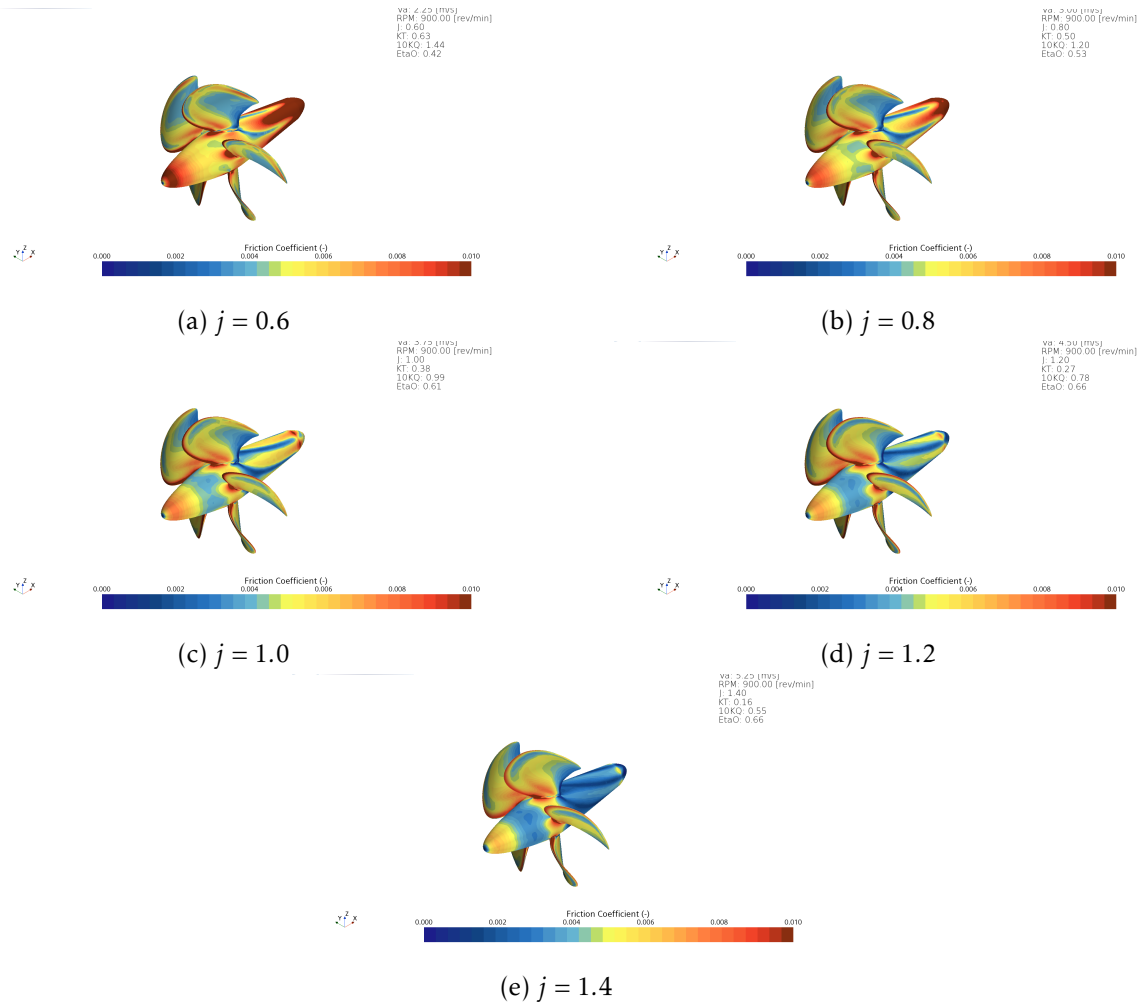


Figure 46: Friction Coefficient

## 11.6. Solution Verification

### 11.6.1. Iterative error

As previously reported in section 10.3.2, scope of the *Solution Verification* is to estimate the error/uncertainty of a given calculation, for which in general the exact solution is not known[1].

In order to consider the *numerical uncertainty* influenced only by the discretization error, the iterative error must be neglected; according to *L. Eça e M. Hoekstra* [16], this could happen when it is two or three orders of magnitude smaller than the discretization error to have a negligible effect in the determination of the latter.

Being unaware of the exact solution, in this study the iterative error has been studied by monitoring the norm  $L_2$  of the residuals,

$$L_2(\phi) = \sqrt{\frac{\sum_{i=1}^{N_{cells}} res^2(\phi_i)}{N_{cells}}} \quad (57)$$

following the work conducted by *J.A. Falcão de Campos et al.* [31] and confirmed by *L. Oberkampf et al.* [17] in which is stated that residuals have the same slope of the iterative error.

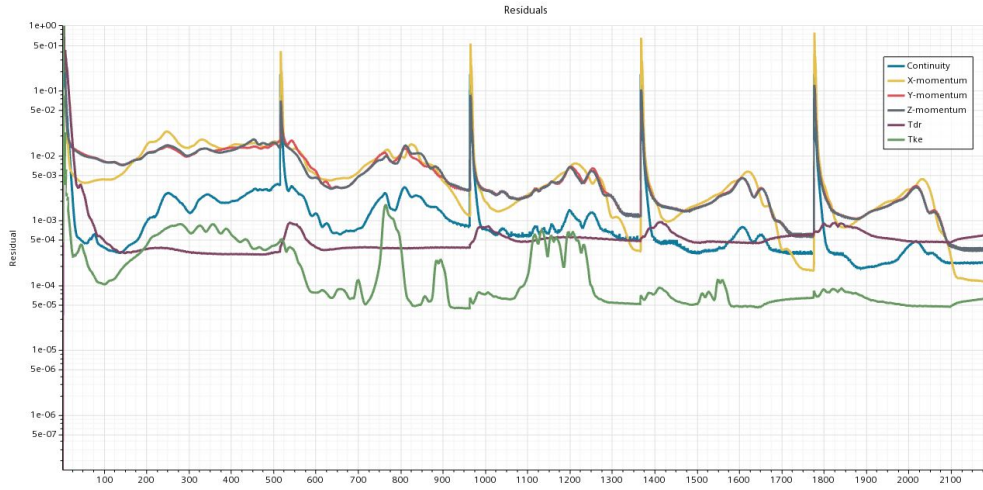
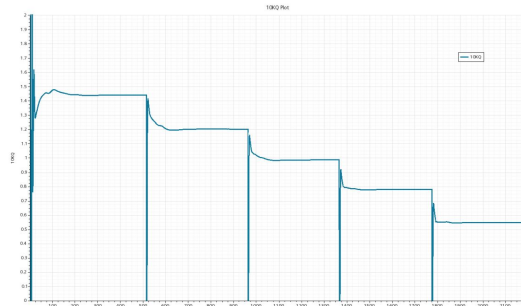


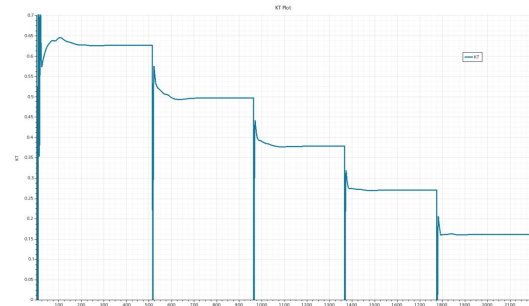
Figure 47: Normalized residuals Vs iterations

According to *J.A. Falcão de Campos et al.*[31], although large normalized residuals are obtained for the flow quantities, figure 47, the influence of the iterative error on the forces predictions is assumed to be small due to the fast convergence of the thrust, torque and, consequently, efficiency coefficients, figures 48b, 48a and 48c. The peaks present in the plots are caused by the changing in the advancing ratio that in the short-term drives up the values of the residuals and the variables that right after reduce again.

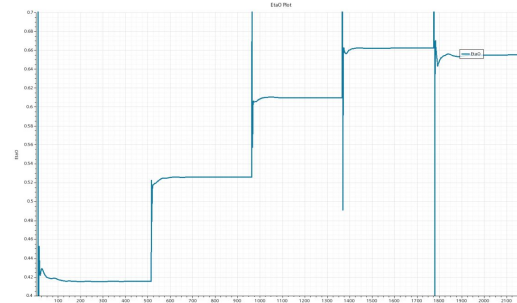
To confirm what has just been said figure 49 shows residuals not normalized. It could be immediately noted that their values are low enough to be considered acceptable. The only exception is the *TDR* residual having an order of magnitude  $\propto 10^{-1}$ , but looking at its normalized value, it faced a reduction around  $\propto 10^{-4}$  orders of magnitudes and so this let us to consider the iterative error negligible.



(a)  $10K_Q$  VS iterations



(b)  $K_T$  VS iterations



(c)  $\eta_0$  VS iterations

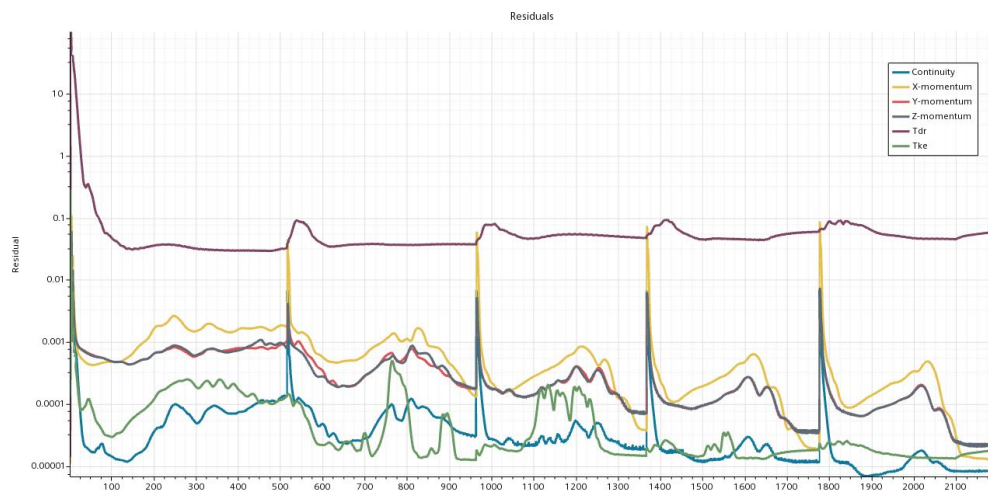


Figure 49: Residuals VS iterations

### 11.6.2. Grid refinement study

To estimate the discretisation error, following *L. Eça e M. Hoekstra* [1], as mentioned before, 4 unstructured conformal grids have been generated,.

Starting from the coarsest grid, the mesh was gradually refined with a constant **refinement ratio** equal to  $\sqrt{2}$  as previously reported. Below, grid refinements studies for the thrust and torque coefficients and for efficiency are shown.

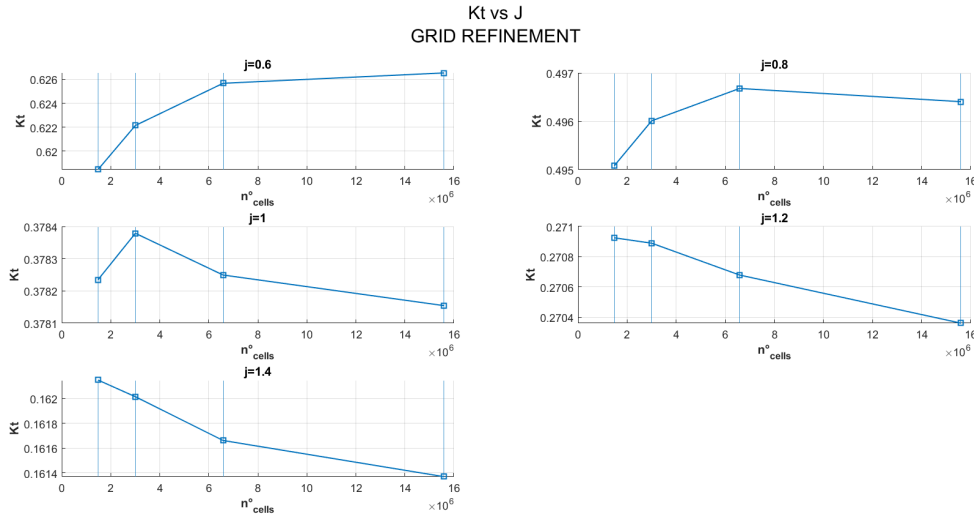


Figure 50: Kt Grid Refinement study at different  $J$

Figure 50 shows the behavior of the  $K_t$  coefficient when refining the grid at different  $J$ . Except for the case at  $j = 0.8$  and  $j = 1$ , the results show a monotonic behavior with a tendency to converge especially for the case at  $J = 0.6$  where it aims a value close to 0.6265; Increasing  $J$ , the behavior changes:  $K_t$  tends to decrease while refining and, for  $j = 1.4$ , it seems to converge to a value close to 0.1614.

Looking at figure 51, as for  $K_T$ , also  $10K_Q$  shows a changing behavior while increasing  $J$ , but the latter occurs at lower  $J$  compared to  $K_T$ .

If initially there is an increase in the value while refining, when  $J$  increases, the CFD results tend to monotonically decrease.

In contrast with the previous two coefficients  $\eta_0$  exhibits an almost constant behavior while increasing  $J$ : it increases while refining and tends to monotonically converge, except for  $j = 1.2$ .

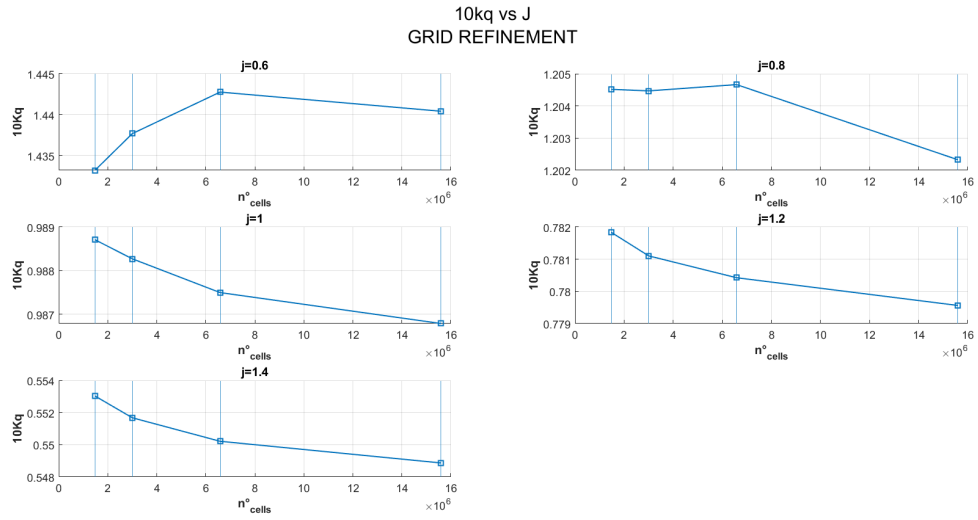


Figure 51: 10K<sub>Q</sub> Grid refinement study at different J

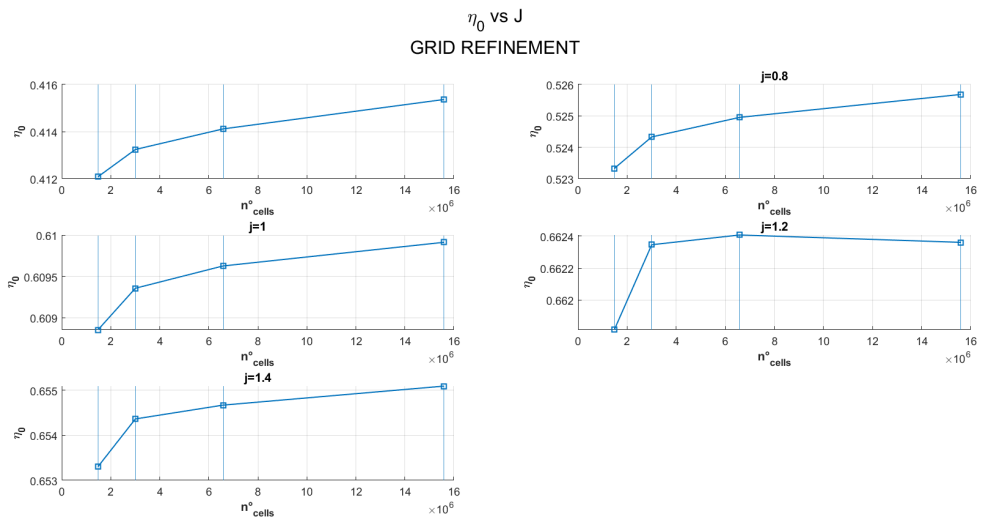


Figure 52:  $\eta_0$  Grid refinement study at different J

### 11.6.3. Uncertainty calculation

After having carried out the simulations for the four different grids, and neglected the iterative error, the numerical uncertainty for the finest grid has been estimated. In order to do so, the *Verification Tool* by MARIN institute, [32] presented in section 10.5, has been used.

In tables 9, 10 and 11 data from the interpolation are presented.

|       | $J$ | $\phi_0$ | $\phi_1$ | $U_{CFD}[\%]$ | $p$   |
|-------|-----|----------|----------|---------------|-------|
| $K_T$ | 0.6 | 0.629    | 0.627    | 0.5           | 1.79  |
|       | 0.8 | 0.497    | 0.496    | 0.4           | 2     |
|       | 1   | 0.377    | 0.378    | 0.4           | * 1,2 |
|       | 1.2 | 0.269    | 0.270    | 0.8           | * 1,2 |
|       | 1.4 | 0.160    | 0.161    | 1.3           | * 1,2 |

\* 1,2 Fit was made using first and second order exponents

Table 9:  $K_t$  interpolated solution, CFD solution, Uncertainty and order of accuracy.

|         | $J$ | $\phi_0$ | $\phi_1$ | $U_{CFD}[\%]$ | $p$   |
|---------|-----|----------|----------|---------------|-------|
| $10K_Q$ | 0.6 | 1.44     | 1.44     | 0.5           | 2     |
|         | 0.8 | 1.200    | 1.200    | 0.7           | * 1,2 |
|         | 1   | 0.983    | 0.987    | 0.5           | * 1,2 |
|         | 1.2 | 0.777    | 0.78     | 0.5           | * 1,2 |
|         | 1.4 | 0.544    | 0.549    | 1.2           | * 1,2 |

\* 1,2 Fit was made using first and second order exponents

Table 10:  $10K_q$  interpolated solution, CFD solution, Uncertainty and order of accuracy.

|          | $J$ | $\phi_0$ | $\phi_1$ | $U_{CFD}[\%]$ | $p$   |
|----------|-----|----------|----------|---------------|-------|
| $\eta_0$ | 0.6 | 0.419    | 0.415    | 1             | * 1,2 |
|          | 0.8 | 0.528    | 0.526    | 0.5           | 1     |
|          | 1   | 0.61     | 0.61     | 0.1           | 2     |
|          | 1.2 | 0.661    | 0.662    | 0.3           | * 1,2 |
|          | 1.4 | 0.656    | 0.655    | 0.2           | 2     |

\* 1,2 Fit was made using first and second order exponents

Table 11:  $\eta_0$  interpolated solution, CFD solution, Uncertainty and order of accuracy.

All the estimated uncertainties are between 0.1% and 1.3% and this could be held as a success considering that they are lower than the ones found in *D. Rijpkema and G. Vaz* [33], which reached a value of 4.8% and that they match the range of uncertainty found in *J.A. Falcão de campos* [31], this latter being between 0.5% and 1.2%. Nevertheless it must be noted that for 9 out of 15 cases the numerical uncertainty was calculated with the first and second order polynomials meaning that the quality of the interpolation it's not so high.

Figure 53 shows the interpolated solution and the relative error bar given by the uncertainty.



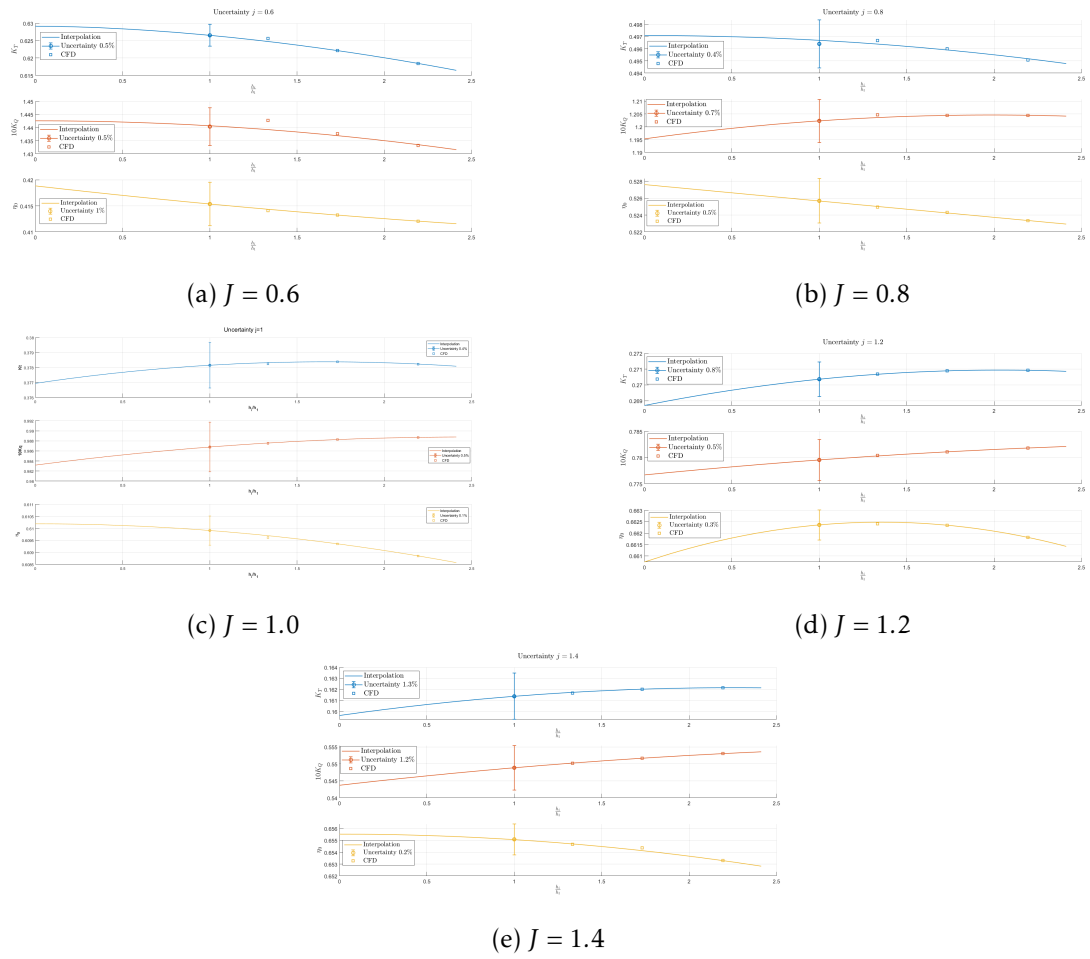


Figure 53: Coefficients Interpolated vs grid refinement with uncertainty bar

#### 11.6.4. Validation

The aim of validation is to estimate the modelling error of a given mathematical model in relation to a given set of experimental data in order to quantify how well the mathematical model represents the physical world. During this process, two quantities are compared: the validation uncertainty,  $U_{VAL}$ , and the comparison error,  $E$ .  $U_{VAL}$  involves the numerical uncertainty, previously estimated, the simulation input parameter uncertainty,  $U_{input}$ , and the experimental one.  $U_{input}$  depends on different random uncertainties and for simplicity is generally assumed equal to 0 according to *K. Dowding et al.* [26], *D. Rijpkema and G. Vaz* [33]. Unfortunately, this latter for the PPTC it's unknown and so a value of 1.5% has been assumed as suggested in [33].

Following the procedure present in *L. Eça and M. Hoekstra* [19], the comparison error and the validation uncertainty have been compared.

|           |          | $U_{CFD}[\%]$ | $U_{EFD}[\%]$ | $E[\%]$ | $U_{val}[\%]$ |
|-----------|----------|---------------|---------------|---------|---------------|
| $J = 0.6$ | $K_T$    | 0.50          | 1.50          | 0.36    | 1.58          |
|           | $K_Q$    | 0.52          | 1.50          | -3.15   | 1.59          |
|           | $\eta_0$ | 0.97          | 1.50          | 3.40    | 1.78          |
| $J = 0.8$ | $K_T$    | 0.39          | 1.50          | 2.67    | 1.55          |
|           | $K_Q$    | 0.71          | 1.50          | -2.07   | 1.66          |
|           | $\eta_0$ | 0.48          | 1.50          | 4.63    | 1.57          |
| $J = 1$   | $K_T$    | 0.38          | 1.50          | 5.32    | 1.55          |
|           | $K_Q$    | 0.51          | 1.50          | -1.22   | 1.58          |
|           | $\eta_0$ | 0.09          | 1.50          | 6.46    | 1.50          |
| $J = 1.2$ | $K_T$    | 0.73          | 1.50          | 8.32    | 1.67          |
|           | $K_Q$    | 0.50          | 1.50          | -0.46   | 1.58          |
|           | $\eta_0$ | 0.27          | 1.50          | 8.74    | 1.52          |
| $J = 1.4$ | $K_T$    | 1.12          | 1.50          | 14.07   | 1.87          |
|           | $K_Q$    | 1.18          | 1.50          | 1.78    | 1.91          |
|           | $\eta_0$ | 0.17          | 1.50          | 12.50   | 1.51          |

Values expressed in percentage of the experimental data

Table 12: Comparison error and validation uncertainty

In table 12 the comparison error and the uncertainty for the finest grid obtained from the verification study are presented. For most of the cases, the error is greater than the validation uncertainty, suggesting that, according to *J.A. Falcão de campos* [31], the comparison error is dominated by the modelling error. Since the open water predictions are made in the critical Reynolds number range, different flow regimes, laminar and turbulent may occur simultaneously on the propeller blades.

Possibly with the current turbulent model the boundary layer flow with its Reynolds number is not correctly captured when both large laminar and turbulent regions are present on the blade.

As can have been envisaged by table 13, only 4 out of 15 cases have been validated. Analyzing these results, can be said that:

1. for the validated cases the code represents adequately the physics of the problem;

|                              | $J$      | 0.6       | 0.8 | 1         | 1.2       | 1.4       |
|------------------------------|----------|-----------|-----|-----------|-----------|-----------|
| Veryfine<br>(15.6 $M$ cells) | $K_T$    | VALIDATED | NV  | NV        | NV        | NV        |
|                              | $10K_Q$  | NV        | NV  | VALIDATED | VALIDATED | VALIDATED |
|                              | $\eta_0$ | NV        | NV  | NV        | NV        | NV        |

Table 13: Validation Results  
(Validated, NV- Not Validated)

2. as previously stated, the code might be affected by the modelling error and improvements could be done by using a different turbulence models such as  $K-\omega$  SST, proposed by *F.R. Menter* [34], and/or a different convection schemes such as a *QUICK* second order convection scheme;
3. having made assumptions on the experimental uncertainty, the real value of this latter could have been larger, within an acceptable range, and thus  $U_{VAL}$  too, consequently bringing to a wider range of validated results.

**$k-\omega$  SST** In order to verify the validity of the turbulence model previously adopted,  $k-\omega$  SST turbulence model was selected . The results reported in table 14 show no relevant changes: also in this case, 4 results out of 15 were validated; in particular the results for  $10K_Q$  at  $J = 0.8$  and  $J = 1$  had also been validated with the previous model.

|                              | $J$      | 0.6       | 0.8       | 1         | 1.2 | 1.4 |
|------------------------------|----------|-----------|-----------|-----------|-----|-----|
| Veryfine<br>(15.6 $M$ cells) | $K_T$    | VALIDATED | NV        | NV        | NV  | NV  |
|                              | $10K_Q$  | NV        | VALIDATED | VALIDATED | NV  | NV  |
|                              | $\eta_0$ | VALIDATED | NV        | NV        | NV  | NV  |

Table 14: Validation Results for  $K-\omega$  SST turbulence model  
(Validated, NV- Not Validated)

**MUSCL  $3^{rd}$  order scheme** Another try was conducted changing the discretization scheme for the convective term. Considering that the *QUICK* is not implemented in *STAR CCM+*, the  $3^{rd}$  order *MUSCL* scheme was used, this latter being similar to the *QUICK* one.

A simulation for all  $J$  was performed with the finest grid (base size of 0.125  $m$ ).

No relevant improvements in the comparison error were detected, therefore no further simulation was carried out.

**Conclusion** In conclusion of this test case the validity of the settings and guidelines in predicting the flow field and then the open water characteristics of a propeller can be recognized.

The consideration previously made have to be taken carefully. In fact, although lot of cases were not validated, the difference between the comparison error and the uncertainty is not so high, and considering that the validation uncertainty is low as well, it can not be argued that the modelling error is consistently affecting the simulation.

We can state that generally the numerical prediction starts failing at high advancing ratios. According to the results obtained, it is suggested to keep using these settings for future open Water characteristics simulations. In addition, it is recommended the use of coarse grids considering that there is no such an improvement while refining.

## 12. Kiso Container Ship (KCS)



Figure 54: KCS hull [35]

The second test case taken into account was the Kiso Container Ship.

The KCS is a container ship geometry/ test case conceived to provide data for both explication of flow physics and CFD validation for a modern container ship with a bulbous bow. The Korea Research Institute for Ships and Ocean Engineering (KRISO) performed towing tank experiments to obtain resistance, mean flow data and free surface waves (Van et al, 1998a,b, Kim et al, 2001). Self propulsion tests were carried out at the Ship Research Institute (now NMRI) in Tokyo and are reported in the Proceedings of the CFD Workshop Tokyo in 2005 (Hino, 2005). Later, resistance tests were also reported by NMRI[36]. Data for pitch, heave, and added resistance are available from Force/Dmi measurements reported in Simonsen et al. (2008).

This geometry has been used over years during different workshops with the aim to assess state-of-the-art CFD methods for ship hydrodynamics, to aid code development and improve the application of CFD for ship design and evaluation.

No full scale ship exists.

| Main particulars                                |                          | Model Scale 1/36<br>Case 2.1 |
|---|--------------------------|------------------------------|
| Body Mass                                       | (Kg)                     | 1646                         |
| Length between perpendiculars                   | $L_{pp}$ (m)             | 7.2786                       |
| Length of waterline                             | $L_{WL}$ (m)             | 7.3577                       |
| Maximum beam of waterline                       | $B_{WL}$ (m)             | 1.0190                       |
| Depth   | D                        | 0.6013                       |
| Draft   | T                        | 0.3418                       |
| Displacement Volume                             | $\nabla$                 | 1.6490                       |
| Wetted surface area w/o rudder                  | $S_W$ (m <sup>2</sup> )  | 9.4379                       |
| Wetted surface area of rudder                   | $S_R$ (m <sup>2</sup> )  | 0.1152                       |
| Block Coefficient (Cb)                          | $\nabla/(L_{pp}B_{WL}T)$ | 0.6505                       |
| Midship section Coefficient (CM)                |                          | 0.9849                       |
| LCB (% $L_{pp}$ ), fwd+                         |                          | -1.48                        |
| Vertical Center of Gravity (from keel)          | $KG$ (m)                 | 0.23                         |
| Metacentric Height                              | $GM$ (m)                 |                              |
| Moment of inertia                               | $K_{xx}/B$               | 0.40                         |
| Moment of inertia                               | $K_{yy}/L_{pp}$          | 0.250                        |
|   | $K_{zz}/L_{pp}$          |                              |
| Propeller center, long. location (from FP)      | $x/L_{pp}$               | 0.9825                       |
| Propeller center, vert. location (below WL)     | $-z/L_{pp}$              | 0.02913                      |
| Propeller rotation direction (view from stern)  |                          | clockwise                    |
| Logitudinal center of gravity from the aft peak | (m)                      | 3.532                        |

Table 15: KCS Ship features

### 12.1. Experimental Test

The case analyzed was the case 2.1 found in the *Tokyo 2015 WORKSHOP* website [35], in which *Resistance, Sink and Trim* were studied.

The conditions of the test were the following:

- Towing
- Calm Water
- Boat free to heave and pitch

|                           | 1                                      | 2                  | 3                  | 4                  | 5                  | 6                  |
|---------------------------|--|--------------------|--------------------|--------------------|--------------------|--------------------|
| Speeds [m/s]              | 0.915                                  | 1.281              | 1.647              | 1.922              | 2.196              | 2.379              |
| Froude Number (Fr)        | 0.108                                  | 0.152              | 0.195              | 0.227              | 0.260              | 0.282              |
| Reynolds number           | $5.23 \times 10^6$                     | $7.33 \times 10^6$ | $9.42 \times 10^6$ | $1.10 \times 10^7$ | $1.26 \times 10^7$ | $1.36 \times 10^7$ |
| Density $\rho$            | 999.5 kg/m <sup>3</sup>                |                    |                    |                    |                    |                    |
| Kinematic viscosity $\nu$ | $1.27 \cdot 10^{-6}$ m <sup>2</sup> /s |                    |                    |                    |                    |                    |
| Gravity $g$               | 9.81 m/s <sup>2</sup>                  |                    |                    |                    |                    |                    |

Table 16: Experimental Test conditions

### 12.2. Benchmarking Conditions

In order to carry out the benchmark test, three Froude numbers were selected. They are reported in table 17 together with the corresponding speeds.

As suggested in the Workshop's instructions, the configuration selected is the one including the ship and the rudder.

| Index                     | Froude number                          | Speed [m/s] | Sinkage at the AP [m] | Trim ° |
|---------------------------|--|-------------|-----------------------|--------|
| $V_1$                     | 0.108                                  | 0.915       | $1.50 \cdot 10^{-4}$  | -0.017 |
| $V_2$                     | 0.195                                  | 1.647       | $1.50 \cdot 10^{-4}$  | -0.097 |
| $V_3$                     | 0.260                                  | 2.196       | $-6.95 \cdot 10^{-3}$ | -0.169 |
| Density $\rho$            | 999.5 kg/m <sup>3</sup>                |             |                       |        |
| Kinematic Viscosity $\nu$ | $1.27 \cdot 10^{-6}$ m <sup>2</sup> /s |             |                       |        |

Table 17: Benchmarking conditions

### 12.3. CFD

#### 12.3.1. Geometry

Initially the geometry suggested by the workshop [35], shown in fig 55 for case 2.1 was selected.

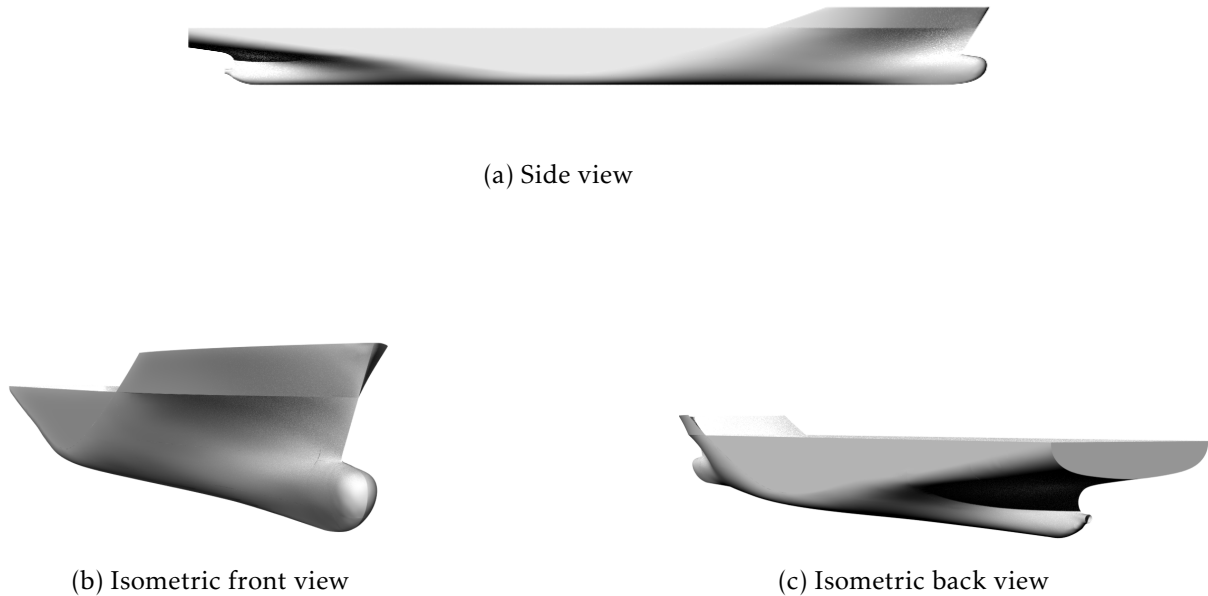


Figure 55: KCS provided geometry

Since the beginning this geometry turned to be problematic. The main problem to deal with was the presence, both at the bow than at the stern, of a *sharp edge*, fig 56. The latter results in the huge difficult in generating a good mesh; common practice in the CFD community is try to avoid the presence of Sharp edges and one way to solve this problem is cutting this latter or adding add a bit of thickness.

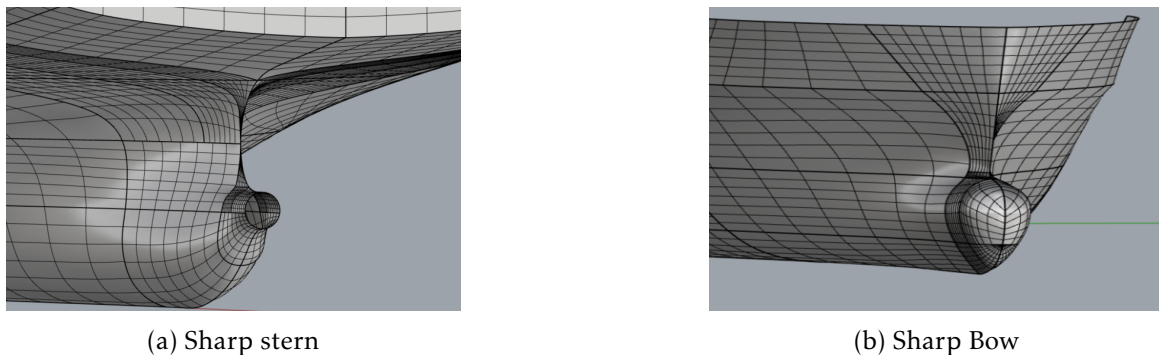
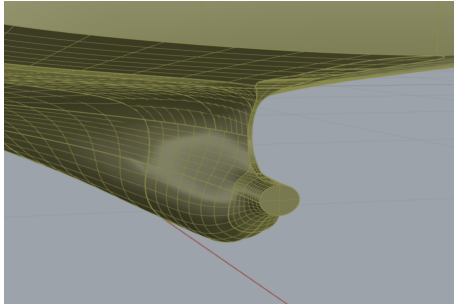


Figure 56: KCS provided geometry: particular of the sharp edges

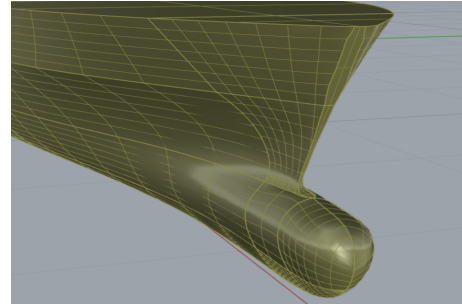
Due to this fact, the geometry underwent few repairing attempts that produced the following geometry, fig 57.

As can be noticed, in order to obtain a good mesh it was opted to add extra thickness to the geometry. This one was enough to influence the result though; this because it was influ-

encing the displacement volume and, of course, the flow field around the bow and the stern.



(a) New stern



(b) New Bow

Figure 57: KCS new geometry: particular of the edges

For this reason, a third hull geometry was considered; this was the one recommended for case 2.11 of the workshop; the latter differed from the one for the case 2.1 only for the presence of extra volume above the waterline, so it was considered acceptable. In addition the surface repair needed was minimum. In table 18 a comparison between the hydrostatic values of the workshop geometry and the one used for the CFD simulation is showed. The hydrostatic data were obtained thanks to the tool *ORCA 3D* present in *Rhinoceros*®.

| Main particulars               |                            | Model Scale 1 : 36 | CFD Model | CFD Model with rudder |
|--------------------------------|----------------------------|--------------------|-----------|-----------------------|
| Body Mass                      | (Kg)                       | 1648.176           | 1647.351  | 1647.351              |
| Length between perpendiculars  | $L_{pp}$ (m)               | 7.2786             |           |                       |
| Length of waterline            | $L_{WL}$ (m)               | 7.3577             | 7.349     | 7.39                  |
| Maximum beam of waterline      | $B_{WL}$ (m)               | 1.0190             | 1.019     | 1.019                 |
| Depth                          | $D$ (m)                    | 0.6013             | 0.751     | 0.751                 |
| Draft                          | $T$ (m)                    | 0.3418             | 0.341     | 0.341                 |
| Displacement Volume            | $\nabla$ (m <sup>3</sup> ) | 1.6490             | 1.648     | 1.648                 |
| Wetted surface area w/o rudder | $S_W$ (m <sup>2</sup> )    | 9.4379             | 9.47      | 9.591                 |
| Block Coefficient (Cb)         | $\nabla/(L_{pp}B_{WL}T)$   | 0.6505             | 0.646     | 0.642                 |
| LCB (% $L_{pp}$ ), fwd+        |                            | -1.48              |           |                       |
| LCB distance fro AP            | (m)                        |                    | 3.537     | 3.535                 |

Table 18: Hydrostatics data from the original model scale and the one used in the CFD simulation

The rudder instead, was taken from the tutorial present in the *STAR CCM+ User guide* [13]; it is the same as the one present in the workshop with all the gaps that have been closed in order to simplify the geometry, avoid meshing and solution problems.

Figure 58 shows different views of the final geometry. Comparing the latter with figure 55 it's clear the the presence of the extra volume above the waterline that, as already said, doesn't effect the hydrostatics values or the computational results.

**Coordinate system** Initially the laboratory CSys and the CAD coincided: they were located longitudinally at the Aft Perpendicular, vertically at the keel and laterally at the symmetry plane. Figure 59 shows its location. The CG referred to this CSys was at (3.532;0,0.232) m.





Figure 58: KCS CFD geometry

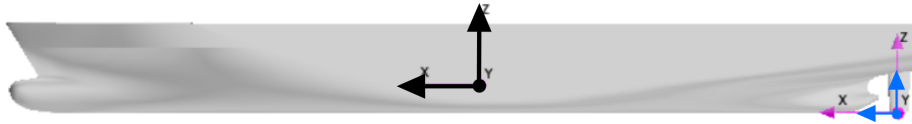


Figure 59: KCS old coordinate system

Before proceeding with the domain creation, the boat was sunk from the initial position along the  $z$ -axis by a quantity equal to the *draft* ( $0.3418\text{ m}$ ) and rotated around the origin of the CAD coordinate system (in blue) in order to have the laboratory coordinate system positioned at the waterline level, with the  $x$ -axis aligned with the flow (as standard at CH) and longitudinally at the aft perpendicular. The coordinates of the Center of Gravity, referred to the laboratory coordinate system, became  $(-3.532; 0; -0.116)\text{ m}$ .

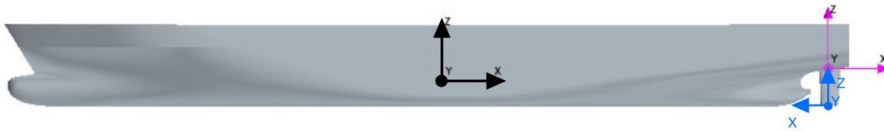


Figure 60: KCS coordinate system

**Computational domain** Once the geometry was ready to be simulated, the computational domain was defined. In order to create the domain block the guidelines from CH were used, these latter follows what is suggested in the *ITTC recommendations* [37]. As already stated in the previous test case, the domain must be big enough because considering that the bounding surfaces are home to boundary conditions, these mustn't influence the flow field in the proximity of the ship; on the other side, the domain mustn't be too wide in order to reduce the number of cells.

Figure 61 shows the domain characteristics. As a reference length the Overall length,  $L_{OA}$ ,

was used, this being longer than the  $L_{pp}$ . The inlet is positioned at 3 times the  $L_{OA}$ , further than what suggested by the ITTC (1-2 times the  $L_{pp}$ ), while the *outlet* is placed 4 times the  $L_{OA}$  behind the stern. Finally, the lateral boundary is placed 3.5 times the  $L_{OA}$  distant from the center of the ship.

The presence of a vertical symmetry plane on the centreline of the ship together with the symmetrical boundary condition, let us simulate **only half of the domain**. In figure 61 the presence of the symmetry plane could be noted.

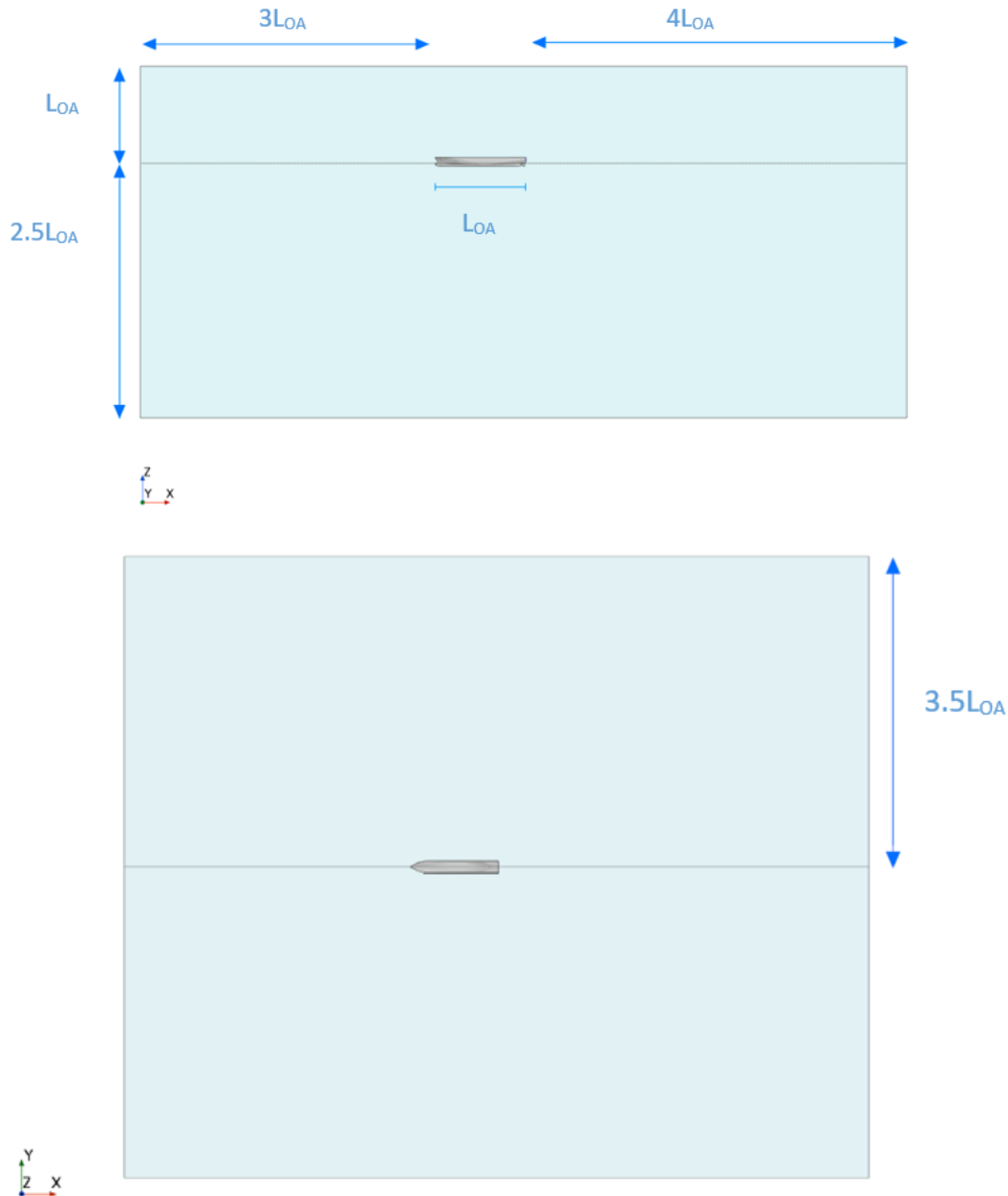
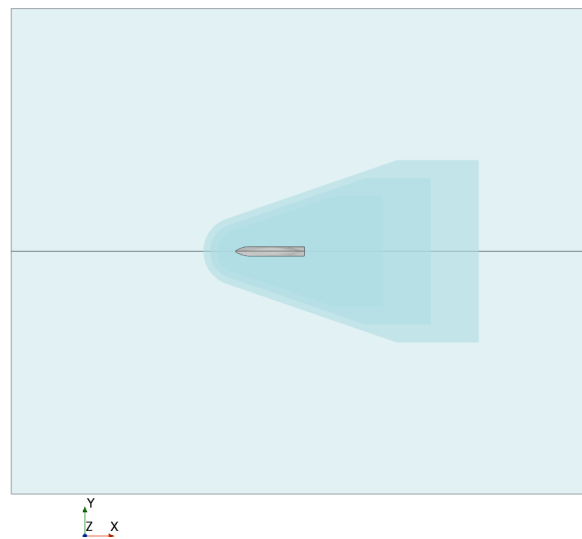


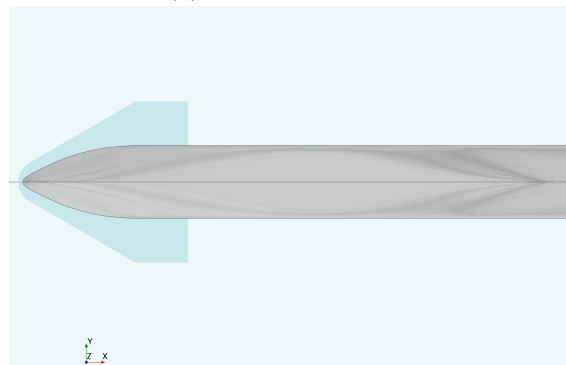
Figure 61: Computational domain: side and top view

**Refinement Volumes** After the definition of Computational domain, the refinement volumes were created.

In section 5.2 it was stated that when a ship moves through the water, it dissipates energy by creating waves. These ones are arranged in a pattern called *Kelvin pattern* which is characterised by an angle of  $19.5^\circ$ . In order to best capture the waves generated by the ship, four refinements were created and are showed in figure 67. Three of this refinements will be characterized, in the meshing phase, by an increasing size of the cells; they are useful for capturing the wave pattern around and in the wake of the boat. The last one, the *Bow refinement*, figure 62b, is focused on best capture the wave pattern in the proximity of the bow.



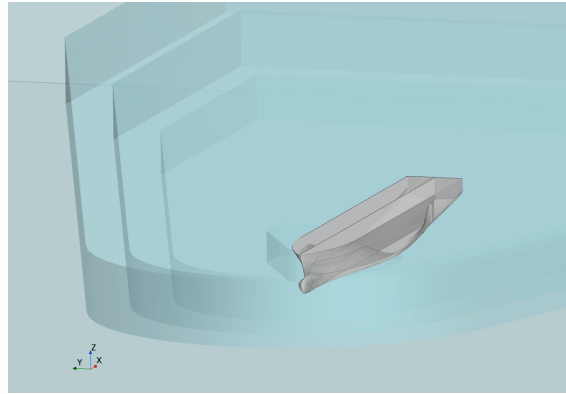
(a) Wake refinements



(b) Kelvin Bow refinement

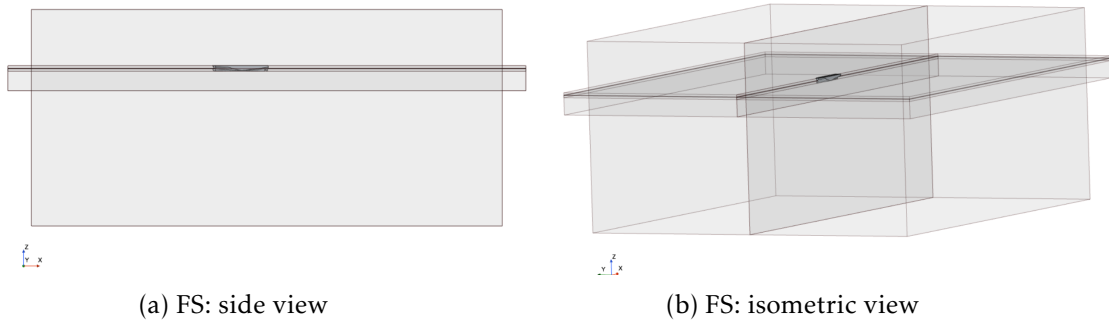
The presence of a free surface that separates the two fluids, air and water, imposes the creation of a volume refinement able to capture the deformation of the free surface; in particular, three rectangular boxes were created to have a cell size gradually finer when approaching the free surface. Figure 101.

In addition to the refinements presented above, three more refinements volume were created. One of this three was supposed to capture the flow field below the hull and affected by the *Down wash*; the other two instead, were created for best capture the turbulent and



(c) isometric view

Figure 62: Kelvin refinements



(a) FS: side view

(b) FS: isometric view

Figure 63: Free surface refinement

recirculating flow caused by the detachment of the fluid vein from the hull in the proximity of the rudder region. Figure 64.

### 12.3.2. Mesh

The next step after the definition of the refinement volumes was *meshing*. As for the *Propeller test case*, a grid convergence study was carried out with the aim to perform, later, a *Verification and Validation* procedure. In the same way, four grid base size were chosen and again a refinement ratio of  $\sqrt{2}$  was used as suggested by *ITTC*. Figure 19.

| Grid number | Base Size (BS) | $n^\circ$ Cells   |
|-------------|----------------|-------------------|
| #1          | 5.44           | $1.32 \cdot 10^6$ |
| #2          | 3.85           | $2.61 \cdot 10^6$ |
| #3          | 2.72           | $5.47 \cdot 10^6$ |
| #4          | 1.925          | $12.6 \cdot 10^6$ |

Table 19:  $n^\circ$  of cells per base size

A **Trimmed mesher** was chosen being a robust and efficient method of producing a high-quality grid; A trimmed mesh is composed predominantly of hexahedral cells with trimmed cells next to the surface. Trimmed cells are polyhedral cells but can usually be recognized

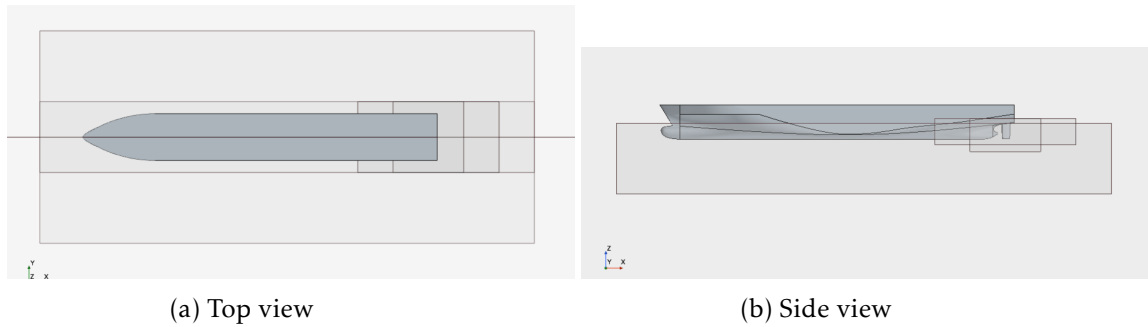


Figure 64: Other refinements

as hexahedral cells with one or more corners and/or edges that are cut off, *Star CCM+ User Guide*[13].

Always when meshing we must keep in mind that the goal is to discretize as best as possible the geometry while keeping the number of cells as lowest as possible.

Looking at figure 65 it can be noted that the cell size around the hull is not constant, this is because 4 different refinement levels were used: the idea was to increase the refinement, reducing the cell size, in that parts of the geometry characterized by an high curvature and therefore by an high pressure and velocity gradient. The same has been done for the rudder which is refined at the leading and trailing edges, at the tip and the intersection with the hull, figure 66.

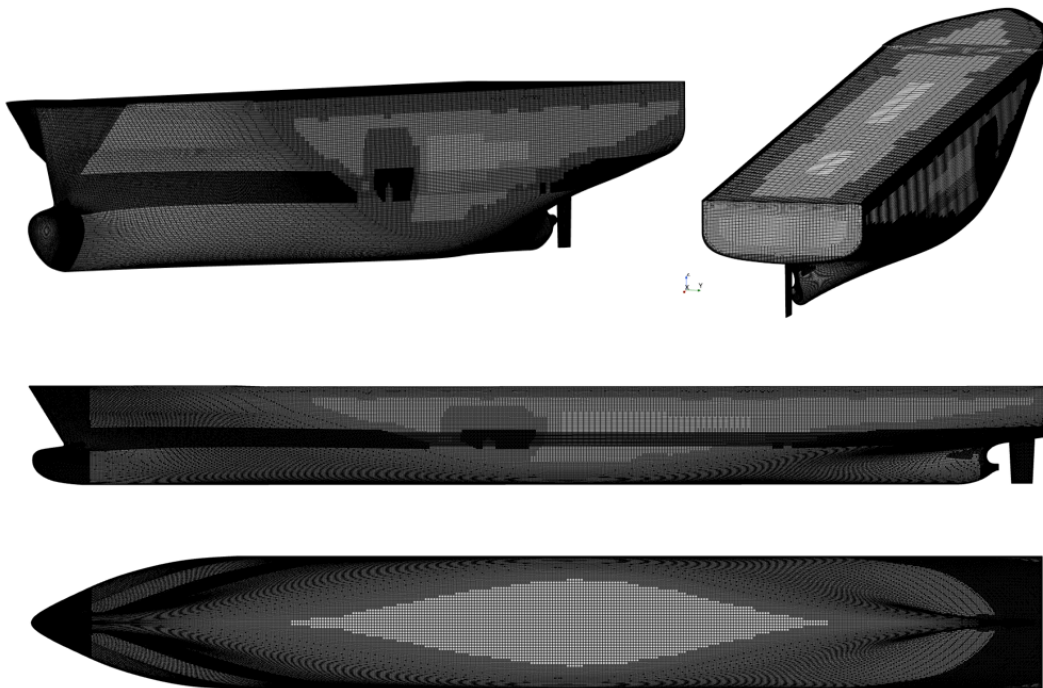


Figure 65: KCS hull mesh

For cells in the proximity of the wall, the *prism layer mesh model* is used to generate orthog-

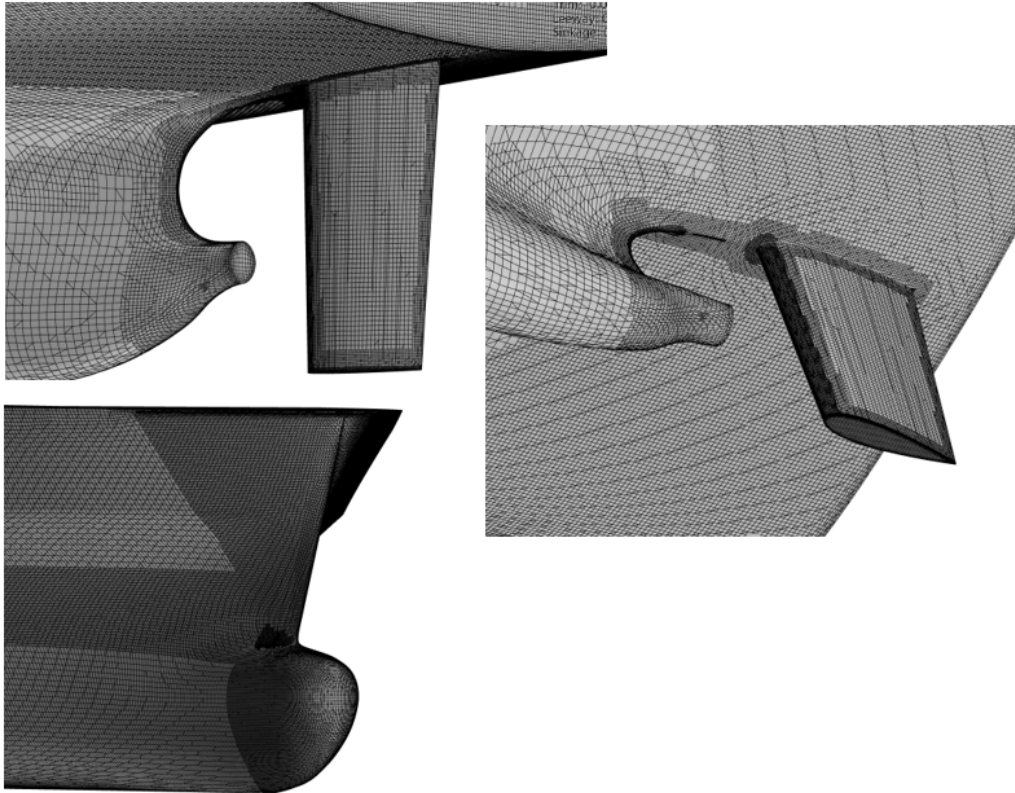


Figure 66: KCS hull mesh details

onal prismatic cells next to wall surfaces. This layer of cells is necessary to improve the accuracy of the flow solution and to best capture the velocity profile inside the boundary layer.

Following the CH guidelines a  $y^+ = 120$  was the target for the hull while a target of 100 was chosen for the rudder. Both these values guarantee that the first cell height falls in the *logarithmic layer*. The value of  $y$  is calculated using the skin friction coefficient given by the flat plate law<sup>2</sup>. It must be underlined that the  $y^+$  is a "target" value, so the real value obtained has to be checked during the post processing by mapping the  $y^+$  value on the hull. Table 20 shows the the values of the first cell height calculated.

| Index | $Fr$  | Speed [m/s] | $Re$              | $y$ [m] |
|-------|-------|-------------|-------------------|---------|
| $V_1$ | 0.108 | 0.915       | $5.23 \cdot 10^6$ | 0.00652 |
| $V_2$ | 0.195 | 1.647       | $9.42 \cdot 10^6$ | 0.00381 |
| $V_3$ | 0.260 | 2.196       | $1.26 \cdot 10^7$ | 0.00293 |

Table 20: First cell height value

The number of prism layers was set to 8 in agreement with what is stated in *ITTC 7.5-03-02-03* [37] where is suggested to use less than 15 points inside the boundary layer when wall

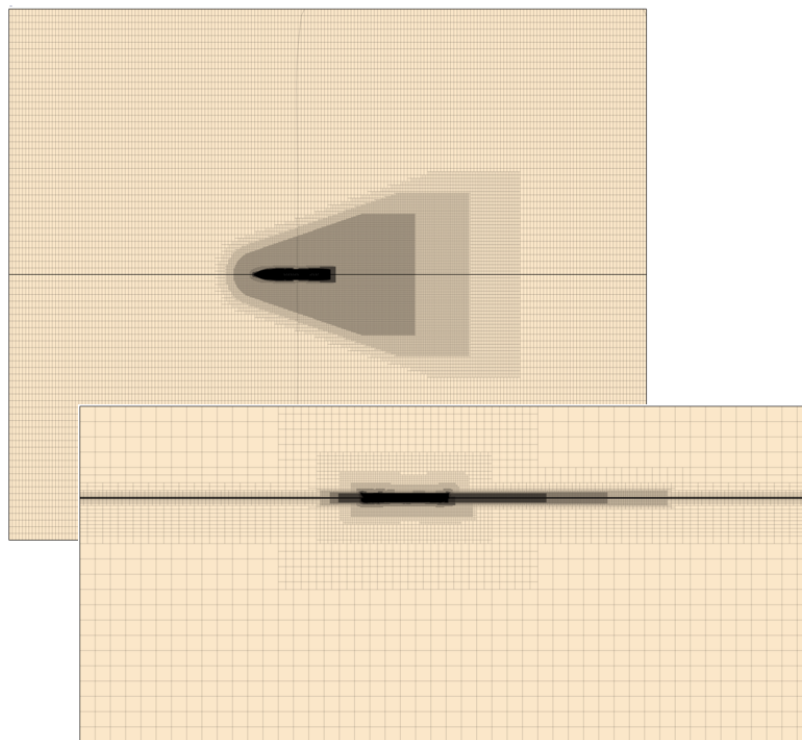
<sup>2</sup>A future development could be the use of the skin friction coefficient given by the correlation line, suggested by ITTC, present in section 5.1.1

functions are used, and this is our case as will be seen below.

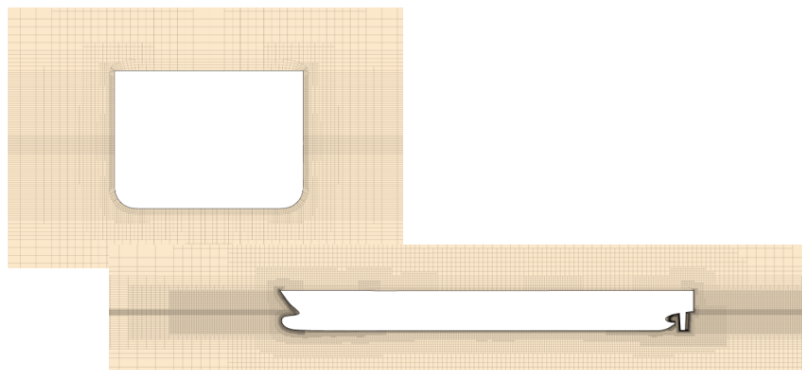
A CH best practice is to scale the *Prism layer total thickness* with the base size with the resulting values for the four grids, from the coarsest to the finest, are: 0.0638 m, 0.0451 m, 0.0319 m and 0.0226 m.

The goal was trying to have the same cell size between the last cell of the prism layer and the first of the core mesh.

Figure 67 shows different view of the meshed domain in which can be noted the various refinements due to the volumetric controls: in figure 67a the kelvin wake and the free surface refinements are shown. Figure 67b shows the free surface more in detail and contemporary the prism layer can be observed.



(a) Domain mesh top and side view



(b) Domain mesh front and side detail

Figure 67: Domain mesh and prism layer



### 12.3.3. Physical Setup

An important step when setting a CFD simulation is to choose the right physics able to replicate in best way the real phenomenon.

As previously done for the propeller, the RANS equations are the ones chosen to be solved to determine the flow field variables inside the computational domain. This choice is driven by the necessity to make a compromise between the accuracy of the result and the computational time/cost. In fact, we are not interested in the fluctuations of the flow field but only in the mean flow. This latter is the one that determines the characteristics of the ship, in terms of Drag, sinkage and trim.

**Turbulence Model** In order to define the relation between the fluid and the turbulent viscosity inside the RANS equations, the  $k-\omega$  SST (Shear Stress Transport) (by F.R. Menter,[34]) turbulence model was chosen. The latter combines the best quality of the  $k-\omega$  and  $k-\epsilon$  models. The use of a  $k-\omega$  formulation in the inner parts of the boundary layer makes the model directly usable all the way down to the wall through the viscous sub-layer, hence the SST  $k-\omega$  model can be used as a Low-Re turbulence model without any extra damping functions. The SST formulation also switches to a  $k-\epsilon$  behaviour in the free-stream and thereby avoids the common  $k-\omega$  problem that the model is too sensitive to the inlet free-stream turbulence properties, *CFD Online* [38]

Together with the SST model, the *All  $y^+$  treatment* for the boundary layer was enabled; this attempts to combine the high  $y^+$  wall treatment for coarse meshes and the low  $y^+$  wall treatment for fine meshes, *Star CCM+ User Guide* [13], section ??.

**Multiphase model** The **Multiphase Volume Of Fluid** (VOF) (section 9.4.5) was selected with the aim to simulate the presence of both *Air* and *Water* and then of a **Free surface** between these two.

Other models related with VOF were selected:

- **VOF Wave model** is used to simulate surface gravity waves on the interface between a light fluid and a heavy fluid. In Star CCM+ there are several wave models implemented, the one chosen was the *fifth order wave* in which a fifth order wave is modeled with a fifth order approximation to the Stokes theory of waves. This wave more closely resembles a real wave than one generated by the first order method. *Star CCM+ User Guide* [13]
- **Wave Damping** The main target of this model is to reduce the size of the computational domain. As best deepened in appendix B, this model forces or damps waves in order to achieve better the boundary conditions.
- **HRIC scheme** (High resolution Interface Capturing) is designed to mimic the convective transport of immiscible fluid components, resulting in a scheme that is suited for tracking sharp interfaces. This computational scheme helps the Vof in capturing the free surface.

**Dynamic Model** The *DFBI* model was enabled to let the ship be free to heave and pitch (2Dof) with translation along the  $z$  axis (heave) and the rotation around the  $y$  axis (pitch). The *Equilibrium* (D) option of the model was enabled in order to quickly achieve the **quasi**



**steady state** equilibrium position although the simulation was set to be **Unsteady**. This because the VOF model needs the time term in the equation to properly solve the free surface. In the *equilibrium model* the body is positioned and oriented in the flow so that the forces and moments acting on it are balanced in the chosen directions. The body moves within the specified directions according to a numerical iterative procedure until the forces and moments are balanced. The numerical procedure to move the rigid body is purely mathematical, that is, there is no true physical motion of the rigid body [13].

**Time step** The fact that the simulation is unsteady means that in the equations being solved by the software, the term involving the variation over time of the variables appears. As a consequence a time step has to be defined in order to define the amount of time the solution is advancing in time after each iteration.

Before launching a simulation, the flow field is initialized with the initial conditions. Once the simulation starts, the body (a ship in this case) is, from a computational point of view, instantaneously immersed in the flow field. The latter has to vary in order to take into account the presence of the body. By doing this, it faces an high increase in pressure. After a transient period the flow fields adapts to the presence of the body and the pressure decreases.

We are not interested in this part of the simulation considering that it is not physically real; a common practice at CH, is to use an high time step for the initial part of the simulation and then gradually reduce its value, following an hyperbolic behaviour, to the one proper to the case analyzed.

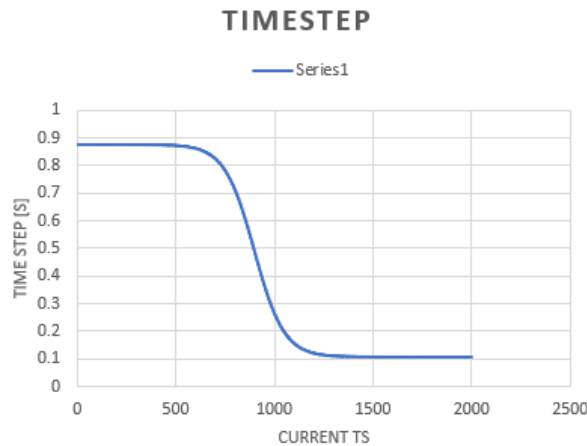


Figure 68: Time step variation

As can be seen in figure 68, starting from an high value, the timestep converges to the final value.

The target timestep changes with the speed, so 3 timesteps were chosen: 0.1093 s, 0.061 s, 0.0455 s.

**CFL** Considering again that our aim is to reach a quasi steady solution, the time marching schemes chosen is *Implicit*; this latter guarantees the possibility to not respect the conditions of  $CFL < 1$ , so bigger timesteps can be used and it is unconditionally stable. It is suggested for this simulations.

The most refined level of the mesh and the timestep were combined in order to have a reasonable  $CFL$  value for the finest grid (highest  $CFL$ ). The highest  $CFL$  value is: 13.3, considered acceptable. Nevertheless, as was the case for  $y^+$ , the  $CFL$  value is a target value only and it's achievement must be checked in the post-processing phase.

**Boundary Conditions** Figure 69 shows the boundary conditions applied to the domain. The majority of the boundaries are set as *Inlet*; this is because of the presence of the VOF wave model. As suggested in the Star Manual, the *inlet* condition has to be applied whenever possible. *Star CCM+ User Guide* [13]

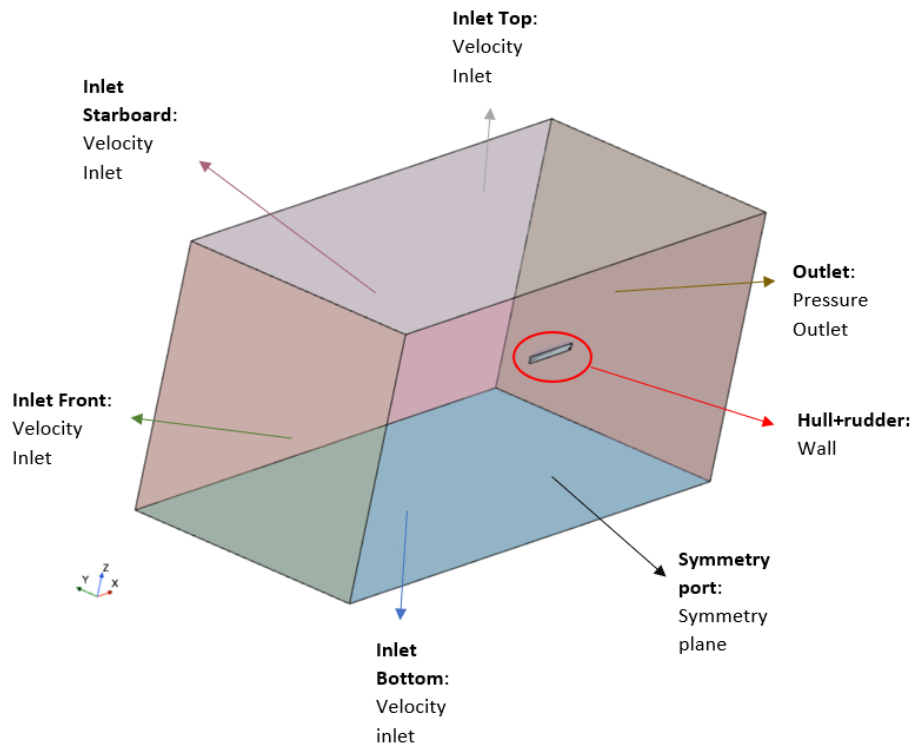


Figure 69: Computational Boundaries

**Initial conditions** The initial conditions were chosen in order to make the convergence to the final steady state easier. In particular, the initial conditions relative to the Sinkage at the AP and the Trim were given taking the experimental values from *Tokyo 2015 Workshop* [35] and reported in table 21.

| Index | Froude number | Speed [m/s] | Sinkage at the AP [m] | Trim ° |
|-------|---------------|-------------|-----------------------|--------|
| $V_1$ | 0.108         | 0.915       | $1.5 \cdot 10^{-4}$   | -0.017 |
| $V_2$ | 0.195         | 1.647       | $1.5 \cdot 10^{-4}$   | -0.097 |
| $V_3$ | 0.260         | 2.196       | $-6.95 \cdot 10^{-3}$ | -0.169 |

Table 21: Initial conditions

**Stopping criteria** The stopping criteria selected were the ones related to the *Max number of time steps*. Originally an other convergence criteria related to the percentage of the force along the three axes was enabled. The use of the equilibrium model led to a misleading convergence. After few trials a value of 3000 was chosen being a good compromise between accuracy and computational cost.

Table 22 summarises all the physics settings.

| Parameter                   | Solver setting  |
|-----------------------------|---|
| Solver                      | 3D segregated, constant density                         |
| Time                        | Implicit unsteady, 1 <sup>st</sup> order discretisation |
| Turbulence model            | RANS $k - \omega$ SST [34]                              |
| Convection Scheme           | 2nd Order upwind  |
| Finite Approximation Scheme | Finite Volume   |
| Computational Model         | pressure correction, two-phase flow treatment           |
|                             | Multiphase VOF, Vof Waves                               |
|                             | VOF Wave Zone distance                                  |
| Boundary layer treatment    | HRIC  |
|                             | all $y^+$ treatment (section ??)                        |
| Dynamic Model               | DFBI equilibrium (D)                                    |

Table 22: Model Setup

#### 12.3.4. Results

In this section the results of the simulation are presented.

**$C_T$ , Trim and Sinkage** In figure 70 the *Coefficient of resistance*, the *Sinkage* and the *Trim* are presented. These values are obtained by averaging the values of the last 50 iterations. We can notice that the  $C_T$  and the trim follow the behaviour of the experimental data, while the same cannot be said for the *sinkage*.

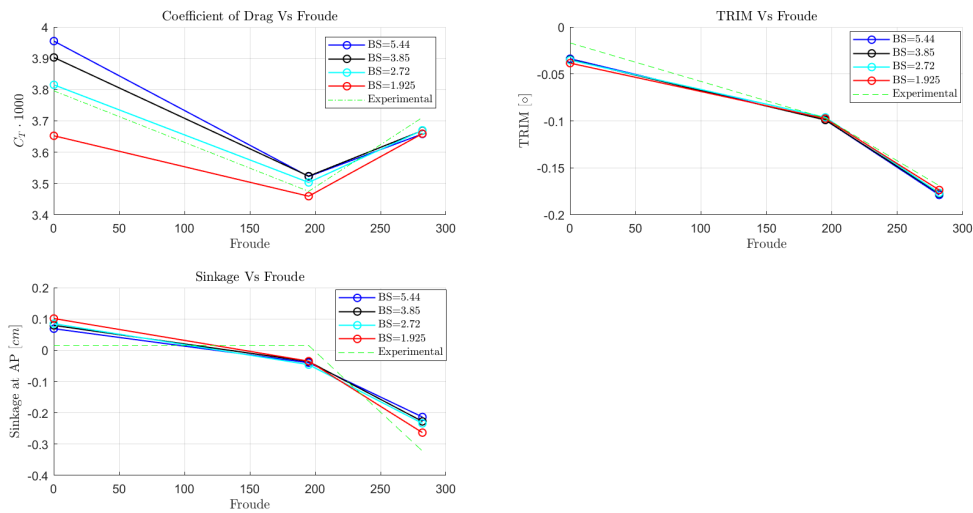


Figure 70:  $C_T$ , trim and sinkage

Looking at table 23 that shows the comparison error expressed as a percentage of the experimental data we can see that:

- the slowest speed is the one that generally presents the highest error, while the highest is the one with the smallest.
- generally the error decreases while refining although this behaviour it's not monotonic as we will see. An evident exception is the case of the sinkage at the slowest speed: in this case the error increases while refining.
- $C_T$  is overpredicted at the slowest and medium speed while it's underpredicted at the highest.

**Tokyo 2015 results** Table 24 shows the average results (without outliers) from the *Tokyo 2015 workshop* at  $Fr = 0.26$ .

Comparing our result from mesh #4 at the same  $Fr$ , we can notice that our results are in absolute value greater than the average of the workshop, the  $C_T$  and sinkage resulted overpredicted while the trim resulted underpredicted by the participants at the workshop as well as in our case.

If we look at the standard deviation we can say that our results concerning the  $C_T$  and the *Trim* fall in the range of the workshop's participants.

|       | Grid # | Cells    | $C_T \cdot 1000$ | $E_{C_T}[\%]$ | $Trim[^\circ]$ | $E_{Trim}[\%]$ | $Sinkage[cm]$ | $E_{Sinkage}[\%]$ |
|-------|--------|----------|------------------|---------------|----------------|----------------|---------------|-------------------|
| $V_1$ | EFD    |          | 3.80             |               | -0.017         |                | 2.000e-2      |                   |
|       | 1      | 1318998  | 3.955            | 4.188         | -0.034         | -98.671        | 7.000e-2      | 358.225           |
|       | 2      | 2608513  | 3.903            | 2.809         | -0.035         | -104.706       | 8.000e-2      | 428.680           |
|       | 3      | 5468481  | 3.815            | 0.506         | -0.035         | -107.529       | 8.000e-2      | 464.974           |
|       | 4      | 12637179 | 3.704            | -2.419        | -0.034         | -99.506        | 1.100e-1      | 603.954           |
| $V_2$ | EFD    |          | 3.480            |               | -0.0970        |                | 2.000e-2      |                   |
|       | 1      | 1319128  | 3.522            | 1.366         | -0.0991        | -2.125         | -4.000e-2     | -366.285          |
|       | 2      | 2614465  | 3.524            | 1.397         | -0.0990        | -2.075         | -4.000e-2     | -340.877          |
|       | 3      | 5477414  | 3.503            | 0.819         | -0.096         | 0.811          | -5.000e-2     | -407.574          |
|       | 4      | 12637695 | 3.459            | -0.448        | -0.098         | -0.511         | -3.000e-2     | -333.162          |
| $V_3$ | EFD    |          | 3.710            |               | -0.169         |                | -3.200e-1     |                   |
|       | 1      | 1319246  | 3.658            | -1.419        | -0.179         | -5.820         | -2.100e-1     | -33.749           |
|       | 2      | 2611473  | 3.669            | -1.130        | -0.177         | -4.941         | -2.300e-1     | -29.372           |
|       | 3      | 5490852  | 3.670            | -1.108        | -0.177         | -4.549         | -2.300e-1     | -27.446           |
|       | 4      | 12645112 | 3.659            | -1.393        | -0.174         | -2.723         | -2.600e-1     | -18.235           |

Table 23: EFD and CFD with comparison error in percentage of the experimental value

| T2015, $Fr = 0.26(2.196m/s)$ |                  |            |                   |               |                      |
|------------------------------|------------------|------------|-------------------|---------------|----------------------|
| $E\% C_T$                    | $\sigma_{C_T}\%$ | $E\% Trim$ | $\sigma_{Trim}\%$ | $E\% Sinkage$ | $\sigma_{Sinkage}\%$ |
| -0.5                         | 1.3              | 0.2        | 2.7               | -0.2          | 5.6                  |

Values expressed as a function of the experimental values

Table 24: Average Results without irregular values from Tokyo 2015 Workshop

**Y+** Figure 71 shows the  $y^+$  value obtained after running the simulation. In the previous section it was stated that the value of  $y^+ = 120$  was a target value so a subsequent control had to be performed. It can be seen that the majority of the surface of the hull lies in the logarithmic layer. Nevertheless it must be noted that the value on average reached is smaller than the target one. This confirms the common practice at CH to aim at an higher  $y^+$ , keeping a safety margin, when the aim is to lie in the log layer.

The rudder results lying in the *Buffer layer*; the current setup of  $y^+$  doesn't work well for walls present in a strongly slow flow, like the case aft of the ship. Hence, careful treatment must be taken for these zones.

**VOF** Figure 72 shows the bottom view and the port view of the Volume fraction of water that is currently wetting the hull. The results are related with the case at  $Fr = 0.26$ , that is the highest speed analyzed, and they involve all the four grids (*BS* stands for Base size). Observing the waterline at the free surface for all the four grids, it could be noted that while refining, the resolution between water and air becomes more pronounced; this is because with a smaller cell size, the HRIC model is more effective in capturing the free surface and so in defining a better demarcation between the two phases.

**Dynamic pressure coefficient** Figure 73 shows the dynamic pressure coefficient around the hull at  $Fr = 0.26$  for the finest mesh. An high value of this corresponds to a slow value in the flow speed over the hull surface. There are mainly 3 areas in which we can find an high value:

- at the bulb;

Heel: -0.00 [deg]  
Trim: -0.17 [deg]  
Leeway: 0.00 [deg]  
Sinkage: -0.00 [m]

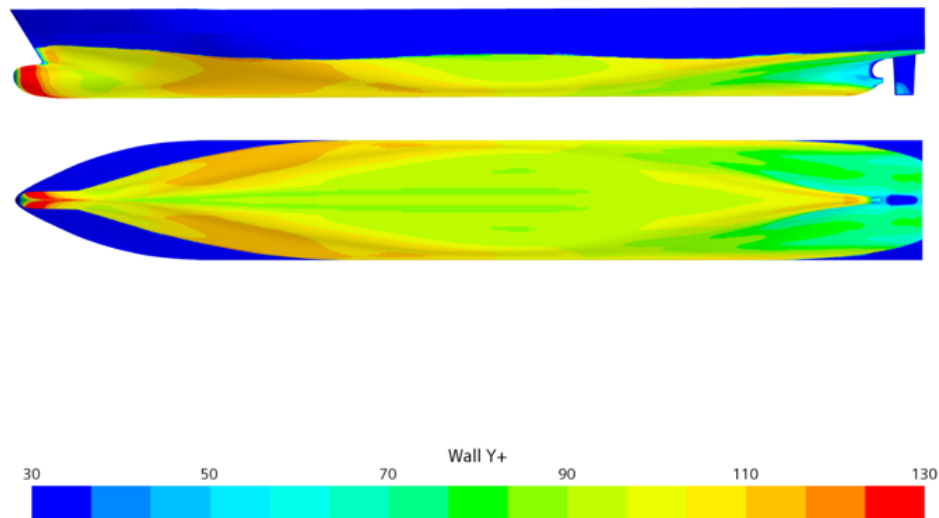


Figure 71:  $Y^+$  on the hull

- at the bow, waterline level;
- in the region close to the rudder, where the propeller should be located.

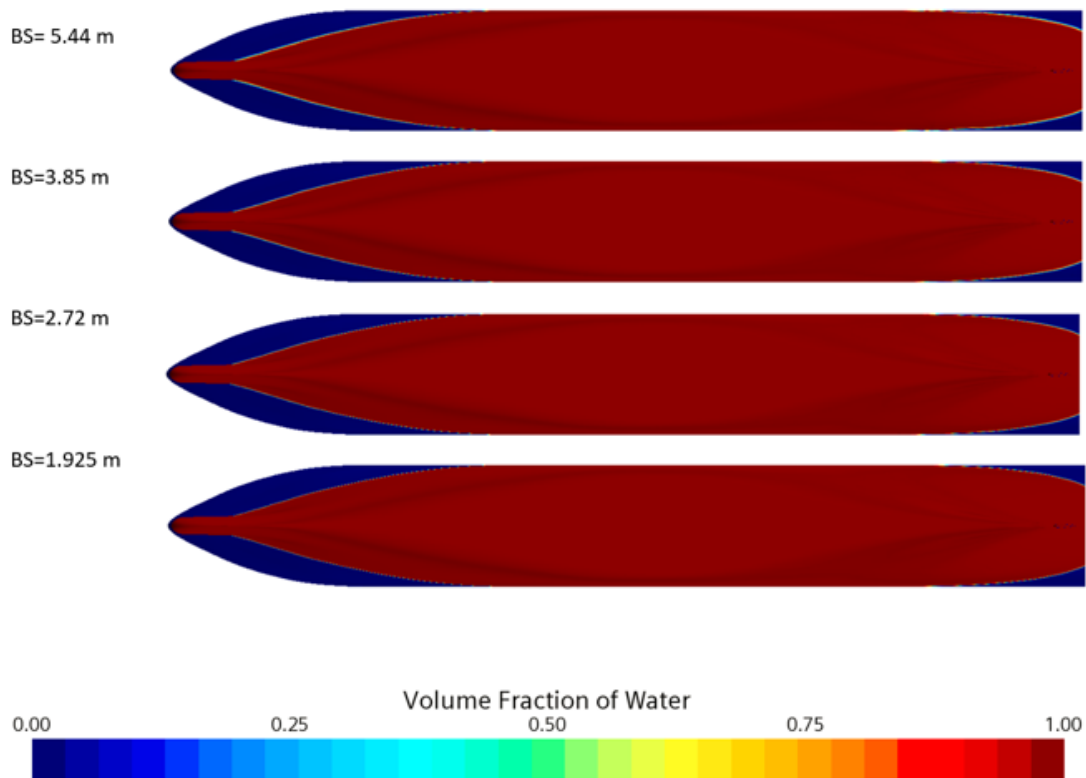
Concerning the bulb, this is because it is the most forward part of the hull wet by the water and the flow field hits the hull and stops at the *stagnation point* located at the bulb. Further downstream, due to the curvature of the hull, the water speed increases again.

The second region is the one at the waterline level, here we have both an increase in pressure because of the water that hits the hull and suddenly stops and due to both the presence of the hull and the breakage of the surface tension of the water.

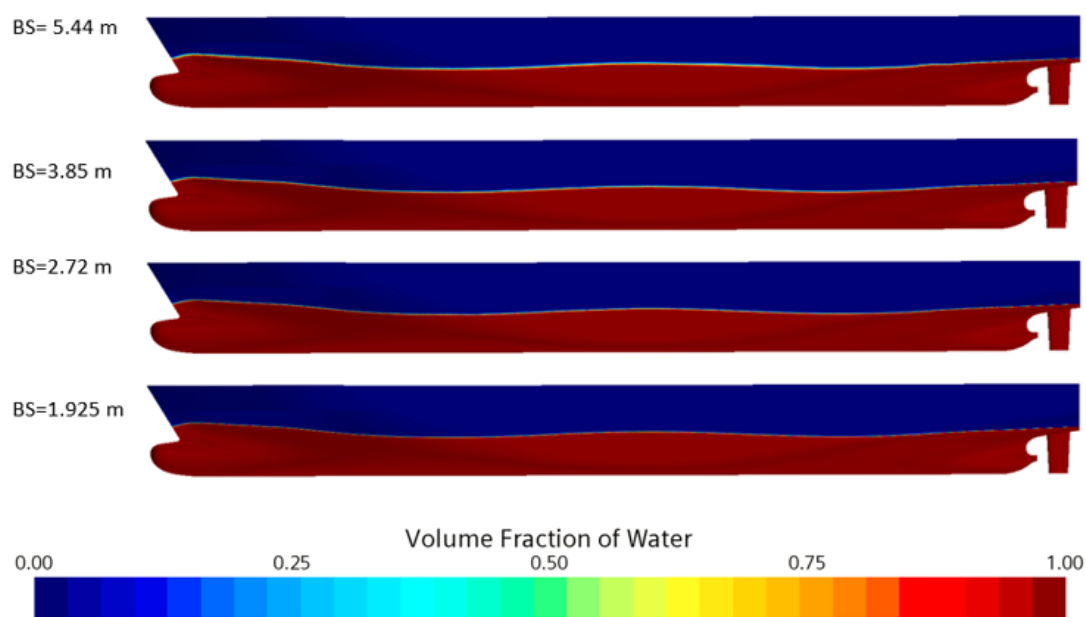
Lastly, the third region is in the propeller area. Here the flow slows down again because of the curvature of the hull that generates a diffuser effects in the absence of the propeller, due to the presence of the detachment of the fluid and consequently the presence of a recirculating zone with high pressure and slow speed.

**Wave pattern** Figure 74 shows the wave pattern at different speeds (and then Froude numbers). It is clearly evident the presence of the Kelvin pattern which become more evident as the boat speed increases; while increasing the speed, the wave period increases as well as the wave height.

Figure 75a presents a wider view of the kelvin pattern at froude 0.26 while figures 75b and 75c focus on the area around respectively the stern and the bow.



(a) Bottom View



(b) Port View

Figure 72: Vof

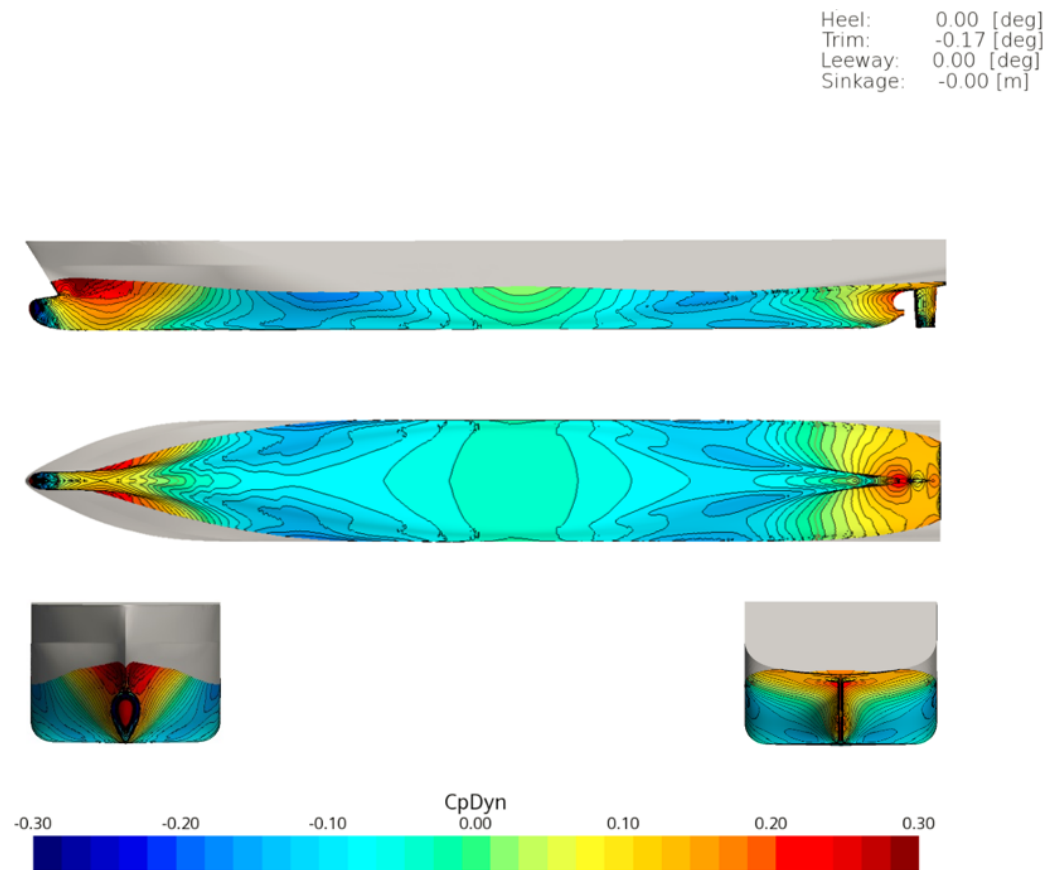


Figure 73: Dynamic Pressure Field

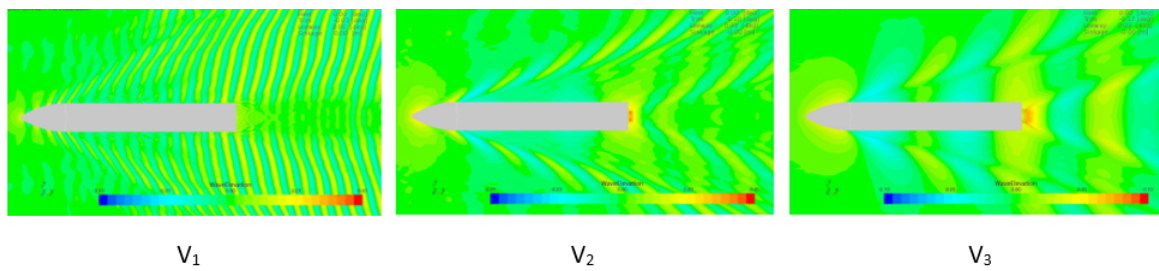
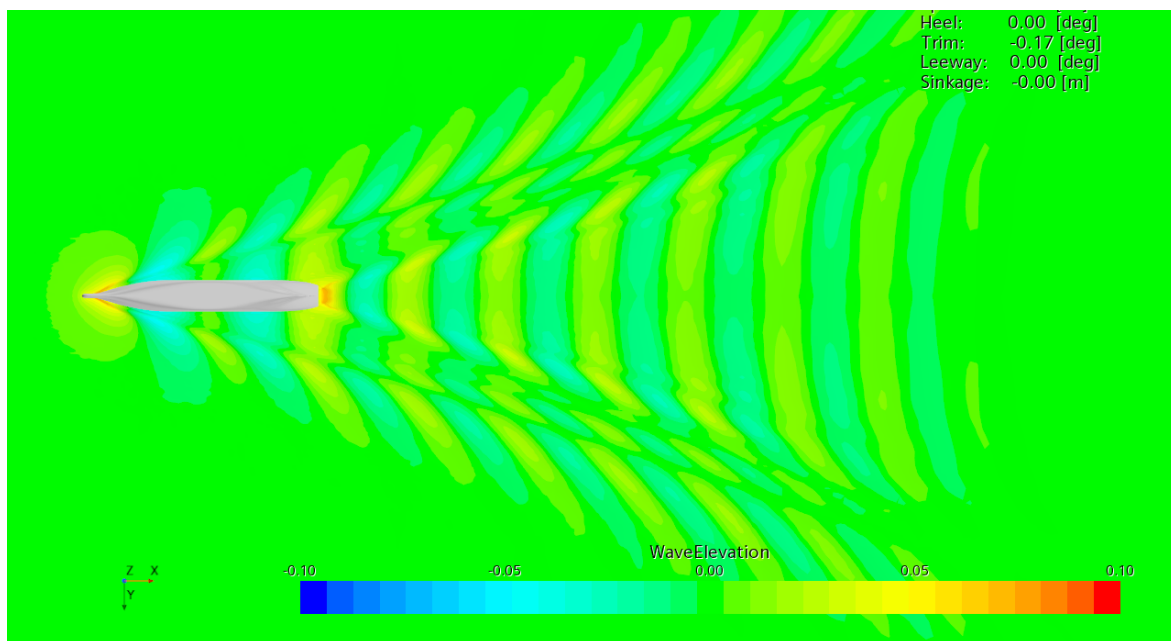
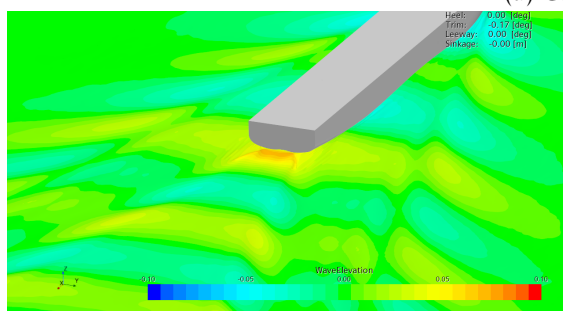


Figure 74: Wave pattern at different froudes

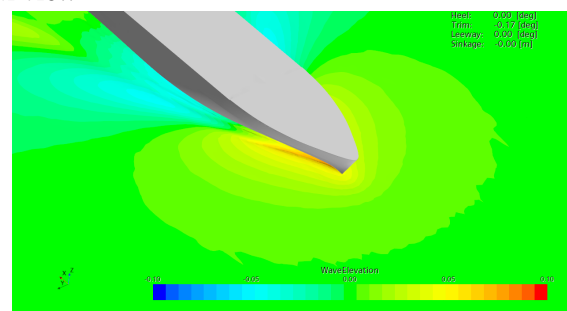




(a) Global view



(b) Stern View



(c) Bow View

Figure 75: Wave pattern Froude 0.26

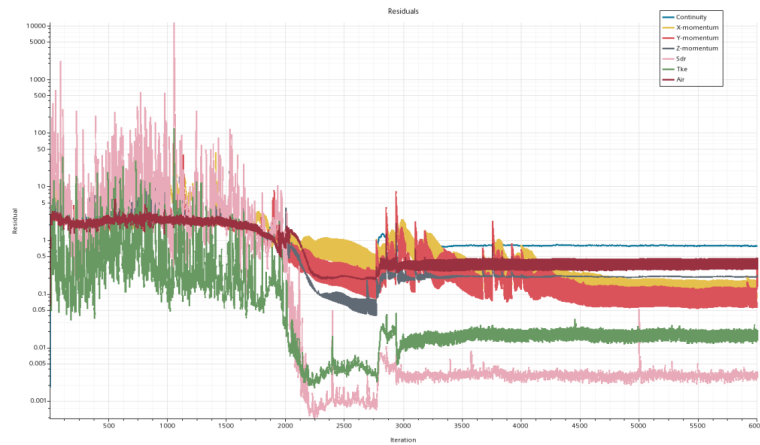
## 12.4. Solution verification

In the same way as for the propeller, the *Verification and Validation* procedure has been carried out.

### 12.4.1. Iterative error

Following again the procedure previously explained in section 10, the iterative error is monitored by monitoring the behaviour of the residuals that, as suggested by *L. Oberkamp et al.* [17], own the same behaviour of the latter.

Looking at figure 76, we can see that all the residuals reach a convergence at the end of the calculation. If we focus on figure 76a, the drop of these residuals is less than 3 order of magnitude as suggested by *L. Eça et al.* [16] to consider the iterative error negligible. Nevertheless, we can say that, looking at picture 76b that shows the residuals not normalized, it can be seen that their absolute value is quite low; therefore if looking at picture 78 it could be noted that the value we are monitoring converged and their oscillation is so low to be considered negligible. Following these assessments, the Iterative error will be considered negligible too.

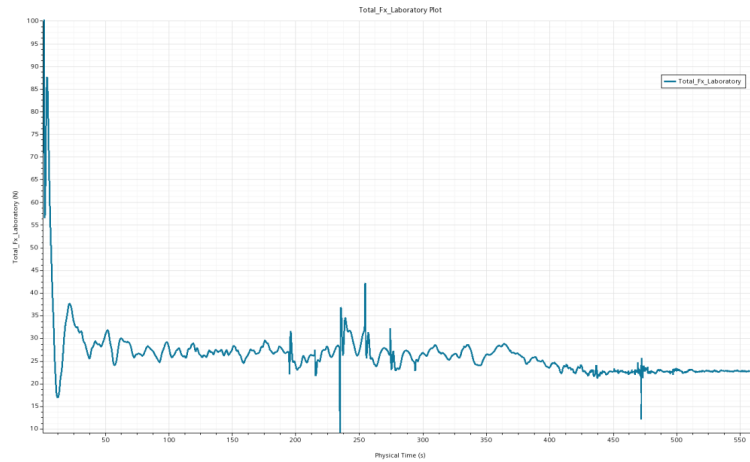


(a) Residuals normalized

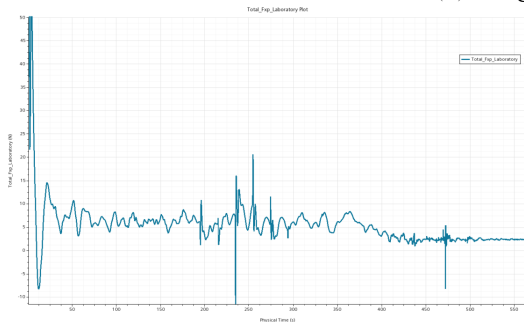


(b) Residuals not normalized

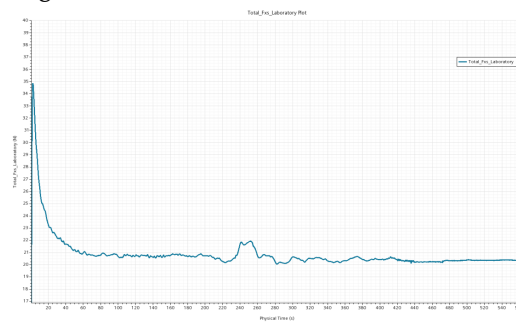
Figure 76: residuals



(a) Drag convergence



(b) Drag: Pressure component convergence



(c) Drag: Shear component convergence

Figure 77: Drag convergence

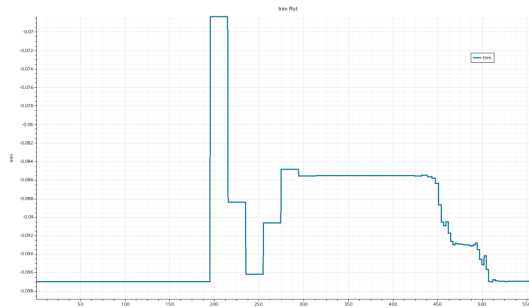
#### 12.4.2. Grid Convergence study

As previously done for the propeller, in order to evaluate the discretisation error, a grid refinement study has been carried out; figures 79a, 79b and 79c show the behaviour of the  $C_T$ ,  $Trim$  and  $Sinkage$  while refining the mesh; in the same graphs the EFD values are plotted.

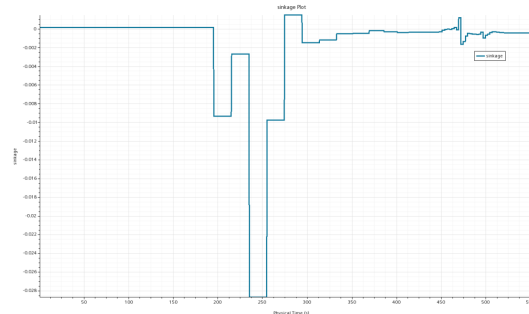
It can be noted that :

- regarding the  $C_T$  it seems to converge at the slowest speed, while is only decreasing without an evident convergent behaviour at speed  $V_2$ . At the highest speed it seems to converge until grid  $n^\circ 3$ , after which it starts reducing its value;
- the trim at slowest speed owns the same behaviour as for the the  $C_T$ . At the speed  $V_2$  it is not following a precise behavior and at the highest speed it seems again to have a convergent behaviour until grid  $n^\circ 3$  and than it starts increasing again.
- The same considerations as for the trim can be done for the sinkage.

We can say that the variation from one grid to another is not generally monotonic.

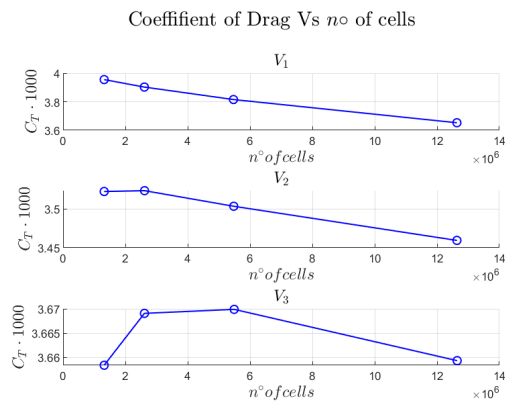


(a) Trim convergence

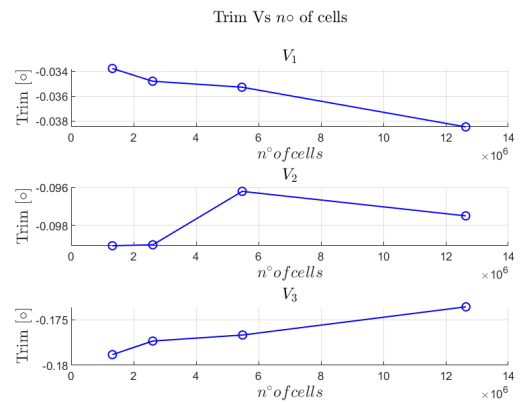


(b) Sinkage convergence

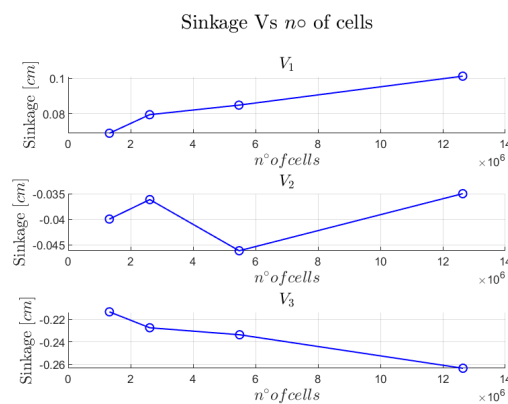
Figure 78: Trim and sinkage convergence



(a) Drag Coefficient VS  $n^\circ$  of cells



(b) Trim VS  $n^\circ$  of cells



(c) Sinkage at AP VS  $n^\circ$  of cells

### 12.4.3. Uncertainty calculation

With the help of the *MARINE* Uncertainty tool, the uncertainty was calculated based on the method defined by Eça et Hoekstra [19] and present in ITTC 7.5-03-01-01 [39], the grid chosen is the  $n^{\circ}3$  with a base size of 2.72 m as it is the one with a number of cells that is normally used in the company. The resulting uncertainty for each variable at each speed is showed in table 25.

|       |             | $\phi_0$      | $\phi_1$      | $p$  | $U_{CFD}[\%]$ |
|-------|-------------|---------------|---------------|------|---------------|
| $V_1$ | $C_T$       | $3.17E-03$    | $3.82E-03$    | 1,2  | 21.2          |
|       | <i>Trim</i> | $-27.20E-03$  | $-35.30E-03$  | 1,2  | 28.4          |
|       | <i>Sink</i> | $1.64E-03$    | $0.847E-03$   | 1,2  | 114.7         |
| $V_2$ | $C_T$       | $3.22E-03$    | $3.50E-03$    | 1,2  | 9.9           |
|       | <i>Trim</i> | $-94.30E-03$  | $-96.20E-03$  | 0.62 | 8.9           |
|       | <i>Sink</i> | $-0.33E-03$   | $-0.46E-03$   | 2    | 40.8          |
| $V_3$ | $C_T$       | $3.59E-03$    | $3.67E-03$    | 1,2  | 2.8           |
|       | <i>Trim</i> | $-164.00E-03$ | $-177.00E-03$ | 1,2  | 8.3           |
|       | <i>Sink</i> | $-3.44E-03$   | $-2.34E-03$   | 1,2  | 57.9          |

\* 1,2 Fit was made using first and second order

Table 25: Numerical uncertainty

We can notice that the values obtained are very high, this could have been envisaged from the grid refinement study where was evident the anomalous behavior of the data while refining. This behavior is confirmed by the fact that for 7 out of 9 cases the uncertainty was calculated by the tool with a first and second order fitting.

### 12.5. Validation

The high value of the numerical uncertainty, together with the not so low experimental uncertainty, brought to an high value of the *validation uncertainty*,  $U_{val}$ , as can be seen in table 26.

|       |             | $U_{CFD}[\%]$ | $U_{EFD}[\%]$ | $E[\%]$ | $U_{val}[\%]$ |
|-------|-------------|---------------|---------------|---------|---------------|
| $V_1$ | $C_T$       | 21.13         | 1.00          | 0.51    | 21.33         |
|       | <i>Trim</i> | 58.90         | 9.60          | -107.53 | 59.71         |
|       | <i>Sink</i> | 648.00        | 8.20          | 464.97  | 648.07        |
| $V_2$ | $C_T$       | 9.98          | 1.00          | -0.82   | 10.03         |
|       | <i>Trim</i> | 8.83          | 4.57          | -0.81   | 9.94          |
|       | <i>Sink</i> | 125.49        | 3.90          | 407.57  | 125.55        |
| $V_3$ | $C_T$       | 2.77          | 1.00          | 1.11    | 2.94          |
|       | <i>Trim</i> | 8.68          | 2.27          | -4.55   | 8.97          |
|       | <i>Sink</i> | 42.00         | 1.85          | -27.45  | 42.05         |

Results are expressed in percentage of the experimental data

Table 26: Comparison error and validation uncertainty

As we know, in order to validate a result, the comparison error  $E$  should be less or equal to the validation uncertainty  $U_{val}$ . We must take into account though, that this result is easy

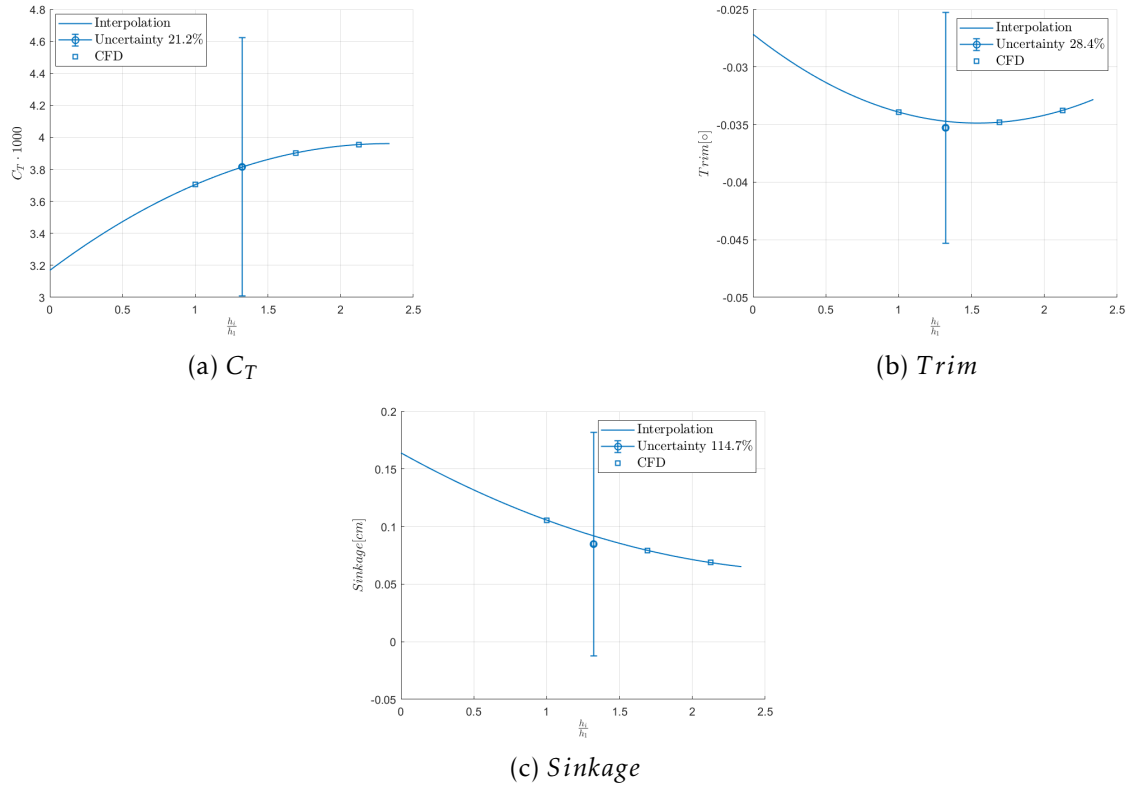


Figure 80: Open water characteristics vs grid refinement with error bar at  $V_1$

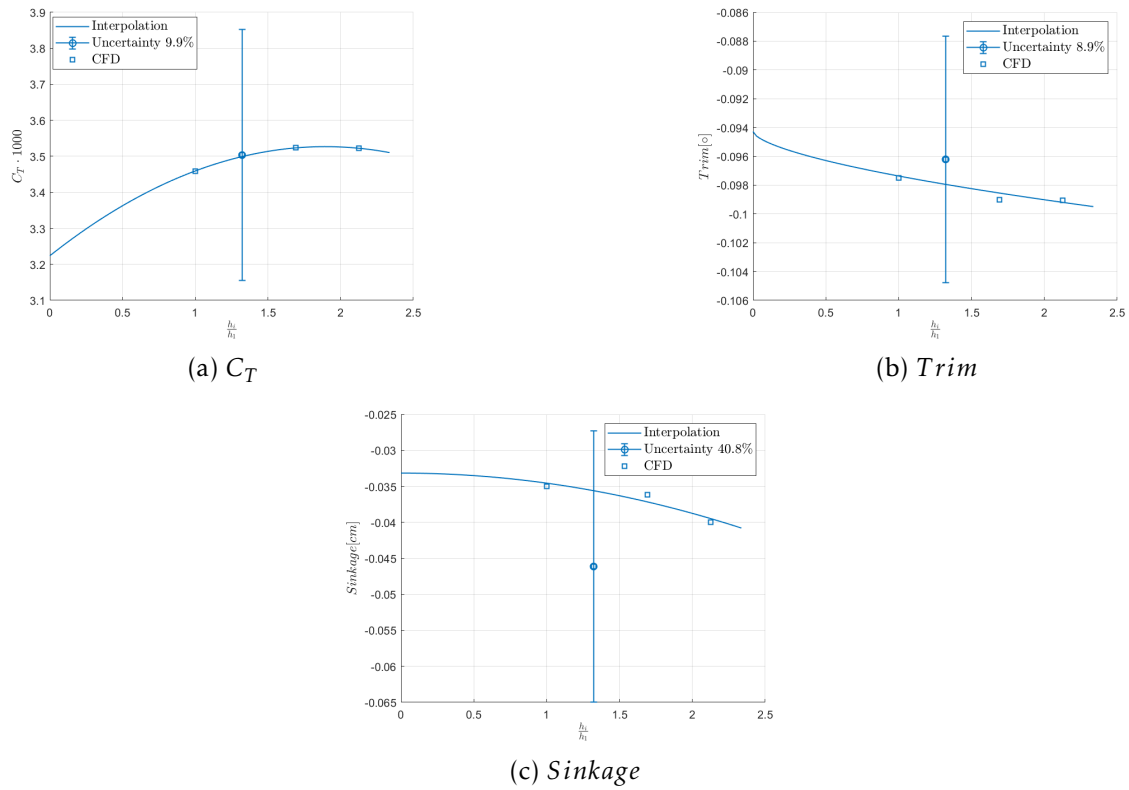


Figure 81: Open water characteristics vs grid refinement with error bar at  $V_2$

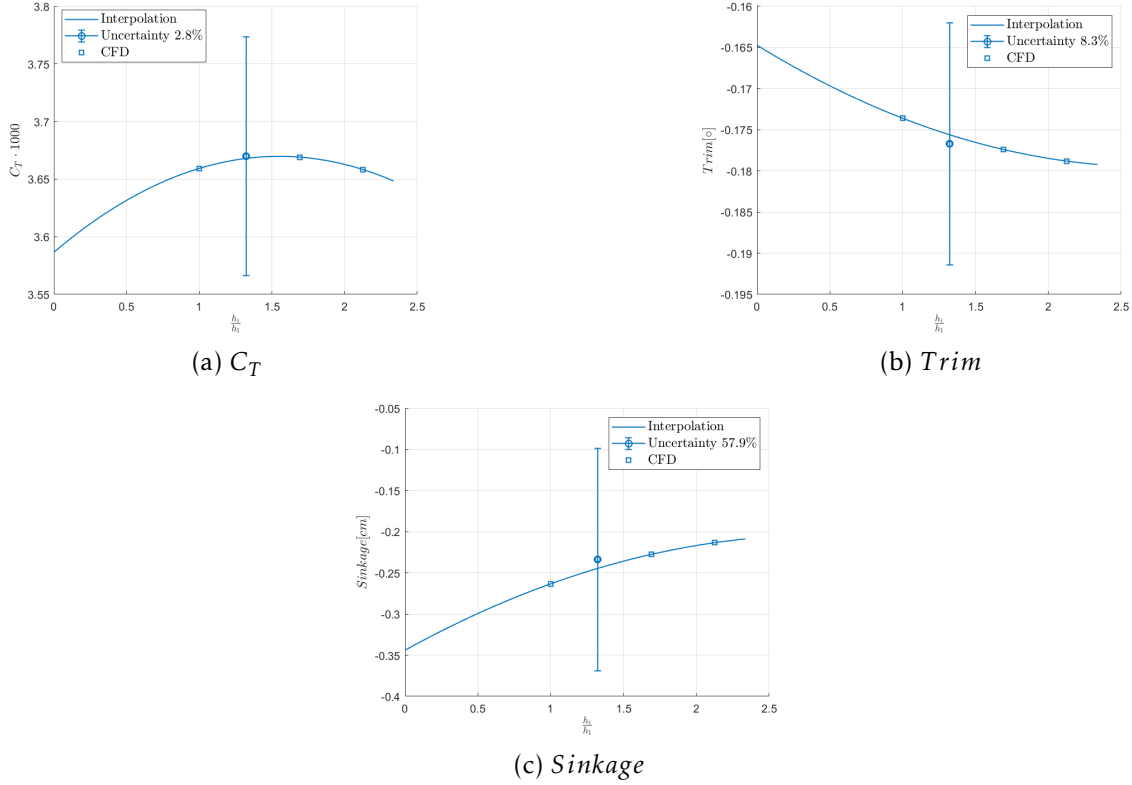


Figure 82: Open water characteristics vs grid refinement with error bar at  $V_3$

to achieve if the uncertainty is high and indeed this is our case where lot of case have been validated, table 27.

|           | $V_1$ | $V_2$ | $V_3$ |
|-----------|-------|-------|-------|
| $C_T$     | V     | V     | V     |
| $Trim$    | NV    | V     | V     |
| $Sinkage$ | V     | NV    | V     |

Table 27: Validation

**Conclusions** Under these considerations, taking into account that the experimental uncertainty is high too, we can consider validated the results with an uncertainty level under the 10%. . Although the numerical uncertainty and the comparison error expressed as a percentage of the experimental data as well, the absolute error can be considered negligible in relation to the length of the ship, i.e. 2 mm are negligible on a 7 m ship.

Looking at the results, we can conclude that they are generally satisfactory; CFD settings are capable of predict the characteristics of a ship at its nominal speed, that in our case is at  $V_3$  or (Froude 0.26, Full scale speed= 24kn), while some difficulties are encountered while dealing with slower speeds. We must bear in mind that, when talking about a CFD company, the aim of this latter is trying to achieve the best result with the lowest computational and therefore economical cost; this often leads to making compromise choices. Nevertheless, in order to improve the results while keeping the computational cost low, it is suggested to

perform later a further study by varying:

- the mesh strategy;
- the boundary conditions: putting a *symmetry plane* condition in the side boundary instead of a *velocity inlet*;
- the turbulence model: it is suggested to try the  $k - \epsilon$  as performed by Perić et al. [40].
- increase the number of iterations within a timestep;
- the  $y^+$ : try to reduce to a value close to 50.

,



## 13. Planing hull

### Azimut-Benetti AZ95rph

The third test case involved the yacht manufacturer *Azimut|Benetti*, the world's largest private group in the yachting sector.

The analyses took into account the **AZ95rph**, a 26 *m* luxury yacht.



Figure 83: AZ95rph cruising [41]

This yacht has previously undergone a study aimed at optimizing hull resistance through the CFD Star CCM+ software, reported in *Cimolin Serra Vatteroni*[41]; for this yacht, a database of experimental results found by physical towing tank experiments at the *Broderski Institut of Zagreb* was available.

| Characteristics                 | 0° trim                      |
|---------------------------------|------------------------------|
| Overall length (with cigars)    | 28.580 <i>m</i>              |
| Design waterline length         | 22.44 <i>m</i>               |
| $L_{pp}$                        | 22.54 <i>m</i>               |
| Maximum beam                    | 6.33 <i>m</i>                |
| Draught at midship              | 1.635 <i>m</i>               |
| Draught forward                 | 1.635 <i>m</i>               |
| Draught at aft                  | 1.635 <i>m</i>               |
| Draught at maximum section area | 1.635 <i>m</i>               |
| Displacement volume             | 101.36 <i>m</i> <sup>3</sup> |
| Displacement mass, naked hull   | 104 <i>t</i>                 |
| Block coefficient               | 0.4343                       |

Table 28: Az95rph characteristics

### 13.1. Experimental Tests

The experiments were carried out at the **Brodarski Institut** of Zagreb with the ship model *M-1357*, with a **scale factor**  $\lambda = 6$ . This model was towed by a carriage and the total resistance was measured. The different tests were conducted at different speeds, different displacements and appendage configurations of the model. The model *M-1357* was balanced and the vertical centre of gravity (*VCG*) was set corresponding value of  $VCG = 3.12\text{ m}$  and  $VCG = 2.90\text{ m}$  for design ( $\Delta = 104.0\text{ t}$ ) and maximum displacement mass ( $\Delta = 115.0\text{ t}$ ), for the full scale respectively.

All results valid for full scale are intended for a sea water condition reported in table 29.

|                     |        |                       |                        |
|---------------------|--------|-----------------------|------------------------|
| Water density       | $\rho$ | $\text{kg/m}^3$       | 1026                   |
| Kinematic viscosity | $\nu$  | $\text{m}^2/\text{s}$ | $1.1883 \cdot 10^{-6}$ |
| Temperature         | $T$    | $^{\circ}\text{C}$    | 15.00                  |

Table 29: Operations Conditions

Application point of **towing force** was at **LCB position**, in the elongation and the direction of propeller shaft (**towing angle**  $9.0^{\circ}$ ). The results are corrected to the horizontal plane and calculations are made with dynamic wetted lengths and surfaces. The conversion from the model to the full-scale ship was done by means of ITTC-1957 correlation line, with total correlation allowance  $C_a = 0.2 \cdot 10^{-3}$  for all the tested draughts. The conversion was made on the presumption that residuary resistance coefficient  $C_R$  is identical for ship and model at certain equal Froude's number. The total resistance coefficient  $C_T$  was obtained in accordance with:

$$C_R = C_{Rm} = C_{Tm} - C_{Fm} \quad (58)$$

$$C_T = C_R + C_F + C_a \quad (59)$$

During the test the rise or fall at *LCB* ( $Z_m$  – model value) and dynamic trim were measured as well. The values of the rise or fall at *LCB* for the full scale are defined as:  $Z = Z_m \lambda$ .

In order to replicate the same turbulence level at full scale and to be sure that the turbulence was fully developed, during the test a *turbulence stimulator* along the bow contour was applied.

### 13.2. Benchmarking Conditions



Figure 84: Naked hull geometry

Among the experimental results, the configuration chosen was the **Naked** one **FULL SCALE**, fig 84, with the displacement equal to 104 t, that corresponds to the model test *n° B1 – 9841* Figure 85.



Figure 85: TEST *B1 – 9841*

This test was characterised by the model in the naked hull geometry trimmed at *even keel* with an angle of 0°.

The Corresponding Hydrostatic data are the ones in table 31.

The model was tested with a speed range between 3.67 m/s and 7.25 m/s; the results from the towing tank test, were interpolated and then scaled to Full Scale in a range between

18 – 34 *kn*. Three speeds were chosen for the benchmark: 18, 26 and 34 *kn*.

| Index                     | Froude number | Speed [ <i>m/s</i> ] | Speed [ <i>kn</i> ]                        | Sinkage at the COG [ <i>m</i> ] | Trim ° |
|---------------------------|---------------|----------------------|--|---------------------------------|--------|
| $V_1$                     | 0.642         | 9.26                 | 18   | –1.681                          | 2.956  |
| $V_2$                     | 0.915         | 13.38                | 26   | –1.458                          | 2.669  |
| $V_3$                     | 1.199         | 17.5                 | 34   | –1.288                          | 2.721  |
| Density $\rho$            |               |                      | 1025 $\text{kg/m}^3$                       |                                 |        |
| Kinematic Viscosity $\nu$ |               |                      | $1.883 \cdot 10^{-6} \text{ m}^2/\text{s}$ |                                 |        |
| LCG                       |               |                      | 9.65 <i>m</i> (from stern)                 |                                 |        |
| VCG                       |               |                      | 3.12 <i>m</i> (from keel)                  |                                 |        |
| Draft                     |               |                      | –1.635 <i>m</i>                            |                                 |        |

Table 30: Benchmarking conditions

| Characteristics                 | Full Scale                              | Model Scale ( $\lambda = 6$ ) |
|---------------------------------|---|-------------------------------|
| $L_{WL}$                        | 22.44 <i>m</i>                          | 3.7407 <i>m</i>               |
| $L_{pp}$                        | 22.54 <i>m</i>                          | 3.7567 <i>m</i>               |
| Beam, maximum section area beam | 6.33 <i>m</i>                           | 1.0557 <i>m</i>               |
| Draught at midship              | 1.635 <i>m</i>                          | 0.2725 <i>m</i>               |
| Draught FP                      | 1.635 <i>m</i>                          | 0.2725 <i>m</i>               |
| Draught at AP                   | 1.635 <i>m</i>                          | 0.2725 <i>m</i>               |
| Draught at maximum section area | 1.635 <i>m</i>                          | 0.2725 <i>m</i>               |
| Displacement volume             | 101.36 $\text{m}^3$                     | 0.4693 $\text{m}^3$           |
| Displacement mass, naked hull   | 104 <i>t</i>                            |                               |
| LCB                             | –1.62 <i>m</i> (aft of midship section) | –0.2704 <i>m</i>              |
| VCG                             |   | 3.12 <i>m</i>                 |
| VCB                             | 1.14 <i>m</i>                           | 0.1904 <i>m</i>               |
| Block coefficient ( $C_b$ )     | 0.4343                                  | 0.4343                        |
| $I_{xx}$                        | 664642 $\text{kg m}^2$                  |                               |
| $I_{yy}$                        | 4592227 $\text{kg m}^2$                 |                               |
| $I_{zz}$                        | 4592227 $\text{kg m}^2$                 |                               |

Table 31: TEST B1 – 9841 Hydrostatic Data

### 13.3. CFD

#### 13.3.1. Geometry

The initial geometry provided by Azimut-Benetti was the one showed in figure 86. As can be seen, it is equipped with spray-rails, side cigars, Bow Thruster aperture and stabilizer fins. The first thing was cleaning the geometry by deleting all these components leaving the hull naked with only the centreline skeg and propeller tunnels, in order to have the geometry that suits for our test case.



Figure 86: Initial geometry

Figure 87 shows in different views the final geometry used for the simulation.

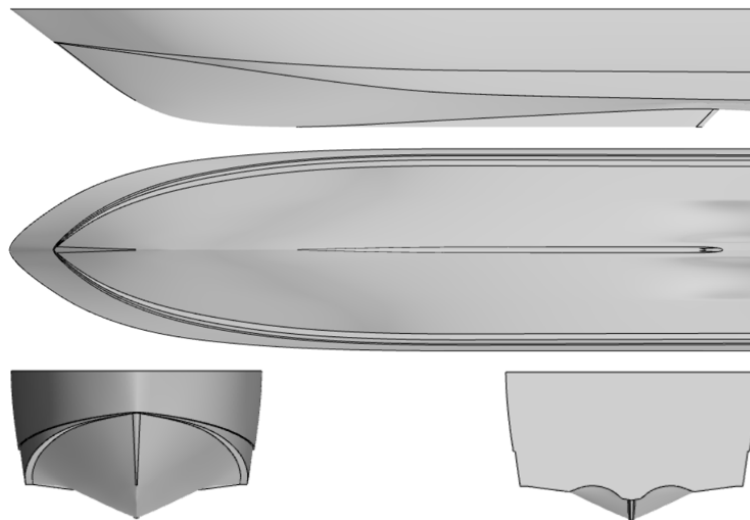


Figure 87: Final geometry

**Coordinate System** As usual, initially the *CAD* (blue) and the *laboratory* (magenta) coordinate system were coincident as shown in figure 88a. The coordinate of the *Lab CSys* (black) in this situation were the ones reported in table 31.

Later the hull was sinked of a quantity equal to the draft plus the sinkage given as initial condition in the simulation, rotated around the CoG in order have the axis aligned with the flow, as for the ship, and rotated again around the  $y$  axes by a quantity equal to the trim given as initial condition. The CoG coordinates remain fixed if referred to the CAD coordinate system while they varied if referred to the laboratory system and they depend on the initial sinkage and trim.

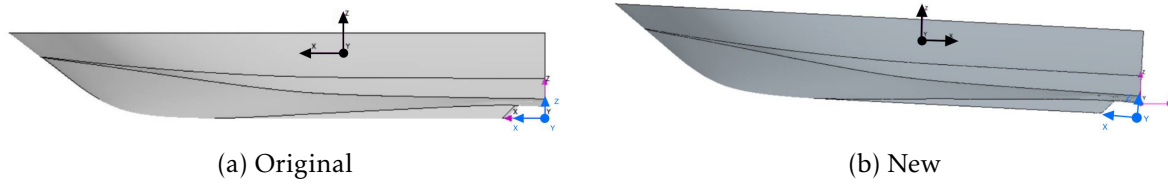


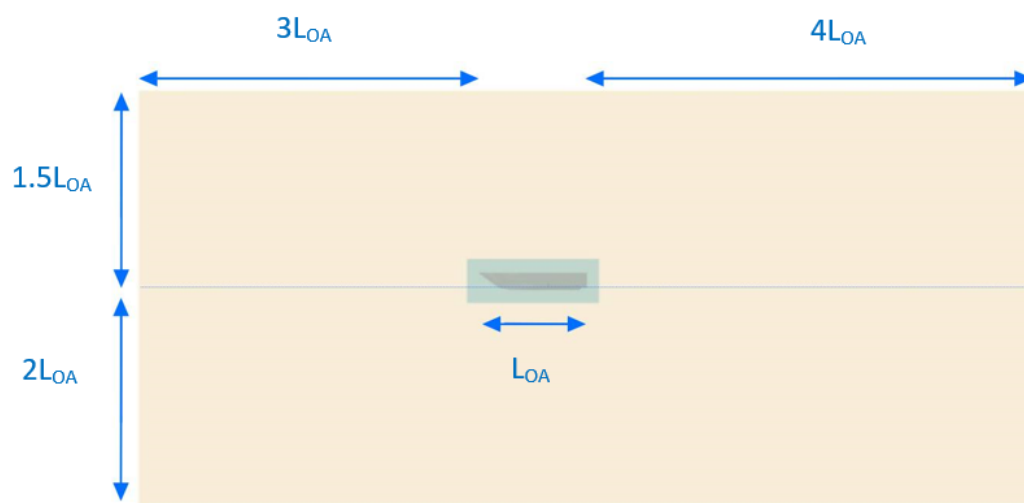
Figure 88: Coordinate systems

**Computational domain** The same considerations as for the ship were taken into account in the creation of the domain for this test case.

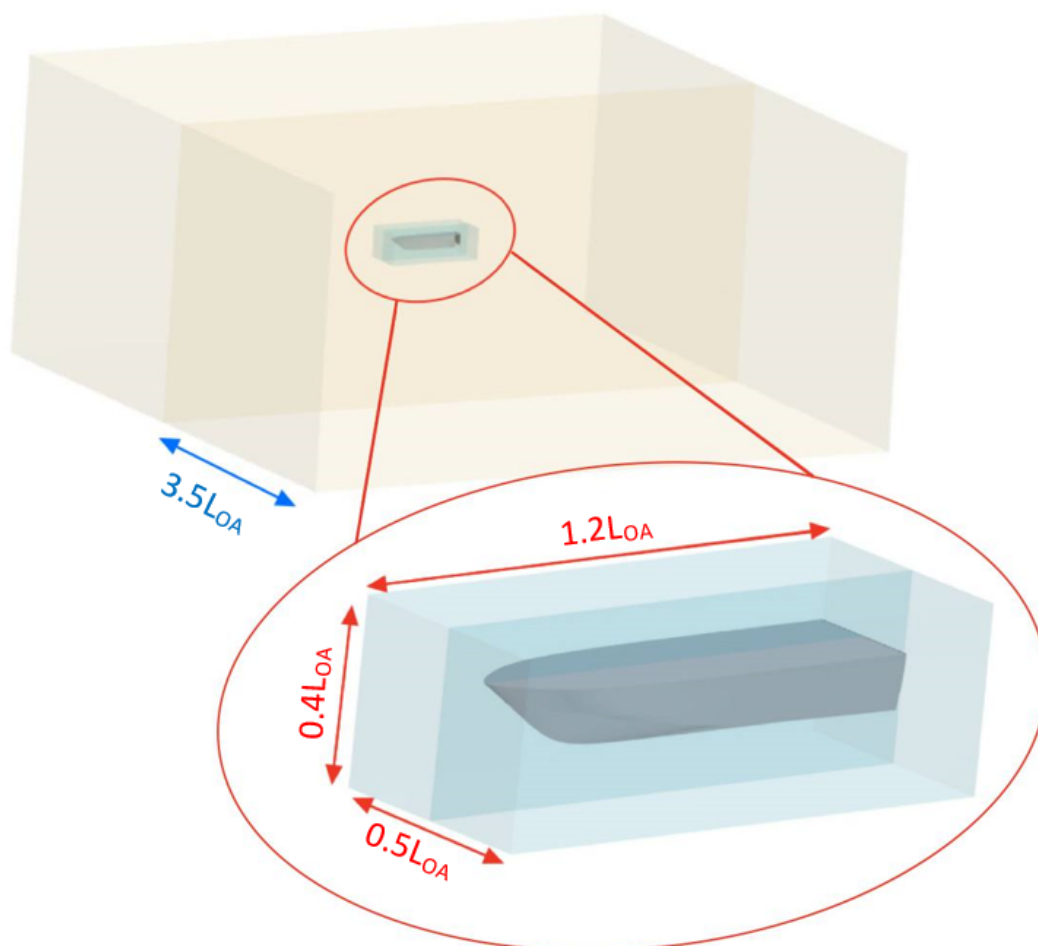
Figure 89a shows the domain characteristics; again as reference length the Overall length,  $L_{OA}$ , was used. The inlet is positioned at 3 times the  $L_{OA}$ , while the *outlet* is placed 4 times the  $L_{OA}$  behind the stern. Finally, the lateral boundary is placed 3.5 times the  $L_{OA}$  distant from the center of the ship.

The presence of a vertical symmetry plane in the ship together with the symmetrical boundary condition, let us simulate **only half of the domain**.

As it will further detailed in the next section, an *overset mesh* was used during this simulation so an overset box surrounding the planing hull, with the dimensions showed in figure 89b, was created.



(a) Domain (background) dimension



(b) Overset dimension

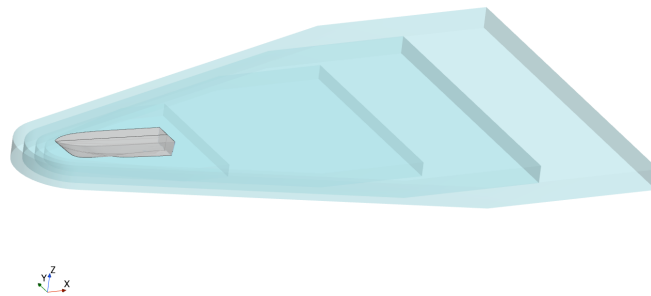
Figure 89: Computational domain

**Refinement volumes** With the same target of capturing the kelvin wake pattern, again 4 volumetric refinements were created as shown in figure 90a.

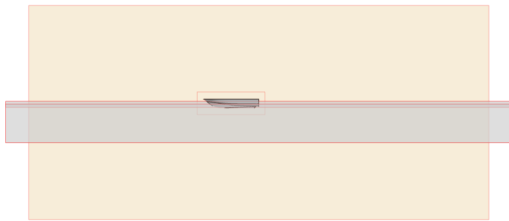
The free surface was again captured by 3 rectangular boxes, figures 90b and 90c.

In addition to these refinements, due to the presence of the overset mesh, a further box refinement was created in order to have a gentle transition between the overset cell size and the core mesh one.

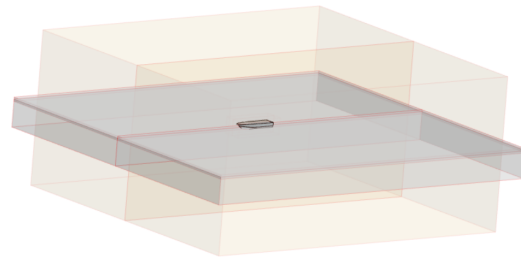
CAPONNETTO HUEBER



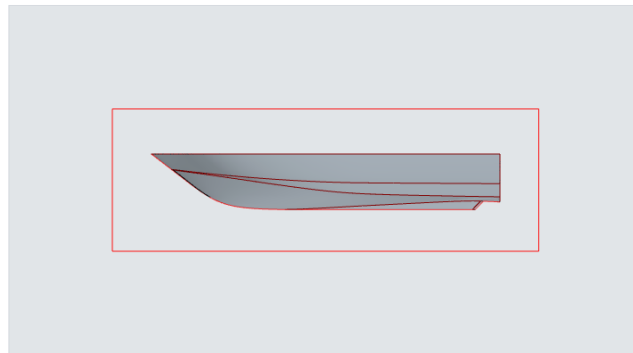
(a) Kelvin refinement



(b) Free surface refinement: side view



(c) Free surface refinement: isometric view



(d) Overset offset box

Figure 90: Volumetric refinements



### 13.3.2. Mesh

The domain creation was followed by the mesh creation. Table 32 shows the base size and their relative number of cells for the four grids that were created. The refinement ratio is always  $\sqrt{2}$  having been identified as the refinement ratio for this thesis work and suggested to CH for Benchmarks and *Verification And Validation* studies.

| Grid number | Base size | $n^\circ$ Cells  |
|-------------|-----------|------------------|
| #1          | 15.2      | $1.9 \cdot 10^6$ |
| #2          | 10.75     | $3.5 \cdot 10^6$ |
| #3          | 7.6       | $6.5 \cdot 10^6$ |
| #4          | 5.37      | $15 \cdot 10^6$  |

Table 32:  $n^\circ$  of cells per base size

Figure 91 shows the mesh around the planing hull. It could be noted that being devoid of appendages, the hull presents large flat areas which result in a mesh very consistent. The major refinements can be found close to the bow, where the curvature increases and at the steps where we have sudden change in the surface inclination that hydro-dynamically results in a high pressure and velocity gradient.

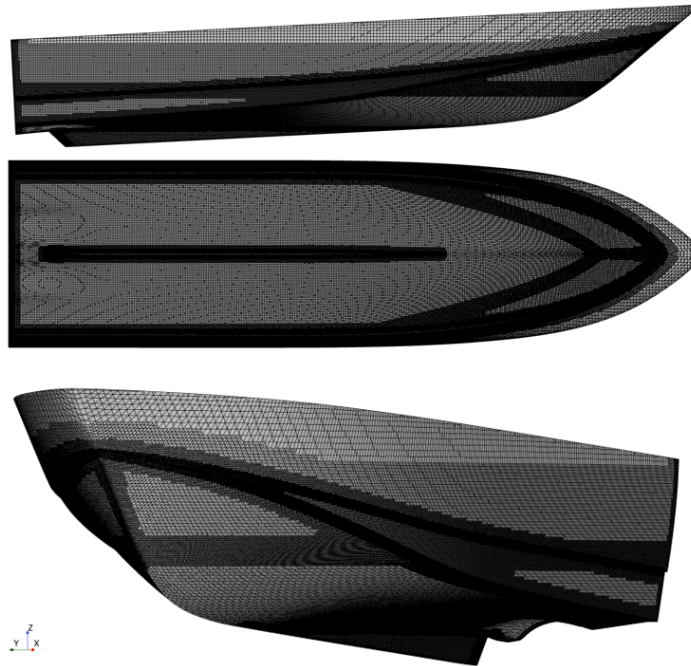


Figure 91: Hull Mesh with refinement area

If we look from the side view we can notice an horizontal refinement stripe: this is due to the free surface volumetric refinement that influences also the mesh on the hull; when meshing the hull, we have to take into account that, due to the planing phenomenon and the high speed, another phenomenon, the *Numerical ventilation*, can take place; it is the (unphysical) penetration of a thin layer of air travelling all across the hull. One of the way to avoid this problem is to have the mesh refinement on the hull in correspondence of the free surface with the same size or one less than the one of the finest free surface refinement; this best

practice avoids the possibility of the *smearing*; in fact, if the hull is refined more than the free surface, this latter is forced to increase the number of cells in correspondence of the hull. This can cause the information to pass from one cell on the free surface to two or more on the hull, enhancing the possibility of having *numerical ventilation*.

In figure 92 the refinement at the bow and at the skeg are showed. The end of the skeg reassembles the shape of a trailing edge, for this reason it was indeed refined in order to capture the high gradients.

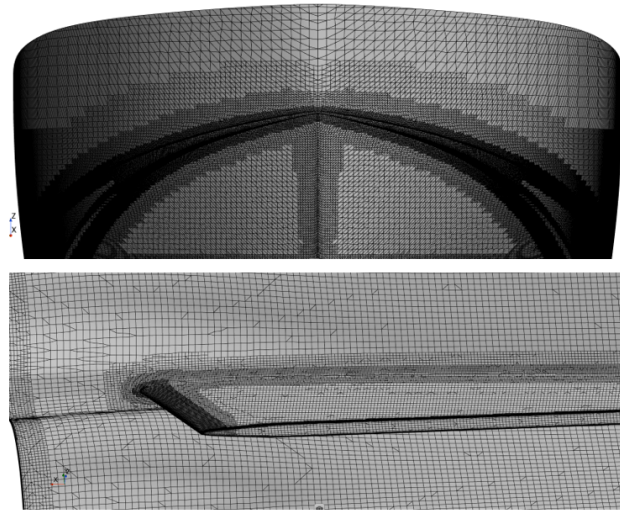


Figure 92: Hull Mesh with refinement particulars

The  $y^+$  target value is again 120 but this time the number of layers which were used in the prism layer increased from 8 to 10; this because, compared with the previous case, the speeds are higher and now we are facing the *planing* phenomenon which involves new forces and the ventilation phenomenon; increasing the number of layers can help in avoiding numerical ventilation by reducing the gradient inside the boundary layer.

Table 33 shows the first cell height value obtained.

| Index | $Fr$  | Speed [m/s] | $Re$         | $y$ [m]      |
|-------|-------|-------------|--------------|--------------|
| $V_1$ | 0.642 | 9.26        | $1.76E + 08$ | $8.34E - 04$ |
| $V_2$ | 0.915 | 13.38       | $2.54E + 08$ | $5.92E - 04$ |
| $V_3$ | 1.199 | 17.49       | $3.32E + 08$ | $4.62E - 04$ |

Table 33: First cell height value

Considering the number of layers and the first cell height, in order to have the same cell size between the last prism layer cells and the first overset cell, the following values of *prism layer total thickness* have been calculated for each base size (from the coarsest to the finest): 0.250 m, 0.176 m, 0.125 m, 0.089 m.

Figure 93 show the detail of the prism layer at the bow and at the stern.

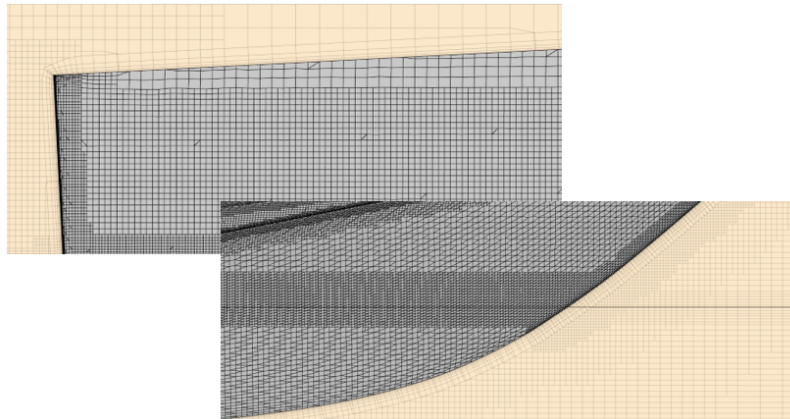


Figure 93: Hull Mesh prism layer

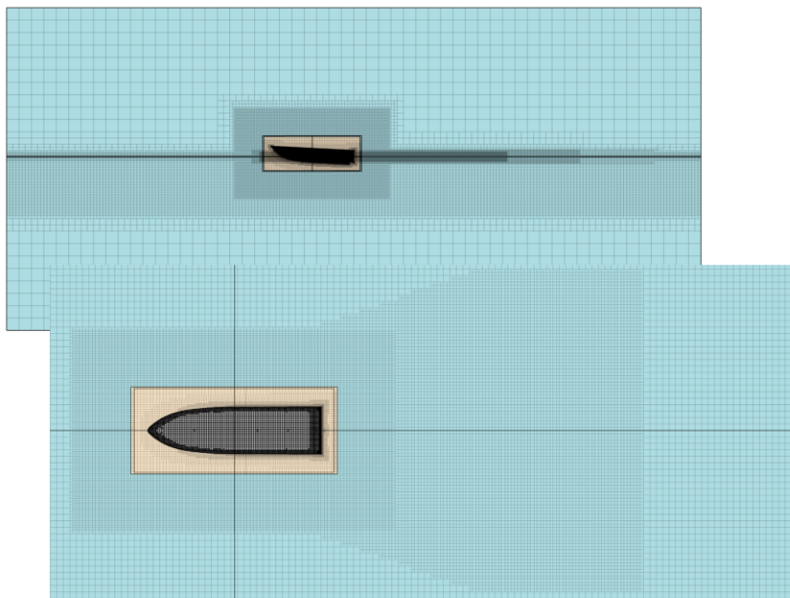


Figure 94: Domain mesh: kelvin, free surface refinements and overset mesh

**Overset mesh** As said before, an overset mesh was defined in order to better capture the movement of the boat. The adoption of this mesh, as aforementioned, implies to split the domain in a stationary region, the *Background*, and a moving one the *Overset region*. These two regions are meshed and the two meshes overlap each other. This mesh was adopted to deal with the free motion through the 2 Dof of the planing hull.

In the overset mesh we can distinguish between different types of cells:

- *Active*: within active cells, discretized governing equations are solved.
- *Inactive*: within inactive cells, no equations are solved. However, these cells can become active if the overset region moves.
- *Acceptor* the Acceptor cells separating active and inactive cells are located at the over-set interface. Variable values are being interpolated from donor cells of one region to

acceptor cells in another region. The donor cells in one region are the active cells that are closest to the acceptor cell from another region. *Star CCM+ User Guide* [13].

In figure 94 its presents is highlighted. Around it an offset refinement is present for smoothing the cell size transition.

For both background and overset mesh a *trimmed mesher* has been used as for the ship. The reason is that, due to the presence of a vessel and a free surface, a trimmed mesh should be used because it is well aligned with flow, thus avoiding smearing at the interface. The latter is much faster to mesh, but normally takes more time to converge.

### 13.4. Physics set-up

The physics settings used to carry out the simulation are showed in table 34. They are basically the same used for the previous simulation although some differences can be highlighted.

| Parameter                   | Solver setting  |
|-----------------------------|---|
| Solver                      | 3D segregated, constant density                         |
| Time                        | Implicit unsteady, 1 <sup>st</sup> order discretisation |
| Turbulence model            | RANS $k - \omega$ SST [34]                              |
| Convection Scheme           | 2nd Order upwind  |
| Finite Approximation Scheme | Finite Volume   |
| Computational Model         | pressure correction, two-phase flow treatment           |
|                             | Multiphase VOF, Vof Waves                               |
|                             | VOF Wave Zone distance                                  |
| Boundary layer treatment    | HRIC  |
|                             | all $y^+$ treatment (section ??)                        |
| Dynamic Model               | DFBI <i>free motion</i>                                 |

Table 34: Model Setup

**Dynamic Model** The *DFBI* model was enabled to let the planing hull be free to heave and pitch (2Dof), the translation along the  $z$  axis (heave) and the rotation around the  $y$  axis (pitch) were consequently released. This time though, the *Free Motion* option was enabled instead of the *equilibrium* one. The free motion let the body be free to move along and around the degree of freedom enabled: the body interacts with the fluid, exchanges forces with it and, in our case, tries to achieve a quasi-steady state status. Since the planing is strongly influenced by the boat sailing condition (speed, trim, sinkage), the equilibrium model is not suggested for planing hulls *Star CCM+ User Guide* [13].

**Towing force** In order to take into account the towing force necessary to carry the model in the towing tank test, a new reference system was defined in the position of center of the propeller disk, (1.40;0;0.22 )  $m$  in the Cad coordinate system. Infact, instead of applying a towing force, a propeller force was applied in origin of the reference system previously defined with an inclination of  $9^\circ$ .

**Time step** The same considerations made for the ship have been made for the planing hull regarding time step and CFL. Not being interested in the initial part of the simulation,

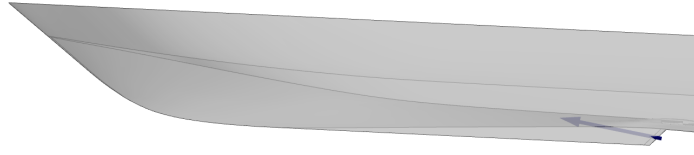


Figure 95: Propeller force

a varying time step was implemented with a time step target, equal to:  $5.4 \cdot 10^{-3} s$ ,  $3.74 \cdot 10^{-3} s$ ,  $2.86 \cdot 10^{-3} s$  for  $V_1$ ,  $V_2$  and  $V_3$  respectively.

**CFL** For what concerning the CFL number, also here the situation didn't change. Again the most refined level of the mesh and the timestep were combined in order to have a reasonable CFL value for the finest grid (highest CFL). This time this resulted in a CFL value equal to 2.38. We can notice the difference with the value of the previous case, this because of the difference in the time step calculation settings between the planing hull and the ship.

**Boundary conditions** As can be seen in figure 96a, the boundary conditions set for the background region were the same used previously.

In this case we have to set new boundaries in order to face with the presence of the over-set mesh. In figure 96b we can see the presence of a symmetry plane and an *Overset mesh* boundary condition. The overset one defines the border of the hole-cutting process, i.e. defines the cells that will be deactivated in the background.

**Initial conditions** The initial conditions are reported in table 35. They are equal to the experimental value; this choice was made to speed up the calculation and let it converge earlier.

| Index | Froude number | Speed [ $m/s$ ] | Speed [ $kn$ ] | Sinkage at the COG [ $m$ ] | Trim $^\circ$ |
|-------|---------------|-----------------|----------------|----------------------------|---------------|
| $V_1$ | 0.642         | 9.26            | 18             | -1.681                     | 2.956         |
| $V_2$ | 0.915         | 13.38           | 26             | -1.458                     | 2.669         |
| $V_3$ | 1.199         | 17.5            | 34             | -1.288                     | 2.721         |

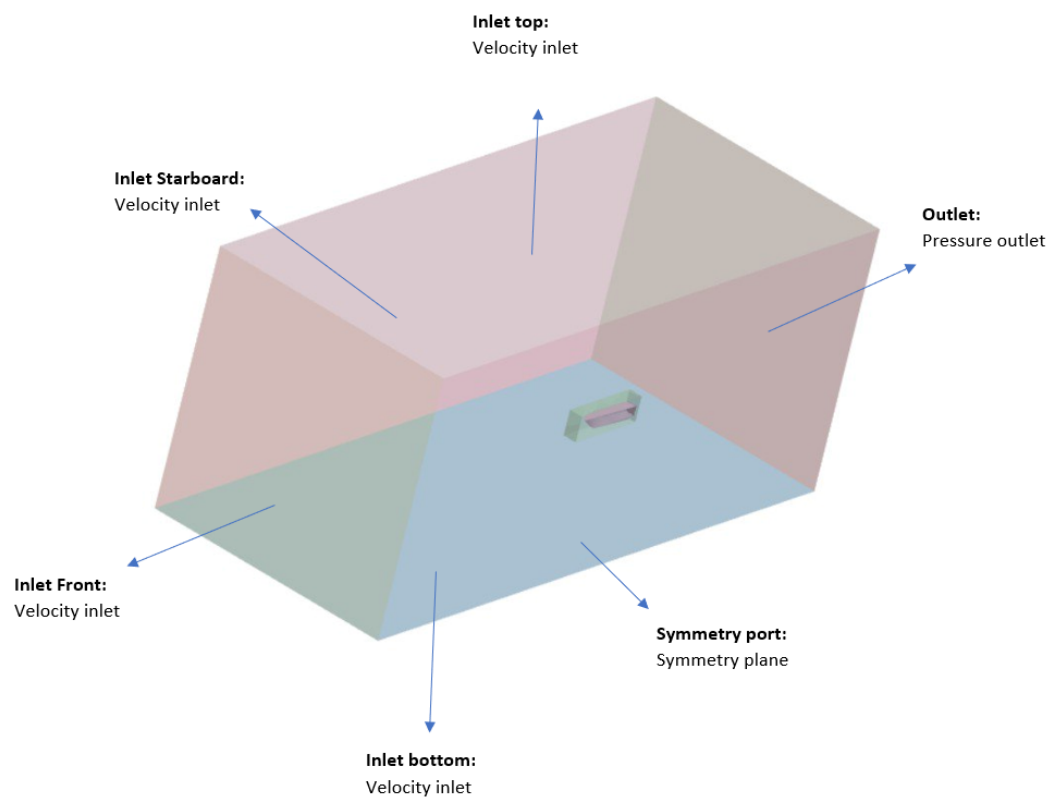
The sinkage value include the draft equal to  $-1.635 m$

Table 35: Initial conditions

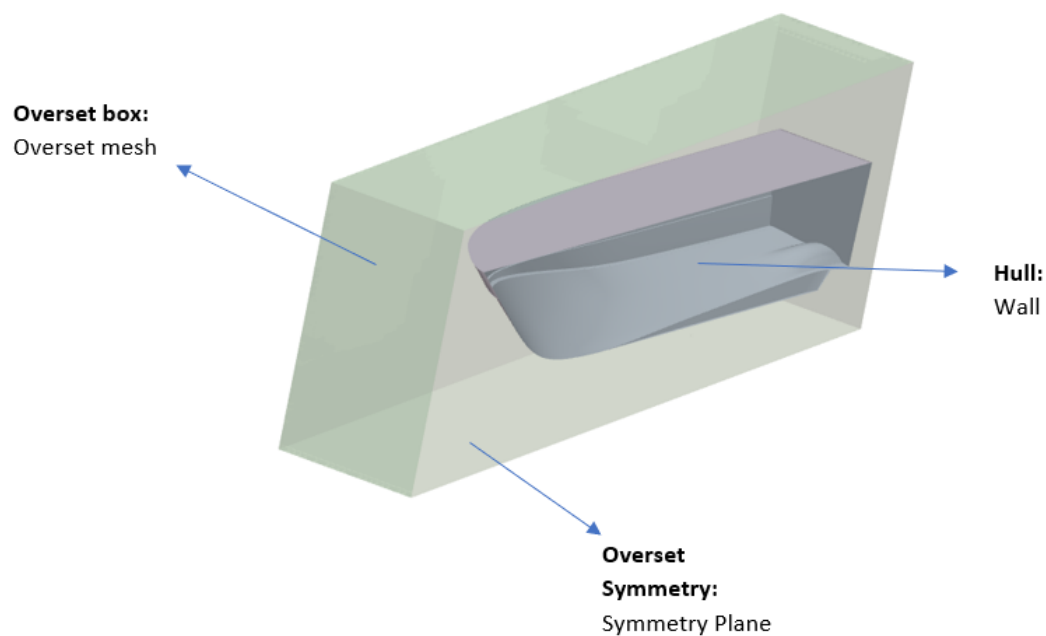
**Stopping criteria** 2000 iterations were chosen as stopping criteria; they are the usual max iterations used by CH in this type of simulations.

**Numerical ventilation** In section 13.3.2 it was already anticipated that planing hull simulation face the problem of the numerical ventilation which consists in the (nonphysical) penetration of a thin layer of air travelling all across the hull. *F. Cimolin and C. Pettinelli* in [42] propose three possible strategies to get rid of this problem; the most efficient seems to be the one deepened in appendix C. It consists in an artificial air extraction with an additional sink term.

A field function based on that method is implemented in the CH macros and was enabled during the simulations carried out for the planing hull.



(a) Domain (background) dimension



(b) Overset boundary condition

Figure 96: Boundary conditions



### 13.5. Results

**Resistance, Sinkage, Trim** In the following the results for  $C_T$ , sinkage and trim are presented. The performance of a full scale planing hull is better predicted than the result obtained in the previous case.

For what concerning the  $C_T$  the results of the 4 grids are overlapped; their difference with the experimental value decreases while the speeds increases. For the highest speed, indeed, the CFD and EFD are stackable.

The sinkage is well predicted; for all the three speeds, in fact, the results coincide.

In regards to the Trim, the latter shows the worst result of the three. Although the difference between the experimental and the numerical result is not so high, the behaviour showed by the numerical result is slightly different from the one showed by the experimental one. The latter in fact, initially decreases and then increases again. The numerical one, instead, continues to decline, but with a different ratio.

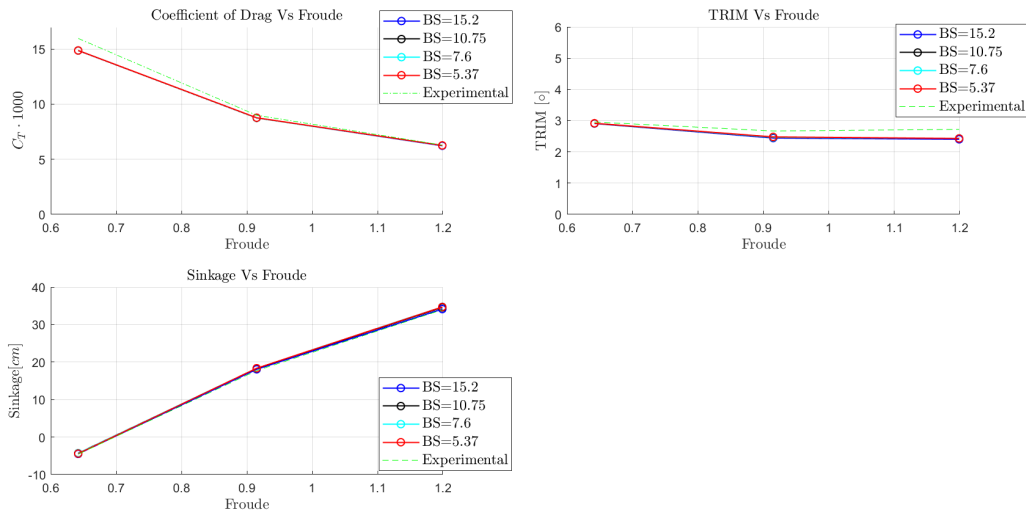


Figure 97:  $C_T$ , trim and sinkage

$Y^+$  Figure 98 is used to check if the  $y^+ = 120$  given as a target was respect by the software when generating the mesh and performing the simulation.

The  $y^+$  has been respected by the software; the  $y^+$  on the hull ranges from a value around 70 to a value around 120 – 130 confirming that we are in the *Logarithmic layer*. In addition could be noted that there are wide areas with the same value because of the presence of large flat areas on the hull.

**Dynamic pressure coefficient** In Figure 99 we can recognise the area characterised by an high pressure coefficient in correspondence of the bow where the stagnation point is located. Besides them, large areas with small or absent curvature characterised by a constant value of the pressure coefficient. A small variation in the  $C_p$  can be noticed in the area close to the stern where the hull exhibits a small curvature; this is where the propeller is allocated.

**VOF** Figure 100 shows the volume fraction of the hull wet by the water (in red).

We can notice that while refining the HRIC is able to capture the free surface in less cells

|       | Grid # | Cells    | $C_T \cdot 1000$ | $E_{C_T}[\%]$ | $Trim[^\circ]$ | $E_{Trim}[\%]$ | $Sinkage[cm]$ | $E_{Sinkage}[\%]$ |
|-------|--------|----------|------------------|---------------|----------------|----------------|---------------|-------------------|
| $V_1$ | EFD    |          | 15.957           |               | 2.956          |                | -4.584        |                   |
|       | 1      | 1821818  | 14.856           | -6.899        | 2.909          | -1.602         | -4.497        | 1.911             |
|       | 2      | 3340871  | 14.859           | -6.880        | 2.913          | -1.443         | -4.292        | 6.369             |
|       | 3      | 6262944  | 14.872           | -6.797        | 2.917          | -1.326         | -4.318        | 5.800             |
|       | 4      | 13353921 | 14.866           | -6.837        | 2.917          | -1.322         | -4.423        | 3.509             |
| $V_2$ | EFD    |          | 8.990            |               | 2.669          |                | 17.709        |                   |
|       | 1      | 1868138  | 8.749            | -2.682        | 2.444          | -8.432         | 18.065        | 2.011             |
|       | 2      | 3438093  | 8.744            | -2.735        | 2.464          | -7.706         | 18.329        | 3.499             |
|       | 3      | 6565170  | 8.753            | -2.634        | 2.469          | -7.519         | 18.355        | 3.644             |
|       | 4      | 14069191 | 8.764            | -2.511        | 2.480          | -7.096         | 18.350        | 3.616             |
| $V_3$ | EFD    |          | 6.286            |               | 2.721          |                | 33.951        |                   |
|       | 1      | 1937850  | 6.223            | -1.004        | 2.404          | -11.656        | 34.135        | 0.540             |
|       | 2      | 3609215  | 6.249            | -0.596        | 2.432          | -10.628        | 34.568        | 1.817             |
|       | 3      | 6974979  | 6.248            | -0.606        | 2.432          | -10.648        | 34.731        | 2.298             |
|       | 4      | 14967654 | 6.254            | -0.501        | 2.430          | -10.701        | 34.695        | 2.190             |

Table 36: EFD and CFD results with comparison error

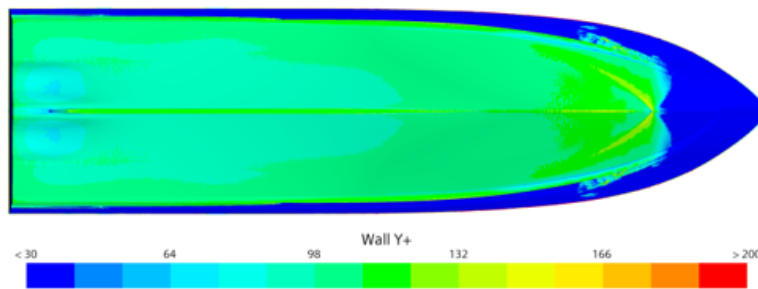


Figure 98:  $Y^+$  on the hull

tending to capture it in only one.

Another thing that can be highlighted is that if focusing on the bow region in figure 100a it is evident that the free surface in that zone is different between the four grids. One explanation for this could be the adoption of the ventilation correction; indeed, this latter is influenced by the Courant number which is in turn influenced by the base size. The different Courant numbers can cause the ventilation correction to act in a different way among the four grids and then not producing a constant result in the air extrapolation which cause a different capture of the free surface.

**Towing tank VS CFD** In figure 101 the picture taken during the towing tank test were placed side by side with two snapshots of the simulation at speed  $V_1$ .

At first, it must be said that the two cases differ by  $0.5 \text{ kn}$  so the conditions showed are not exactly the same. What we can say is that, as we can see in the CFD the spray is not properly captured because it is not the purpose of the settings by CH; therefore, a comparison of the spray between the experimental test and the numerical one cannot be performed because besides the difference in speed, another thing is that the experimental case is in model scale while the numerical one is in Full scale. In section 4 it was stated that in towing tank test is impossible to satisfy all the requirements for a complete hydrodynamic similarity



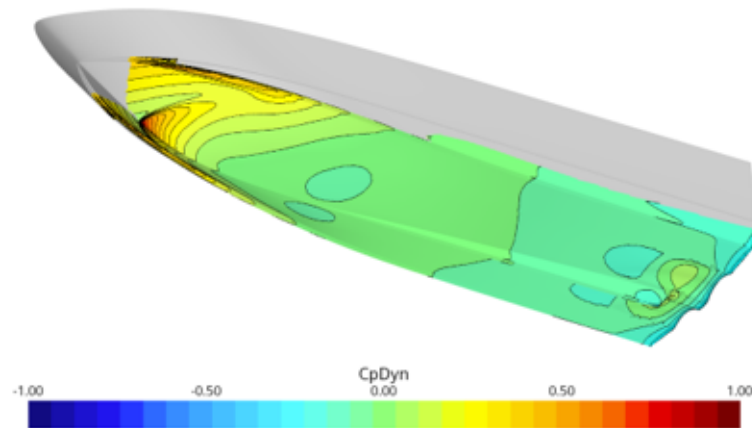


Figure 99: Dynamic pressure coefficient

simulations: due to this, the *Weber number* that regulates the balance between the inertia forces and the surface tension is not the same between the two cases, so this means that the spray and the wave breaking are not the same.

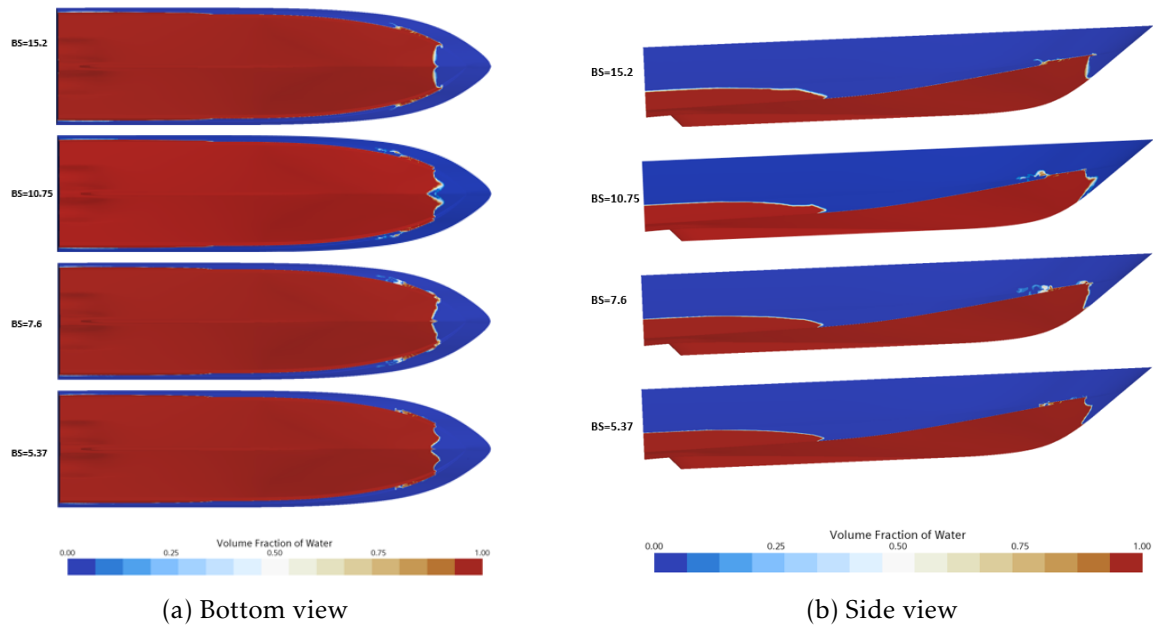
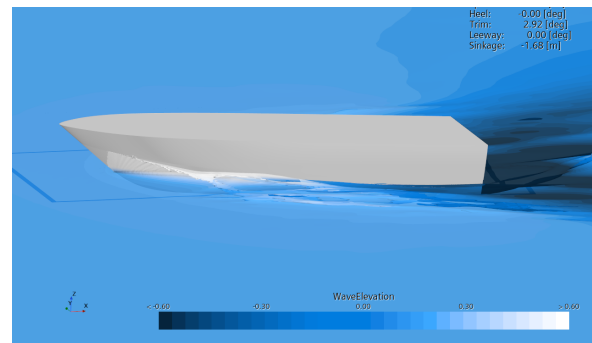


Figure 100: VOF at different grids



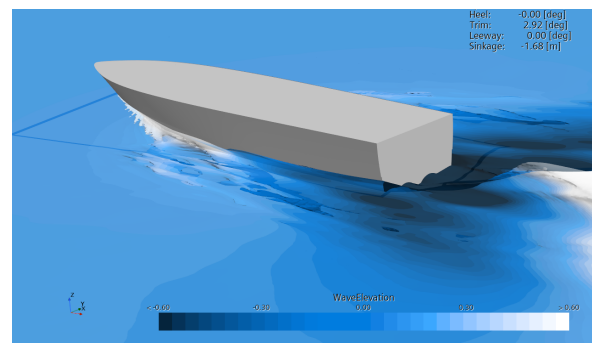
(a) EFD Side view



(b) CFD side view



(c) EFD Back view



(d) CFD back view

Figure 101: Wave pattern experimental (17.5  $Kn$ ) vs CFD ( $V_1 = 18 Kn$ )

## 13.6. Solution Verification

### 13.6.1. Iterative error

Like in earlier cases, in order to consider the iterative error negligible, according to *L.Eça et al* [16], a drop of 2/3 orders of magnitude in the residuals is required. If looking at figures 102a and 102b we can figure out that, although there is a convergence of the residuals, there is not a sufficient drop that can let us retain negligible the iterative error. As a further confirmation there is not a full convergence of sinkage and trim.

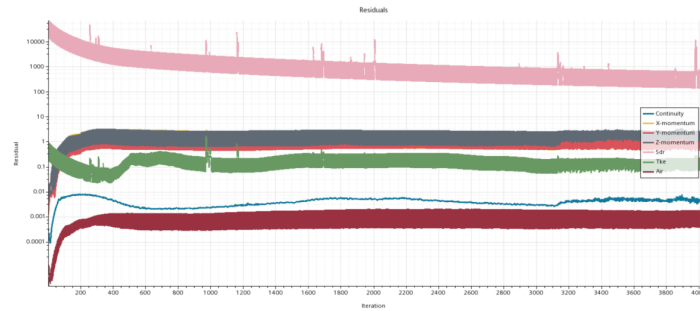
For this reason an iterative uncertainty was quantified; following the procedure laid out by *Yu et al* [24]. The iterative uncertainty has been defined by the following formula:

$$U_I = \frac{RM_{MAX} - RM_{MIN}}{2} \quad (60)$$

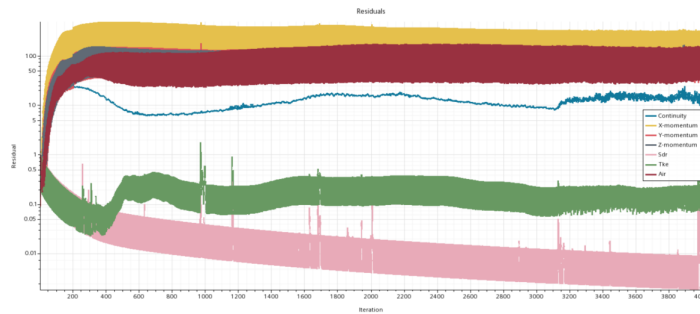
where  $RM_{MAX}$  and  $RM_{MIN}$  are respectively the maximum and the minimum value of the last oscillation of the mean time history. In this case the last 200 time steps were considered.

|           | $U_I[\%]$ |       |       |
|-----------|-----------|-------|-------|
|           | $V_1$     | $V_2$ | $V_3$ |
| $C_T$     | 0.22      | 0.44  | 0.53  |
| $Trim$    | 0.13      | 0.17  | 0.41  |
| $Sinkage$ | 2.63      | 0.15  | 0.28  |

Table 37: Iterative uncertainty as a percentage of the experimental value

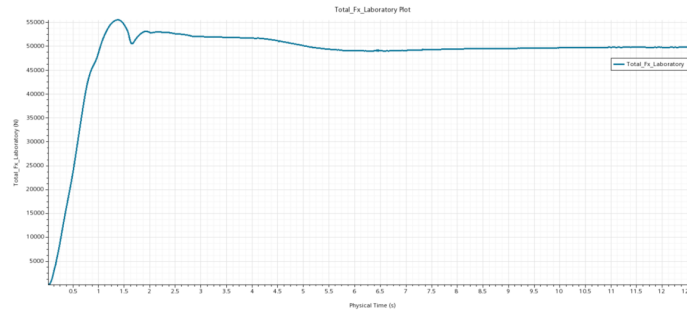


(a) Residuals normalized

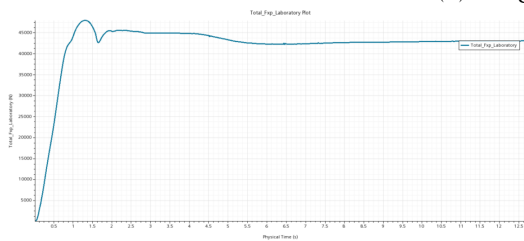


(b) Residuals not normalized

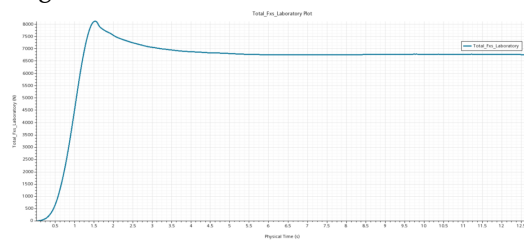
Figure 102: Residuals



(a) Drag convergence

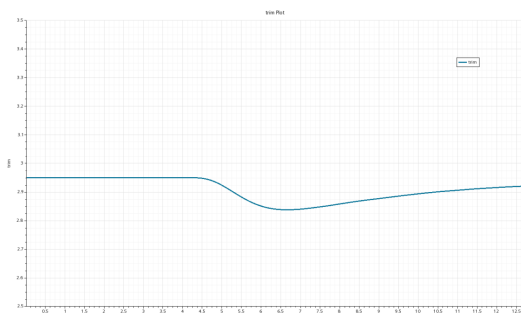


(b) Drag: Pressure component convergence

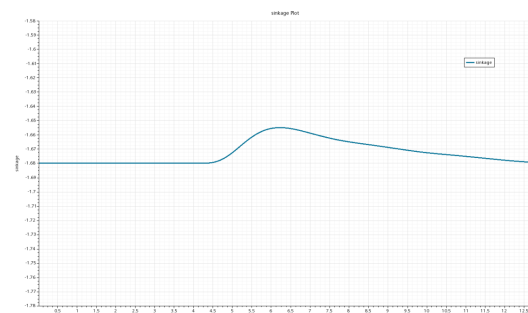


(c) Drag: Shear component convergence

Figure 103: Drag convergence



(a) Trim convergence

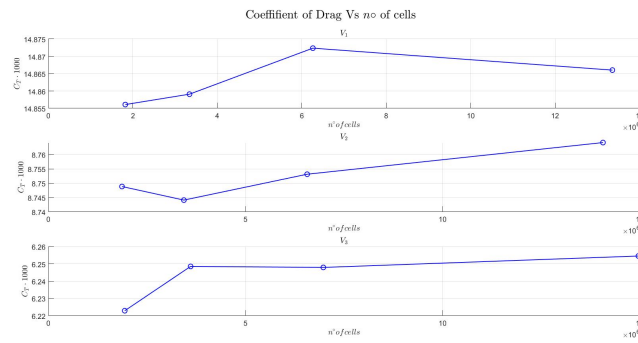


(b) Sinkage convergence

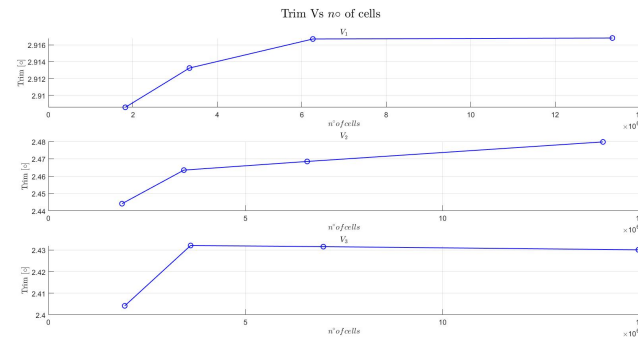
Figure 104: Trim and sinkage convergence

### 13.6.2. Grid convergence study

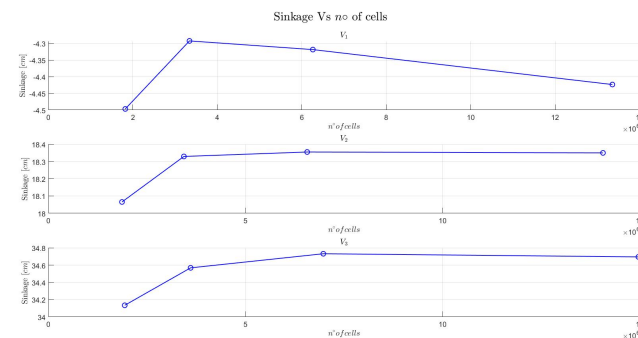
The grid convergence study presented in figures 105a, 105b and 105c shows the good precision of the calculation. It could be noted, in fact, that for  $C_T$  and trim, the solutions in the 4 grids differ for a quantity that is in the order of  $\sim 10^{-2}/10^{-3}$ . If we compare with the ship test case, we can see more often the convergence behaviour typical of the grid convergence study, that reflects the good quality of the data. Nevertheless, there still are anomalous behaviour like sinkage at the lowest speed which initially grows and then starts reducing its value almost linearly. These time this behaviours could be caused by the non complete convergence of the results.



(a)  $C_T$  vs  $n^\circ$  of cells



(b)  $Trim$  vs  $n^\circ$  of cells



(c)  $Sinkage$  vs  $n^\circ$  of cells

Figure 105: Convergence study

### 13.7. Numerical uncertainty calculation

Once that the simulations for all the grids were carried out, the numerical uncertainty was calculated. In this case, taking into account what asserted in section 13.6.1, it's better to refer this time to it as **Grid Uncertainty** considering that the numerical one includes this latter and the iterative one.

$$U_{CFD} = \sqrt{U_I^2 + U_{grid}^2} \quad (61)$$

|       |             | $\phi_0$  | $\phi_1$   | $p$  | $U_{grid}[\%]$ |
|-------|-------------|-----------|------------|------|----------------|
| $V_1$ | $C_T$       | 0.15E-01  | 1.49E-01   | 0.76 | 0.2            |
|       | <i>Trim</i> | 29.20E-01 | 29.20E-01  | 2    | 0.6            |
|       | <i>Sink</i> | -0.6E-01  | -0.432E-01 | 1,2  | 50.1           |
| $V_2$ | $C_T$       | 0.09E-01  | 0.09E-01   | 1,2  | 1.8            |
|       | <i>Trim</i> | 24.90E-01 | 24.70E-01  | 2    | 2.7            |
|       | <i>Sink</i> | 1.72E-01  | 1.84E-01   | 1,2  | 8.3            |
| $V_3$ | $C_T$       | 0.06E-01  | 0.06E-01   | 1,2  | 2.0            |
|       | <i>Trim</i> | 23.00E-01 | 24.30E-01  | 1.2  | 7.6            |
|       | <i>Sink</i> | 3.50E-01  | 3.47E-01   | 2    | 3.5            |

\* 1,2 Fit was made using first and second order exponents

Table 38: Numerical Uncertainty

The results for the grid uncertainty, calculated for grid #3, are showed in table 38.

Except for the sinkage at  $V_1$ , all the uncertainties are under the 10%, this shows the good quality of the results that is confirmed by the fact that more results than the previous test cases presents a polynomial exponent between 0.5 and 2

The high uncertainty showed by the sinkage at the lowest speed may be explained by the not monotonic behaviour of this latter, as showed in figure 105c; this behaviour led to a bad quality of the interpolation that resulted in a high value of the uncertainty.

Figures 106, 107 and 108 show the value interpolated for the grid uncertainty calculation with the latter as an error bar.

### 13.8. Validation

In the end, the validation uncertainty was calculated by taking into account the iterative one, the grid one and the experimental one. This latter was provided by the towing tank that took into account the uncertainty given by:

- *geometry*: assumed negligible;
- *installation* of the instrumentation: assumed negligible;
- *calibration*: considered less than the 0.5%
- *electronic*: amplifiers total system error 0.044% and excitation bridge voltage stability 0.01%;
- *Repeatability*: around 0.5%
- *Carriage speed*: around 0.012%;
- *temperature*  $\pm 0.2^\circ$

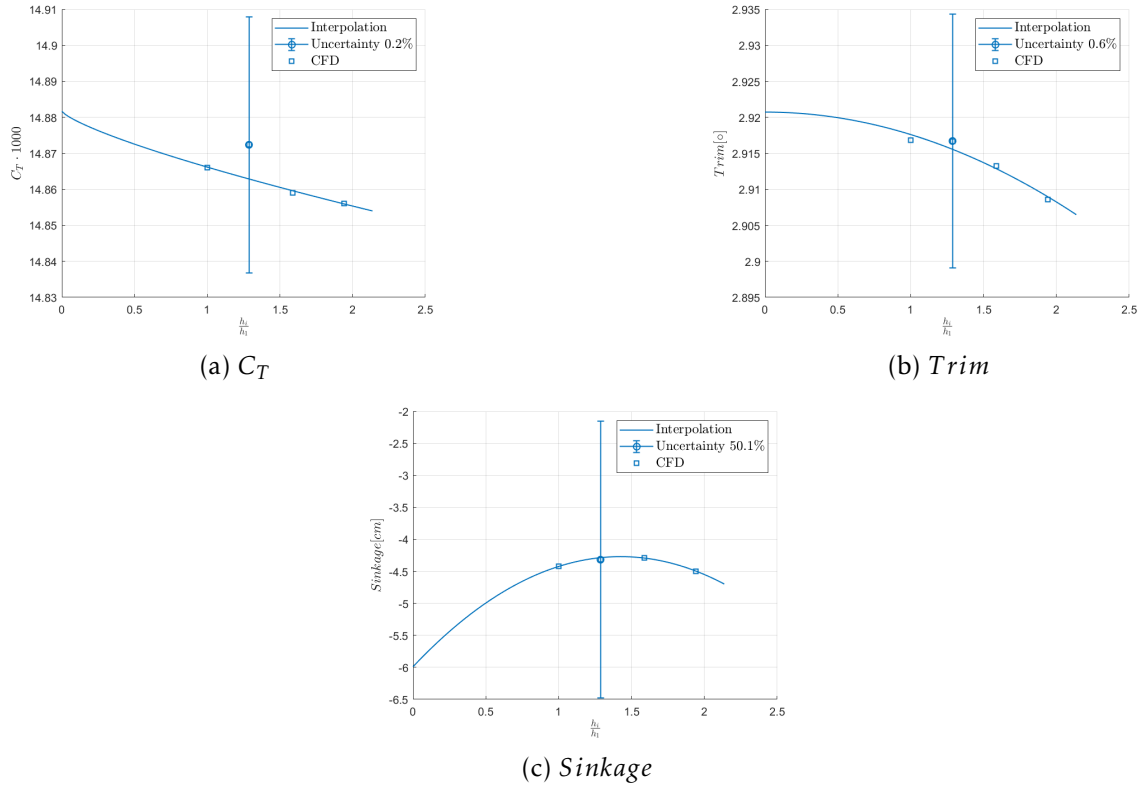


Figure 106: Open water characteristics vs grid refinement with error bar at  $V_1$

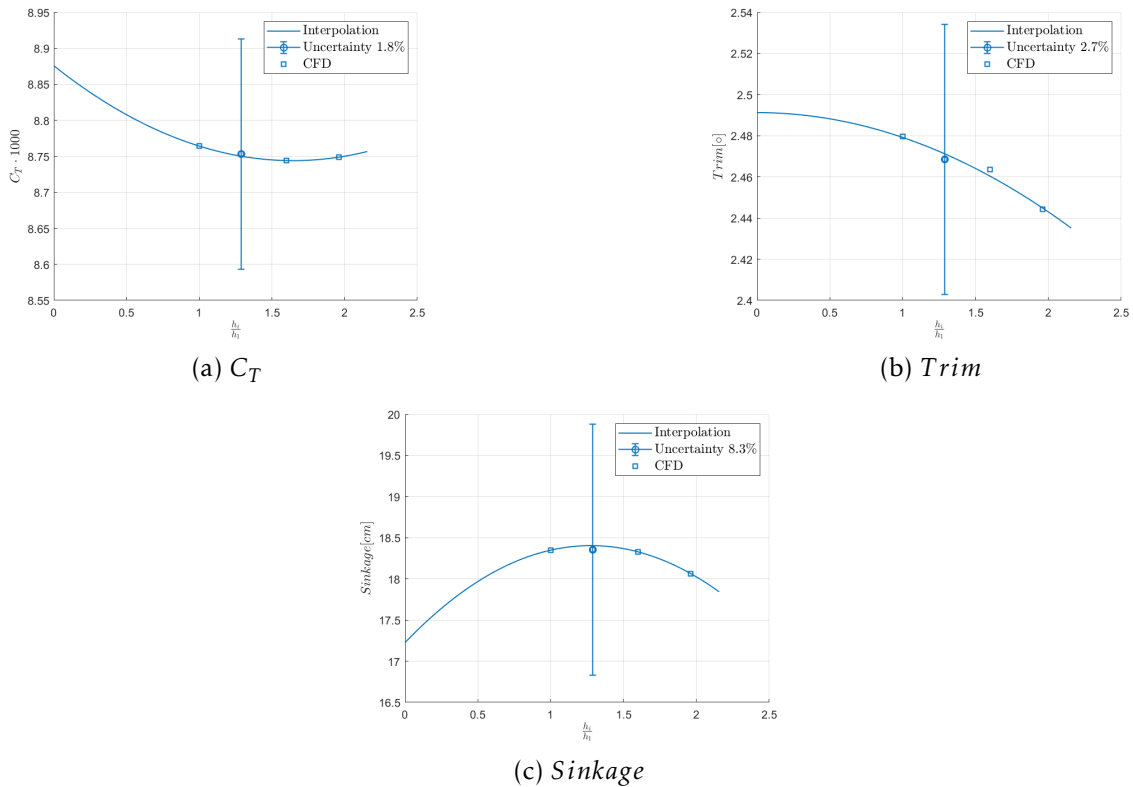


Figure 107: Open water characteristics vs grid refinement with error bar at  $V_2$

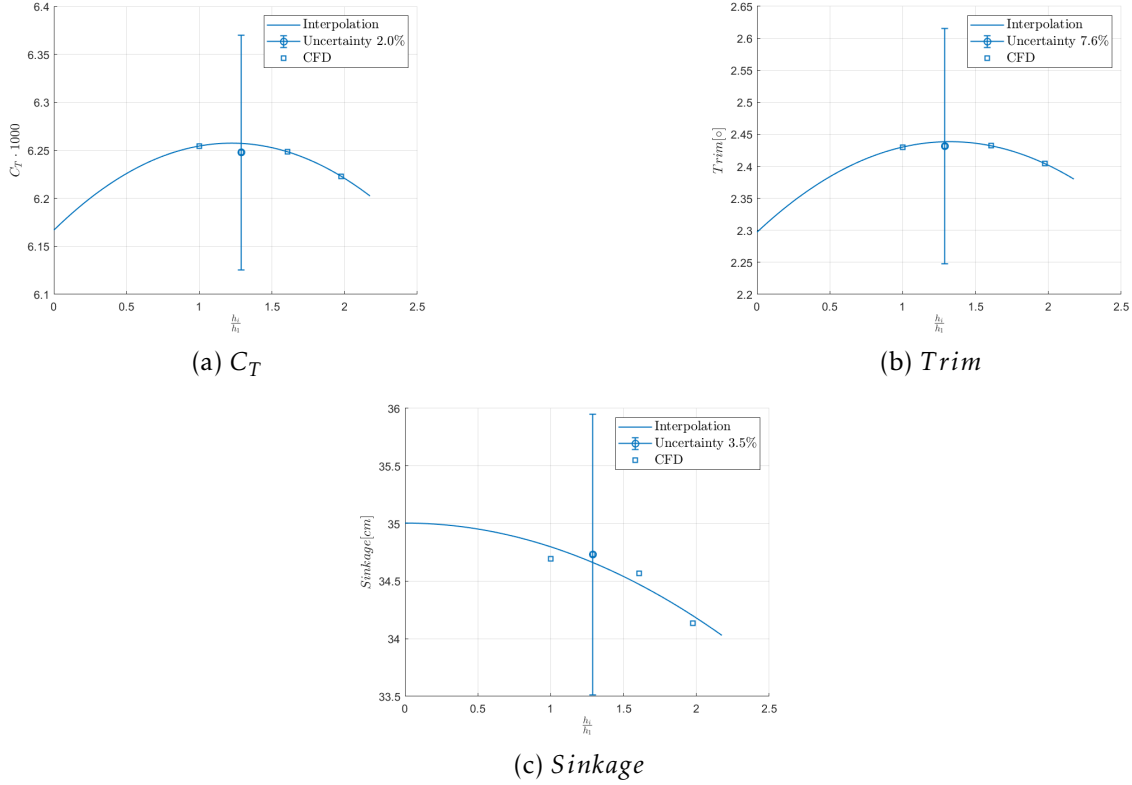


Figure 108: Open water characteristics vs grid refinement with error bar at  $V_3$

To sum up all influential parameters, the resultant uncertainty is between  $\pm 0.5\%$  and  $0.75\%$ . In order to be conservative, the value of  $0.75\%$  was assumed as  $U_{val}$ .

$$U_{Val} = \sqrt{U_I^2 + U_{grid}^2 + U_{EFD}^2} \quad (62)$$

Table 40 show the results of the validation: almost 50% of the results were validated. However, some consideration must be made:

- Although it has been validated, the result for the sinkage at the slowest speed present an high uncertainty that led to not consider reliable the validation; the result is characterized by the presence of the iterative (due to the not full convergence) or the discretisation error ( due to the bad behaviour while refining);
- Among the not validated results, some present a comparison error that is just slightly above the validation uncertainty; in this case, considering also the low value of the uncertainty, it cannot be said that the modelling error is affecting the simulation. For this reason, although these results are not algebraically validated, they are considered reliable.
- The iteration uncertainty has a small impact on the validation uncertainty.

**Conclusion** Considering the above comments and assumptions, the obtained results confirm the validity of the settings used in the prediction of the flow around a planing hull. In order to obtain even better results one could increase the number of maximum time steps



|       |                | $U_I$ [%] | $U_{grid}$ [%] | $U_{EFD}$ [%] | $E$ [%] | $U_{val}$ [%] |
|-------|----------------|-----------|----------------|---------------|---------|---------------|
| $V_1$ | $C_T$          | 0.22      | 0.19           | 0.75          | -6.75   | 0.80          |
|       | <i>Trim</i>    | 0.13      | 0.59           | 0.75          | -1.32   | 0.96          |
|       | <i>Sinkage</i> | 2.63      | 47.20          | 0.75          | -5.81   | 47.20         |
| $V_2$ | $C_T$          | 0.44      | 1.76           | 0.75          | -2.64   | 1.96          |
|       | <i>Trim</i>    | 0.17      | 2.50           | 0.75          | -7.53   | 2.61          |
|       | <i>Sinkage</i> | 0.15      | 8.59           | 0.75          | 3.64    | 8.62          |
| $V_3$ | $C_T$          | 0.53      | 1.99           | 0.75          | -0.61   | 2.19          |
|       | <i>Trim</i>    | 0.41      | 6.80           | 0.75          | -10.70  | 6.85          |
|       | <i>Sinkage</i> | 0.28      | 3.59           | 0.75          | 2.29    | 3.68          |

Values are expressed in percentage of the experimental data

Table 39: Comparison error and validation uncertainty

|                | $V_1$ | $V_2$ | $V_3$ |
|----------------|-------|-------|-------|
| $C_T$          | NV    | NV    | V     |
| <i>Trim</i>    | NV    | NV    | NV    |
| <i>Sinkage</i> | V     | V     | V     |

Table 40: Validation

and/or inner iterations at each time steps in order to be sure to have reached a full convergence of the results. In addition, further improvements (especially for the sinkage) may possibly be obtained by studying the sensitivity of the ventilation correction to the Courant number, the number of prism layer and the hull/free surface refinement.

## 14. Sailing yacht

### SYRF



The mission of the Sailing Yacht Research Foundation is to develop and catalog the science underlying sailboat performance, resulting in more accurate sailboat handicapping formulae for the benefit of all racing sailors. The Foundation serves an international user base of those focused on sailing performance prediction, including naval architects and handicap rule makers. The Foundation supports research efforts using scientific and engineering principles, utilizing the best research facilities and individuals, and reports all findings in public forums. In addition, the Foundation maintains and continuously updates a free-access library of past research, data and papers relevant to the science of performance sailing. The Foundation is sustained through charitable contributions and grants, and its success will be measured by the widespread use and impact of its research, ultimately resulting in fairer yacht racing, which in turn will stimulate more participation.[43]

#### Wide and light project

The “Wide-Light” label is meant to describe the design of the modern high performance sailboats. These so-called Wide-Light boats present many of the hydro-dynamic effects that are a challenge to predict: semi-planing hull forms, immersed transom effects, spray creation, keels operating close to the water surface, rudders, dagger-boards and canting keels that generate vertical force, the list goes on. The complexity of these interacting effects is challenging for the designer and a minefield for yacht handicappers who are obligated to handicap all boats equitably, both new and old.

It is therefore the goal of this project to provide data and conclusions of what might be seen as best practice or state-of-the-art modelling methods so as to better inform and equip handicapping systems and box rules to address Wide-Light designs. Projects such as the Delft Systematic Yacht Hull Series and the nine model series performed at the Canadian National Research Council (NRC) have established the current database of hydrodynamics, but they are no longer representative of today’s racing fleets. This project is the first step toward expanding the public database to include modern yachts.

The Wide-Light project aligns with the SYRF mission to develop and catalogue the science underlying sailing performance and handicapping, by:

1. Publishing an assessment of alternative methodologies to specify and analyze sailing yacht hydrodynamic resistance using computational tools,
2. Making the data available for researchers, and students as an accessible experimental data set for a contemporary sailing yacht, and
3. Demonstrating how this type of study can be used to inform the handicapping process. It is expected that the project will also be particularly valuable for academics as it will allow students, researchers and lecturers to frame new research projects most effectively.

### 14.1. Experimental Tests

#### MODEL M1108

Tests were carried out on a Mini Maxi style model hull with and without appendages to produce a set of data to be used as a comparative benchmark for the SYRF computational fluid dynamics (CFD) studies undertaken.

A previously tested model canoe body was donated to the project (as arranged by SYRF). This hull was modified to lines supplied by SYRF, re-faired to CNC manufactured templates, painted and marked up. The model was re-commissioned for testing and fitted with a keel fin and bulb and a movable single rudder that had already been used previously. The model was designated Wolfson Unit model number M1108. The 3D CAD geometry is showed in figure 109 and the main characteristics are presented in table 41. The drawing of the waterlines is reported in appendix E.

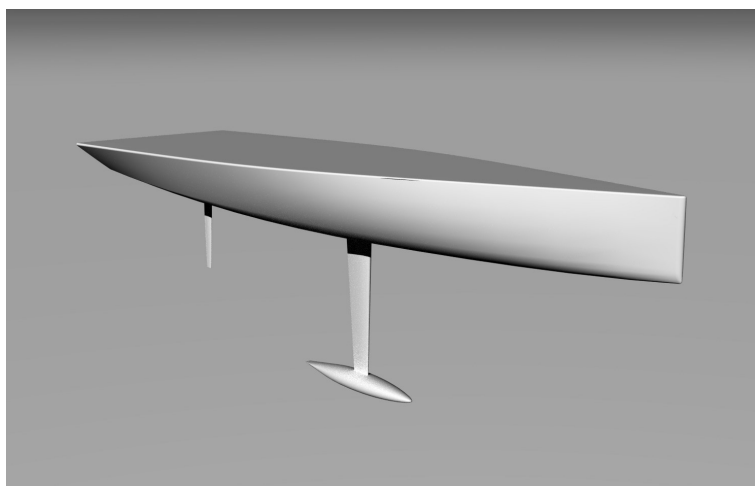


Figure 109: M-1108 geometry

The ship tank at QinetiQ, Haslar, Gosport was used for the tests; the tank is 12 *m* wide *x* 5.5 *m* deep *x* 270 *m* long. The model was towed using a purpose designed 3-post sailing yacht test dynamometer which allowed the model freedom to heave and pitch, but provided restraint in yaw, sway and roll. The tow system longitudinal centre was mounted at the equivalent of 2.400 *m* aft of the hull datum DWL (forward most tip of bow). The dynamometer vertical centre was 0.172 *m* above DWL. Figure 110.

In the upright condition, measurements were made of resistance, trim (+ bow up) and heave

| M1108                     |        |
|---------------------------|--------|
| Overall length            | 4.88 m |
| $L_{WL}$                  | 4.6 m  |
| Displacement (appended)   | 215 kg |
| Displacement (canoe body) | 197 kg |
| Maximum beam              | 1.28 m |
| Draft to datum            | 1.15 m |
| LCG                       | 2.44   |
| VCG                       | 0      |

Table 41: W&L M-1108 Characteristics

(+ up) at the tow point. An uncertainty analysis (broadly based on ITTC procedure 7.5-02-02-02) summarising the measurement of resistance in this condition at 3 speed settings is presented in Table 50 in appendix E. The axis system for the displacements, rotations, forces and moments were then converted to the same axis system as adopted in the associated CFD studies.

The **longitudinal datum** is the forward most extent of the hull; **transverse datum** is on the vessel centreline and the **vertical datum** is DWL.

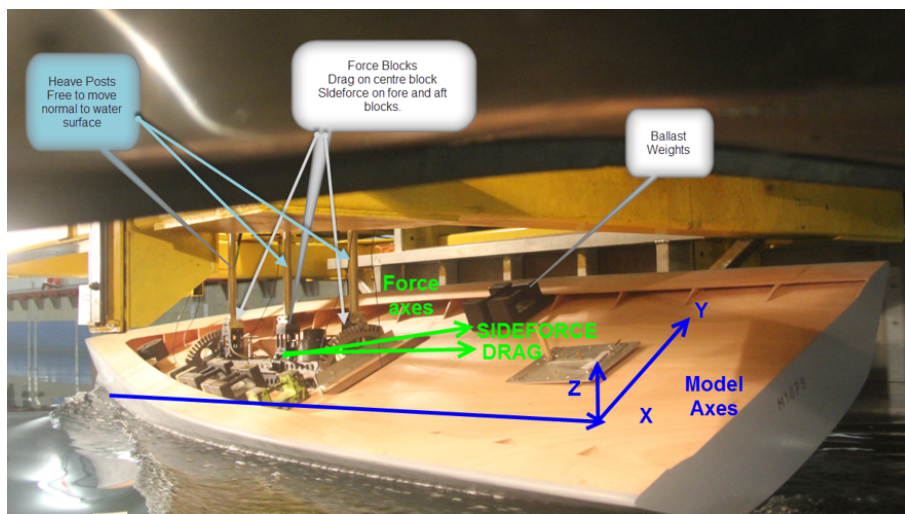


Figure 110: Model Test Set Up

At the time of test the model was ballasted to the specified displacement and trimmed to float parallel to DWL. For each test, a trim moment was applied that equated to the change in LCG outlined in the SYRF run schedule.

The following measurements were taken:

- $F_X$  - Drag (N); parallel to boat track axis, parallel to the waterplane, positive in the aft direction;
- $F_Y$  - Sideforce (N); perpendicular to boat track axis, parallel to the waterplane, positive to port;
- $F_Z$  - Heave (m); vertical displacement, parallel to the waterplane measured at 2.484 m

aft of datum referenced to the static zero speed and LCG condition, positive upwards;

- $M_X$  - Roll moment ( $N \cdot m$ ); moment in  $YZ$  plane, at datum vertical height, positive clockwise when viewed from astern;
- $M_Y$  - Pitch ( $^\circ$ ); angular rotation in  $XZ$  plane, referenced to the static zero speed and LCG condition, positive bow up;
- $M_Z$  - Yaw moment ( $N \cdot m$ ); moment in  $XY$  plane measured at 2.484 m aft of datum, positive anticlockwise when viewed from above.

Measurements were also made of the **wave height** within the wake at a position 970 mm aft of the transom on the tank centreline (on vessel centreline with zero leeway) using a sonic wave measuring device.

#### Turbulent stimulator

To ensure consistent model boundary layer conditions, the model was fitted with turbulence inducing studs (3.2 mm diameter and 2.5 mm high). These were located at 25 mm spacing around a section girth at 300 mm aft of datum. The appendages were in their previously tested condition. The bulb used a carborundum grain strip at 20% of the chord length. The keel fin and rudder were fitted with smaller studs (1 mm diameter and 0.7 mm high) with 10 mm spacing at 25% of the chord length. The model elements resistance data were corrected to allow for the resistance of these studs and for the region of laminar flow ahead of them. Figures 137 and 138 show the model under test in the Upright position.

### 14.2. Benchmarking conditions

Among the fifteen speeds at which the boat was tested, three of them were chosen in order to carry out the benchmarking, they are reported in table 42. The configuration chosen was the one **Appended** and at **Full Scale**

| Index                     | Froude number                            | Reynolds number    | Speed [m/s] | Sinkage [cm] | Trim[°] | LCG [m] |
|---------------------------|--|--------------------|-------------|--------------|---------|---------|
| $V_1$                     | 0.10                                     | $2.92 \cdot 10^6$  | 0.68        | 0.0          | 0.02    | 2.39    |
| $V_2$                     | 0.45                                     | $13.10 \cdot 10^6$ | 3.07        | -2.0         | 0.29    | 2.51    |
| $V_3$                     | 0.80                                     | $23.30 \cdot 10^6$ | 5.45        | -2.5         | 1.20    | 2.75    |
| Density $\rho$            | 999.1 kg/m <sup>3</sup>                  |                    |             |              |         |         |
| Kinematic viscosity $\nu$ | $1.14 \cdot 10^{-6} \text{m}^2/\text{s}$ |                    |             |              |         |         |

$\rho$  and  $\nu$  are calculated based on a fresh water temperature of 15°

Table 42: Benchmarking conditions

### 14.3. CFD

#### 14.3.1. Initial tests

Once the test condition were defined, the numerical simulations for the sailing yacht were performed.

The settings used were the same used for the planing hull, both in the mesh strategy, with adoption of the Overset grid and in the physical models with the  $k - \omega$  SST and the *DFBI free motion*.

Unexpectedly the solutions obtained were numerically unstable, with the boat starts oscillating after the **2Dof** was released, figure 111.

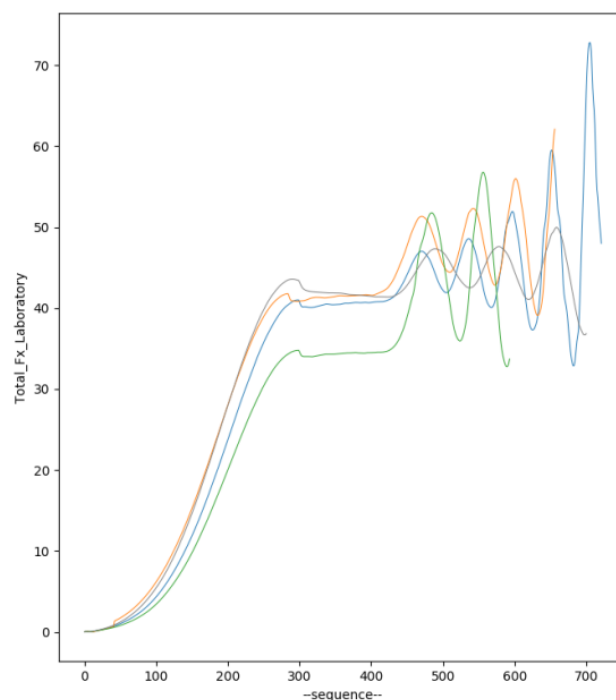


Figure 111: Unstable simulations

Few attempts were done by changing some parameters but no improvements were detected. For this reason a set of new settings were tested in this case study.

### 14.3.2. Geometry

The initial hull geometry provided by the *SYRF* presented many problems in particular at the bow that did not let it be meshed. In figure 112c can be see that the two surfaces the were constituting the hull surface presented a gap between them.

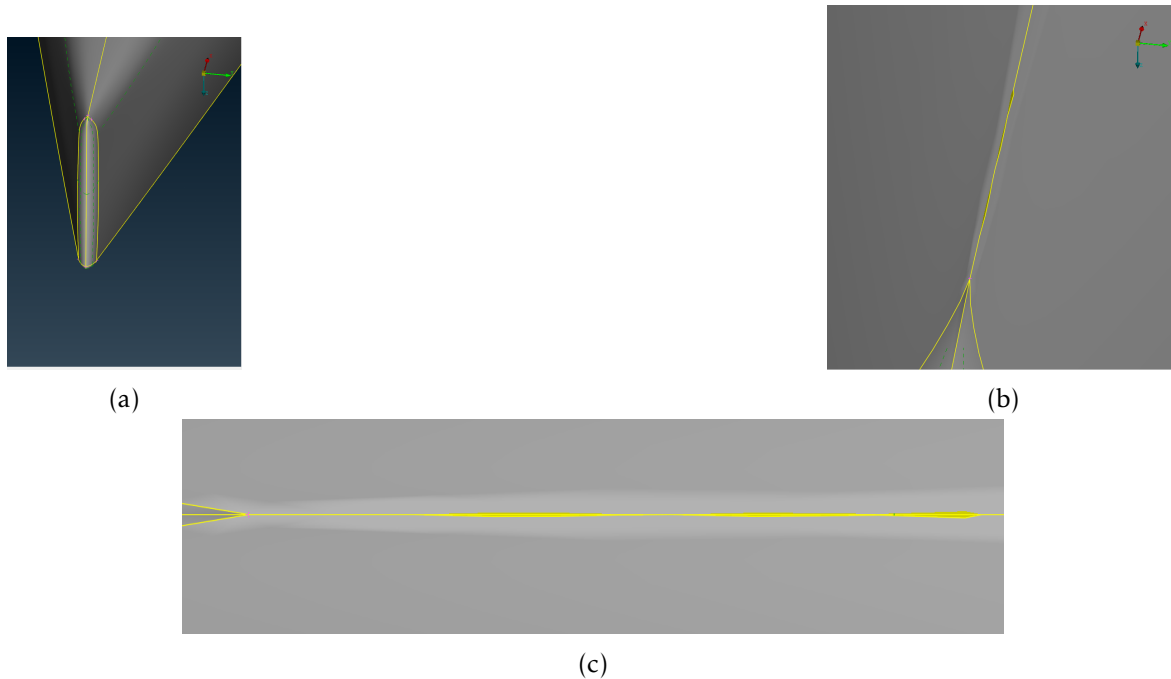


Figure 112: Geometry problem

The problem just showed was solved by reconstructing the entire hull surface and by modifying the geometry above the waterline in order not to influence too much the boat's hydrostatics. In figure 113 different views of the new hull are presented.

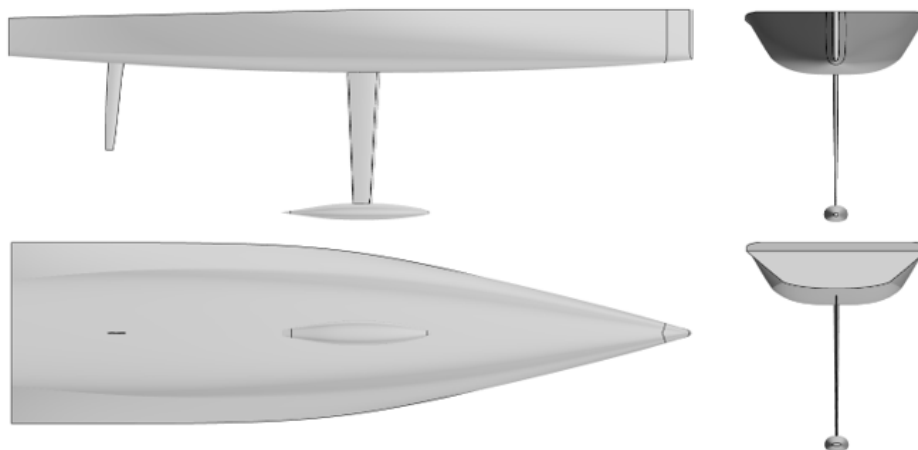


Figure 113: New geometry appended

The hydrostatics of the new hull were calculated and are reported in table 43 together with the one of the previous hull.

Rudder, daggerboard and bulb remained unchanged.

| Characteristics                 | SYRF Geometry                    | Repaired geometry    |
|---------------------------------|----------------------------------|----------------------|
| $L_{OA}$                        | 4.88 m                           | 4.88                 |
| $L_{WL}$                        | 4.6 m                            | 4.6 m                |
| Beam, maximum section area beam | 1.28 m                           | 1.28 m               |
| Draught to datum                | 1.15 m                           | 1.15 m               |
| Displacement volume             |                                  | 0.181 m <sup>3</sup> |
| Displacement mass appended hull | 215 kg                           | 215 kg               |
| Wetted Area                     |                                  | 3.882 m <sup>2</sup> |
| LCG                             | 2.484 m from datum               | 2.484 m from datum   |
| LCB                             |                                  | 2.456 m from datum   |
| VCG                             | 0 m                              | 0 m                  |
| VCB                             |                                  | 0.104 m              |
| Block coefficient ( $C_b$ )     |                                  | 0.039                |
| $I_{xx}$                        | $5.64 \cdot 10^4 \text{ kg m}^2$ |                      |
| $I_{yy}$                        | $3.20 \cdot 10^5 \text{ kg m}^2$ |                      |
| $I_{zz}$                        | $3.20 \cdot 10^5 \text{ kg m}^2$ |                      |

Table 43: Hydrostatics old and new hull

**Coordinate System (CSys)** In these new settings, the approach used for the coordinate systems was different. Figure 114a shows the initial set up of the coordinate systems. In **blue** there is the laboratory that coincides with the CAD coordinate system in **red** which are located longitudinally in most forward point of the hull and vertically at the waterline; in **black** the CoG coordinate system.

The boat was moved in order to have the Lab CSys longitudinally at the stern of the hull and vertically at the baseline, than it was rotated to have the  $x$  axes of the Lab CSys pointing forward and the  $y$  axes pointing to the port direction.

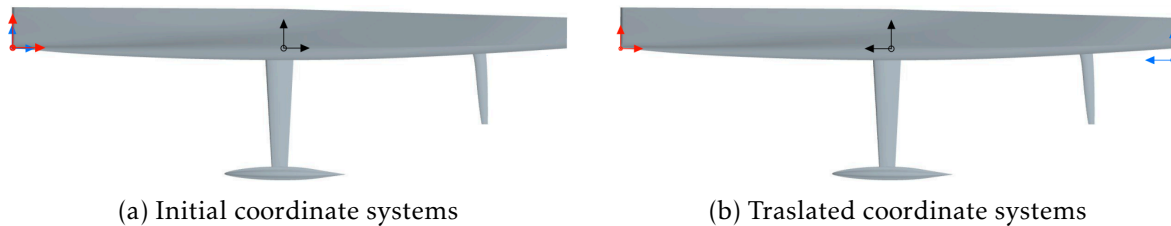


Figure 114: Coordinate systems

**Computational Domain** In the new setting also the computational domain, showed in figure 115, undergone few modifications in the dimensions; it is generally tighter than the previous one. Nevertheless it still respects the *ITTC* regulations. Due to the symmetry in the geometry and in the conditions applied, also in this case only **half of the domain** was simulated.

**Refinement Volumes** The kelvin wake and the free surface refinements didn't change a lot. They are still based on three consecutive blocks in which, later, the mesh will be finer as the refinement box become smaller.

A quite difference concerns the hull refinements. This time, there a lot of volumetric blocks



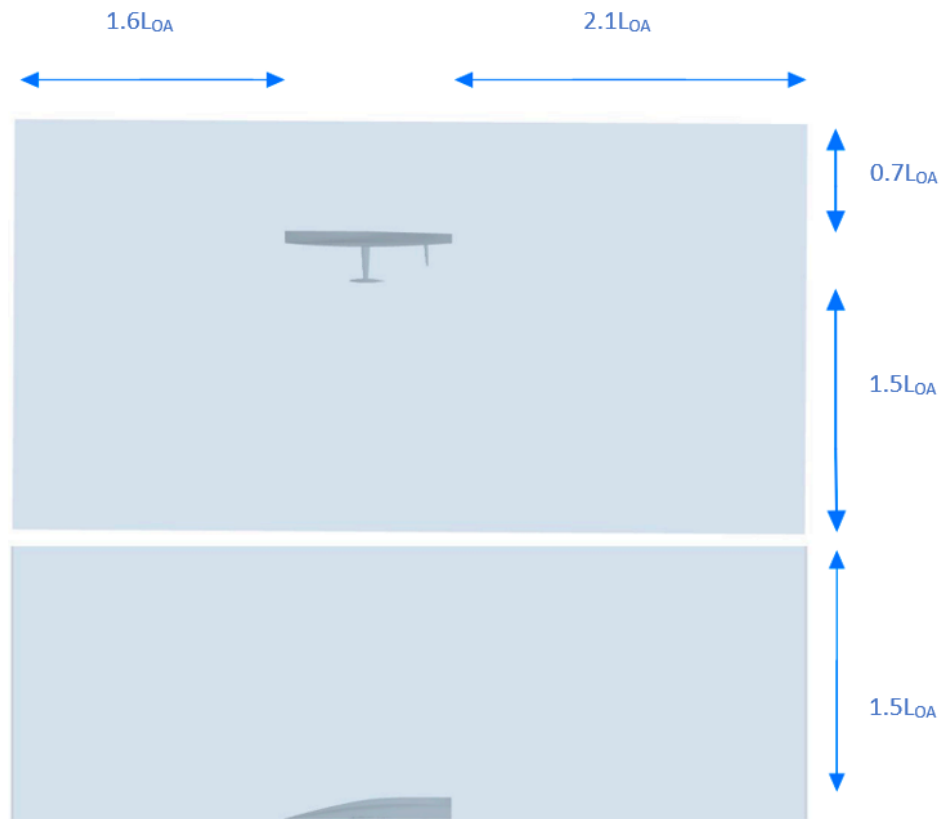
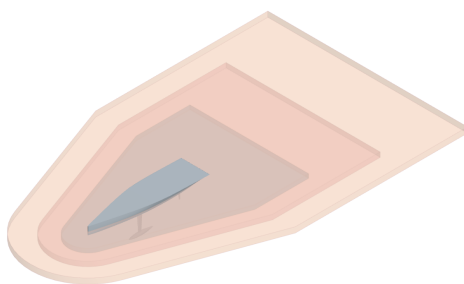
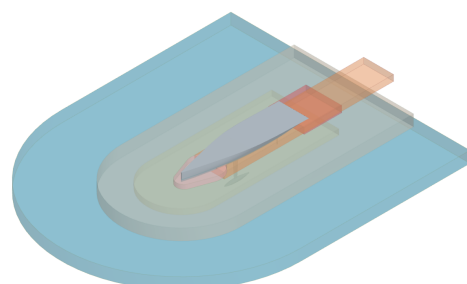


Figure 115: New domain dimensions

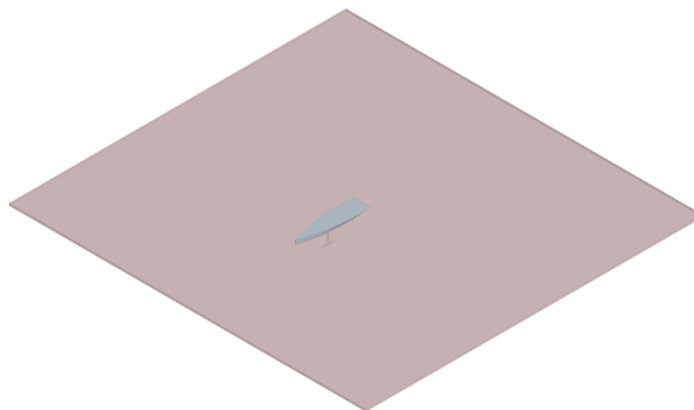
around the hull. One is designed to capture the flow field close to the bow, two of them are designed to capture the wave created at the stern, the remaining are designed to capture the flow field around the hull.



(a) Kelvin refinements



(b) Hull refinements



(c) Free surface refinements

Figure 116: Volumetric Refinements

### 14.3.3. Mesh

After the geometry set up it was time for meshing.

With this new method a new approach to mesh was implemented, the **Multi Mesh Sequencing** (MMS). The basic idea behind this method is to define a number of sequences, i.e. how many times, we want to refine the mesh; in this case a value of 5 was chosen. After that, we define a target base size, that for each grid is reported in table 44; subsequently a *counter* is set and with the use of the following formula

$$\text{Current mesh base size} = \text{Target Base Size} \cdot \sqrt{2}^{\text{Sequence}-\text{Counter}} \quad (63)$$

a routine is launched. The latter consists in meshing and solving the flow fields a number of times equal to the *sequencies* defined previously. After each sequence the mesh will be more and more refined (and with more cells) until we reach the target base size.

| Grid number | Base size | $n^\circ$ Cells  |
|-------------|-----------|------------------|
| #1          | 0.244     | $1.2 \cdot 10^6$ |
| #2          | 0.172     | $2.3 \cdot 10^6$ |
| #3          | 0.1219    | $4.7 \cdot 10^6$ |
| #4          | 0.0862    | $11 \cdot 10^6$  |

Table 44:  $n^\circ$  of cells per base size

In figure 117 the mesh of the yacht appended is showed.

As for the case of the planing hull, the hull is not so refined because of the presence of wide areas with low curvature, therefore low pressure and speed gradient.

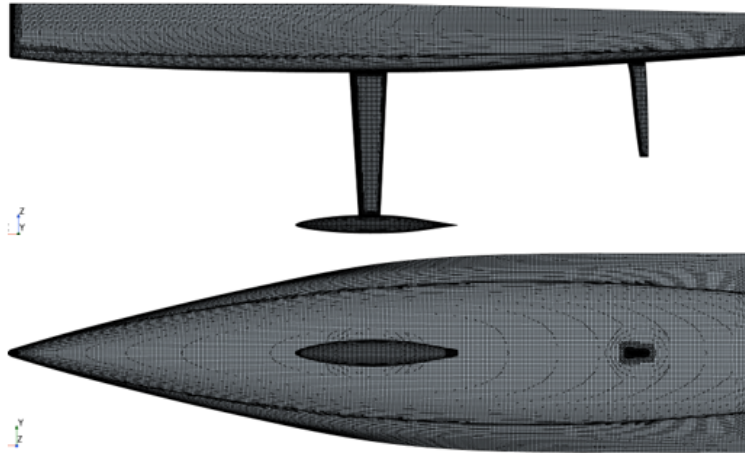


Figure 117: Hull mesh

These high gradients are present instead in the proximity of the bow and around the appendages; for this reason, as we can see in figure 118, the bow, the leading and trailing edges together with the intersections were all refined.

This time the  $Y^+$  target value was reduced to 100.

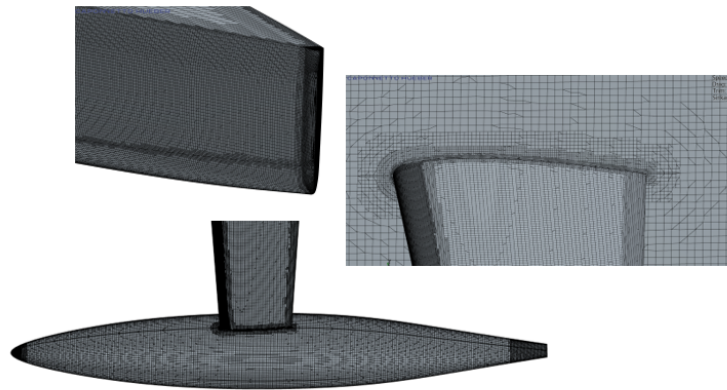


Figure 118: Hull mesh details

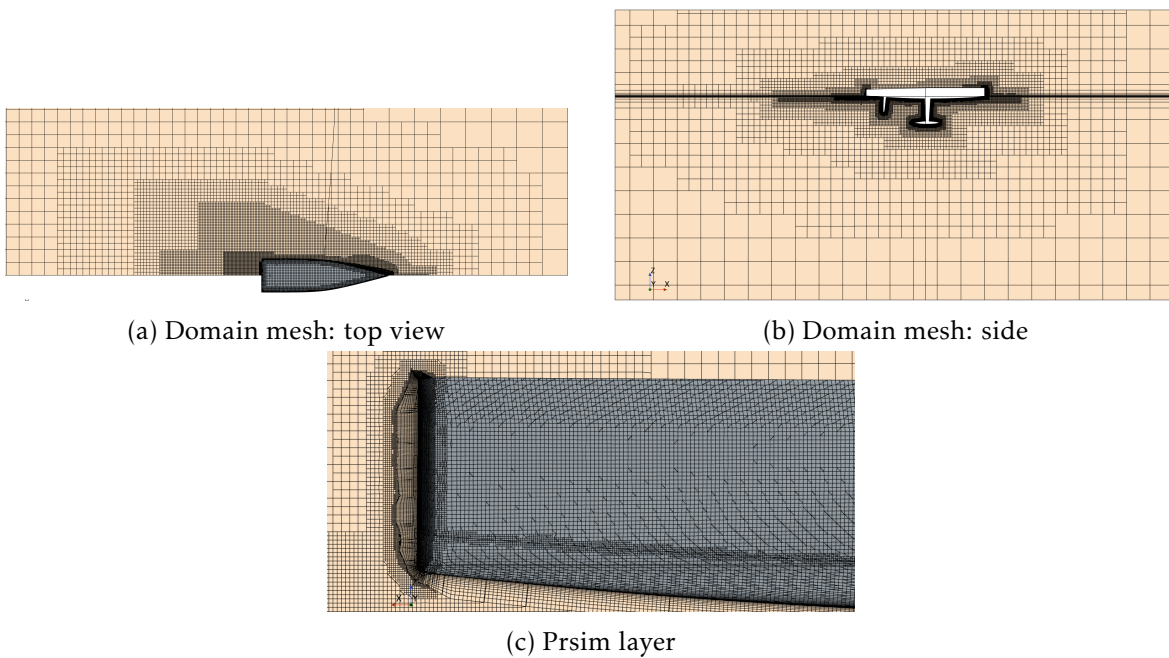


Figure 119: Domain and prism layer mesh

#### 14.3.4. Physical Setup

The physical settings were not so different from the one previously used by CH.

**Dynamic Model** This time, considering that the sailing boat's speed was not so high, the *Equilibrium* option for the DFBI model was chosen with **2Dof**. Due to the presence of the MMS, alongside the equilibrium model, the **DFBI mesh morpher** model was activated. Morphing is a mesh method which displaces mesh vertices according to the motion of boundaries or regions. The Morphing motion in STAR-CCM+ redistributes mesh vertices in response to the movement of a set of control points, which you can consider as being a cloud of points overlaid onto the mesh domain. Control points, and their associated displacements, form the underlying framework that the morpher requires to generate an interpolation field. The DFBI Morphing motion is a variant of the Morphing motion that is used for DFBI (Dynamic Fluid Body Interaction). It activates customized boundary conditions so that you can use morphing in DFBI without making time-consuming adjustments, *Star CCM+ User Guide* [13].

**Towing force** Considering what stated in section 14.1 regarding the variation of the CoG, in order to take in to account of the sail trim moment, **no towing force was applied**.

**Time step** Instead of using the Hyperbolic formula influenced by the flow speed as for the previous cases, this time a new approach has been followed. Initially a convection time scale is calculated

$$t_c = L_{OA}/V \quad (64)$$

where  $L_{OA}$  is the length overall of the boat and  $V$  is the flow speed. Subsequently the time step is defined by choosing the minimum between

$$t_c/50 \quad \text{and} \quad \frac{t_c}{100 * \sqrt{2}^{Sequences-counter}} \quad (65)$$

**Boundary conditions** In figure 120 could be noted that the boundary condition are the same as for the previous cases.

**Initial Conditions** At the beginning the speed was set at the inlet equal to the one chosen for the test case and the boat was positioned horizontal on the water (no initial trim) and without initial sinkage.

In table 45 the new physical settings are summarised.

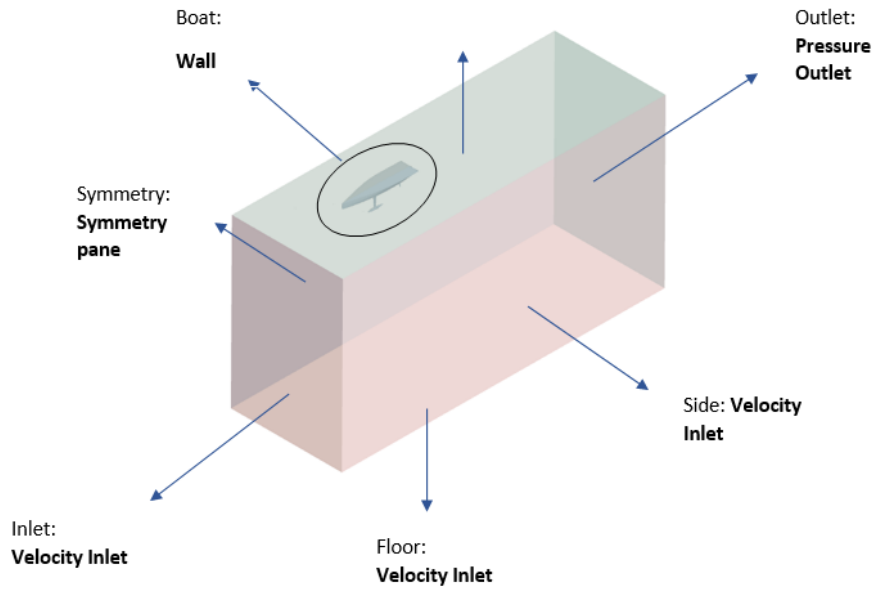


Figure 120: Computational boundaries

| Parameter                   | Solver setting  |
|-----------------------------|---|
| Solver                      | 3D segregated, constant density                         |
| Time                        | Implicit unsteady, 1 <sup>st</sup> order discretisation |
| Turbulence model            | <i>RANS <math>k - \omega</math> SST</i> [34]            |
| Convection Scheme           | 2nd Order upwind  |
| Finite Approximation Scheme | Finite Volume   |
| Computational Model         | Multiphase <i>VOF</i> , Vof flat wave                   |
|                             | <i>VOF</i> Wave Zone distance                           |
|                             | <i>HRIC</i>   |
| Boundary layer treatment    | all $y^+$ treatment (section 9.4.8)                     |
| Dynamic Model               | <i>DFBI equilibrium</i> and mesh Morpher:RBF            |

Table 45: Computational Model Setup

### 14.3.5. Results

**Drag, Sinkage, Trim** This new settings adopted by CH, seems to be reliable in the prediction of the behaviour of Drag and trim, the same cannot be said for the sinkage. The numerical results of the latter in fact, show a substantial difference both in the absolute value and in the trend. The experimental values show a monotonic increase in absolute value of the sinkage while the numerical results predicts a an initial increasing and then a decreasing in modulus. As we will see in the following, also for Drag and trim the difference in modulus is not negligible, especially at high speed.

A possible explanation for this is the transition from a displacement configuration to a planing one for which the *DFBI equilibrium* model is not properly suited.

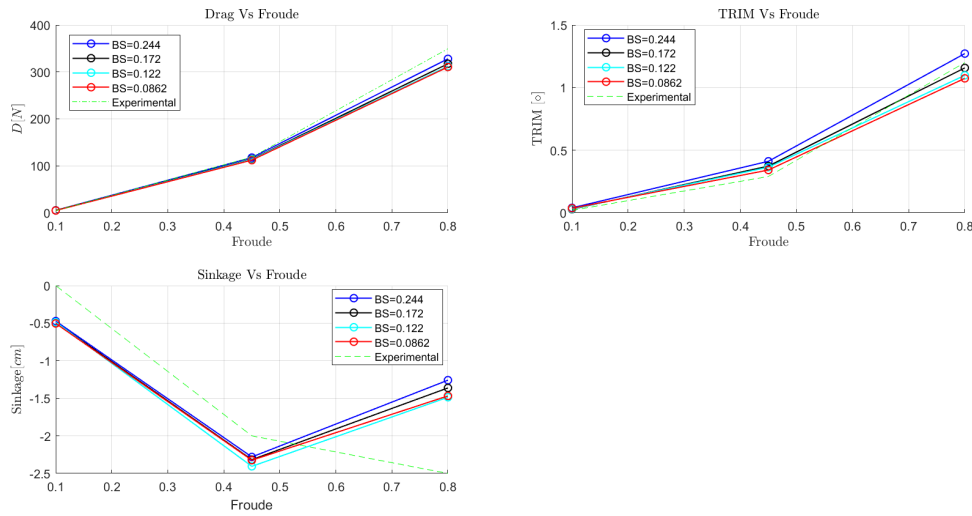


Figure 121: Drag, Trim and Sinkage

|       | Grid # | Cells    | Drag    | $E_{Drag}[\%]$ | Trim[°] | $E_{Trim}[\%]$ | Sinkage[cm] | $E_{Sinkage}[\%]$ |
|-------|--------|----------|---------|----------------|---------|----------------|-------------|-------------------|
| $V_1$ | EFD    |          | 4.560   |                | 0.02    |                | 0           |                   |
|       | 1      | 1118222  | 5.277   | 15.721         | 0.040   | 98.243         | -0.472      | ND                |
|       | 2      | 2060891  | 5.102   | 11.896         | 0.029   | 43.031         | -0.490      | ND                |
|       | 3      | 3921104  | 4.788   | 5.003          | 0.031   | 55.548         | -0.486      | ND                |
|       | 4      | 8126351  | 4.886   | 7.152          | 0.036   | 82.119         | -0.503      | ND                |
| $V_2$ | EFD    |          | 118.570 |                | 0.290   |                | -2.000      |                   |
|       | 1      | 1176194  | 117.618 | -0.803         | 0.411   | 41.859         | -2.281      | -12.312           |
|       | 2      | 2304478  | 114.305 | -3.597         | 0.373   | 28.663         | -2.317      | -13.669           |
|       | 3      | 4726558  | 113.515 | -4.264         | 0.364   | 25.502         | -2.406      | -16.862           |
|       | 4      | 10451227 | 112.210 | -5.364         | 0.342   | 17.803         | -2.324      | -13.938           |
| $V_3$ | EFD    |          | 349.380 |                | 1.200   |                | -2.500      |                   |
|       | 1      | 1231175  | 327.933 | -6.139         | 1.272   | 5.969          | -1.259      | 98.632            |
|       | 2      | 2473067  | 317.399 | -9.154         | 1.157   | -3.558         | -1.362      | 83.572            |
|       | 3      | 5297072  | 312.212 | -10.638        | 1.098   | -8.521         | -1.486      | 68.251            |
|       | 4      | 12194100 | 310.567 | -11.109        | 1.074   | -10.509        | -1.468      | 70.295            |

Table 46: EFD and CFD with comparison error

**$y^+$**  During the mesh phase, the target  $y^+$  value was set equal to 100. In figure 123 the plot on the hull and appendages is shown. The value averagely achieved that lies between 70 and 80 is satisfactory; the hull first cell height lies entirely in the logarithmic layer. Concerning the appendages, the latter lies in the logarithmic layer as well, except for the leading and the trailing for which the value belongs to the Buffer layer. The appendages, due to the size and the high curvature, especially along the leading and trailing edge, are characterized by a small cells size, this leads to a failure by the mesher to achieve a first cell height equal to the target one. As a consequence a smaller  $y^+$  is achieved.

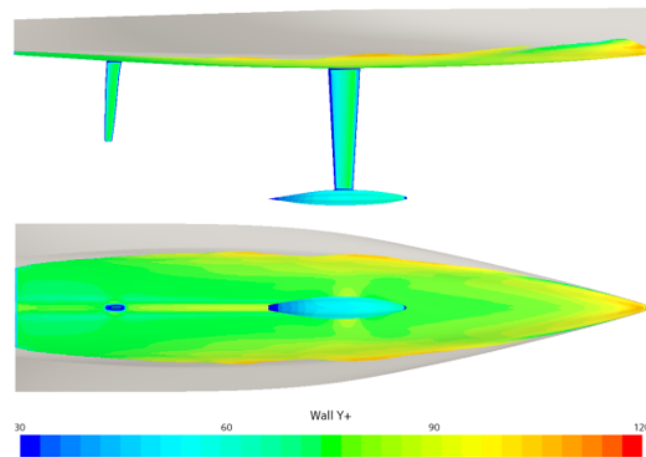


Figure 122:  $y^+$  on the Hull

**Dynamic pressure coefficient** The pressure distribution confirms the assumption made during the meshing phase: the wide and flat hull shape is characterized by a pressure distribution almost constant. At the center of the hull the flow field manages to recover the pressure of the free stream. An higher value is found in proximity of the bow where the curvature is higher. Obviously, the appendages are characterised by a fast variation of the pressure due to the higher curvature and the small length.

**VOF** In figure 124 the volume of water that wets the hull is represented this time against the three speeds. It is evident the change in shape and in size of the wetted surface as soon as the speed increases. At the slowest speed the sailing yacht is characterized by a displacement motion with the shape of the wetted surface that resembles the one of the ship: the same curved shape could be found close to the stern.

When the speed increases the bow starts to rise from the free surface and the planing regime initiates. The wetted area has no the displacement shape anymore, it reaches the edge of the stern and reduces as the speed increases.

**Wave Pattern** What just said about the wetted surface it is even more evident in figure 125. As the boat speed increases the height of the waves produced by the hull increases greatly and again the bow rises above the water surface.



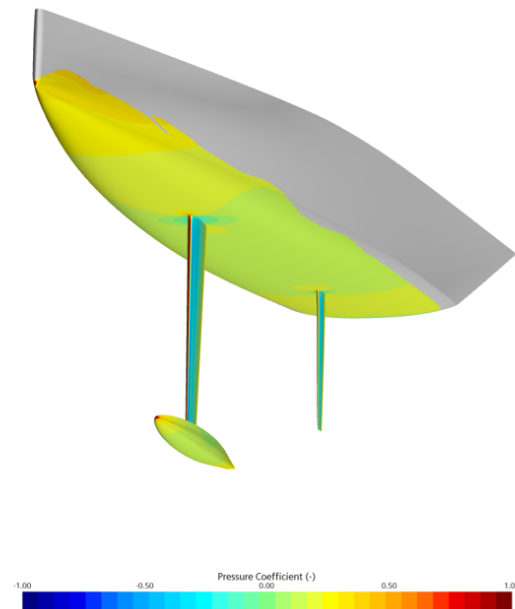


Figure 123: Dynamic pressure Coefficient

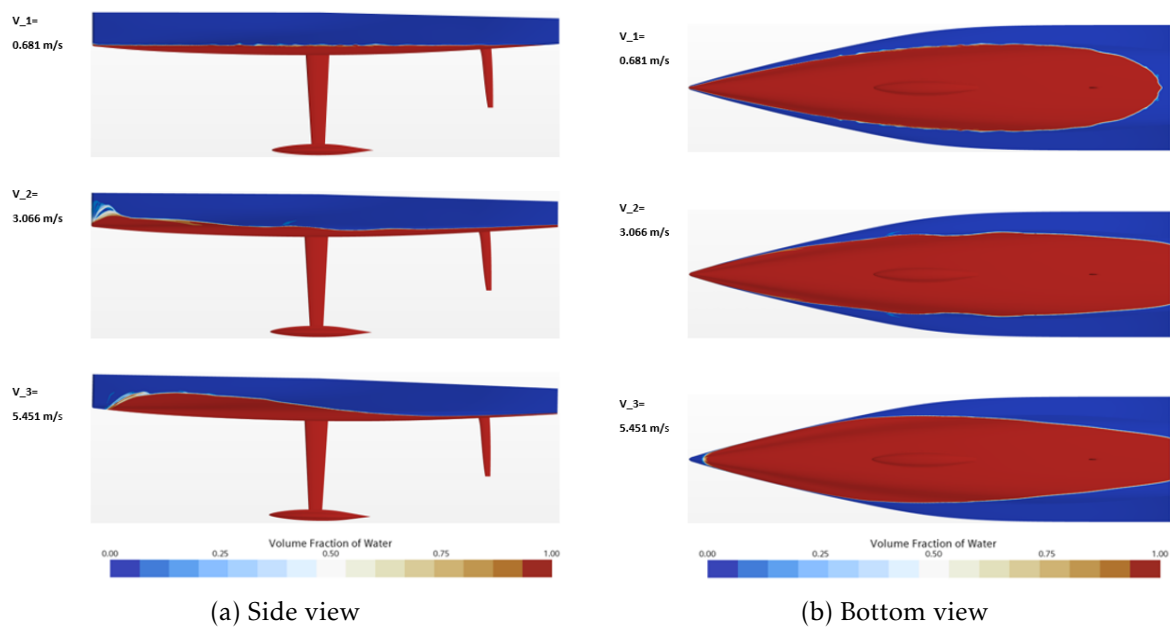


Figure 124: Bottom view

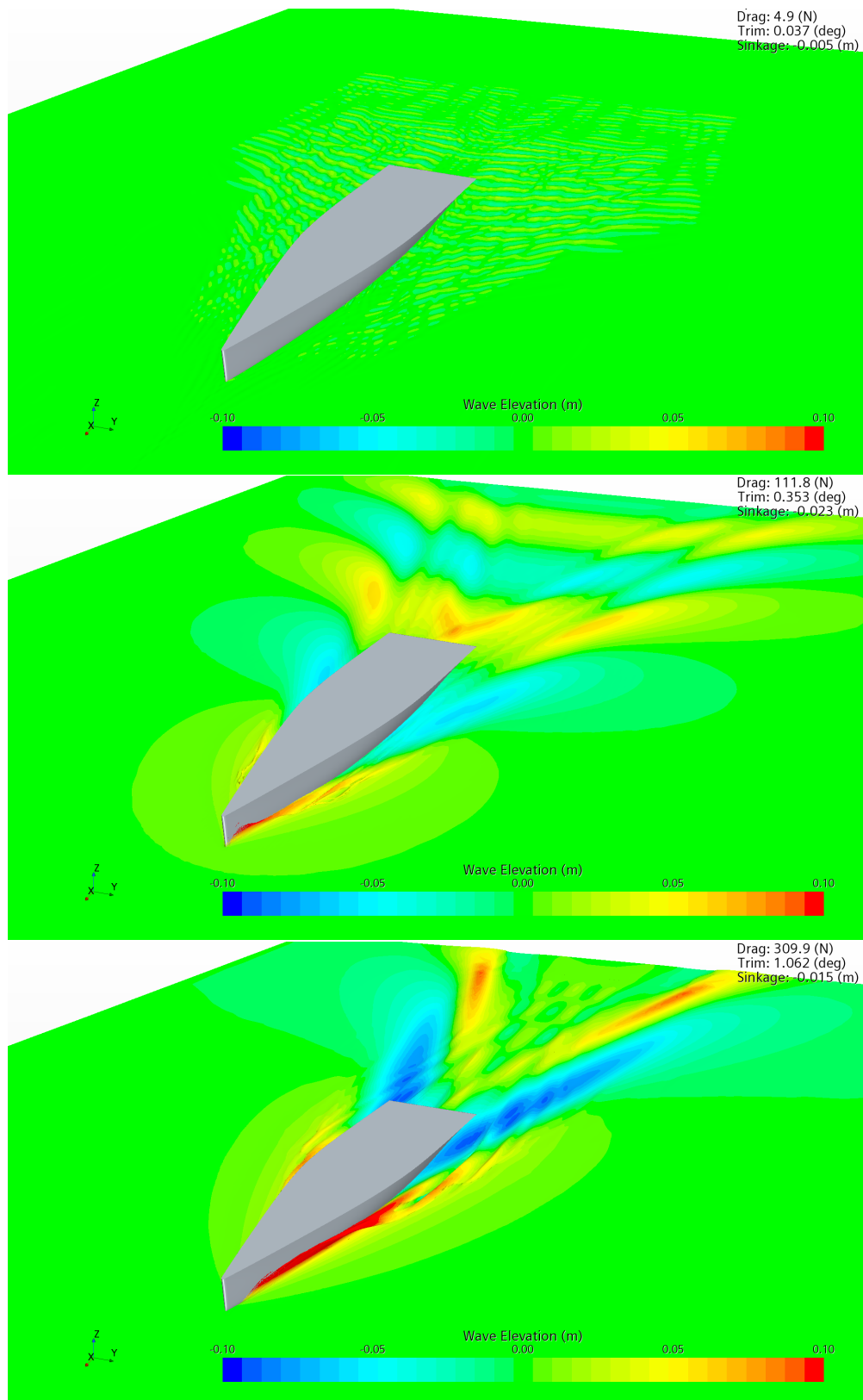


Figure 125: Wave pattern

## 14.4. Solution verification

### 14.4.1. Iterative error

A drop of 2/3 order of magnitude could be noted in figure 126a where the residuals normalized are shown; in addition they reach a low absolute value, except for the *sdr*, as shown in figure 126b. Under this consideration and monitoring the convergence of Drag, sinkage and trim, 127a, the iterative error is assumed to be negligible compared to the discretization error.

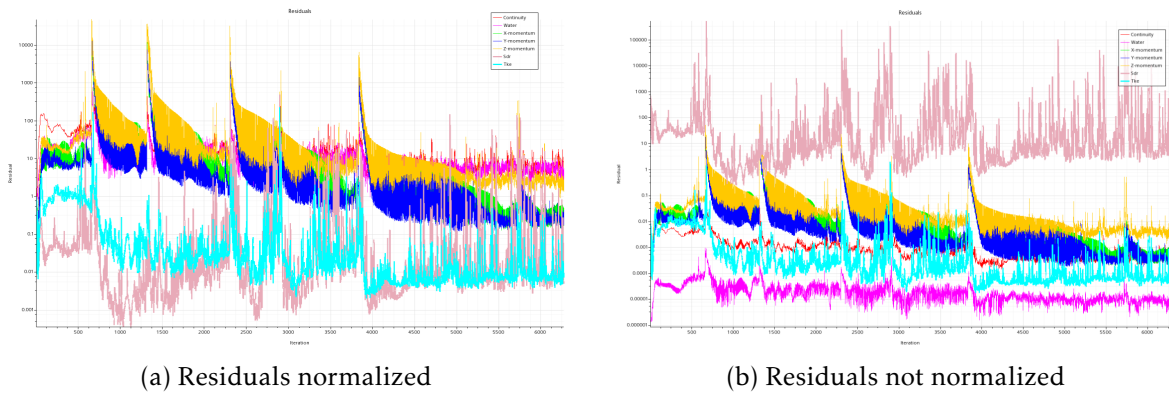


Figure 126: Residuals

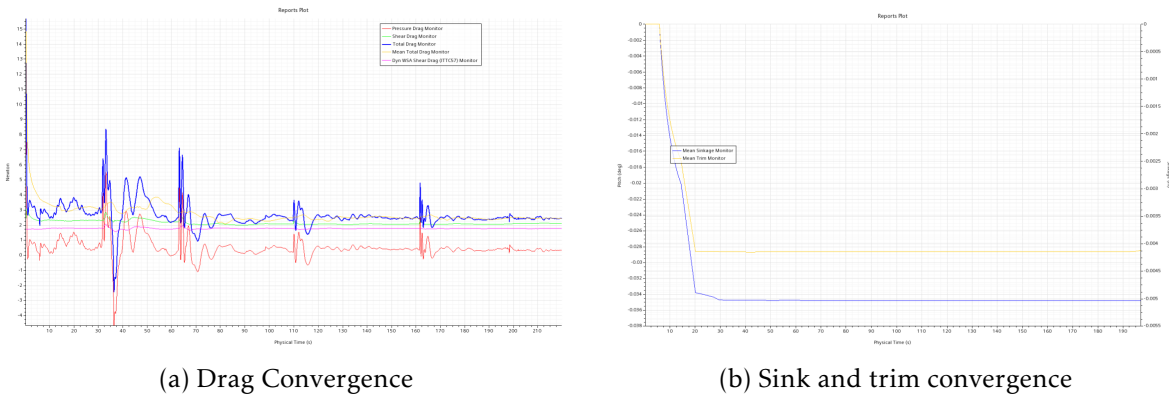


Figure 127: Variables convergence

### 14.4.2. Grid Convergence study

At first we can notice that 6 out of 9 cases present a monotonic behaviour and this, as we will see, is reflected in the quality of the interpolation that is defined by the grade of  $p$ : all but one presents a value between 0.5 and 2. Nevertheless as can be seen in figure 128, the difference with the experimental case is high enough especially for the sinkage.

### 14.4.3. Uncertainty calculation

Considering the lower number of cells obtained with the new meshing method adopted, the uncertainty calculation was carried out on the finest grid. In table 47 the numerical

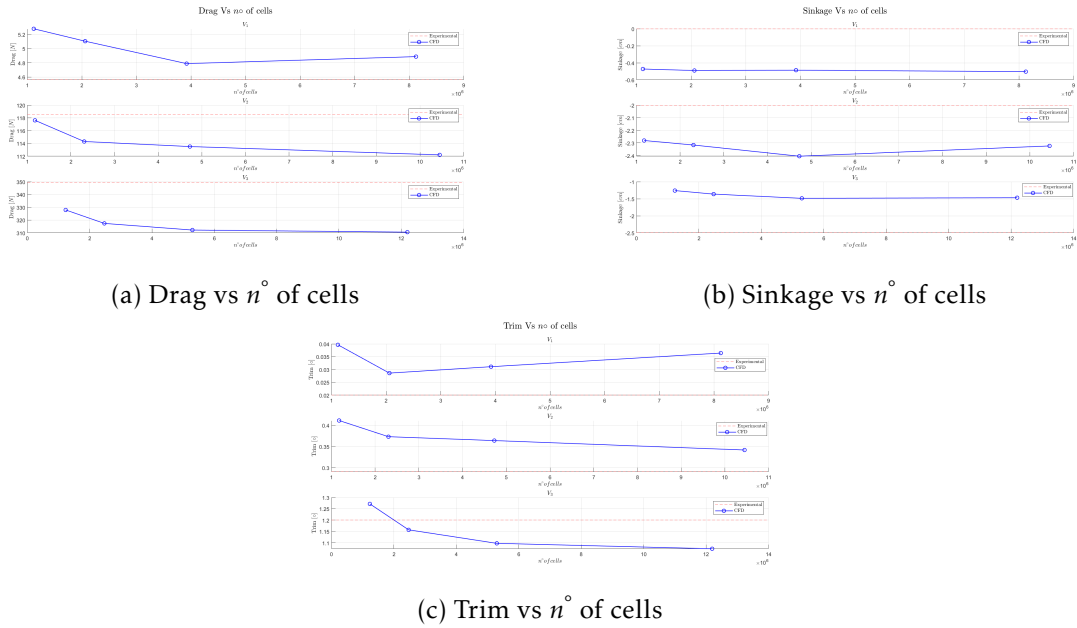


Figure 128: Variables vs  $n^\circ$  of cells

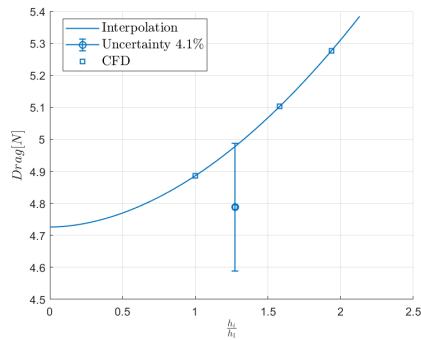
uncertainty is reported. As previously mentioned  $p$  expresses the good quality of the interpolation that is mirrored in the low value of the uncertainty. Only one solution presents an interpolation made with the first and second order polynomials that presents indeed an high value of uncertainty.

Figures 129, 130 and 131 show the value interpolated for the grid uncertainty calculation with the latter as an error bar.

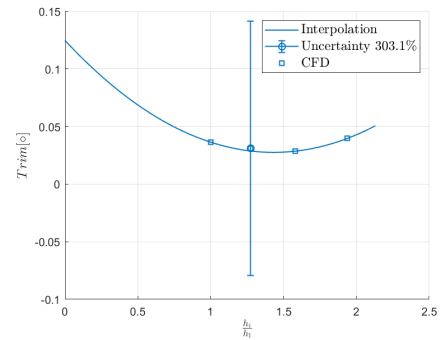
|       |        | $\phi_0$ | $\phi_1$ | $p$  | $U_{CFD}[\%]$ |
|-------|--------|----------|----------|------|---------------|
| $V_1$ | $D$    | 4.730    | 4.890    | 1.87 | 4.1           |
|       | $Trim$ | 0.125    | 0.036    | 1,2  | 303.1         |
|       | $Sink$ | -0.005   | -0.005   | 0.75 | 12.9          |
| $V_2$ | $D$    | 111.000  | 112.000  | 2    | 4.5           |
|       | $Trim$ | 0.320    | 0.342    | 1.85 | 11.5          |
|       | $Sink$ | -0.023   | -0.023   | 2    | 2.3           |
| $V_3$ | $D$    | 304.000  | 311.000  | 2    | 5.7           |
|       | $Trim$ | 1.01     | 1.070    | 2    | 17.9          |
|       | $Sink$ | -0.015   | -0.015   | 2    | 12.1          |

\* 1,2 Fit was made using first and second order exponents

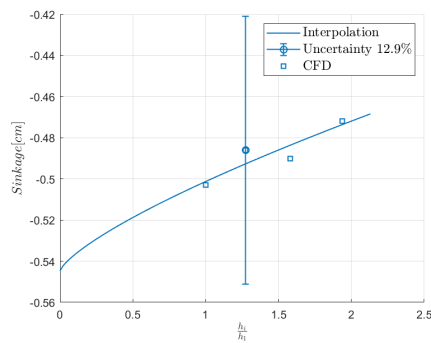
Table 47: Numerical uncertainty



(a) Drag

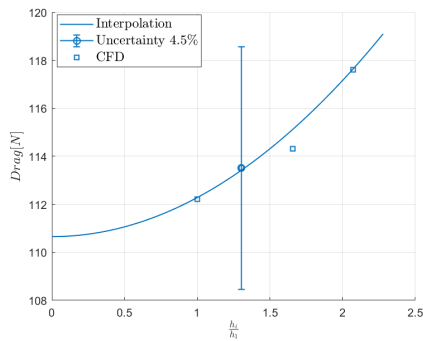


(b) Trim

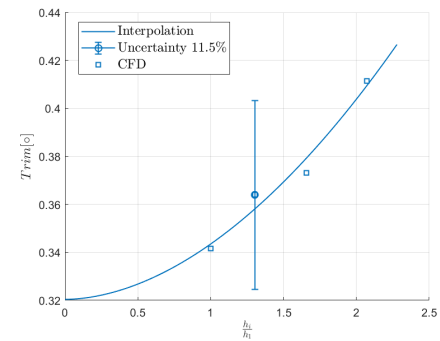


(c) Sinkage

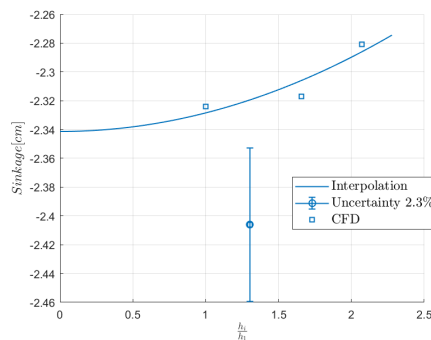
Figure 129: Open water characteristics vs grid refinement with error bar at  $V_1$



(a) Drag

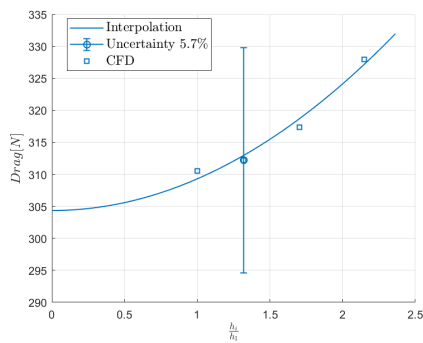


(b) Trim

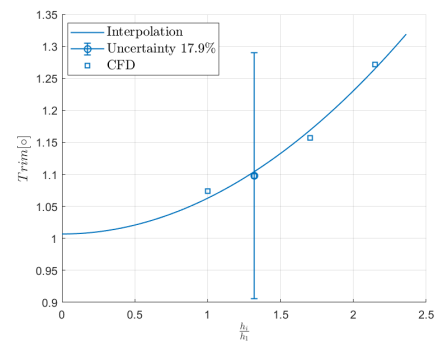


(c) Sinkage

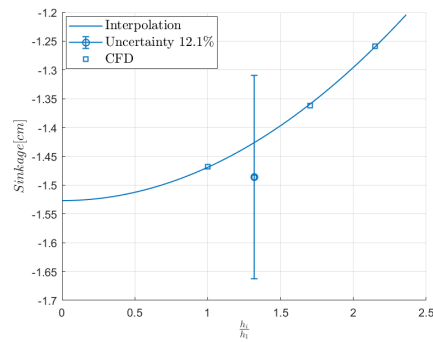
Figure 130: Open water characteristics vs grid refinement with error bar at  $V_2$



(a) Drag



(b) Trim



(c) Sinkage

Figure 131: Open water characteristics vs grid refinement with error bar at  $V_3$

### 14.5. Validation

The towing tank provided the experimental uncertainty, calculated following the *ITTC 7.5-02-02-02* procedure, only for the Drag. Due to this, the validation has been carried out only for the latter at the three speeds. The validation procedure produced validated

|       |                | $U_{CFD}[\%]$ | $U_{EFD}[\%]$ | $E[\%]$  | $U_{val}[\%]$ |
|-------|----------------|---------------|---------------|----------|---------------|
|       | <i>D</i>       | 4.39          | 0.50          | 7.15     | 4.42          |
| $V_1$ | <i>Trim</i>    | 552.00        |               | 82.12    |               |
|       | <i>Sinkage</i> | $\infty$      |               | $\infty$ |               |
|       | <i>D</i>       | 4.26          | 0.40          | -5.36    | 4.28          |
| $V_2$ | <i>Trim</i>    | 13.55         |               | 17.80    |               |
|       | <i>Sinkage</i> | -2.67         |               | -16.20   |               |
|       | <i>D</i>       | 5.07          | 0.30          | -11.11   | 5.08          |
| $V_3$ | <i>Trim</i>    | 16.02         |               | -10.51   |               |
|       | <i>Sinkage</i> | -7.11         |               | 41.28    |               |

Values are expressed in percentage of the experimental data

Table 48: Comparison error and validation uncertainty

results considering only the Drag cases. This must not be seen as a failure because the comparison error it's only slightly bigger than the validation uncertainty that in turn, is low enough. For what concerning the drag we cannot say that the modelling error is affecting the results.

|          | $V_1$ | $V_2$ | $V_3$ |
|----------|-------|-------|-------|
| <i>D</i> | NV    | NV    | NV    |

Table 49: Validation

**Conclusion** The new settings implemented solved the instability problems encountered during the first analysis.

These new settings led to an high quality level of the interpolation and then to a low value of  $U_{CFD}$  which means that the discretisation error is sufficiently low. This new method though, produced an high value in the comparison error that, can be interpreted as a signal of a strong influence of the modelling error. In fact if, as said before, the modelling error doesn't seem to strongly affect the drag solution, the same cannot be said for sinkage and trim whose comparison error results higher especially for the second one.

The explanation, can possibly be attributed to the equilibrium model. In the previous test case it was stated that this is not well suited for a planing hull. If initially the sailing yacht is in a displacement configuration, as we saw before, then it starts planing and makes the equilibrium model inappropriate for the simulation.

## 15. Conclusion

In the present work four test cases concerning a propeller, a ship, a planing hull and a sailing yacht undergone a Verification and Validation study. The latter has been carried out following the procedure developed for the maritime industry by *Luis Eça and Martin Hoekstra* [1]. In order to carry out the latter, a grid refinement study for each condition has been performed; four grids ranging from 1.5M to 15M cells have been used with constant refinement ratio of  $\sqrt{2}$ . For each characteristic analyzed a comparison error between the numerical and experimental value was computed and then for each condition a validation uncertainty was also obtained. In the end these two were compared and the result were validated.

In particular the propeller simulations show the highest precision. The comparison error in percentage shows values under the 10% for all the advancing ratios but the last one which presented the highest value for all the open water characteristics. The validation process generated 4 out of 15 cases validated. This is not deemed as a negative results considering the low value of the validation uncertainty which made the validation threshold more restrictive. Thus the propeller simulations are not considered affected by the model error.

The ship settings showed a good behaviour in predicting the ship performance. In contrast the comparison error showed an high value especially for the lowest speed. Nevertheless, if looking at the absolute value of the error, e.g. for the sinkage at  $V_1$  it consists in less then 1 mm on a 7 m model scale boat. 7 out of 9 cases were validated, but only the ones with an uncertainty smaller than 10 % were considered reliable.

The planing hull setting showed one of the best behaviour in performance prediction. Except for the trim at high speed, that shows the highest error around the 10%, the CFD results are almost stackable with the experimental ones. 4 out of 9 cases have been validated. As for the propeller, this is due to the low value of the validation uncertainty. An exception is the sinkage at  $V_3$  not retained reliable due to the high value of the uncertainty.

In the end, the last test case was the most problematic. It initially presented a numerical instability that was solved by modifying the settings and adopting the Multi Mesh Sequencing. The settings showed optimum capacity in predicting the drag but faced a few problems for trim and sinkage maybe caused by the DFBI equilibrium model adoption. For this test case the experimental uncertainty for the drag was the only one available. No condition was validated, however the difference between comparison error and uncertainty was marginal.

By way of conclusion of this thesis it can be said that CFD settings exposed in this work showed their capacity to well predict the flow field and the performance of the propeller and the vessels analyzed.

Benchmarking together with Verification and Validation is a good practice to verify the validity of the CFD settings without thrusting them blindly and keep them always updated. The CFD benchmarking lets the author be aware of the capacity of the CFD settings used.

The Verification and Validation procedure, although being a powerful tool in the hands of the CFD user in understanding the quality of its simulation, is still complicated and relies on the judgement of the user when it comes to be simplified. In the author's point of view, an automation of the process is necessary.

An important phase of this work has been the experimental data collection. The experimental data of towing tank test are not easy to find on internet and are often partially incomplete. This makes difficult to replicate numerically the same physical conditions. Therefore, the data needed and collected during a towing tank test sometimes don't match with the ones needed by CFD engineers to compare them with the numerical one. To solve this prob-



lem, it is recommended to CFD companies or research center, who are about to benchmark their settings, to be involved in the experimental campaign in order to be able to collect all the data needed.

**Future works** Following this thesis work, future studies can be conducted in order to get CFD results closer to the experimental one:

- Vary the mesh strategy;
- perform grid refinement study with a coarser range of grids in order to understand which is the minimum number of cells that still gives a good result;
- reduce the  $y^+$  value (aiming  $y^+ = 50$ ) while still lying inside the logarithmic layer;
- increase the number of iterations within a time step;
- evaluate the sensibility and the influence of the ventilation correction on the Courant number;
- evaluate the substitution of the inlet boundary condition at the symmetry plane with a symmetry boundary.

Nevertheless, it is very important as well to keep in mind the trade-off between computational cost and accuracy.

## References

- [1] M. Hoekstra L. Eça. “A procedure for the estimation of the numerical uncertainty of CFD calculations based on grid refinement studies”. In: *Journal of Computational physics* 262 (Jan. 2014), pp. 104–130.
- [2] Timothy G. Trucano William L. Oberkampf. “Verification and validation in computational fluid dynamics”. In: *Progress in aerospace science* 38 (2002), pp. 200–272.
- [3] “Dictionary of Ship Hydrodynamics”. In: International Towing Tank Conference. 2008.
- [4] H. C. Raven L. Larsson. *Ship resistance and flow*. Jersey city, New Jersey: J. Randolph Paulling, 2010.
- [5] United States Naval Academy. *RESISTANCE AND POWERING OF SHIPS*. URL: [https://www.usna.edu/NAOE/\\_files/documents/Courses/EN400/02.07%20Chapter%207.pdf](https://www.usna.edu/NAOE/_files/documents/Courses/EN400/02.07%20Chapter%207.pdf) (visited on 08/01/2022).
- [6] M. Orych L. Larsson R. E Eliasson. *Principles of yacht Design*. Fifth. London, England: Adlard Coles, 2022.
- [7] J. Carlton. *Marine Propellers and Propulsion*. Fourth. Cambridge, MA 02139, USA: Butterworth-Heinemann, 2018.
- [8] D.D’ambrosio. *Dispense di Fluidodinamica computazionale, Politecnico di Torino*. 2020.
- [9] K.T. Kim et al. “Transient implicit wave propagation dynamics with overlapping finite elements”. In: *Computers Structures* (Apr. 2018), pp. 18–33.
- [10] A. Bakker. *Lectures on Applied Computational Fluid Dynamics*. 2008. URL: <https://www.bakker.org/Lectures-Applied-CFD.pdf> (visited on 09/27/2022).
- [11] D. Tordella. *Dispense di Flussi Turbolenti, Politecnico di Torino*. 2020.
- [12] CFD online. *Wilcox’s k-omega model*. URL: [https://www.cfd-online.com/Wiki/Wilcox%5C%27s\\_k-omega\\_model](https://www.cfd-online.com/Wiki/Wilcox%5C%27s_k-omega_model) (visited on 09/13/2022).
- [13] Siemens. *STAR CCM+ Manual*.
- [14] J. Haider. “Numerical Modelling of Evaporation and Condensation Phenomena”. In: (Aug. 2013).
- [15] A. Dutta. *Boundary layer over a flat plate*. URL: <https://www.quora.com/Could-you-explain-the-mechanism-of-the-formation-of-the-boundary-layer-in-a-fluid-flowing-over-a-flat-plate> (visited on 09/27/2022).
- [16] G. Vaz L. Eça and M. Hoekstra. “A Verification and Validation exercise for the flow over a backward facing step”. In: V European Conference on Computational Fluid Dynamics. Lisbon, Portugal, 2010.
- [17] Christopher J. Roy William L. Oberkampf. *Verification and Validation in Scientific Computing*. Cambridge University Press, 2010.
- [18] Roache PJ. *Foundamentals of Verification and Validation*. Albuquerque, New Mexico: Hermosa publishers, 2009.
- [19] M. Hoekstra L. Eça. “Verification and Validation for marine Application of CFD”. In: 29th Symposium on Naval Hydrodynamics. Gothenburg, Sweden, Aug. 2012.
- [20] G. Vaz L. Eça. “Workshop on Verification and Validation of CFD for Offshore”. In: 2012.

- 
- [21] C.Liu J.Tu GH.Yeoh. *Computational fluid dynamics: a Pratical Approach*. Third. Cambridge, MA 02139, USA: Butterworth-Heinemann, 2018.
  - [22] M Hoekstra L. Eça. "Evaluation of numerical error estimation based on grid refinement studies with the method of the manufactured solutions". In: *Computers & Fluids* 38.021001-1 (Sept. 2009).
  - [23] Roache PJ. *Verification and Validation in computational science and engineering*. Albuquerque, New Mexico: Hermosa publishers, Aug. 1998.
  - [24] G. Chen A. Yu D. Wan. "Verification and validation for the resistance of a kriso container ship in calm water". In: International Ocean and Polar engineering Conference. Honolulu,Hawaii,USA, June 2019.
  - [25] A.De Marco et al. "Experimental and numerical hydrodynamic analysis of a stepped planing hull". In: *Journal of Applied Ocean Research* 64 (2017), pp. 135–154.
  - [26] P.J. Roache L. Eça K. Dowding. "On the interpretation and scope of the VV 20 Standard for verification and validation in Computational Fluid Dynamics and Heat transfer". In: VV Verification and validation Symposium. Baltimore,Usa, 2020.
  - [27] Schiffbau-Versuchsanstalt Potsdam. *SVA Potsdam*. <https://www.sva-potsdam.de/en/potsdam-propeller-test-case-pptc/>. Accessed: 2022-04-05.
  - [28] *Potsdam Propeller Test Case (PPTC) Open Water Tests with the Model Propeller VP1304*. report 3752. Schiffbau-Versuchsanstalt Potsdam GmbH, Marquardter Chaussee 100, 14469 Potsdam: SVA: Potsdam Model Basin, Apr. 2011.
  - [29] "Uncertainty analysis in CFD, Verification and Validation, Methodology and Procedures". In: ITTC-Recommended Procedures and Guidelines 7.5-03-01-01. International Towing Tank Conference. 2017.
  - [30] "Potsdam Propeller Test Case (PPTC) Open Water Test with the Model Propeller VP1304 Case 2.1". In: Second International Symposium on Marine Propulsors 2011. Potsdam, Germany, May 2011. URL: [https://www.sva-potsdam.de/wp-content/uploads/2016/03/smp11\\_case21\\_eval\\_OWT.pdf](https://www.sva-potsdam.de/wp-content/uploads/2016/03/smp11_case21_eval_OWT.pdf).
  - [31] D.R. Rijpkema J.M. Baltazar and J.A.Falcão de Campos. "Numerical studies for verification and validation of Open-Water propeller Rans Computations". In: VI International Conference on Computational Methods in Marine Engineering. Rome, 2015.
  - [32] MARITIME RESEARCH INSTITUTE NETHERLANDS. *VERIFICATION TOOLS*. 2022. URL: <https://www.marin.nl/en/free-resources/verification-and-validation/verification-tools> (visited on 05/17/2022).
  - [33] G. Vaz D. Rijpkema. "Viscous flow computations on propulsors: verification, validation and scale effects". In: RINA International Conference Developments in Marine CFD. London, UK, Mar. 2011.
  - [34] F. R. Menter. "Two-equation eddy-viscosity turbulence models for engineering applications". In: *AIAA journal* 32.8 (Aug. 1994).
  - [35] National Maritime Research Institute. *Tokyo 2015 A Workshop on CFD in Ship Hydrodynamics*. 2015. URL: <https://www.t2015.nmri.go.jp/index.html> (visited on 06/14/2022).
  - [36] L. Zou and L. Larsson. "Additional data for resistance, sinkage and trim". In: *Numerical Ship Hydrodynamics – An Assessment of the Gothenburg 2010 Workshop*. Ed. by Springer Business Media. Dordrecht.
-

- [37] “Uncertainty analysis in CFD, Verification and Validation, Methodology and Procedures”. In: ITTC-Recommended Procedures and Guidelines 7.5-03-02-03. International Towing Tank Conference. 2011.
- [38] CFD online. *SST k-omega model*. URL: [https://www.cfd-online.com/Wiki/SST\\_k-omega\\_model](https://www.cfd-online.com/Wiki/SST_k-omega_model) (visited on 08/24/2022).
- [39] *Uncertainty analysis in CFD Verification and Validation, Methodology and Procedures*. Tech. rep. International Towing Tank Conference, Sept. 2017.
- [40] R. Perić S. Enger M. Perić. “Simulation of Flow around KCS-hull”. In: ().
- [41] G. Vatteroni F.Cimolin F.Serra. “Optimization of the hull resistance for the Azimut 95’ yacht with CFD”. In: *Analisi E calcolo*. Jenuary/february 2015.
- [42] C. Pettinelli F. Cimolin. “Techniques to deal with numerical ventilation on fast planing hulls”. In: CD-adapco Turin Office, Jenuary 2016.
- [43] Land Rover BAR Andy Cloughton. *WIDE - LIGHT PROJECT*. Report. 1643 Warwick Avenue, Box 300 Warwick, Rhode Island 02889 USA: Sailing Yacht Research Foundation, Nov. 2015.

## A. PPTC Pre Tests

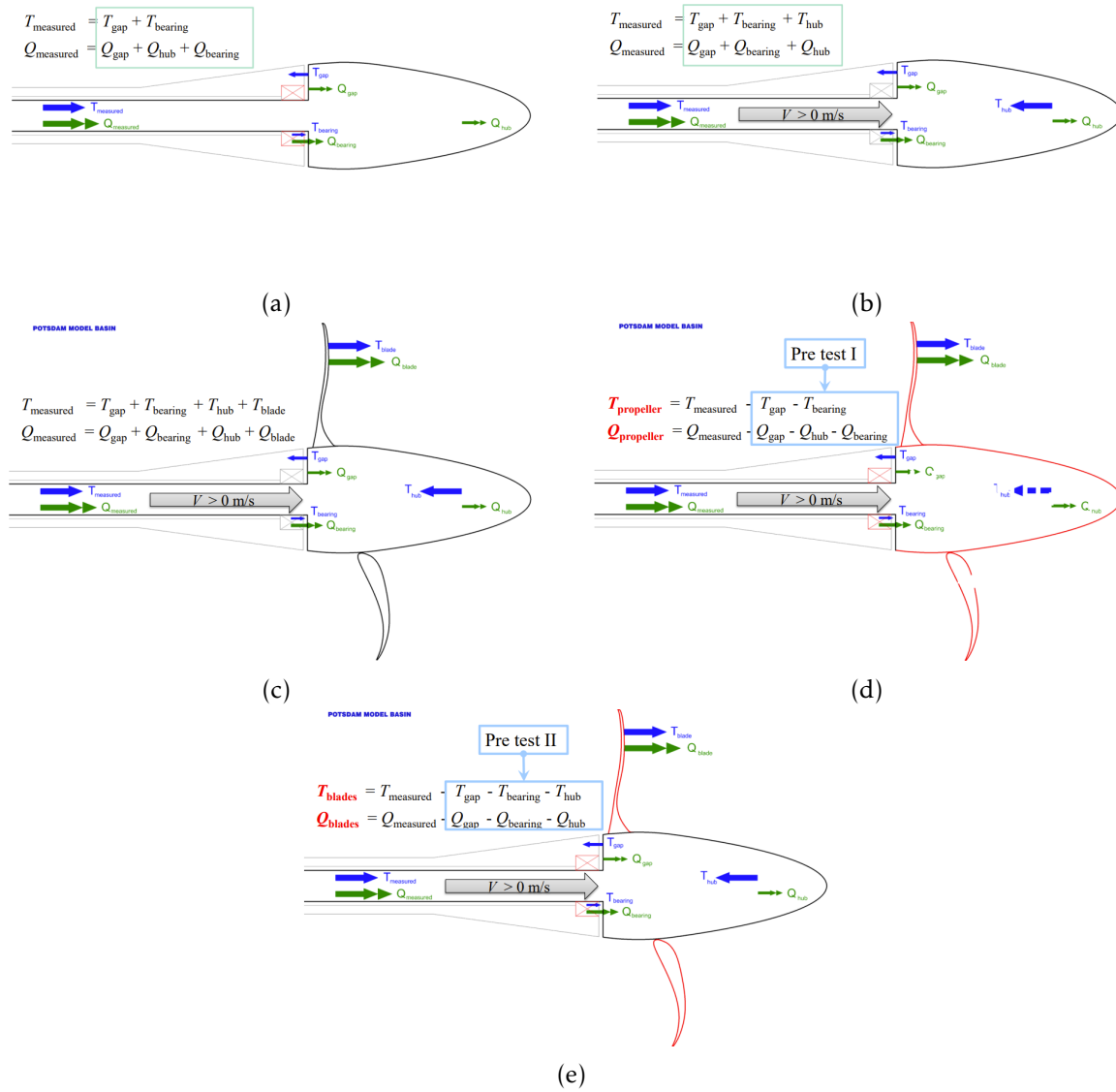


Figure 132: Pre Tests

## B. VOF WAVE Forcing and Damping

The VOF Waves model includes both wave forcing and wave damping capabilities. Although the flow usually takes place in a large domain, there is normally the need to know the solution only in the immediate vicinity of the body. Simcenter STAR-CCM+ can reduce the size of the computational domain and thus reduce the computing effort while not compromising the accuracy and reliability of the solution. To achieve this, the solution of the 3D Navier-Stokes equations is forced towards a solution that is based on a simplified theory (or a 2D solution in a larger domain) over some distance around the body. Momentum sources only are used—no Phase sources or Turbulence sources are applied. The forcing source terms adapt the solution to the simplified solution that is imposed at the reduced domain boundary. This forcing resolves the problem of specifying boundary conditions on the reduced solution domain boundaries.

Forcing can be used to damp the upstream-propagating waves before they reach the inlet boundary, allowing long-lasting simulations to be performed on a reduced domain. Disturbances by reflections from boundaries must be eliminated, particularly when the incoming waves are irregular and possible extreme events need to be captured reliably.

A VOF wave can also be damped in the vicinity of selected boundaries to reduce wave oscillation near those boundaries. The damping introduces vertical resistance to the vertical motion. For example, waves that are generated by floating bodies can be damped to avoid their reflection at boundaries. However, this damping approach cannot be applied at the inlet since the incoming waves would be damped as well. You can apply both forcing and damping to a region or boundary.

**Wave Damping** Damping of waves is possible by introducing resistance to vertical motion. Simcenter STAR-CCM+ implements the damping, adding a resistance term to the equation for  $w$ -velocity:

$$S_z^d = \rho(f_1 + f_2|w|)\frac{e^k - 1}{e^1 - 1}w$$

with

$$k = \left( \frac{x - x_{sd}}{x_{ed} - x_{sd}} \right)^{n_d}$$

where

- $x_{SD}$  is the starting point for wave damping (propagation in the  $x$  direction);
- $x_{ed}$  is the end point for wave damping (boundary)
- $f_1$ ,  $f_2$  and  $n_d$  are parameters of the damping model
- $w$  is the vertical velocity component.

considering that, the damping strength indicator  $r^d$  is given by:

$$r^d = \frac{e^k - 1}{e^1 - 1}$$

[13]

## C. Numerical Ventilation

A well-known problem with numerical simulations of marine vessels is the (unphysical) penetration of a thin layer of air travelling all across the hull. This can happen to both displacement hulls and planing hulls, although for the latter category it is usually far more relevant. Besides this could appear as a relatively small numerical error, it turns out to dramatically affect the global value of hull resistance, which is usually the most important outcome of the simulation. This is due to the fact that the shear component of the computed force is directly weighted by the phase volume fraction.

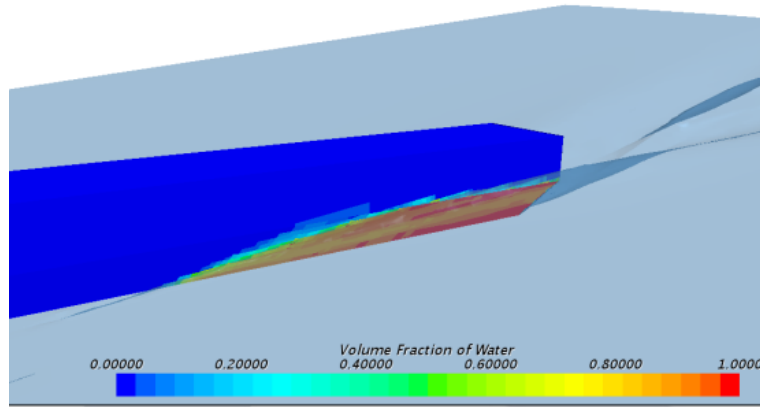


Figure 133: Hull with ventilation

### C.1. Possible strategies to fix the ventilation problem

Provided that we are sure that the air penetration below the hull is just numerical and not physical, to fix the problem we can select one of the following strategies:

- Manual correction of the shear component of the resistance force: simply accept the problem and get a corrected value as a postprocessing step (works well with moderate air ventilation).
- Local mesh refinement in the critical zones where the air enters below the hull (in principle best approach, but not always straightforward, computationally intensive)
- Artificial air extraction with an additional sink term (if properly set at the beginning of the simulation, automatically gives a corrected result)

If at the impingement zone the free surface is well defined, the air gets trapped below the hull just in the last layer of prisms. From there, there is no possibility to go away, since the Finite Volume solver is conservative. Hence, once the air is entered, it travels across all the remaining wet part of the hull.

Let's focus on a first prism layer cell where at regime there is such a travelling amount of air. Fig 134.

We can pick the integral form of the transport equation for the volume fraction of air and prescribe an air sink corresponding exactly to the quantity of air entering the cell.

$$\frac{\partial}{\partial t} \int_V \alpha_{air} dV + \int_S \alpha_{air} \vec{v} \cdot \vec{n} dS = \int_V S_{\alpha_{air}} dV \quad (66)$$

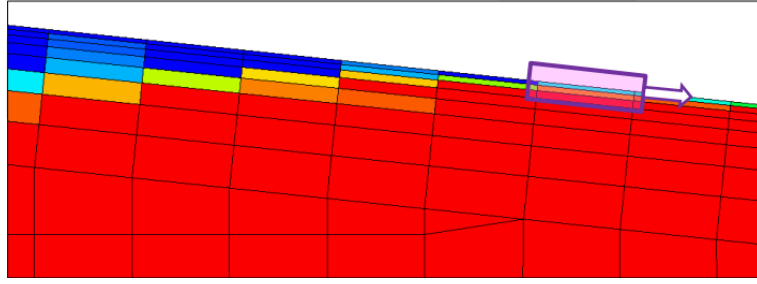


Figure 134: Hull with ventilation: last layer

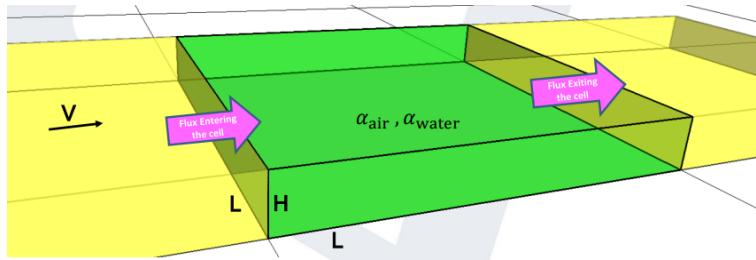


Figure 135: Air entering in the cell

for a cell size of  $L \times L \times H$  and flow velocity  $V$ , we have:

$$s_{\alpha_{air}} L^2 H = -\alpha_{air} V L H$$

$$s_{\alpha_{air}} = -\alpha_{air} \frac{V}{L}$$

Using the definition of Courant number  $C$  and time step  $\Delta t$ :

$$C = \frac{V \cdot \Delta t}{L}$$

we can get as final formula

$$s_{\alpha_{air}} = -k \alpha_{air} \frac{C}{L} \quad (67)$$

where  $k$  is a tuning coefficient with the meaning of the ratio of entering air eliminated through a single cell.

The formula for the air source is easily implemented in STAR-CCM+ via Field Functions, possibly limiting the maximum Courant Number to  $C_{max}$  to prevent stability problems (i.e. with  $C_{max} = 10$ ):

$$s_{\alpha_{air}} = -k \alpha_{air} \frac{\min(C, C_{max})}{\Delta t}$$

It is however recommended to activate the source term only where there is concrete risk of air entrapment, and not in the whole domain. Hence, we need to build a “zone” indicator function to use as multiplier for the air source, having value 1 only in the cells that are:

- **WET**  $\alpha_{air} > 0.5$



- Adjacent to the hull up to a certain distance
- Possibly within a certain range in  $X$
- ...

Air extraction is a very effective method to artificially remove the numerical ventilation issue

The method should be applied only where necessary (through the definition of a proper “zone” via Field Functions)

- It can work well only if the underlying assumptions hold true, namely:
  - The ventilation is only numerical and not physical;
  - The free surface doesn’t get smeared before impinging the hull;
  - The air gets entrapped only in the very first prism layer cells

## D. DFBI: Equilibrium

*Equilibrium body motion* it's an option to help you quickly achieve a quasi steady-state equilibrium position of a rigid body that is subject to fluid forces or other external forces. A marine *sink and trim* simulation is an example of such a case.

This option could be used to position and orient the rigid body in the flow so that the forces and moments acting on it are balanced in the chosen directions. The equilibrium body motion option has up to 6 *degrees of freedom*. The body moves within the specified directions according to a numerical iterative procedure until the forces and moments in these directions are balanced.

The numerical procedure to move the rigid body is purely mathematical, that is, there is no true physical motion of the rigid body. During the procedure, STAR-CCM+ moves the body in a stepwise manner, but does not solve an equation of motion. The body mass only plays a role for the gravity force which might need to be balanced to zero in the equilibrium state. The numerical procedure for finding the equilibrium position operates iteratively:

1. At a time-step, the numerical procedure calculates a translation and/or rotation step size;
2. The rigid body moves (translates and/or rotates) by the calculated translation and/or rotation step size as determined by the numerical procedure. The flow must then adapt to this change in position;
3. In this new position, inner time-steps are performed that calculate the forces and moments until STAR-CCM+ reaches either the Force and Moment Tolerance or the Maximum Inner Time-Steps. (Inner time-steps are regular time-steps. They are called inner time-steps because they apply between incremental movements of the body.). At this point, Simcenter STAR-CCM+ triggers any DFBI Equilibrium Forces Converged events that are associated with the body. These events in turn cause an update to any plots that depend on them.
4. The rigid body moves again by a certain distance as determined by the numerical procedure.

This process is repeated until the total of forces and the total of moments in the specified directions become zero. To reach good convergence of the procedure, forces and moments must converge well during the inner time-steps.

## E. Wide & Light M-1108

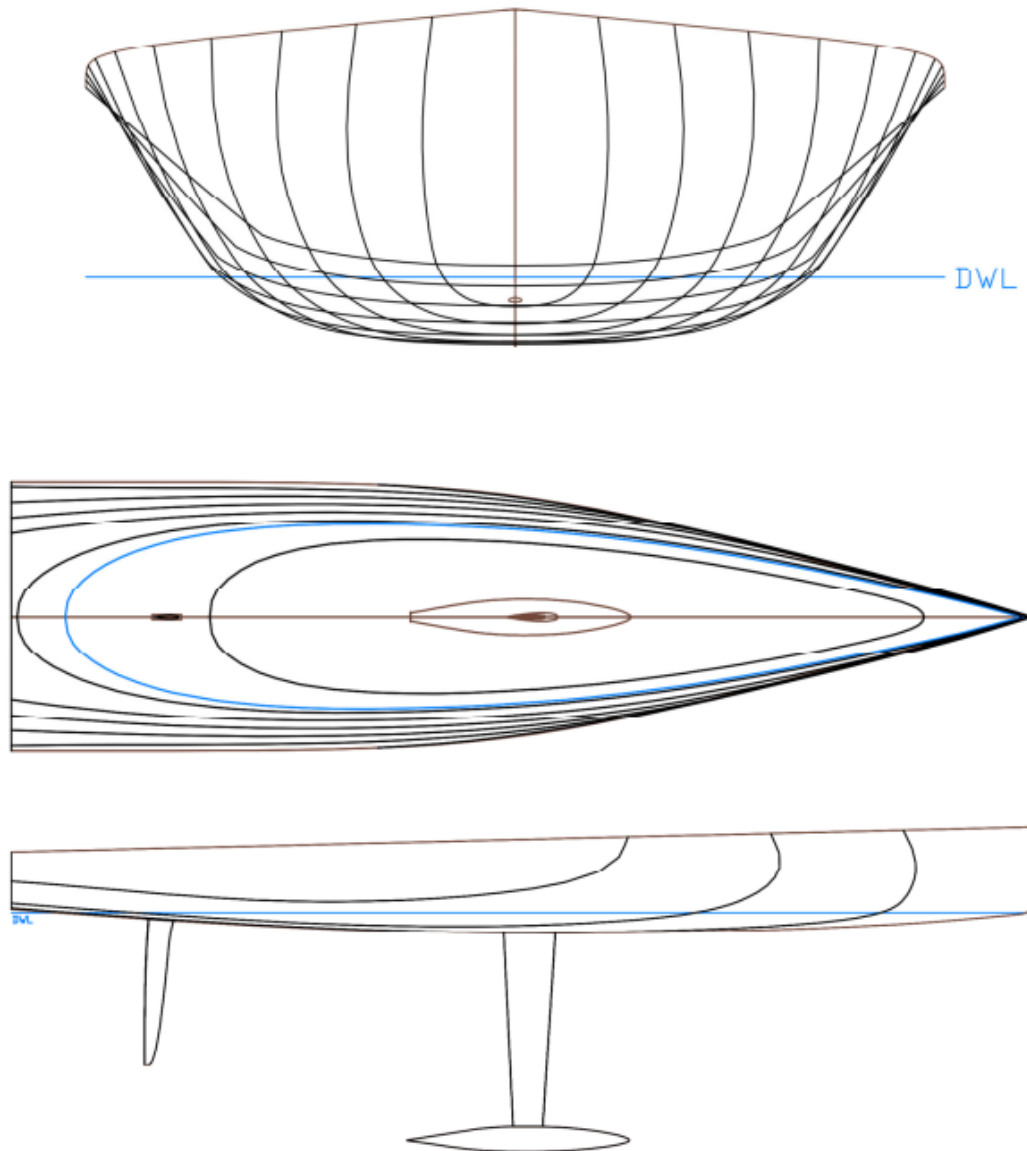
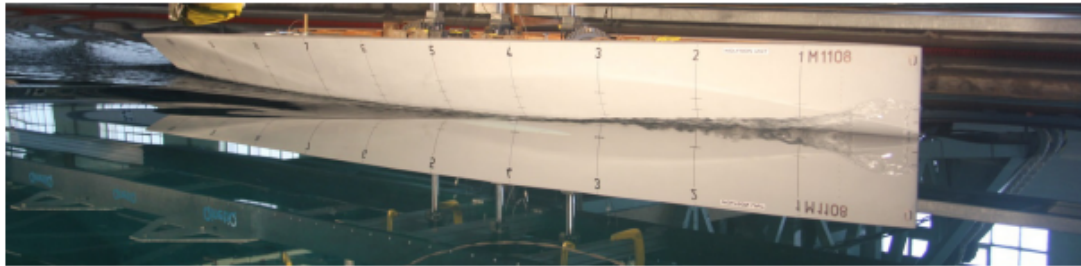


Figure 136: M-1108 waterlines

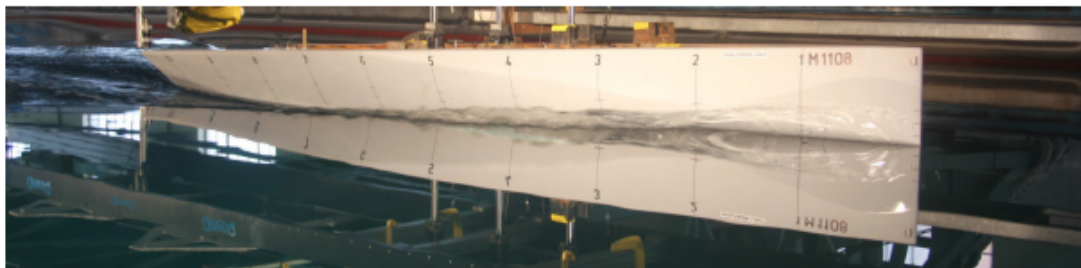
### E.1. Towing tank test

|                  |            | Speed 6 | Speed 9 | Speed 15 |
|------------------|------------|---------|---------|----------|
| Drag Bias        | $B_{Drag}$ | 0.1965  | 0.4596  | 1.0065   |
| Drag Precision   | $P_{Drag}$ | 0.1852  | 0.2805  | 0.5458   |
| Drag Uncertainty | $U_{Drag}$ | 0.2700  | 0.5384  | 1.1450   |
|                  | % error    | 0.5%    | 0.4%    | 0.3%     |

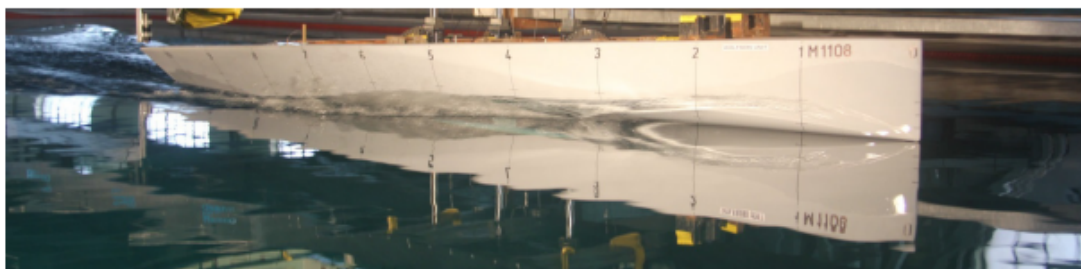
Table 50: Experimental Uncertainty Analysis



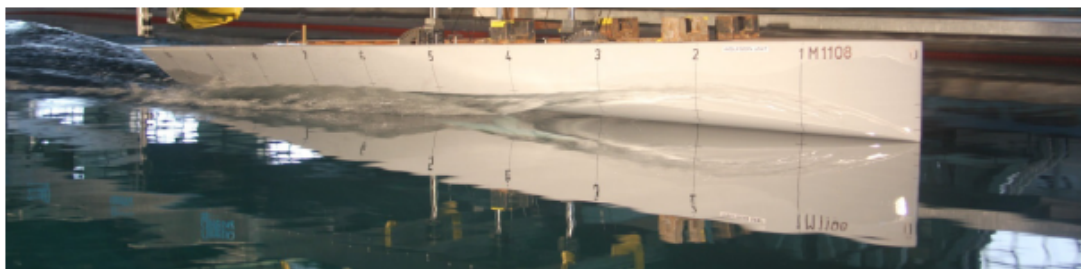
Speed Index 6, LCG Index 6



Speed Index 10, LCG Index 10



Speed Index 12, LCG Index 12



Speed Index 14, LCG Index 14

Figure 137: Towing test M-1108 upright, forward



Speed Index 6, LCG Index 6



Speed Index 10, LCG Index 10



Speed Index 12, LCG Index 12



Speed Index 14, LCG Index 14

Figure 138: Towing test M-1108 upright, backward



## F. TEST B1-9841

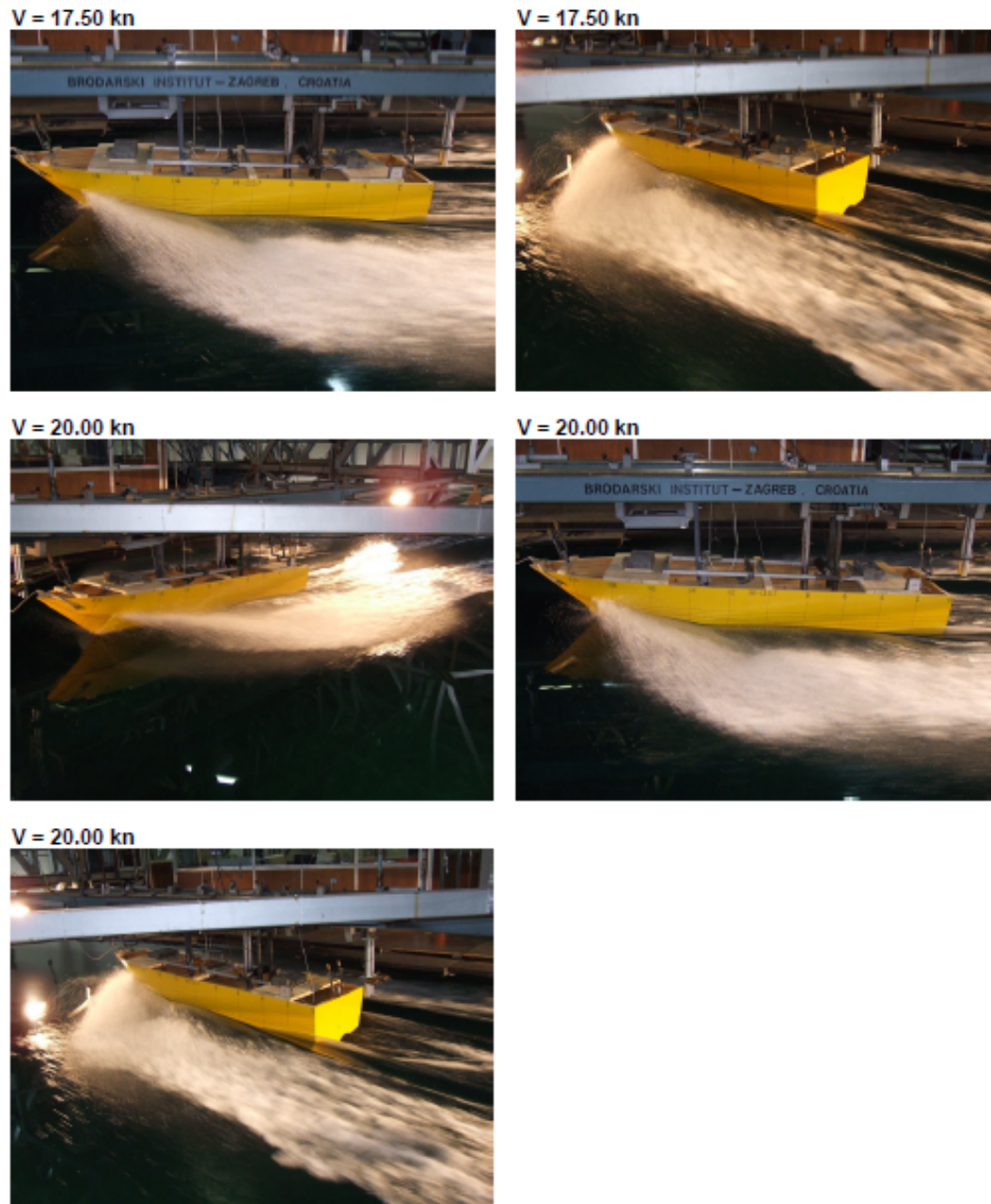


Figure 139: Towing test 9841

